THESE

En vue de l'obtention du

DOCTORAT DE L'UNIVERSITÉ DE TOULOUSE

Délivré par Institut National Polytechnique de Toulouse
Discipline ou spécialité : Enérgetique et Transferts

Par Patricia SIERRA SÁNCHEZ
Soutenue le : 23 janvier 2012

MODELING THE DISPERSION AND EVAPORATION OF SPRAYS IN AERONAUTICAL COMBUSTION CHAMBERS

JURY

R. FOX	Professeur à l'Université d'Iowa	Rapporteur
J. REVEILLON	Professeur à l'Université de Rouen	Rapporteur
O. SIMONIN	Professeur à l'INP de Toulouse	Président du jury
S. JAY	Chargé de recherche de l'IFP	Examinateur
A. ROUX	Ingénieur à Turbomeca	Examinateur
L. GICQUEL	Ingénieur au CERFACS	Directeur de thèse

École doctorale : Mécanique, Energétique, Génie civil, Procédés
Unité de recherche : CERFACS
Directeur de Thèse : Laurent GICQUEL
Co-Directeur de Thèse : Eleonore RIBER

THÈSE

présentée pour obtenir le titre de

DOCTEUR DE
L'INSTITUT NATIONAL POLYTECHNIQUE DE TOULOUSE

Ecole doctorale:	MeGeP
Spécialité:	Enérgetique et Transferts
Directeur:	Laurent GICQUEL
Co-directeur:	Eleonore RIBER

Par **Patricia SIERRA SÁNCHEZ**

MODELING THE DISPERSION AND EVAPORATION OF SPRAYS IN AERONAUTICAL COMBUSTION CHAMBERS

Soutenue le 23 Janvier 2012 devant le jury composé de:

R. O. FOX	Professeur à l'Université d'Iowa	Rapporteur
J. REVEILLON	Professeur à l'Université de Rouen	Rapporteur
O. SIMONIN	Professeur à l'INP de Toulouse	Examinateur
S. JAY	Docteur (IFP-EN)	Examinateur
A. ROUX	Docteur (Turbomeca)	Examinateur
L. GICQUEL	Chercheur au CERFACS	Directeur de thèse

Réf. CERFACS : TH/CFD/12/6

Abstract

Combustion still represents about 90% of the energy production in the world. Most industrial burners are fuelled with liquid hydrocarbons. However, most studies have been dedicated to gaseous ßames and the impact of liquid spray is still misunderstood. The purpose of this study is to improve the modelisation of two main phenomena occurring between atomization and combustion, i.e. the droplet dispersion in the turbulent gaseous flow and the evaporation process, in the context of Large Eddy Simulation (LES) of complex configurations.

First, the mesoscopic Euler-Euler approach (Février *et al.* (2005)) based on a conditioned ensemble averaging and implemented in AVBP is improved. The closure model (Simonin *et al.* (2001), Kaufmann (2004)) for the second-order moments appearing in the transport equations solved fails in mean-sheared configurations (Riber (2007)). Several new models proposed by Masi (2010) and a priori tested in a particle-laden slab are tested a posteriori in the same configuration. A quantitative analysis based on several calculations varying the Stokes number, the gaseous Reynolds number and the grid resolution allows to retain a non-linear model using the particle rate-of-strain tensor as timescale and called 2ΦEASM3.

The second part consists in improving the evaporation model implemented in AVBP which assumes infinite conduction in the liquid and spherical symmetry in the gas phase along with simplified thermodynamics and transport properties calculation. A new model is proposed, where the dependence of gaseous mixture viscosity on local composition is accounted for, and the Prandtl and Schmidt numbers are fixed by a reference equilibrium calculation using complex thermodynamics and transport properties. This method shows good agreement with experimental measurements in the configuration of an isolated droplet evaporating in quiescent N_2 without further increasing the computational cost.

Finally, the impact of the new models is analysed in the LES of the MERCATO semi-industrial configuration (García-Rosa (2008)). Although the experimental data are not sufficient to confirm the results, both the droplet distribution and the fuel mass fraction are significantly affected, which would eventually affect the ignition process.

Resumé

Dés nos jours, la combustion représente encore un 90% de la production totale d'énergie au monde. La plupart des brûleurs de type industriel utilisent comme carburant des hydrocarbures en forme liquide. Cependant, un grand nombre d'études ont été dédiés aux flammes gazeuses et l'impact du spray liquide est encore loin d'être totalement compris. Le but de cet étude est l'amélioration de la modélisation des deux phénomènes principaux qui ont lieu entre l'atomisation du spray et la combustion, i.e. la dispersion des gouttes par la turbulence gazeuse et le procès d'évaporation dans le contexte de la Simulation Aux Grandes Echelles (SGE) des configurations complexes.

Premièrement, l'approche Euler-Euler mésoscopique (Février *et al.* (2005)), basée sur une moyenne d'ensemble conditionnée et implémentée dans AVBP est amélioré. Le modèle de fermeture (Simonin *et al.* (2001); Kaufmann (2004)) pour les moments de deuxième ordre qui apparait dans les équations de transport résolues échoue quand appliqué à des configurations cisaillées (Riber (2007)). Plusieurs modèles proposés récemment par Masi (2010) et qui ont été valides *a priori* dans une configuration de nappe chargée de particules sont validés *a posteriori* dans la même configuration. Un analyse quantitative sur plusieurs cas avec diffèrent nombres de Stokes, nombres de Reynolds de la phase gazeuse et résolutions du maillage ont permit de retenir un modèle non-linéaire nommé 2ΦEASM3, qui utilise le tenseur de déformations de la phase dispersée comme échelle de temps caractéristique.

La deuxième partie a pour but l'amélioration du modèle d'évaporation implémenté dans AVBP. Ce modèle suppose une conduction infinie dans la phase liquide et symétrie sphérique dans la phase gazeuse ainsi que des lois simplifiées pour les propriétés thermodynamiques et de transport. Un nouveau modèle prenant en compte la dépendance de la viscosité du mélange gazeux avec la composition locale, et des nombres de Prandtl et Schmidt fixés par les valeurs à l'équilibre obtenus par moyen d'une simulation prenant en compte des lois complèxes pour les propriétés thermodynamiques et de transport est proposé. Cette nouvelle méthode produit des résultats en bon accord avec les mesures expérimentales pour l'évaporation d'une goutte isolé en une atmosphère d'azote au calme sans pourtant augmenter le cout du calcul.

Finalement, l'impacte des nouveaux modèles est analysé dans une SGE de la configuration semi-industrielle MERCATO (García-Rosa (2008)). Bien que les données expérimentales ne soient pas suffisantes pour confirmer les résultats, les distributions de gouttes et de carburant gazeux sont significativement affectés par les modèles, ce qui pourrait avoir un impact directe sur le procès d'allumage.

Contents

Acknowledgements

Après trois ans merveilleux passées entre autres à travailler sur cette thèse, le moment est arrivée de remercier ceux qui d'une facon ou d'une autre ont contribué a que cet instant soit arrivée.

Je voudrais commencer par remercier sincèrement les membres du jury de thèse qui ont d'abord accepté de faire partie de ce moment ultime de la vie d'une thèse et qui ont aussi lu ce manuscrit et apporté ses opinions et conseils. Ce travail a pu être mené a terme dans les meilleures conditions possibles grâce aux ressources fournis par le CERFACS, qui sont nombreux. Un grand merci donc au laboratoire et en spécial à Thierry Poinsot de m'avoir accueilli au sein de l'équipe CFD. Merci aussi a Laurent et Bénédicte, vos conseils et idées ont été précieuses et l'encadrement exceptionnel. Comme exceptionnel a été le suivi de la part de Eleonore. Comme j'ai déjà dit à la soutenance, elle a été le moteur derrière ce travail, je pense que je serais pas en train d'écrire ces lignes si elle m'aurait pas été ma co-directrice, elle a suivi pas par pas mon travail, et m'a guidé tout le long de ces trois ans. Un grand merci de tout mon coeur Ele! Merci aussi à Olivier, qui m'a toujours aidé quand j'arrivais en criant: "Olivieeeer, ca ne marche pas!!!!", toujours souriant, c'est un vrai plaisir de travailler avec des gens comme ca. Et merci a Gab pour son aide, même tard le soir par téléphone.

Merci aussi au reste de l'équipe CFD, Marie et Nicole en particulier, à l'équipe administrative, Michèle et Chantal vous êtes uniques!!! Et je ne peux pas oublier l'équipe CSG au complet qui sont toujours là pour résoudre nos problèmes informatiques... vous tous, faites que nos thèses se passent mieux!

Disait Olivier Simonin pendant la soutenance que j'ai résisté a Enrica, et que ca ce n'est pas gagné. Tout au contraire, je pense que ca a été une énorme chance de pouvoir compter sur elle pendant ce travail, toujours dispo, toujours à l'écoute, à des heures quand la plupart des gens dort, Enrica parlait avec moi de mésoscopique, tenseurs et modèles, sans jamais s'endormir! Merci beaucoup bella! Merci aussi a Jérôme qui a apporté ses idées à ce travail, même si à la fin on n'a pas pu avoir des thèse jumelles, elles sont quand même cousines au moins! Je promets faire un petit détour par la Californie pour vous rendre visite.

Je voudrais aussi remercier Prof. Polifka et tout l'équipe de TUM qui m'ont accueilli pendant trois mois de dur hiver bavarois, spécialement Fred, Gary, Alejandro, Eva, Patrick , etc... J'ai adoré mon séjour à Munich!!!

Ce temps passé à Toulouse m'a donne beaucoup plus qu'un titre de Docteur à ajouter au CV, j'ai voyagé et j'ai connu des gens merveilleux. Jorge, Camilo, Elsa, Marta (a ver si nos vemos por Chicago y me llevas a esas tiendas chulas que me dijiste), Kerstin (on doit aller boire une Dunkel-Weissbier au Oktoberfest un de ces jours), Felix, Jean-Mattieu, Alex, Jean-Philippe, Geoffy et tant d'autres! Une spécial dédicace méritent le grand allemand et la petite italienne. Merci Matthias, t'as été un grand support, les galères en fin de thèse, partagées sont moins galères. T'es vraiment la personne la plus gentil que je connaisse, et aussi la plus forte, nous supporter à Beni et à moi pendant trois ans sans devenir complètement fou a du mérite! Et Benedetta! un enooormissime merci pour ta joie de vivre, tes rigolades qui me font toujours sourire, et tous ces moments qu'on a partagé ensemble, je crois qu'on a fait un bon équipe entre tous! Les petits déjs au marché vont trop me manquer! Merci aussi a Roberto qui a trop géré le jour de ma soutenance. Finalement, entre toutes ces personnes merveilleuses que j'ai rencontré, j'ai aussi trouvé mon ami, mon guide, cette personne unique, merci d'être là Victor.

J'ai toujours pensée que où que je puisse arriver, je l'aurait fait grâce à mes parents. Etant petite ils m'ont appris la valeur du travail bien fait, que persévérer est égal à réussir et surtout que je peux faire tout ce que je me propose, que la limite c'est moi même (ce qui n'est pas négligeable!). Ils ont toujours accepté mes choix (plus

ou moins facilement) et ils m'ont toujours soutenu dans mes décisions. Pas seulement ca, mais ils ont réussi á me convaincre de continuer quand je voulais tout abandonner. Leur support, et surtout leur affection ont été des éléments clé pendant ces trois ans. Je ne peux pas m'empêcher de penser que j'ai la meilleur famille au monde. Merci de tout mon coeur.

Finalement, le moment tant espéré est déjà passé, on tend a penser que ca n'arrivera jamais, mais il approche tellement rapidement que on dirait que c'était hier quand je commencais à faire de la biblio et les fameux (infâmes ?) QPFs! On apprend tellement de choses en faisant une thèse qu'à la fin on ne se rend pas compte de la place que ca prend (plus en concret 5 boites en carton 30x40x60 cm), mais ca reste toujours avec nous et nous donne un nouveau regard sur plein de choses. Maintenant j'espère juste ne pas perdre ce regard critique dans les étapes qui m'attend maintenant de l'autre cote de l'Atlantique.

List of symbols

Roman letters

Symbol	Description	Units
b	Exponent of the Power law	
$b^*_{p,ij}$	RUM anisotropy stress tensor	
$\mathbf{c}_p$	Particle veloctiy	[m/s]
C_D	Drag coefficient	[-]
C_m	Added-mass force constant	[-]
C_p	Specific heat capacity at constant pressure of the fluid	$[\mathrm{J}/(\mathrm{kgK})]$
C_v	Specific heat capacity at constant volume of the fluid	$[\mathrm{J}/(\mathrm{kgK})]$
C_w	Constant of the Smagorinsky model	[-]
D_k	Molecular diffusivity of the species k	$[\mathrm{m}^2/\mathrm{s}]$
e_s	Specific sensible energy of the fluid phase	$[\mathrm{J}/\mathrm{kg}]$
E	Total non-chemical energy	$[\mathrm{J}/\mathrm{kg}]$
$E(\kappa)$	Energy spectrum	
f_i	Component (i) of the volumetric force vector	$[\mathrm{kg}/(\mathrm{ms}^2)]$
f_p	PDF function	
F_{AM}	Added-mass force	[N]
F_D	Drag force	[N]
F_H	Basset force	[N]
F_L	Lift force	[N]
$F_{p,i}$	Component (i) of the vector of forces acting upon a particle	$[\mathrm{kg}/(\mathrm{ms}^2)]$
$F^u_{p,i}$	Component (i) of the vector of forces that would act on a fluid particle occupying the position of the particle	$[\mathrm{kg}/(\mathrm{ms}^2)]$
$F^p_{p,i}$	Component (i) of the vector of forces acting upon a particle due to perturbations on the fluid field due to the presence of the particle	$[\mathrm{kg}/(\mathrm{ms}^2)]$
$\mathcal{F}^{\mathcal{I}}$	Inviscid flux tensor of conservative variables	$[\mathrm{kg}/(\mathrm{m}^2\mathrm{s}^2)]$
$\mathcal{F}^{\mathcal{V}}$	Viscous flux tensor of conservative variables	$[\mathrm{kg}/(\mathrm{m}^2\mathrm{s}^2)]$
$\mathcal{F}_p$	Particle flux tensor	
$\mathcal{F}^{\mathcal{U}}_p$	Particle flux tensor due to the uncorrelated motion	
$\mathcal{F}^{\mathcal{M}}_p$	Particle flux tensor due to convection of the mesoscopic motion	
g_i	Component (i) of the gravity vector	$[\mathrm{kg}/(\mathrm{ms}^2)]$
G_Δ	Low-pass filter	
h_s	Sensible enthalpy of the fluid/ gas phase	$[\mathrm{J}/(\mathrm{kg})]$
$h_{s,l}$	Sensible enthalpy of the liquid/ particle	$[\mathrm{J}/(\mathrm{kg})]$
h_p	Particle enthalpy	[J/(kg)
$\mathcal{H}_f$	Carrier fluid realization	
$\mathcal{H}_p$	Particle phase realization	
$\mathbf{I}$	Identity matrix	
$J_{j,k}$	Component (j) of the diffusive flux vector of the species k	$[\mathrm{kg}/(\mathrm{ms}^2)]$
k	Turbulent kinetic energy	$[\mathrm{m}^2/\mathrm{s}^2]$
$\mathcal{L}$	Characteristic length scale	[m]
L_{evap}	Latent heat of evaporation	$[\mathrm{J}/(\mathrm{kg})]$
m_p	Particle mass	[kg]
$\dot{m}_F$, $\dot{m}_p$	Mass transfer rate	[kg/m^3s]
$\delta\breve{M}_{p,ijmn}$	4^{th} order particle uncorrelated velocity correlations tensor	
n_p	Number of particles per unit volume	$[1/m^3]$
N_p	Number of particles	
P_g	Pressure	$[\mathrm{N}/\mathrm{m}^2]$
q^2_f	Fluid turbulent kinetic energy	[J]

q_{fp}	Fluid-particle correlation	[J]
$q^2_{f@p}$	Fluid turbulent kinetic energy sampled along particle trajectories	[J]
$q_{g,i}$	Component (i) of the heat flux vector	$[\mathrm{J}/(\mathrm{m}^2\mathrm{s})]$
q^2_p	Particle kinetic energy	[J]
δq^2_p	Particle Random Uncorrelated Energy	[J]
$\delta\breve{Q}_{p,ijm}$	3^{rd} order particle uncorrelated velocity correlations tensor	
r	Gas constant of a mixture (mass)	[J/(kg K)]
$r_p(d_p)$	Particle radius (diameter)	[m]
$\mathcal{R}$	Universal gas constant (molar)	[J/(mol K)]
$\breve{\mathbb{R}}_{p,ij}$	Mean mesoscopic stress tensor	
$\delta\mathbb{R}_{p,ij}$	Mean RUM stress tensor	
$\delta\breve{R}_{p,ij}$	Component (i,j) of the uncorrelated motion stress tensor	$[\mathrm{m}^2/\mathrm{s}^2]$
$\delta\breve{R}^*_{p,ij}$	Component (i,j) of the uncorrelated motion deviatoric stress tensor	$[\mathrm{m}^2/\mathrm{s}^2]$
s	Specific entropy of the fluid phase	$[\mathrm{J}/\mathrm{kg}]$
$\mathbf{s_{l-g}}$	Source term vector (liquid to gaseous phase)	
$\mathbf{s_{p-g}}$	Source term vector (particle to gaseous phase)	
$\mathbf{s_p}$	Source term vector (particle phase)	
$\mathbf{s_{g-p}}$	Source term vector (gaseous to particle phase)	
$\mathbf{s}_\theta$	Source term vector (linked to the uncorrelated motion)	
s_{ij}	Component (i,j) of the velocity deformation tensor	$[\mathrm{m}/\mathrm{s}^2]$
$S_{g,ij}$, $S_{p,ij}$	Rate of strain tensor in the gas/dispersed phase	[1/s]
$\mathbf{S}$	Particle rate-of-strain tensor	$[s^{-1}]$
T	Temperature of the fluid/ gas	[K]
T_p	Temperature of the particle	[K]
$\mathbf{u}$, u_i	Fluid velocity vector/ component (i)	[m/s]
$u_{p,i}$	Component (i) of the particle velocity vector	[m/s]
$\mathbf{u}_{f@p}$, $\mathbf{u}_{f@p,i}$	Undisturbed fluid velocity vector at the position of the particle/ component (i)	[m/s]
$\mathcal{U}$	Characteristic velocity	[m/s]
$\mathbf{v_p}$, $\mathbf{v_{p,i}}$	Particle velocity vector/ component (i)	[m/s]
V^c_i	Component (i) of the correction diffusion velocity	[m/s]
$V^{k,i}$	Component (i) of the diffusion velocity of the species k	[m/s]
$\mathbf{w}$	Conservative variables vector for the carrier fluid	
$\mathbf{w}_p$	Conservative variables vector for the dispersed phase	
$\mathcal{W}$, $\mathcal{W}_k$	Molecular weight of gaseous mixture/ of species k	$[\mathrm{kg}/\mathrm{m}^3]$
W_θ	Drag force source term	
$x_{p,i}$	Component (i) of the particle position vector	[m]
X_k	Molar fraction of the species k	[-]
Y_k	Mass fraction of the species k	[-]

Greek letters

Symbol	Description	Units
α_l, α_p	Liquid (particle) volume fraction	[-]
$\delta(\cdot)$	Dirac delta function	[-]
δ_{ij}	Component (i,j) of the Kronecker delta	[-]
$\delta\theta_p$	Random Uncorrelated Energy	[J]
Δ	Characteristic filter width	[m]
$\Delta h^0_{f,k}$	Formation enthalpy of the species k	$[\mathrm{J}/\mathrm{kg}]$
ϵ	Turbulent dissipation rate	
η_k, η	Kolmogorov length scale	[m]

Γ	Mass evaporation rate	[kg/m^3s]
κ_{RUM}	Uncorrelated diffusion coefficient	[kgm^2/s]
λ_g	Thermal conductivity of the fluid/ gas	[J/(mKs)]
μ_g	Dynamic viscosity	[kg/(ms)]
μ_p	Particle mass	[kg]
ν_g	Kinematic viscosity	[m^2/s]
ν_{RUM}	RUM viscoisty	[Js]
ν_t	Turbulent kinematic viscosity	[m^2/s]
Ω_g	Fluid vorticity	[s^{-1}]
$\mathbf{\Omega}$	Particle mesoscopic rotation tensor	[s^{-1}]
Φ_p	Heat transfer rate	[W/m^3]
Φ^c	Particle conductive heat flux	[J/s]
Φ^{cv}	Particle convective heat flux	[J/s]
Π_g	Sensible energy transfer rate due to evaporation and thermal conduction	[W/m^3]
ρ_g	Fluid/ gas density	[kg/m^3]
ρ_k	Partial density of the species k	[kg/m^3]
ρ_l, ρ_p	Particle/ liquid density	[kg/m^3]
u_η	Kolmogorov velocity scale	[m/s]
τ_η	Kolmogorov timescale	[s]
τ_{cv}	Characteristic convective time scale	[s]
τ_{ev}	Droplet evaporation time scale	[s]
τ_f^t	Lagrangian turbulent time-scale	[s]
τ_{fp}^F	Mean particle relaxation time	[s]
$\tau_{g,ij}$	Component (i, j) of the stress tensor	[N/m^2]
τ_p	Particle relaxation time scale	[s]
θ_S	Spray angle	[°]
ζ	Artificial viscosity sensor	[-]
ζ_p	Particle temperature	[K]

Non-dimensional numbers

Symbol	Description
B_M	Spalding number for mass transfer
B_T	Spalding number for heat transfer
Kn	Knudsen number
Le	Lewis number
Nu	Nusselt number
Pr	Prandtl number
Re	Reynolds number
Re_p	Particle Reynolds number
St	Stokes number
Sc	Schmidt number
Sh	Sherwood number
We	Weber number

Subscripts

Symbol	Description
0	Plane of the atomizer orifice
0	Thermodynamic reference state
∞	State in the far-field
ζ	Interface between particle and fluid

cc	Point on the saturation curve
f	Index of the carrier fluid
F	Index of gaseous fuel
g	Index of the gaseous phase
k	General index of the species
l	Index of the liquid phase
lam	Laminar component
p	Index of the particle phase
ref	Index of the reference state
t	Turbulent component
v	Index of the vapor species
wb	Wet-bulb

Superscripts

Symbol	Description
f	Filtered quantity
$\hat{f}$	Density weighted filtered quantity
$\breve{f}$	Ensemble averaged quantity
$\breve{f}$	Mesoscopic liquid quantity in the Eulerian framework
f'	Fluctuation
f^i	Invscid component
f^{sgs}	Subgrid-scale contribution
f^v	Viscous component
(k)	Index of the k^{th} particle
δf	Uncorrelated part of a quantity
$*$	Traceless tensor

Abreviations

Acronym	Description
CPS	Computational Fluid Dynamics
DNS	Direct Numerical Simulation
DQMOM	Direct Quadrature Method Of Moments
DPS	Discrete Particle Simulation
EE	Euler-Euler
EL	Euler-Lagrange
EMSM	Eulerian Multi Size Moment
EMVM	Eulerian Multi Fluid Multi Velocity
HIT	Homegenous Isotropic Turbulence
IMFT	Institut de Mécanique de Fluides de Toulouse
LES	Large-Eddy Simulation
MEF	Mesoscopic Eulerian Formalism
MERCATO	Moyen d'Étude et de Recherche en Combustion Aérobie par Techniques Optiques
MYPLANET	Massively Parallel Computations of Combustion and Emissions Simulations
NS	Navier-Stokes
NSCBC	Navier-Stokes Characteristic Boundary Condition
PDF	Probability Density Function
PTC	Particle Trajectory Crossing
RANS	Reynolds Averaged Navier-Stokes
RMS	Root Mean Square
RUE	Random Uncorrelated Energy

RUM	Random Uncorrelated Motion
WALE	Wall-Adapting Local Eddy-viscosity

Chapter 1

General Introduction

In today's industrial society more than 80% of the energy consumed on earth is produced by burning fossil fuels. However, the progressive exhaustion of fossil fuels and the ecological problems derived require an important technological progress in order to optimize the combustion processes. In this context of fuel depletion, growing pollution and global earth warming, this statement is globally recognized. Indeed, regulations on pollutant emissions recently adopted by many countries oblige a drastic reduction of emissions and fuel consumption. Many other energy sources, alternatives to combustion, exist such as nuclear, wind, solar and hydraulic power, biomass, etc. However, in the domain of aeronautical transport, few other sources of energy other than hydrocarbons start to be considered nowadays. This limited impact is mainly due to the necessity of a high power/weight ratio that only combustion of liquid fuels can provide due to their high specific energy content and high volumetric energy density.

Many chemical components are produced during combustion. Some, like H_2O or CO_2, are intrinsic to the process itself and cannot be avoided. Some others, like NO_x, CO, unburnt hydrocarbons and soot are also produced when burning hydrocarbon fuels. All these components can be grouped under the term "pollutant emissions". In order to reduce the quantity of these species produced during combustion, several strategies may be adopted. The production of CO_2 is directly linked to the quantity of fuel burnt. For this reason, in order to reduce CO_2 production, fuel comsumption must be reduced meaning that more efficient engines must be designed. The formation of other pollutants is mainly linked to the combustion mode. High temperature combustion increases the emissions of NO_x, lean combustion promotes the formation of CO and unburnt hydrocarbons. Pureness of the fuel itself has also a direct impact on particle emissions.

Therefore, an improvement of the combustion process used in current aeronautical engines is necessary both to increase the efficiency of combustion process and to reduce derived pollutant emissions. For this reason, many efforts are being invested in research and development of new, more efficient and less pollutant engines. Numerical simulations have become very important tools in this framework. Indeed, during the past decades, the advances in computing resources and simulation methods allow sophisticated simulations at industrial scale (Boileau (2007), Wolf *et al.* (2010)). This work is situated in this context since the improvement of the actual techniques can only be achieved through a better comprehension of the processes and phenomena taking place inside the engines.

1.1 The Numerical Simulation as a powerful tool

As an illustrative example, Figure 1.1 displays a cut of an aircraft engine showing its main parts. Despite the specificity of this choice, the same general statements (with some modifications, especially regarding the configuration and the thermodynamic cycle) may be applied to piston engines and other applications.

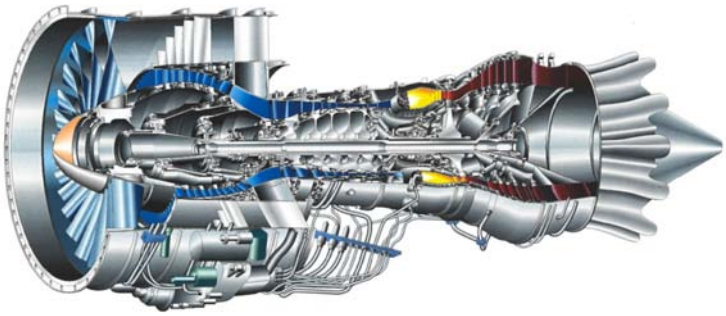

Figure 1.1: *Mid-plane cut of an aircraft engine. (Source http://web.engr.oregonstate.edu).*

The process to generate power is as follows: air enters the engine through the compressor, where the pressure of the flow is increased. Then it enters the combustion chamber where it is mixed with the liquid fuel injected in spray form. The spray evaporates, mixes with air and then burns. The exhaust gases exit the engine through the turbine where the flow energy is transformed into work. The burnt gases may be diluted with some air to decrease their temperature in order to reduce possible damages to the first stages of the turbine. From the thermodynamic point of view, three main processes take place (Fig. 1.2):

1. Isentropic compression in the compressor
2. Isobaric combustion in the combustion chamber
3. Isentropic expansion in the turbine

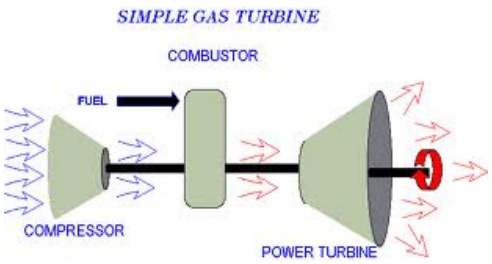

Figure 1.2: *Simplified sketch of the thermodynamic cycle of a gas turbine. Source Wikipedia.*

In this work, only the processes taking place in the combustion chamber are of interest, and more precisely the phenomena related to liquid fuel spray. For this reason, the compressor and the turbine will not be taken into account. Moreover, since the phenomena involving the spray are of a high complexity, the scope of this work is reduced to non-reactive cases.

In the past decades, Computational Fluid Dynamics (CFD) has become a very powerful tool both in academic research and industrial applications. On one side, it permits the validation of analytical models in a simple and fast manner. On the other side, they have partly replaced experiments in the industrial field for the design of new components. Indeed, simulations are faster and much cheaper than experiments when complex geometries are taken into account. This is due to the difficulties related to the simultaneous characterization of the different

phenomena occuring in the flow (such as in two-phase reacting flows) and to access the flow field in complex geometries. Moreover, it is rather simple to perform parametric studies using CFD which allows to study the influence of individual parameters on the industrial device performances.

There are three main strategies regarding CFD simulations:

- Direct Numerical Simulation (DNS), which completely solves flow dynamics up to the smallest scales, requiring no modeling (i.e. all turbulence scales are explicitly determined), but is computationally very expensive. Furthermore, when including two-phase flows, it can quickly become prohibitive and it is certainly not applicable today to real industrial configurations. For this reason, its use is limited to canonical test cases, where it greatly contributes to the understanding and related modeling efforts of many different types of flows.
- Reynolds Averaged Navier-Stokes (RANS) simulations (Jameson (1991), Lathouwers & Bellan (2001)), which only solve the mean flow field (Chassaing (2000), Pope (2000)). The balance equations for mass-weighted averaged quantities are obtained by averaging the instantaneous balance equations. The average equations require closure models for the turbulent dynamics of the flow. The greatest advantage of RANS is its low computational cost and the years of research and development invested in this approach. However, this approach is not suitable for the simulation of unsteady or transient flows.
- Large Eddy Simulation (LES) (Smagorinsky (1963), Lilly (1967), Deardorff (1974)), in the middle between DNS and RANS simulations, solves the largest scales of the flow up to a certain length-scale and the scales smaller than that are modeled by means of subgrid models. The balance equations are obtained by spatially filtering the instantaneous equations. The size of this filter determines the size of the scales that are solved and those that are modeled. This approach provides information about transient phenomena and is very suitable to perform unsteady flows simulations. Most developments on LES derive from the study of academic configurations such as Homogeneous Isotropic Turbulence (Kraichnan (1976), Chasnov (1991)) or turbulent channel flow (Deardorff (1970), Schumann (1975), Moin & Kim (1982)). However, it has also been used in industrial configurations (Haworth *et al.* (2000)). The computational cost of LES is bigger than that of RANS simulations and moderate compared to DNS (depending on the size of the scales that are solved), but affordable in most cases. It is in fact a very good compromise between accuracy and computational time.

Nowadays CFD uses DNS for the validation of numerical models in canonical test cases. In real industrial applications RANS is a suitable approach for the simulation of the compressor and the turbine in aircraft engines. Due to the unsteady nature of the phenomena occuring in the combustion chamber, LES is the most suitable approach for the simulations of this part of the engine. In the context of this work, stress is applied to model validation in a first part. DNS of academic configurations is used to assess the validity of algebraic models. On a second part, where the application to more complex configurations is studied, LES is used.

1.2 The role of the liquid sprays

Many industrial applications involve liquid sprays. Most of them are used for power generation (liquid rocket engines, diesel engines, jet engines, etc.), but there are many other applications involving droplet/particle laden flows (refrigeration, fluidized beds, etc.). The study of turbulent gaseous flows is a timely research topic. The study of liquid sprays in turbulent flows is more recent. For this reason, there is still a long path to propose models for the simulation of two-phase turbulent flows which account for all the phenomena involved in the dynamics of sprays in turbulent gaseous flows. The lack of experimental data in industrial configurations at real conditions is an important impediment for the validation of models and numerical results. This is due to the high complexity of this type of systems. The measuring techniques used nowadays to perform experiments need further developpement. It is crucial to obtain simultaneous data on different quantities (related to the gaseous and the dispersed phase) to characterize the flow. Indeed, two-phase flows include a number of processes involving very different time and length scales. Simplifications must be done in order to be able to reproduce part of these phenomena. The characteristic length-scales of an evaporating two-phase flow range from the size of the smallest droplets of the spray (of the order of a micrometer) to the size of the combustion chamber (of several centimeters). The characteristic time-scales of the flow depend on the size of the droplet, which has a major impact on the inertia and the lifetime of the droplets.

Here, a brief overview of the principal processes involving the dispersed phase is provided.

1.2.1 Injection

The injection system represents one of the essential components of the combustion chamber. It provides the liquid fuel and plays an important part in internal reacting flow aerodynamics. The liquid fuel is injected in the form of a cylindrical column or a thin liquid sheet that due to an aerodnamic destructive effect is atomized into a cloud of droplets. The characteristics of this cloud, such as the droplet density and size, strongly depend on the injection parameters and geometry.

There are many types of injectors. Here, only three types are recalled:

- Rotary atomizers. The liquid flow is forced into a rotating device before entering the combustion chamber. The rotation velocity of this device determines the size of the droplets that are formed. These devices can control very tightly the final diameter of the droplets and generate very fine clouds. However, they are too complex to be employed in aeronautical combustion chambers.

- Airblast atomizers. The shear effect of accelerated air flow parallel to the the fuel injection is used to atomize the liquid fuel. A complex interaction between the air and the fuel produces the formation of the droplet cloud. These mechanisms work at low relative speed and high air flow. The configuratio of the injection streams can be planar or annular.

- Pressure atomizers. The liquid is forced to flow through a small hole by means of a strong pressure force, generating a conical spray. The inlet can have a planar or annular geometry, combined or not with a swirl diffusor. The liquid sheet is subjected to strong shear on both sides, which provokes its disintegration into small droplets.

In aircraft engines, fuel is generally injected by means of pressure swirl atomizers. The characteristics of the spray pattern highly depends not only on the parameters of the injection device, but also on the gaseous flow inside the combustion chamber and the properties of the liquid fuel: for example the viscosity (directly influencing the droplet size) and the fuel volatility (which impacts the vaporization process). Pressure swirl atomizers and the influence of the different parameters on the resulting droplet cloud have been extensively studied in the literature (Lefebvre (1989), Taylor (1948), Bayvel & Orzechowski (1993), Jones & Whitelaw (1982)).

1.2.2 Atomization

Fuels used in aircraft engines are not volatile enough to be ignited and burnt if the surface in contact with the oxydizer is not augmented by pulverization. The liquid sheet exiting the injector must be atomized into a cloud of droplets. The atomization process can be described as the ensemble of mechanisms that occur in the injection of a high pressure liquid through a small fence. Two different phenomena can be distinguished in this process: the primary atomization takes place in the region near the orifice, the secondary atomization usually extends much further.

The mechanisms of liquid sheet disintegration have been widely studied. Several studies focus on the linear stability analysis of the sheet oscillation by means of Navier-Stokes temporal stability analysis of liquid sheets injected into still gaseous flow (Squire (1953), Taylor (1959)). These studies conclude that the atomization process is caused by two types of instabilities (Reitz (1978)) formed in the liquid sheet interface (sinusoidal antisymmetrical oscillations and symmetrical dilatation instabilities). The waves caused by the sinusoidal mode are not strong enough to cause the liquid sheet break-up. Rangel & Sirignano (1991) stated that the sheet may disintegrate following the growth of the amplitude of the dilatation waves, producing a pinch resulting in the sheet break-up. Very fine liquid ligaments are formed that suffer further disintegration into droplets of different sizes (secondary breakup). The primary atomization has been studied experimentally by Stapper & Samuelsen (1990), Marmottant & Villermaux (2004), Carvalho *et al.* (2002), Lefebvre (1989) and Lozano *et al.* (2001) amongst others.

The numerical simulation of the primary atomization process requires the explicit resolution of the Navier-Stokes (NS) equations for both phases and the coupling between them through jump relations at the interface. In addition, the position and motion of the interface must be accurately described (Couderc & J.-L. (2003), Trontin (2009)). DNS of the primary atomization process needs extremely high resolution meshes since the length scale of the smallest liquid structures can become very small as the liquid ligaments approach their breakup. In general the mesh size is determined by the smallest droplet diameter. At least two to five computational cells per droplets are needed (Gorokhovski & Herrmann (2008)). This feature prevents the numerical simulations of the primary atomization at industrial scale. However, as small droplets are only present at the periphery of the liquid sheet, mesh adaptation techniques (Berger (1982), Almgren *et al.* (1993), Sussman *et al.* (1999), Zuzio (2010)) can be used in order to reduce the computational cost. Level-Set (Osher & Fedwik (2003)) and Volume of Fluid (VOF, DeBar (1974)) methods are suitable approaches for this task (Menard *et al.* (2007)). Desjardins *et al.* (2008) developped a Level-Set method combined with high-order implicit transport schemes to preserve mass conservation. Moreau & Desjardins (2008) implemented a high-order Ghost Fluid method. Both approaches show accurate results. Due to the large range of length and timescales involved in the process, direct and detailed numerical predictions of the primary atomization process are computationally very expensive and not affordable at large scales. Their application is limited in terms of Reynolds number and geometry complexity. However, RANS and LES approaches for the simulation of the primary atomisation exist (Beau *et al.* (2006, Paper 98166), Chesnel (2010)).

Once the liquid sheet has decomposed into fine liquid ligaments, further disintegration occurs and droplets of different sizes arise due to air entrainment and aerodynamical forces acting on the ligaments. This process is called secondary breakup. Several regimes, depending on the Weber number, exist. The Weber number is a dimensionless number relating the aerodynamic forces acting on the droplet and its surface tension. Those two forces have opposite effects on a droplet: the surface tension stabilizes the droplet and the aerodynamic force tends to break it. This is a process of high difficulty in terms of modeling and simulation. Indeed, there are many effects that must be taken into account, such as the droplet deformations prior to breakup (which modifies the drag force law) and collisions and coalescence which are predominant in this zone of the spray. Indeed, in the secondary breakup zone, the spray is very dense, which increases the probability of collision between droplets. Numerical studies of this problem may rely on different approaches (Fig 1.3 is an example for the case of the atomization of a liquid column). DNS using an interface tracking method being out of reach for realistic applications, simplifications have been proposed in literature. Apte *et al.* (2003*a*) use a Lagrangian method, neglecting the liquid column and taking into account secondary breakup only. Rachner *et al.* (2002) use a Lagrangian method combined with modified laws for drag force and models for the column breakup based on empirical correlations. Finally, a common solution consists on considering the primary atomization as a boundary condition for the dispersed phase from which a distribution of droplets is directly injected.

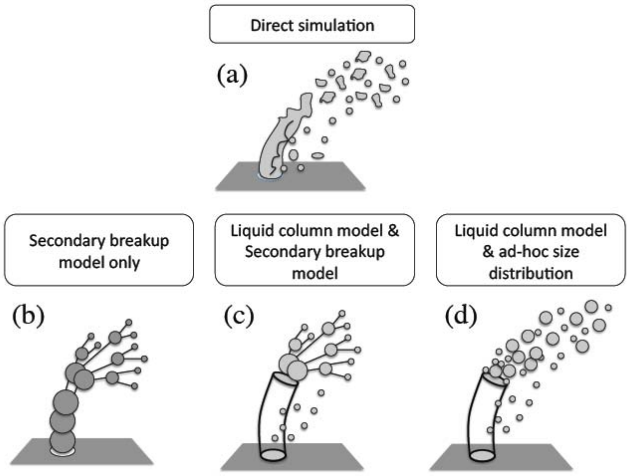

Figure 1.3: *Schematic of the modeling approaches for a liquid jet-in-cross-flow case. (Extracted from Jaegle (2009)).*

Figure 1.4 shows a sketch of the main phenomena following the liquid injection. The secondary atomization produces a cloud of droplets of different sizes. In this zone, far from the injection where the spray is much denser, the volume fraction of droplets is very small compared to that of the gas phase. Droplet/particle laden two-phase flows can be classified taking into account the particle volume (α_p) and mass fractions (M_p) of the spray (Fede *et al.* (2004)):

- $\alpha_p < 10^{-4}$ and $M_p < 10^{-2}$: very diluted flows. Inter-particle collisions and effects of particles on the carrier fluid phase can be neglected due to the low inertia of the particles.
- $\alpha_p < 10^{-4}$ and $M_p > 10^{-2}$: diluted flows. Two-way coupling between the gaseous and the dispersed phases must be taken into account.
- $10^{-4} < \alpha_p < 10^{-1}$: moderately dense sprays. Inter-particle collisions become important in this type of flows. However, the carrier phase flow remains the main contribution to particle motion
- $\alpha_p > 10^{-1}$: very dense sprays. Inter-particle collisions are the most important contribution to the particle motion.

This work focuses on the diluted regime zone located after the secondary breakup zone. Only diluted and very diluted flows are considered. Thus, inter-particle collisions are ignored and one-way or two-way coupling with the carrier fluid is considered depending on the configuration. In this type of flows, the principal physical phenomena is the particle dispersion due to the gaseous turbulence. If two-way coupling is considered, the fluid turbulent energy tends to decrease due to the presence of the dispersed phase. Note that throughout this work particle phase refers to a dispersed phase composed by solid particles, liquid phase to a dispersed phase composed by liquid droplets and the term dispersed phase is used indistinctly for both.

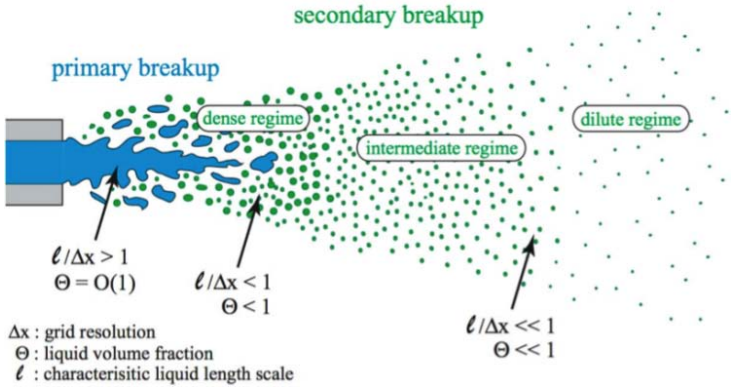

Figure 1.4: *Phenomenology of the atomization of a spray. (Source M. Hermann, Summer Program of the CTR, Stanford).*

1.2.3 Dipersion and Evaporation

In the diluted regime, dispersion and evaporation become predominant. In this case, particle trajectories are directly influenced by the carrier flow turbulence. However, their response to the gaseous flow depends also on their inertia. The Stokes number (St) relates the characteristic particle response timescale (τ_p) to the characterisitc fluid timescale (τ_f), giving a measure of the particle inertia. Very inertial particles ($St >> 1$) have trajectories quite independent from the carrier fluid flow. On the contrary, very low inertial particles ($St << 1$) quickly respond to changes in the gaseous flow. In industrial applications, the inertia of the particles varies because their size and mass change due to evaporation and polydispersion effects. Very different behaviors take place at the same time. When the evaporation timescale of the droplets (τ_{ev}) is very short, droplets evaporate very quickly and very few droplets are present far from the injection zone. If, on the contrary, the droplet lifetime is long, droplets are present further downstream.

The dispersion of particles has been deeply studied. The first studies on particle motion date from the nineteenth century. Later on, Tchen (1947) and Reeks (1991), amongst others, performed theoretical analysis of particle dispersion which led to the definition of the main length and time-scales of the particle motion in gaseous turbulence. Maxey (1987) proposed analytical methods able to predict complex phenomena such as preferential concentration effects (i.e. cummulation of particles in low-vorticity and high-strain regions, also called particle segragation (Squires & Eaton (1991*a*)), Eaton & Fessler (1994)) or particle trajectory crossing (Wells & Stock (1983)), which characterise the interactions of the particles with the gaseous turbulence. The modulation of the turbulence by the presence of the particles is also a process of interest. It is often assumed that the carrier fluid flow turbulence is not affected by the presence of the particles (one-way coupling). This hypothesis is valid in very diluted regime. However, in diluted regime inverse coupling in not negligible and the effects of the dispersed phase on the fluid turbulence must be accounted for (Fede *et al.* (2004)). Turbulence modification due to the presence of particles has been widely studied in particle-laden Homogeneous Isotropic Turbulence (HIT) flows (Squires & Eaton (1990), Elghobashi & Truesdell (1993) (accounting for two-way coupling), Boivin *et al.* (1998) (using DNS of the gaseous phase), Sundaram & Collins (1999)) and mean sheared configurations (Vermorel *et al.* (2003), Vermorel (2003)).

Particle dipersion in gaseous turbulence has been widely studied experimentally (Snyder & Lumley (1971)) and numerically (Squires & Eaton (1991*a*), Deutsch (1992), Mei *et al.* (1991) (accounting for Basset force and gravity settling effects), Laviéille (1997) (taking into account interparticle collisions), Elghobashi & Truesdell (1992) (using DNS) and Boivin *et al.* (2000) (using LES and accounting for two-way coupling) in HIT, Reeks (1993) in simple shear flows, Simonin (1991) in particle-laden jets, Vance *et al.* (2006), Wang & Pletcher (1996) (using LES), Yamamoto *et al.* (2001) (in vertical channel configuration using LES and accounting for collisions) in particle-laden turbulent channel flows, Apte *et al.* (2003*a*) in swirling flows, etc).

Regarding the vaporization process many models exist. Models are mainly based on empirical results on single isolated droplets, which have been modified to include the effects of neighbouring droplets, convection,

multicomponent fuels, etc. (cf Part III). Many parameters have an influence on the vaporization process. Indeed, the characteristics of the fuel, the spray and the carrier flow play an important role and directly influence the evaporation of droplets inside the combustion chamber. An exhaustive review of the theoretical models for droplet vaporization can be found in Sazhin (2006) or in classical textbooks such as Sirignano (1999), Kuo (2005) or Williams (1985).

Experimental studies on droplet vaporization are often performed on isolated droplets, taking into account or not the effects of convection (Wong & Lin (1992)), radiation, heat conduction through the support fiber (Yang & Wong (2002), Chauveau *et al.* (2008)), multicomponent fuels (Ghassemi *et al.* (2006)) and for high pressure and temperature (Matlosz *et al.* (1972), Kadota & Hiroyasu (1976), Nomura *et al.* (1996) Morin *et al.* (2004)).

From the numerical point of view, the effect of ambient gas and fuel properties has been studied by Hubbard *et al.* (1975). Yang & Chang (2001) performed a numerical study on the effects of the heat conduction through the support fiber and the radiation of the furnace in the experiments of Nomura *et al.* (1996).

Evaporation has an important effect on the dispersion of particles in turbulent flows. Albrecht *et al.* (1999) studied the dispersion of evaporating droplets in HIT flow, Réveillon & Vervisch (2004) studied the dispersion of evaporating droplets in turbulent flows taking into account polydispersion effects.

1.2.4 Combustion of droplets

The combustion process considered often involves chemical reactions that only take place in the gaseous phase (Williams (1971)). Thus, the evaporation of liquid fuel droplets is a necessary step for the combustion to take place. However, two main types of combustion exist: single-phase combustion and two-phase combustion. These two regimes depend on the ratio between the characteristic evaporation time and the convection time of the carrier phase. When the characteristic evaporation time of the droplets is very small compared to the convection time, the droplets completely evaporate before reaching the flame front. Combustion taking place in the single-phase regime, it only depends on the gaseous fuel repartition in the chamber. The gaseous fuel field will however depend on the characteristics of the evaporation process and the dispersion of the droplets. On the other hand, when the evaporation time is longer than the convection time, flame and spray are coupled. The droplets may reach the flame front and the characteristics of the flame strongly depends on the spray parameters.

Isolated droplet combustion studies can be found in the work of Godsave (1953)

Numerical results obtained using DNS of sprays in different combustion regimes provide an extra classification of the phenomena coupling spray and reaction (Réveillon & Vervisch (2005)). Two-phase flow combustion has different characteristics than gaseous phase combustion. The characteristics of the flame are modified due to the presence of liquid droplets and strongly depend on the quantity of fuel that has been evaporated before reaching the flame front. Indeed, the gaseous field is modified by the presence of droplets upstream from the flame which may lead to flame instabilities. Note also that the evaporation rate depends, amongst other things, on the concentration of droplets. This may create zones of very high concentration of gaseous fuel and very lean zones too. The mixing is then different from the case where gaseous fuel is directly injected into the chamber.

Furthermore, if the droplets reach the flame front, the evaporation and combustion zones overlap, leading to different combustion regimes. Réveillon & Vervisch (2005) give a symmetric description of the spray flame structures that is recalled here. They classify the different modes depending on a dimensionless number, G, which is the ratio between the droplet evaporation rate and the diffusion rate of hot gases within the droplet cloud. When convection is more important than diffusion, G is approximated as follows:

$$G \approx \frac{5N_p^{\frac{2}{3}}}{S} \tag{1.1}$$

where N_p is the number of droplets in the cloud and S is a mean doplet spacing parameter linking the characteristic average distance between droplets to the diffusion flame radius.

For large G numbers, the spray is very dense and diffusion inside the cloud is low, only the droplets located at the periphery of the cloud evaporate. The flame enveloppes the whole cloud of droplets. It is referred to as external sheath combustion. For diluted spray regimes, where $G << 1$ droplets are far from each other and the evaporation rate increases due to hot gases diffusion. Separated flames surround each droplet, which burn individually. Intermediate regimes exist between these two extremes: for G numbers slightly larger than one, the flame surrounds the whole cloud of droplets but hot gases diffusion is high enough, thus the droplets in the center of the cloud vaporize. When $G < 1$, the center of the cloud burns in an external combustion regime and the droplets located at the periphery burn in an isolated manner. Figure 1.5, taken from Réveillon & Vervisch (2005), illustrates four distinct modes of spray combustion regimes depending on G.

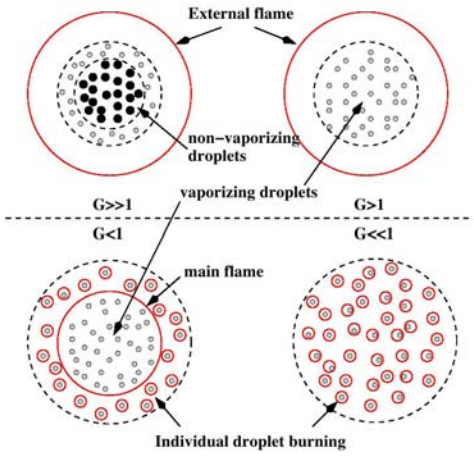

Figure 1.5: *Classification of different spray combustion regimes. Extracted from Réveillon & Vervisch (2005).*

Borghi (1996*a*) and Borghi & Champion (2000) propose another classification based on the characteristic evaporation time τ_{ev}, the characteristic time of the flame τ_f and the flame thickness δ_f. When $\tau_{ev} << \tau_f$, droplets evaporate in the preheating zone upstream from the flame which burns in a premixed regime. In this case, spray characteristics fluctuations may lead to partially-premixed flames. When the evaporation time is longer than the flame characteristic timescale, two distinct regimes are possible depending on the ration between the flame thickness and the droplet flame radius. If the radius of the flame surrounding the droplets is small compared to the flame thickness, burning droplets cross the flame front and burn in a secondary reaction zone. On the contrary, for flame thicknesses smaller than the radius of the flame surrounding the droplet, the presence of the last modify the behavior of the flame front, thicknening it. This classification does not take into account turbulence effects and equivalence ratio variations. Réveillon & Vervisch (2005) provide a different classification based on numerical results of two-dimensional spray flames in counterflow:

- External combustion regime: in a case of low equivalence ratio, the premixed flame consumes the totality of the fuel (liquid and gaseous). When the equivalence ratio is high, the fuel burns in diffusion regime.

- Group combustion regime: droplet clusters individually burn on rich premixed flames ussually followed by diffusion flames.

- Hybrid combustion regime: intermediate conditions between the external and the group combustion regimes.

Reviews on droplet and spray combustion can be found in Faeth (1983), Faeth (1987), Law (1982) or Sirignano (1983).

1.2.5 Numerical simulation of sprays

Two-phase flows involve complex physical phenomena, such as liquid-gas, or liquid-surface interactions, atomization process, droplet dynamics and heat and mass transfer. Up to date, no analytical treatment exist for a general representation of the complete set of processes involving particle/droplet laden flows. Therefore, numerical modeling and simulations have been increasingly employed. Numerical simulations are often preferred over experiments because they can usually be carried out faster due to a shorter lead-time and with less expense. Aditionally, control is easier and they can be used to study a much wider range of conditions, some of which are physically inaccesible (Liu (2000)). DNS of two-phase flows are not accesible for realistic configurations. Indeed, a direct simulation of the dispersed phase implies the resolution of the flow field around each individual droplet and, in the case of liquid droplets, inside the droplet too. In realistic configurations, where evaporation of liquid sprays is usually accounted for, droplets can reach very small sizes (less than a micrometer), which need very fine computational grids. The computational cost related is very high, both in time and memory requirements. Therefore, DNS of two-phase flows is limited to canonical test cases in academical research. However, several options for the modelisation of the dispersed phase exist. They can be coupled with DNS or LES of the gaseous phase. An exhaustive review on LES approaches for the dispersed phase can be found in Fox (2012).

In this work, two modeling frameworks to simulate sprays in diluted regimes are used. The developments presented in this work concern the Euler-Euler approach. The Euler-Lagrange approach is used for validation when no experimental data are available:

- In the Lagrangian approach (Sankaran & Menon (2002), Apte *et al.* (2003*a*)), the individual trajectory of each particle is tracked in its own frame of reference. Droplets are treated through the point source approximation and their trajectories are evaluated through force balance at each point (Maxey & Patel (2001)). The carrier fluid flow is usually computed by solving the Navier-Stokes (NS) equations. In the Lagrangian computations, the location of the discrete particle not necessarily coincide with the computational grid. Therefore, in order to account for coupling between the gaseous and the dispersed phases, the properties of the carrier fluid must be interpolated at the location of the droplet or particle. An accurate numerical algorithm is needed for this task, which increases the numerical complexity of this method. Moreover, the difficulty increases when the gaseous flow is computed with a LES approach, since not all the scales of the carrier phase are resolved, and the effects of the unresolved scales on the particle motion must be taken into account (Dukowicz (1980)). On the other hand, polydispersity can easily be accounted for. The Lagrangian methods may become computationally very expensive when the number of particles to be followed increases. However, physical particles can be substituted by numerical particles representing a cluster of various real particles, which reduces the computational cost. On the other hand, parallelization tasks must be carefully handled, since in configurations where particle cummulation takes place (e.g. zones close to the injector), a bad load balance between processors takes place, for which adapted partitioning algorithms should be used (García (2009)).

- Another alternative approach is the Eulerian method, which considers both phases (the carrier and the dispersed phase) as continuum and captures only averaged quantities of the dispersed phase (Ferry & Balachandar (2002)). Depending on the formalismm used, the spray properties are averaged in a volumetric (Whitaker (1999)) or ensemble (Zhang & Prosperetti (1994), Simonin (1991)) sense and calculated through the evolution of a probability density function (pdf) equation. In general, the dispersed phase is solved using a set of conservation equations for the moments of the pdf equation. Accounting for polydispersity is less obvious in this case. However, it may be reproduced by discretizing the droplet size distribution leading the so called sectional methods (Greenberg *et al.* (1993), Laurent *et al.* (2004), Vié (2010)); a complete set of transport equations is solved for each section, which increases the computational cost and the complexity due to the exchanges between each section when phenomena such as evaporation are taken into account.

Both methods have advantages and drawbacks. Table 1.1 displays a non-exhaustive comparison between both approaches. Here, the supplementary modeling effort and the special treatment for particle trajectory crossing (PTC) are stressed. Indeed, the Mesoscopic Eulerian Formalism (MEF) used in this work needs closure for some terms appearing in the transport equations for the dispersed phase. These terms are linked to the modelisation of

PTC related phenomena. On the same way, the coupling terms between phases, such as drag force and evaporation source terms also need modeling.

Euler-Euler	Euler-Lagrange
Advantages	
⊕ Numerical straightforward treatment of dense zones. ⊕ Similarity with gaseous equations. ⊕ Direct transport of Eulerian quantities. ⊕ Similarity with gaseous computer paralelism	⊕ Numerically straightforward modeling of particle movements and interations. ⊕ Robust and accurate if enough particles are used. ⊕ Size distributions are easy to describe. ⊕ Numerically straightforward to implement physical phenomena (e.g heat and mass transfer, wall-particle interaction).
Drawbacks	
⊖ Difficult description of polydispersion. ⊖ Difficulty of droplet crossing treatment. ⊖ Limitation of the method in very diluted zones.	⊖ Delicate coupling with combustion. ⊖ Difficult parallel implementation. ⊖ CPU time spent in locating particles on unstructured grids.

Table 1.1: *Advantages and drawbacks of Euler-Euler and Euler-Lagrange approches. Extracted from García (2009).*

The CFD code used in this work, AVBP, has two different solvers for the dispersed phase, a Lagrangian one and an Eulerian one. Here, only the Eulerian solver is used. It is based on the Mesoscopic Eulerian Formalism (MEF, Février *et al.* (2005)) defined in Chapter 2. The basic idea is the distinction between two different contributions in the particle velocity: an ensemble velocity, shared by all the particles and an uncorrelated part, which is specific to each individual particle. Due to the contribution of the uncorrelated part of the particle velocity field, unclosed terms appear in the transport equations for the dispersed phase. These terms are closed by means of algebraic models.

1.3 Objectives of the present work

This thesis has been supported by CERFACS (Centre Européen de Recherche et Formation Avancée en Calcul Scientifique) and the European Union in the framework of the MYPLANET project (Massively Parallel Computations of Combustion and Emission Simulations) in an initiative to train a new generation of engineers in the field of high performance computing applied to the numerical combustion simulation, energy conversion processes and related atmospheric pollution issues.

This work proposes to improve the modeling of the dispersion and evaporation phenomena for diluted regimes oriented to the pre-vaporised combustion of sprays on industrial aeronautical chambers. Several models are implemented in the AVBP code, dedicated to LES in complex geometries and tested on academic and semi-industrial configurations. The results obtained are compared with reference data (either Lagrangian simulations or experimental measurements) in order to assess the validity of the models.

Combustion, both purely gaseous as well as spray combustion, is out of the scope of this study. This brief overview of the main phenomena related to the dispersed phase in aeronautical combustion chambers helps limiting the phenomena adressed in this work. Figure 1.6 displays a sketch of the processes followed by the dispersed phase after the injection of the fuel in the combustion chamber. Here, only the dispersion and the evaporation of droplets in non-reactive flows are taken into account.

Section 1.3.1 briefly recalls the previous developements performed on dispersed phase modeling with the MEF for the Eulerian approach. Section 1.3.2 presents the global outline of this manuscript.

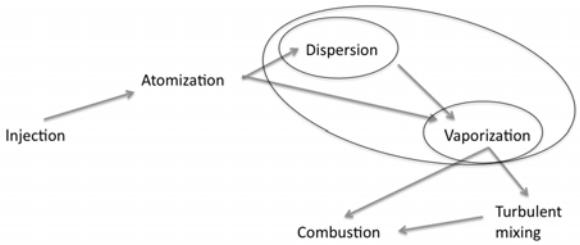

Figure 1.6: *Sketch of the principal phenomena related to the dispersed phase in combustion chambers.*

1.3.1 Previous developments

The main tool used during this work is the code AVBP. This finite-volume and finite-element unstructured hybrid solver has been jointly developped by CERFACS and IFP-EN (Institut Francais du Pétrole - Energies Nouvelles) over the last 20 years. AVBP is a massively parallel code that explicitely solves both DNS and LES Navier-Stokes equations in compressible form. It is based on the cell-vertex approach (Schønfeld & Poinsot (1999)). High-order numerical schemes and characteristics boundary conditions (Poinsot & Lele (1992)) are available. More information on AVBP can be found in Lamarque (2007).

Several studies involving the MEF for Eulerian approach for the simulation of two-phase flows have been conducted until now. Février *et al.* (2005) introduced the MEF that allows the simulation of the dispersed phase coupled with DNS or LES of the gaseous phase. Closure models for the transport equations for the dispersed phase were firstly proposed by Simonin (2002) and Kaufmann *et al.* (2005). Kaufmann (2004) implemented the MEF in AVBP and performed the first numerical simulations in particle-laden HIT using DNS for the simulation of the carrier fluid flow. Validation of the implementation was performed through comparisons with reference data from Lagrangian computations. Moreau (2006) and Riber (2007) extended the MEF, until that time available only in the context of DNS, to LES. Closure models for the subgrid-scale terms were *a priori* developped in the particle-laden decaying HIT (already studied by Kaufmann (2004)) and Moreau (2006) and *a posteriori* validated in the same configuration by Riber (2007). Riber (2007) alse performed studies on more complex configurations (Hishida *et al.* (1987), Borée *et al.* (2001)). Mossa (2005) extended the MEF in order to take into account polydispersion. The MEF has also been employed in industrial configurations taking into account gaseous combustion (Pascaud (2006)). Boileau (2007) demonstrated the capability of this approach to simulate complex industrial configurations in real conditions presenting a LES of the two-phase reacting flow of a complete helicopter annular combustion chamber. Sanjosé (2009) implemented the FIM-UR methodology for the modelisation of the spray injection. Roux *et al.* (2009) developped new numerical schemes more adapted to the simulation of the dispersed phase. Masi (2010) recently proposed new algebraic equations for the modelisation of the unclosed terms appearing in the transport equations of the dispersed phase for DNS and LES and for the modelisation of the uncorrelated part of the particle temperature field from *a priori* simulations of a mean-sheared particle-laden flow (Vermorel (2003)). Vié (2010) included the possibility of taking into account polydispersion effects using a multi-section method. Recently Dombard (2011) studied the effects of the uncorrelated motion in anisothermal mean-sheared configurations.

The MEF is currently used for the simulation of reactive flows in complex geometries. Polydispersion effects can be accounted for. However, spray combustion is not taken into account and reactions occur only in the gaseous phase. Regarding the modelisation of the unclosed terms related to the uncorrelated motion (RUM, Février *et al.* (2005)), only one model (Simonin *et al.* (2001)) has been tested until now in complex geometries. The studies performed on particle-laden HIT showed that the RUM must be taken into account when low and high inertia particles are simulated. Otherwise, the simulation is numerically unstable. However, the viscosity-type model proposed by Simonin *et al.* (2001) based on a local-equilibrium assumption, leads to a re-laminarization of the dispersed phase flow in configurations with mean-shear (Riber (2007)). Several studies have revealed the importance of the mesh resolution in dispersed phase simulations. Indeed, a high resolution is needed in order to capture phenomena such as the preferential concentration. Eulerian simulations of complex geometries not accounting for the RUM show

accurate mean particle velocity distributions but lead to an underestimation of the velocity fluctuations.

1.3.2 Plan of the manuscript

This work is organized as follows:

- Part I describes the governing equations for both the gaseous and the liquid phases in the context of non-reactive two-phase flows. Chapter 2 presents the Navier-Stokes (NS) equations for the gaseous phase in DNS as well as the equations for the dispersed phase in the Euler-Lagrange and the Euler-Euler approaches. The Mesoscopic Eulerian Formalism is presented and the transport equations and coupling terms with the gas phase described.

  Chapter 3 presents the concept of LES and briefly describes the filtering process underneath the approach. It presents the filtered governing equations for the gas and the dispersed phases. The WALE model for gaseous phase and the filtered equations for the dispersed phase (Moreau (2006)) used for the simulation of the MERCATO configuration in Part IV are summarized.

- Part II is dedicated to the analysis and validation of different closure models for the deviatoric part of the RUM stress tensor. First, Chapter 4 presents the different models (Masi (2010)) retained for their evaluation in AVBP. These models have been proposed by Masi (2010) during her thesis performed at IMFT (Institut de Mécanique de Fluides de Toulouse). Masi developped several closure models and performed an *a priori* analysis in the configuration of a particle-laden slab (Vermorel (2003)). Nine out of the eleven models developped by Masi along with the classic viscosity-type model already implemented in AVBP (Simonin *et al.* (2001)) have been implemented in AVBP and *a posteriori* validated against the Euler-Lagrange results of Masi (2010) in the same configuration (Fig. 1.7). A classification of the models following two criteria (the order of the model and the characteristic time scale used) as proposed by Masi (2010) is provided.

  Chapter 5 presents the results obtained for the configuration of Fig. 1.7. This academic configuration aims at being representative of the phenomena encountered in a hollow-cone type spray injection, where the liquid fuel droplets are subject to very strong shear due to the effect of air entrainment. Two different levels of turbulence and three levels of particle inertia have been tested. The models have been evaluated using the same numerical setup in order to simplify the comparisons. Low-order and high-order statistics have been compared as well as instantaneous fields of the droplet number density, droplet velocity and Random Uncorrelated Energy (RUE). The results obtained distinguish one model as the one giving the best performances (2ΦEASM3). This model has been retained for the simulation of the configuration presented in Part IV.

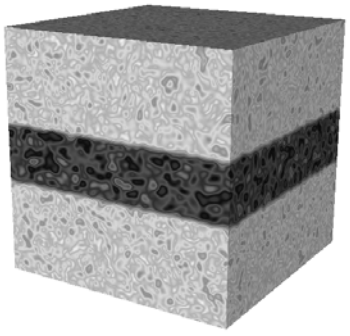

Figure 1.7: *Sketch of the case studied in Part II corresponding to the configuration initialy studied by Vermorel (2003).*

- Part III focuses on the development of a new model for the simulation of the evaporation process of liquid fuel droplets. This part is motivated by the recent publication of experimental results on isolated droplet

evaporation (Chauveau *et al.* (2008)) which are very different from the classical results (Nomura *et al.* (1996).

Chapter 6 proposed a classification of the different evaporation models and introduces the assumptions employed in the model implemented in AVBP. The equations used for the calculation of the main thermodynamic and transport properties are presented. A comparison between simulations performed with two different calculations of the transport and thermodynamic properties (as previously done by Sanjosé (2009)) allowed the identification of the parameters having a major influence on the process. Taking this into account, a new approach for the simulation of the evaporation process is proposed. Chapter 7 shows the results obtained with the classical approach implemented in AVBP and the new approach for both the Spalding and the Abramzon-Sirignano models for the evaporation of single isolated droplets. The results are presented for two fuels for a wide range of conditions (temperature and pressure).

- Finally, Part IV presents the simulations performed in the MERCATO configuration (Fig. 1.8) in order to assess the applicability of RUM and evaporation models to complex configurations. The MERCATO test rig is a semi-industrial configuration used for the study of spray autoignition at high altitude conditions. Four cases are presented, they are issued by the combination between two evaporation approaches and two RUM strategies (noRUM, which does not take into account the RUM contribution and 2ΦEASM3 model). The mean and instantaneous gaseous and liquid fields are studied. Both the gaseous and the liquid mean and root mean sqaure (RMS) velocity profiles are analyzed, as well as the mean and RMS droplet diameter profiles. Particle velocity fields are validated against the experimental data of García-Rosa (2008). For those quantities such as the particle volume fraction, for which experimental data is not available, comparison with the classical models implemented in AVBP are performed. The effects of the evaporation approach and the RUM model are assessed separately.

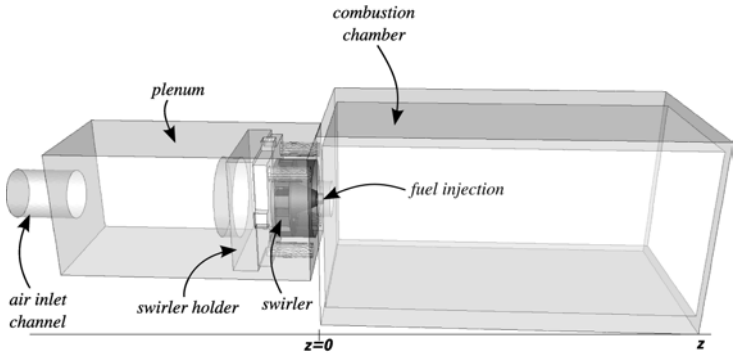

Figure 1.8: *Sketch of the MERCATO configuration studied in Part IV. Extracted from Senoner (2010).*

- Chapter presents the main conclusions obtained and proposes new paths for the continuation of this work.
- The Appendices include additional data which may be useful for a deeper analysis of the RUM models but have not been included in the manuscript itself for the sake of simplicity.

Part I

Equations and models for turbulent two-phase flows

Chapter 2

Transport equations for dispersed two-phase flows

This part aims at describing the compressible Navier-Stokes (NS) equations as found in many text books (Anderson (1990), Hirsch (2007)). Section 2.1 presents the NS equations for the gaseous phase. Reactive terms are not be considered as combustion is not studied in this work. Section 2.2 presents the conservation equations for the dispersed phase, both in the Euler-Lagrange (EL) and in the Euler-Euler (EE) frameworks as implemented in AVBP. The implementation retained in AVBP is based on the Mesoscopic Eulerian Formalism (MEF) for the Euler-Euler framework. It is described in Section 2.2.4. As comparisons with the Euler-Lagrange approach are needed for validation and assessment of the Eulerian closure models, the Euler-Lagrange approach is briefly described in Section 2.2.2. Coupling terms between both phases which are common to both formalismsare finally described in Section 2.3.

2.1 Conservation equations for compressible gaseous flows

Assuming no chemical reaction, one may write the set of conservation equations that describes a compressible gas flow as follows:

$$\frac{\partial}{\partial t}\rho_k + \frac{\partial}{\partial x_j}\rho_k u_{g,j} = -\frac{\partial}{\partial x_j}J_{j,k} \tag{2.1}$$

$$\frac{\partial}{\partial t}\rho_g u_{g,i} + \frac{\partial}{\partial x_j}\rho_g u_{g,i}u_{g,j} = -\frac{\partial}{\partial x_j}\left[P_g\delta_{ij} - \tau_{g,ij}\right] \tag{2.2}$$

$$\frac{\partial}{\partial t}\rho_g E_g + \frac{\partial}{\partial x_j}\rho_g E_g u_{g,j} = -\frac{\partial}{\partial x_j}\left[u_{g,i}(P_g\delta_{ij} - \tau_{g,ij}) + q_{g,j}\right]. \tag{2.3}$$

Equations (2.1) - (2.3) describe the conservation laws for species, momentum and total energy respectively, where ρ_k is the density of each species k composing the gaseous mixture ($\rho_k = \rho_g Y_k$, T_k is the mass fraction of species k), ρ_g is the gaseous mixture density ($\rho_g = \sum_{k=1}^{N}\rho_k$), $J_{j,k}$ is the mass diffusive flux of species k (Eq. (2.26)), $u_{g,i}$ is the $i-th$ component of the gaseous velocity, E_g denotes the gaseous total non-chemical energy, $\tau_{g,ij}$ denotes the viscous stress tensor and $q_{g,j}$ is the diffusive heat flux vector (Eq. (2.27)). The species conservation imposes $\sum_{k=1}^{N} Y_k = 1$.

This set of equations can be written in compressed form:

$$\frac{\partial}{\partial t}\mathbf{w} + \nabla\cdot\mathcal{F} = \mathbf{s_{l-g}}, \tag{2.4}$$

where $\mathbf{w} = (\rho_k, \rho_g u_{g,i}, \rho_g E_g)^T$ is the vector of conservative variables, $\mathcal{F}$ is the flux tensor and $\mathbf{s_{l-g}}$ is the source term vector due to the influence of the dispersed phase on the gaseous phase. The flux tensor can be decomposed into an inviscid $\mathcal{F}^{\mathcal{I}}$ and a viscous $\mathcal{F}^{\mathcal{V}}$ part which read:

$$\mathcal{F}^{\mathcal{I}} = \begin{pmatrix} \rho_k u_{g,j} \\ \rho_g u_{g,i} u_{g,j} + P_g \delta_{ij} \\ (\rho_g E_g + P_g \delta_{ij}) u_{g,j} \end{pmatrix}, \qquad \mathcal{F}^{\mathcal{V}} = \begin{pmatrix} J_{j,k} \\ -\tau_{g,ij} \\ -(u_{g,i}\tau_{g,ij}) + q_{g,j} \end{pmatrix}. \tag{2.5}$$

The hydrostatic pressure (P_g) is determined by the equation of state for perfect gases:

$$P_g = \rho_g \frac{\mathcal{R}}{\mathcal{W}_g} T_g \tag{2.6}$$

where $\mathcal{R} = 8.3143 J/(mol \cdot K)$ is the universal gas constant, $\mathcal{W}_g$ is the molecular weight of the gaseous mixture and T_g its temperature. The gaseous phase is usually composed by multiple species. It is considered as a perfect mixture of N perfect gases, whose state is defined by Eq. (2.6), where, $\mathcal{W}_g$ is the molecular weight of the mixture:

$$\frac{1}{\mathcal{W}_g} = \sum_{k=1}^{N} \frac{Y_k}{\mathcal{W}_k}. \tag{2.7}$$

The set of equations Eqs. (2.1) - (2.3) are closed provided the viscous flux tensor is modeled. In practical situations, all fluids are assumed to be Newtonian, so the stress tensor is given by a Newton law (Eq. (2.8)):

$$\tau_{g,ij} = 2\mu_g \left(S_{g,ij} - \frac{1}{3}\delta_{ij} S_{g,ll} \right), \tag{2.8}$$

where μ_g is the dynamic viscosity of the gaseous mixture. $S_{g,ij}$ is the gaseous rate-of-strain tensor:

$$S_{g,ij} = \frac{1}{2} \left(\frac{\partial u_{g,j}}{\partial x_i} - \frac{\partial u_{g,i}}{\partial x_j} \right). \tag{2.9}$$

2.1.1 Thermodynamical laws for the gaseous phase

The thermodynamical properties of the gaseous mixture are calculated as a mass average of the properties of each individual species. Thus, the mixture constant r and the heat capacities at constant pressure or volume depend on the local composition of the mixture and are written as follows:

$$\overline{r} = \frac{\mathcal{R}}{\mathcal{W}_g} = \sum_{k=1}^{N} \mathcal{R} \frac{Y_k}{\mathcal{W}_k} = \sum_{k=1}^{N} Y_k r_k, \tag{2.10}$$

$$\overline{C_p} = \sum_{k=1}^{N} Y_k C_{p,k}, \tag{2.11}$$

$$\overline{C_v} = \sum_{k=1}^{N} Y_k C_{v,k}. \tag{2.12}$$

For the sake of clarity, the subscript g for the gas phase has been omitted; the superscript m denotes molar quantities.

In AVBP, the thermodynamical properties (sensible enthalpy $h_{s,k}$ and sensible entropy s_k) are tabulated for each species. The tables include values from $0K$ to $5000K$ every $100K$. They are referenced at $T_0 = 0K$ and $1bar$. The values in the tables are extracted from the JANAF tables (Stull & Prophet (1971)). The sensible

enthalpy of each species is calculated from the tabulated values as in Eq. (2.13), as well as the sensible entropy as in Eq. (2.14). Finally the sensible energy is calculated using Eq. (2.15).

$$h_{s,k}(T) = \int_{T_0}^{T} C_{p,k}\,\mathrm{d}T = \frac{h^m_{s,k}(T) - h^m_{s,k}(T_0)}{\mathcal{W}_k}, \tag{2.13}$$

$$s_k(T) = \frac{s^m_k(T) - s^m_k(T_0)}{\mathcal{W}_k}, \tag{2.14}$$

$$e_{s,k}(T) = \int_{T_0}^{T} C_{v,k}\,\mathrm{d}T = h_{s,k}(T) - r_k T. \tag{2.15}$$

The sensible enthalpy (h_s) and sensible energy (e_s) are defined as follows:

$$h_s = \sum_{k=1}^{N} Y_k h_{s,k}, \tag{2.16}$$

$$e_s = \sum_{k=1}^{N} Y_k e_{s,k}. \tag{2.17}$$

The heat capacities are considered as constant on each interval of $100K$ corresponding to the gap between two consecutive values in the tables. They are evaluated as:

$$C_{p,k} = \frac{\partial h_{s,k}}{\partial T}, \qquad C_{v,k} = \frac{\partial e_{s,k}}{\partial T}. \tag{2.18}$$

2.1.2 Transport laws for the gaseous phase

In gaseous flow, there are two main mechanisms involving diffusion: the molecular diffusion due to local differences in composition, and the heat diffusion due to local differences in temperature.

Diffusion coefficients for mass and heat transport

Molecular and heat diffusion laws depend on several transport properties, such as the dynamic viscosity of the mixture (μ_g), its thermal conductivity (λ_g) or the diffusion coefficient of species k in the mixture (D_k).

The dynamic viscosity is assumed independent of the composition. It is calculated using a Power law which takes into account the variations of temperature. μ_{ref} and T_{ref} are the reference viscosity and temperature whereas b is the Power law exponent:

$$\mu_g = \mu_{ref}\left(\frac{T}{T_{ref}}\right)^b. \tag{2.19}$$

The thermal conductivity of the mixture is evaluated assuming a constant value for the Prandtl number (Pr), it depends on the dynamic viscosity and the heat capacity of the mixture:

$$\lambda_g = \frac{\mu_g \overline{C_p}}{Pr}. \tag{2.20}$$

The Prandlt number is a dimensionless number representing the ratio of momentum diffusivity to thermal diffusivity:

$$Pr = \frac{\nu}{\alpha} = \frac{viscous\ diffusion\ rate}{thermal\ diffusion\ rate}. \tag{2.21}$$

The molecular diffusion of each species k into the mixture is calculated assuming that the Schmidt number of each species (Sc_k) is constant; it depends on the dynamic viscosity and the density of the mixture:

$$D_k = \frac{\mu_g}{\rho_g Sc_k}. \tag{2.22}$$

The Schmidt number is a dimensionless number representing the ratio of momentum diffusivity and mass diffusivity. It relates the relative thickness of the hydrodynamic layer and the mass-transfer boundary layer:

$$Sc_k = \frac{\nu_k}{D_k} = \frac{viscous\ diffusion\ rate}{molecular\ diffusion\ rate}. \tag{2.23}$$

Mass transport law

When the gaseous phase is composed of several species, the conservation equation (2.24) must be satisfied. The species diffusion velocity $V_{k,i}$ is approximated by the Hirschfelder-Curtis relation (Hirsch (1990)):

$$Y_k V_{k,i} = -D_k \frac{\mathcal{W}_k}{\mathcal{W}} \frac{\partial X_k}{\partial x_i}, \tag{2.24}$$

where D_k is the diffusion coefficient of the species k into the mixture given by Eq. (2.22). This approximation does not ensure the conservation of total mass for mixtures composed of more than two species. A correction velocity V_i^c is thus introduced to ensure mass conservation (Poinsot & Veynante (2005)):

$$V_i^c = \sum_{k=1}^{N} D_k \frac{\mathcal{W}_k}{\mathcal{W}} \frac{\partial X_k}{\partial x_i}. \tag{2.25}$$

The diffusive flux taking into account this correction reads:

$$J_{i,k} = -\rho_g \left(D_k \frac{\mathcal{W}_k}{\mathcal{W}} \frac{\partial X_k}{\partial x_i} - Y_k V_i^c \right). \tag{2.26}$$

Heat transport law

The total heat flux $\mathbf{q}$ is composed of two contributions: the conductive heat flux and the heat flux through species diffusion. The conductive heat flux is modeled by Fourier's law. λ_g is the thermal conductivity of the mixture given by Eq. (2.20):

$$q_i = -\lambda_g \frac{\partial T}{\partial x_i} + \sum_{k=1}^{N} J_{i,k} h_{s,k}. \tag{2.27}$$

2.2 Conservation equations for the dispersed phase

While the gaseous phase is usually described as a continuum iwith an Eulerian approach, there are different approaches for the description of the dispersed phase. Recently, Fox (2012) has provided a classification of the different approaches for the DNS of two-phase flows (Fig. 2.1). CPS-RESUME DE FOX:2012

Two main frameworks for the simulation of the dispersed phase are used in this work: the Euler-Lagrange approach and the so-called Mesoscopic Eulerian Formalism (MEF). Whatever the approach used, to describe the behavior of droplets or particles in a gaseous flow, the first step os to determine the forces acting on them (Section 2.2.1). Generally, then the conservation equations taking into account those forces can be written. Section 2.2.2 briefly describes the Euler-Lagrange approach, introducing the quantities of interest for this work. Section 2.2.3 positions the MEF among the multiple Euler-Euler approaches. Finally, Section 2.2.4 describes the MEF itself and the transport equations which will be solved.

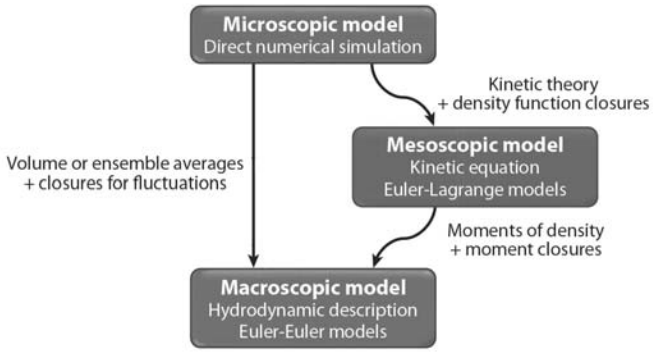

Figure 2.1: *Classification of modeling approaches for DNS of two-phase flows. Extracted from Fox (2012).*

2.2.1 Review of forces acting on an isolated particle

The first descriptions of the forces acting on an isolated particle date from the end of the 19^{th} century. Boussinesq (1885), Basset (1888) and Oseen (1927) studied the settling motion of particles in a quiescent flow due to the action of gravity. However, it was Tchen (1947) who applied their conclusions to particles in turbulent flows for the first time. He extended their work to the motion of rigid spherical particles in Homogeneous Isotropic Turbulence (HIT). Tchen took into account the main forces described by Boussinesq, Basset and Oseen, namely the Stokes drag, the pressure gradient force, the added mass, the Basset force and the lift force. More recently, the work of Tchen has been revisited by Maxey & Riley (1983). They considered isolated rigid spherical particles, with constant diameter d_p and density ρ_p.

The kinematic equation for a particle that translates at velocity (rotation is excluded) $\mathbf{v}_{p,i}$ reads:

$$\frac{d}{dt}x_{p,i} = \mathbf{v}_{p,i}. \tag{2.28}$$

The momentum conservation equation is written as:

$$m_p \frac{d}{dt}\mathbf{v}_{p,i} = F_{p,i} = F^u_{p,i} + F^p_{p,i}. \tag{2.29}$$

The total force $F_{p,i}$ is the sum of two contributions: $F^u_{p,i}$ is the force that would act on a fluid particle occupying the position of the particle; $F^p_{p,i}$ denotes the force exerted upon the particle due to the perturbation of the fluid velocity fields caused by the presence of the particle.

It is assumed that the particle diameter is small compared to the smallest scales of the fluid motion (the Kolmogorov scale η_k in a turbulent flow as described in Chapter 3):

$$d_p \ll \eta_k \ , \tag{2.30}$$

and a small particle Reynolds number Re_p which reads:

$$Re_p = \frac{d_p|\mathbf{u}_{f@p} - \mathbf{v}_p|}{\nu_g} \ , \tag{2.31}$$

where ν_g stands for the gaseous kinematic viscosity.

The term $F^u_{p,i}$ assumes that the forces due to pressure and viscous stress, that would have acted on a fluid particle occupying the volume where the particle is actually located, are transmitted to the particle. Maxey & Riley (1983) and Gatignol (1983) suggest:

$$F^u_{p,i} = \frac{\pi d_p^3}{6}\left[\rho_g \frac{D}{Dt}\mathbf{u}_{f@p,i} + (\rho_p - \rho_g)g_i\right], \tag{2.32}$$

where g_i denotes the $i-th$ component of the gravity vector, $\mathbf{u}_{f@p}$ is the undisturbed fluid velocity at the particle location, ρ is the density. The subscript g and p stands for the gas (or fluid) and the particle respectively. D/Dt represents the total derivative along particle trajectories:

$$\frac{D}{Dt} = \frac{\partial}{\partial t} + \mathbf{u}_{f@p,i}\frac{\partial}{\partial x_i}. \tag{2.33}$$

The first term in the Right-Hand-Side (RHS) of Eq. (2.32) accounts for pressure and viscous stresses and the second one for buoyancy effects.

The term $F^p_{p,i}$ stands for the aerodynamic forces acting on the particle: drag force, added-mass force, Basset force and lift force.

Drag force

The drag force F_D accounts for pressure and viscous stresses exerted on the particle surface. It corresponds to the force originally derived by Stokes (1851) in quiescent fluid for small Re_p, which allows to neglect inertial effects of the fluid flow.

$$F_D = \frac{3}{4}\rho_g\frac{\pi d_p^3}{6}\frac{1}{d_p}C_D|\mathbf{u}_{f@p} - \mathbf{v}_p|(\mathbf{u}_{f@p} - \mathbf{v}_p). \tag{2.34}$$

where C_D is the Stokes drag coefficient. Another definition introduces the particle response time τ_p to describe the drag force:

$$F_D = \frac{m_p}{\tau_p}(\mathbf{u}_{f@p} - \mathbf{v}_p)\ , \tag{2.35}$$

where:

$$\tau_p = \frac{4}{3}\frac{\rho_p}{\rho_g}\frac{d_p}{C_D}|\mathbf{u}_{f@p} - \mathbf{v}_p|^{-1}. \tag{2.36}$$

There are three main formulations for the Stokes drag coefficient C_D, depending on the particle Reynolds number. Stokes (1851) developped an analytical solution for $Re_p \ll 1$:

$$C_D = \frac{24}{Re_p}, \tag{2.37}$$

Oseen (1927) proposed a correction of the Stokes' relation to take into account inertial effects which is valid for $1 \leq Re_p \leq 5$:

$$C_D = \frac{24}{Re_p}\left(1 + \frac{3}{16}Re_p\right) \tag{2.38}$$

For larger Re_p, semi-empirical correlations are available. Up to $Re_p = 1000$, the correlation proposed by Schiller & Nauman (1935) is widely accepted (this is, in fact, the correlation inplemented in AVBP and used in this work):

$$C_D = \frac{24}{Re_p}(1 + 0.15Re_p^{0.687}). \tag{2.39}$$

For applications where $Re_p > 1000$, following Clift *et al.* (1978), the drag coefficient remains unaffected by the wake behind the particle and stays constant:

$$C_D = 0.44. \tag{2.40}$$

Added-mass force

The added-mass force accounts for the acceleration of the fluid due to the particle motion. When a particle accelerates in a fluid, it implies an acceleration of the surrounding fluid at the expense of the work exerted by the particle.

It is usually written as:

$$F_{AM} = \frac{\pi d_p^3}{6}\rho_g C_m \left(\frac{D}{Dt}\mathbf{u}_{f@p} - \frac{d}{dt}\mathbf{v}_p\right). \tag{2.41}$$

where C_m is the added-mass force constant: $C_m = 0.5$.

Since the added-mass froce depends on the fluid density, it is often neglected for particles much denser than the fluid (Hinze (1975), Desjonqueres *et al.* (1986)). In this work, it is assumed that the ratio between the particle's density and the density of the fluid is larger than 10^3 ($\rho_p/\rho_g > 1000$), so that the added-mass force can be neglected. In those cases where the fluid is denser than the particles (or their densities are comparable), neglecting the added-mass force may lead to significant errors, since the virtual added-mass may become larger than the particle mass itself.

Basset force

The History or Basset force is linked to the memory of the particle, the history of its past accelerations. It accounts for the temporal delay in the boundary layer development due to the changes in the relative velocity between the particle and the fluid (Crowe *et al.* (1998)):

$$F_H = \frac{\pi d_p^3}{6}\frac{9\rho_g}{d_p}\left(\frac{\nu_g}{\pi}\right)^{1/2}\int_\infty^t \frac{d}{d\tau}(\mathbf{u}_{f@p} - \mathbf{v}_p)\frac{d\tau}{\sqrt{t-\tau}}. \tag{2.42}$$

It is usually neglected due to the dificulties of implementation (that is the case in this work). However, neglecting it may lead to significant errors when the particle is accelerated at high rate (Thomas (1992), Johnson (1998)), which is not the case in the configurations studied in this work.

Lift force

The lift force is due to the fluid vorticity Ω_g, it is non-negligible for large particles where the fluid velocity gradient differs significantly from one side of the particle to the other. It usually reads:

$$F_L = \frac{\pi d_p^3}{6}\rho_g C_L(\mathbf{u}_{f@p} - \mathbf{v}_p) \times \Omega_g. \tag{2.43}$$

Hinze (1975) and Desjonqueres *et al.* (1986) showed that not only the added-mass force, but also the pressure gradient and the Basset forces can be neglected when $\rho_p/\rho_g > 1000$, since they are small compared to the particle agitation and dispersion mechanisms. In HIT, Elghobashi & Truesdell (1993) showed that those two mechanisms are mainly due to Stokes drag and gravity.

2.2.2 Euler-Lagrange

The Lagrangian approach for the simulation of two-phase flows considers that the discrete phase is composed of an ensemble of particles (physical individual particles or numerical particles representing a cluster of real particles) each one with its own velocity. The individual trajectory of each particle is tracked and the point mechanics equations are solved with momentum, mass and heat coupling with the gas phase (treated with an Eulerian approach).

This method is also referred as Discrete Particle Simulation (DPS). It has been widely used for the simulation of gas-solid flows (Tchen (1947), Hinze (1975), Desjonqueres *et al.* (1986), Squires & Eaton (1990), Deutsch & Simonin (1991), Druzhinin (1995), Boivin *et al.* (1998), Février *et al.* (2005), Moreau (2006)), Masi (2010) in academic configurations. Following Boivin *et al.* (2000), this approach is limited to weakly loaded flows ($\alpha_p \leq 0.001$, where α_p is the particle volume fraction, i.e. the ratio between the total mass of the particles and the total mass of the gas) and particle response times larger than the characteristic time of the gaseous flow. Indeed, a large

amount of particles implies that the individual equations of each particle must be solved, considerably increasing the computational cost of this approach.

The Euler-Lagrange (EL) approach has, however, an important advantage: it requires few modeling efforts. The treatment of polydispersion, for example, is straightforward. This method is commonly employed in Reynolds-Averaged-Navier-Stokes (RANS) codes and its potential in LES has been stated (Mahesh *et al.* (2002), Mashayek & Pandya (2003), Pandya & Mashayek (2002), García (2009)). It has also been applied to LES of industrial configurations (Senoner (2010)). There are still numerical issues to be handled: the location of particles in the Eulerian mesh needs very efficient algorithms. Another issue is the interpolation of the coupling terms from the Eulerian mesh nodes to the particle position and vice-versa. In order to avoid numerical errors, high-order numerical schemes are requested, which notably increases the computational cost. In parallel computing, the transfer of particles exiting the domain of one processor and entering a different one is crucial and very efficient domain partitioning algorithms are needed in order to avoir load balancing problems due to inhomogeneous repartition of the particles in the computational domain (García (2009)).

Equations for the Euler-Lagrange approach:

In the EL approach, the gas phase is described by means of the Navier-Stokes equations described in Section 2.1. Assuming that the only forces acting on a particle are the Stokes-drag and the gravity, the position $\mathbf{x}_p^{(k)}$ and the velocity $\mathbf{v}_p^{(k)}$ of particle k are calculated at each time step as follows:

$$\frac{d}{dt}\mathbf{x}_p^{(k)} = \mathbf{v}_p^{(k)} \tag{2.44}$$

$$\frac{d}{dt}(m_p^{(k)}\mathbf{v}_p^{(k)}) = F_{p,i}^{(k)} \tag{2.45}$$

$$\frac{d}{dt}m_p^{(k)} = \dot{m}_p^{(k)} \tag{2.46}$$

$$\frac{d}{dt}(m_p^{(k)}C_p^{(k)}T_p^{(k)}) = \dot{Q}_p^{(k)}\ , \tag{2.47}$$

where $m_p^{(k)}$ is the mass of the particle k, $C_p^{(k)}$ is its specific heat at constant pressure, $T_p^{(k)}$ is its temperature, $\dot{m}_p^{(k)}$ is the mass transfer rate due to evaporation (otherwise the mass of the particle remains constant) and $\dot{Q}_p^{(k)}$ is the heat transfert rate from the gas phase to the particle.

Useful Lagrangian quantities

The averaging operator associated with the particle-phase is noted $\langle\cdot\rangle_p$, it is defined, for every Lagrangian quantity $\Phi^{(k)}$, as:

$$\langle\Phi^{(k)}(\mathbf{x}_p^{(k)})\rangle_p = \frac{1}{N_p}\sum_{k=1}^{k=N_p}\Phi^{(k)}(\mathbf{x}_p^{(k)} - \delta\mathbf{x}_p) \tag{2.48}$$

where N_p is the total number of particles. The mean particle velocity is then expressed as:

$$\mathbf{V}_p = \langle\mathbf{v}_p\rangle_p \tag{2.49}$$

and the fluctuating contribution as:

$$\mathbf{v}'_p = \mathbf{v}_p - \mathbf{V}_p \tag{2.50}$$

Then, the particle kinetic energy q_p^2, and the fluid-particle correlation q_{fp} (where the subscript $_f$ is used to denote the carrier fluid) yield:

$$q_p^2 = \frac{1}{2}\langle\mathbf{v}_p^{(k)}\cdot\mathbf{v}_p^{(k)}\rangle_p \tag{2.51}$$

$$q_{fp} = \langle \mathbf{v}_p^{(k)} \cdot \mathbf{u}_f(x_p^{(k)}) \rangle_p. \tag{2.52}$$

For the gas phase, the fluid turbulent kinetic energy q_f^2 can be defined using the classical Reynolds average operator (Hinze (1975)), noted $\langle \cdot \rangle_f$ and corresponding to a statistical mean of N flow realizations:

$$q_f^2 = \frac{1}{2} \langle \mathbf{u}'_f \cdot \mathbf{u}'_f \rangle_f \ , \tag{2.53}$$

where $\mathbf{u}'_f$ is the fluctuating part of the fluid velocity.

Tchen's theory

Tchen (1947) proposed, for stationnary particle-laden HIT flows, a link between the previous quantities through Eqs. (2.54)-(2.55), needed to have correspondance between the two operators applied to the fluid and particle fields. These relations require two main assumptions: first, the aerodynamic force acting on the particle must consist only of Stokes drag given by Eq. (2.35). Secondly, the relative velocity between the particle and the fluid must be very small.

$$q_{fp} = \frac{2}{1+St} q_f^2, \tag{2.54}$$

$$2q_p^2 = q_{fp} \tag{2.55}$$

where $St = \tau_p / \tau_f^t$ stands for the Stokes number, and τ_f^t is the Lagrangian turbulent time-scale (Haworth & Pope (1986)).

Deutsch & Simonin's extended theory

In order to relax the second assumption in Tchen's theory, Deutsch & Simonin (1991) proposed an extension of Tchen's theory using the fluid velocity along particle trajectories $\mathbf{u}_{f@p}$ introduced in Section 2.2.1. Consequently, the fluid turbulent kinetic energy sampled along particle trajectories $q_{f@p}^2$ reads:

$$q_{f@p}^2 = \frac{1}{2} \langle \mathbf{u}'_{f@p} \cdot \mathbf{u}'_{f@p} \rangle_p, \tag{2.56}$$

$$q_{fp} = \frac{2}{1+St'} q_{f@p}^2, \tag{2.57}$$

$$2q_p^2 = q_{fp}. \tag{2.58}$$

where $St' = c/\tau_p$ is a modified Stokes number and $\tau_{f@p}^t$ is a characteristic timescale using $\mathbf{u}_{f@p}$. In the limit of very small Stokes numbers, $\tau_{f@p}^t \to \tau_f^t$. Since $\tau_{f@p}^t$ and $q_{f@p}^2$ are difficult to quantify, Eqs. (2.54) and (2.55) are often used as a first approximation to evaluate q_p^2.

2.2.3 Euler-Euler approach

In the Euler-Euler approach (EE), the dispersed phase is treated as a continuous phase, and instead of computing the properties of each individual particle, the local average properties are calculated. There are two main types of average operator: the volume average and the statistical average. For these approaches, the same numerical approach used for the gaseous phase may be applied to the dispersed phase, which greatly simplifies its implementation in parallel CFD codes. Moreover, no interpolation procedure is needed for the coupling between phases, since the information for both liquid and gaseous phases are stored at the same nodes of the grid. However, an important modeling effort is required which nowadays remains the main challenge.

For very low-inertial particles, the modeling effort is reduced, since the particles behave like tracers and almost follow the fluid flow. The equilibrium approach (Ferry & Balachandar (2002), Rani & Balachandar (2004)) has proved its efficiency and accuracy in the simulation of this type of flows. It consists in the solution of one transport equation for the particle number density (n_p, the number of particles per unit volume) and a Taylor expansion of the fluid velocity in particle relaxation time τ_p to predict the particle velocity (Maxey (1987)). When heavier particles are to be modeled, their response time become larger and the method reaches its applicability limits.

The two-fluid approach, originally developped by Druzhinin & Elghobashi (1998), is based on a spatial average of the instantaneous equations for the gaseous and dispersed phases over a length scale of the order of the Kolmogorov length scale (assuming that the particle diameter and the smallest length scale of the particle velocity are significantly smaller than the Kolmogorov length scale, so the unity of the particle velocity in the filtering volume is ensured). The two-fluid approach shows good results in the simulation of particle-laden decaying HIT flow for particles with small Stokes number.

In configurations where the average values are not sufficient for a realistic representation of the dispersed phase, the complexity of modeling increases. This is the case, for example, for polydispersed sprays. Following Greenberg *et al.* (1993), Laurent & Massot (2001) proposed to divide the dispersed phase into different sections, each one containing one class of diameter. Then, a different set of Eulerian equations needs to be solved for each of the sections. This increases notably the computational cost, but, the authors showed that a few sections are sufficient to obtain an accurate representation of a spray with a wide distribution of diameters. Another challenge of this approach, called Eulerian Multi Size Moment (EMSM), is the treatment of the exchanges between different classes of diameters; when including evaporation, the droplet diameter reduces as they evaporate and they must be transferred to a lower diameter class. Mossa (2005) proposed another approach where the addition of one equation for the particle droplet surface allows the representation of polydispersion effects.

Collision and crossing trajectories are difficult to model in the Eulerian approach. Indeed, Eulerian models derived from the Williams-Boltzmann equation through a near-equilibrium assumption along with closures for the second-order velocity moments are unable to capture the multiple values of particle velocity at the same time and location when particle trajectory crossing (PTC) takes place. The near-equilibrium assumption is a strong hypothesis, and although those methods may be able to capture when PTC takes place, they lead to singularities called δ-shocks (de Chaisemartin *et al.* (2008), de Chaisemartin (2009)). However, it has been stated (Desjardins *et al.* (2006)) that it is possibe to predict the crossing of particle trajectories in an Eulerian framework using the DQMOM approach (Marchisio & Fox (2005), Fox *et al.* (2008)). More recently, Kah (2010) proposed a new method called Eulerian Multi-Fluid Multi-Velocity (EMVM), using quadrature-based moment methods (Fox *et al.* (2008), Fox (2008), Fox (2009)), preserving the moment phase-space realizability. Indeed, Wright (2007) showed that, in general, high-order, finite-volume schemes do not guarantee realizable moments (i.e. the independent transport of the moments with schemes of order greater than one, may lead to invalid moment sets), and thus new realizable high-order algorithms must be used (Kah *et al.* (2011)). More details about this high-order algorithm as well as EMSM and EMVM methods can be found in Kah (2010).

Finally, it is to be noted that the Eulerian approach implies some difficulties from the numerical point of view due to high compressibility effects that require to transport very stiff gradients difficult to handle numerically. Riber *et al.* (2006) showed that the use of low dispersion numerical schemes along with an adapted artificial viscosity operator may be a solution.

The methods based on volume filtering show important limits when simulating flows with high inertial particles. The reasons for this failure were first pointed out by Février *et al.* (2005). The authors proposed a new method where the paticle velocity is split into two different contributions: a spatially correlated part and a spatially uncorrelated part, which becomes negligible for very low inertial particles. The Mesoscopic Eulerian Formalism (MEF) is based on a conditional ensemble averaging (Section 2.2.4). This average operator leads to unclosed terms that need to be modeled (Part II). The resulting set of equations is presented in Section 2.3. Figure 2.2 shows a classification of all these Euler-Euler formalisms.

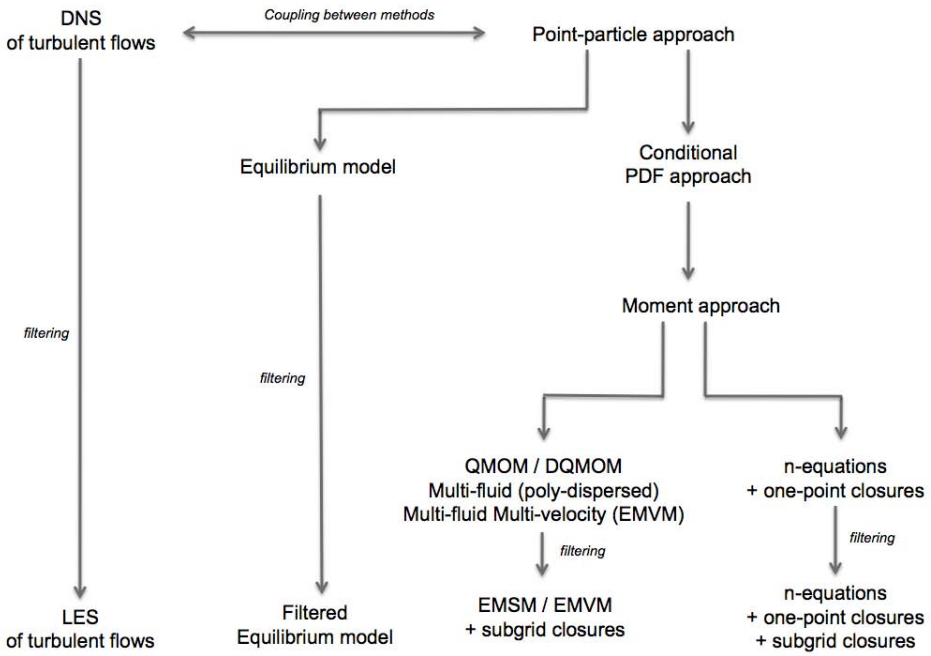

Figure 2.2: *Classification of EE modelling approaches for the dispersed phase interacting with turbulent flows. Modified from Masi (2010).*

2.2.4 Mesoscopic Eulerian approach

The MEF is the approach that has been implement in AVBP (Kaufmann (2004)). The main idea in the MEF is the distinction made between the properties of an ensemble of particles and the properties of an individual particle. The statistically averaged Euler-Euler (EE) equations are obtained from a Probability Density function (PDF) used to define a set of transport equations based on the kinetic theory of gases of Boltzmann (Chapman & Cowling (1939 (digital reprint 1999), Reeks (1991)). Based on this PDF evolution equation, direct integrations yield the transport equations of the desired moments for which unknowns naturally arise. Once the set of equations has been established, models are to be supplied. Contrary to the volume filtering of the equilibrium and two-fluid approaches, no assumption regarding the size of the filter is required at this stage.

The main steps in the procedure for the development of the MEF transport equations are:

1. The function $W_p^{(k)}$ describes the dynamics of the particles with respect to time and space. Each particle is identified by its position $\mathbf{x}$ at time t, its mass μ_p, its velocity $\mathbf{c}_p$ and its temperature ζ_p:

$$W_p^{(k)}(\mathbf{c}_p, \zeta_p, \mu_p, \mathbf{x}, t) = \delta\left(\mathbf{c}_p - \mathbf{u}_p^{(k)}(t)\right)\delta\left(\zeta_p - \zeta_p^{(k)}(t)\right)\delta\left(\mu_p - \mu_p^{(k)}(t)\right)\delta\left(\mathbf{x} - \mathbf{x}_p^{(k)}(t)\right) \quad . \tag{2.59}$$

   where δ is the Dirac's delta function.

2. Applying an ensemble averaging over a large number of particle realisations $\mathcal{H}_p$, conditioned by one realisation of the carrier fluid $\mathcal{H}_f$, a PDF for the particle presence is defined as:

$$\breve{f}_p(\mathbf{c}_p, \zeta_p, \mu_p, \mathbf{x}, t|\mathcal{H}_f) = \lim_{N_p \to \infty}\left[\frac{1}{N_p}\sum_{N_p}\sum_{k=1}^{N_p} W_p^{(k)}(\mathbf{c}_p, \zeta_p, \mu_p, \mathbf{x}, t, \mathcal{H}_p|\mathcal{H}_f)\right] \quad . \tag{2.60}$$

3. The Boltzmann type equation that describes the evolution of this PDF yields:

$$\frac{\partial}{\partial t}\breve{f}_p + \frac{\partial}{\partial x_j}\left[c_{p,j}\breve{f}_p\right] + \frac{\mathrm{d}}{\mathrm{d}c_{p,j}}\left[\frac{du_{p,j}}{dt}\breve{f}_p\right] + \frac{\mathrm{d}}{\mathrm{d}\zeta_p}\left[\frac{dT_p}{dt}\breve{f}_p\right] + \frac{\mathrm{d}}{\mathrm{d}\mu_p}\left[\frac{dm_p}{dt}\breve{f}_p\right] = \left(\frac{\mathrm{d}\breve{f}_p}{\mathrm{d}t}\right)_{coll}. \quad (2.61)$$

   where $\left(\frac{\mathrm{d}\breve{f}_p}{\mathrm{d}t}\right)_{coll}$ accounts for the inter-particle interactions.

4. A statistical average operator is defined to decribe the average properties of the dispersed phase. The mesoscopic quantities $\breve{\breve{\mathbf{\Psi}}}$ are defined by their mass ensemble average and correspond to the moments of the PDF obtained by multiplication of Eq. (2.61) by $\mathbf{\Psi}$ and integration over the phase space:

$$\breve{\breve{\mathbf{\Psi}}} = \langle\mathbf{\Psi}\rangle_p = \frac{1}{\rho_p\breve{\alpha}_p}\int \mu_p\mathbf{\Psi}(\mathbf{c}_p,\zeta_p,\mu_p)\breve{f}_p(\mathbf{c}_p,\zeta_p,\mu_p,\mathbf{x},t|\mathcal{H}_f)d\mathbf{c}_p d\zeta_p d\mu_p. \quad (2.62)$$

5. The general Enskog equation describing the evolution of the mesoscopic quantity $\mathbf{\Psi}$ is written as follows:

$$\begin{aligned}\frac{\partial}{\partial t}\rho_p\breve{\alpha}_p\langle\mathbf{\Psi}\rangle_p = \frac{\partial}{\partial x_i}\rho_p\breve{\alpha}_p\langle u_{p,j}\Psi\rangle_p &= \mathbb{C}(m_p\mathbf{\Psi}) \\ &+ \rho_p\breve{\alpha}_p\langle\frac{\mathrm{d}u_{p,j}}{\mathrm{d}t}\frac{\partial\mathbf{\Psi}}{\partial u_{p,j}}\rangle_p + \rho_p\breve{\alpha}_p\langle\frac{\mathrm{d}T_p}{\mathrm{d}t}\frac{\partial\mathbf{\Psi}}{\partial T_p}\rangle_p \\ &+ \rho_p\breve{\alpha}_p\langle\frac{\mathrm{d}m_p}{\mathrm{d}t}\left(\frac{\partial\mathbf{\Psi}}{\partial m_p}+\frac{\mathbf{\Psi}}{m_p}\right)\rangle_p \end{aligned} \quad (2.63)$$

6. The substitution of $\mathbf{\Psi}$ by the transported quantities produces a system of conservation equations that describes the mean mesoscopic field.

In AVBP, the first five moments are transported, they correspond to the following mesoscopic quantities: $\breve{n}_p$ is the particle number density (number of particles per unit volume), $\breve{\alpha}_p$ is the volume fraction of particles, $\breve{\mathbf{u}}_p$ is the particle velocity, $\delta\breve{\theta}_p$ is the uncorrelated energy and $\breve{h}_p$ is the enthalpy. In the following inter-particle interactions are neglected.

As an example, in order to obtain the transport equation for the first moment (the particle number density), $\mathbf{\Psi} = \frac{1}{m_p}$, which gives:

$$\frac{\partial}{\partial t}\breve{n}_p + \frac{\partial}{\partial x_j}\breve{n}_p\breve{u}_{p,j} = -\frac{\partial}{\partial x_j}\breve{n}_p\{\delta u_{p,j}\}_p \quad (2.64)$$

where $\{\}_p$ is the particle number density weighted average operator. The first term on the RHS of Eq. (2.64) represents the change on particle number density due to turbulent mixing of particles with different diameter. For this first moment transport equation this term is simply neglected. Note also that in AVBP, when in evaporating context, the evaporation process is stopped when the droplets reach a sufficiently small diameter. Detailed information about the derivation of the rest of transport equations can be found in Mossa (2005).

Definiton of correlated and uncorrelated motions.

The phenomenon of preferential concentration of particles in regions of low vorticity and/or high strain rate has been widely studied (Squires & Eaton (1991*b*), Rouson & Eaton (2001), Rani & Balachandar (2004)). The origin resides in the interactions between the particle phase and the carrier fluid and relates to the particle Stokes number. For low Stokes numbers, the particles follow the fluid flow and their velocity vectors are close to those of the carrier phase. Moreover, neighbouring particles have similar velocity vectors. On the contrary, for larger Stokes numbers, the particles do no follow the carrier fluid flow and the velocities of neighboring particles are not similar. This difference is due to the particle response time τ_p compared to a characteristic time of the fluid flow. For small Stokes numbers, τ_p is small, which means that the particles react rapidly to the velocity changes that take place in the carrier fluid flow. When τ_p increases, the particles are less sensitive to the surrounding changes, and

the velocity samples obtained at a certain location correspond to particles coming from very distant regions of the flow.

Such observations are at the origin of the formalism proposed by Février *et al.* (2005). The Lagrangian velocity of each particle is splitted into a spatially correlated part and an uncorrelated part, sketched in Fig. 2.3, as follows:

$$\mathbf{u}_p^{(k)}(t) = \breve{\mathbf{u}}_p(\mathbf{x}_p^{(k)}(t), t) + \delta\mathbf{u}_p^{(k)}(t), \tag{2.65}$$

where $\breve{\mathbf{u}}_p$ is the mesoscopic velocity defined in the Eulerian framework, which corresponds to the velocity shared by all the particles. It provides a description of the structure of the velocity distribution and is often called correlated velocity and $\delta\mathbf{u}_p^{(k)}(t)$ is the residual velocity component of the particle, or Random Uncorrelated Velocity (RUV), defined for each individual particle along particle trajectories.

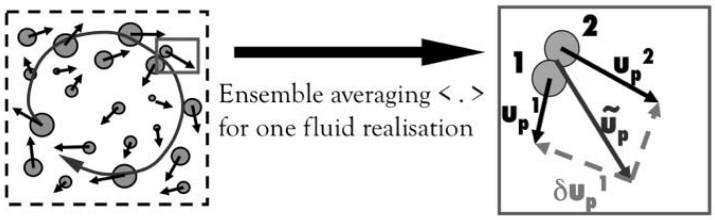

Figure 2.3: *Sketch of the correlated and uncorrelated motions in the MEF. Extracted from Riber (2007).*

The particle velocity may also be split in a mean and a fluctuating parts. As the Lagrangian mean field and the mesoscopic mean field are identical (Février *et al.* (2005)), fluctuating velocity contributions may also be written in terms of mesoscopic and residual contributions as follows:

$$\mathbf{u}'_p(t) = \breve{\mathbf{u}}'_p(\mathbf{x}_p^{(k)}(t), t|\mathcal{H}_f) + \delta\mathbf{u}'^{(k)}_p(t). \tag{2.66}$$

where the fluctuating part of the mesoscopic velocity is expressed as:

$$\breve{\mathbf{u}}'_p = \breve{\mathbf{u}}_p - \langle\breve{\mathbf{u}}_p\rangle_p \tag{2.67}$$

and the fluctuating part of the residual contribution is:

$$\delta\mathbf{u}'_p = \delta\mathbf{u}_p - \langle\delta\mathbf{u}_p\rangle_p \tag{2.68}$$

Using the properties of the statistical average operator $\langle\cdot\rangle$, several relations for the Eulerian equivalent of the quantities defined in Section 2.2.2 can be obtained:

- the ensemble average of the particle uncorrelated velocity is zero:

$$\langle\delta\mathbf{u}_p^{(k)}|\mathcal{H}_f\rangle = 0; \tag{2.69}$$

- the particle uncorrelated velocity is spatially decorrelated from the fluid velocity:

$$\langle\breve{\mathbf{u}}_f \cdot \delta\mathbf{u}_p^{(k)}|\mathcal{H}_f\rangle = 0; \tag{2.70}$$

- the particle uncorrelated velocity component is spatially decorrelated from the particle mesoscopic velocity:

$$\langle\breve{\mathbf{u}}_p \cdot \delta\mathbf{u}_p^{(k)}|\mathcal{H}_f\rangle = 0. \tag{2.71}$$

The turbulent kinetic energy q_p^2, the correlated kinetic energy $\breve{q}_p^2$ and the Random Uncorrelated Energy δq_p^2 are defined as follows:

$$q_p^2 = \breve{q}_p^2 + \delta q_p^2, \tag{2.72}$$

$$\breve{q}_p^2 = \frac{1}{2}\frac{\langle \breve{n}_p \breve{u}'_{p,i} \breve{u}'_{p,i} \rangle}{\langle \breve{n}_p \rangle}, \tag{2.73}$$

$$\delta q_p^2 = \frac{\langle \breve{n}_p \delta\breve{\theta}_p \rangle}{\langle \breve{n}_p \rangle}, \tag{2.74}$$

where $\delta\breve{\theta}_p$ is the Random Uncorrelated Energy (RUE) that will be defined later in this section. Dependencies of $\breve{n}_p$, $\breve{u}'_{p,i}$ and $\delta\breve{\theta}_p$ with space and time have been omitted in Eqs. (2.73) and (2.74) and summation convention is adopted for Latin indices other than p.

A first attempt to evaluate the two contributions (mesoscopic and uncorrelated) was made by Février *et al.* (2005) in a DPS of a particle-laden stationnary HIT flow. He found that the ratio of kinetic RUE to total particle kinetic energy increased with the particle inertia. Vance *et al.* (2006) showed the same trend in a fully-developped channel flow for both colliding and non-colliding particles.

Particle mesoscopic transport equations

The transport equations for the mesoscopic variables are given in Eqs. (2.75)-(2.78). Γ denotes the mass transfer rate from the liquid to the gas phase, Φ_p is the enthalpy transfer rate from the gaseous to the liquid phase, $\mathbf{F}_D$ is the drag force exerted by the fluid on the particles and $\delta\breve{R}_{p,ij}$ denotes the 2^{nd} order particle uncorrelated velocity correlations tensor, $\delta\breve{R}_{p,ij}(\mathbf{x},t) = \langle \breve{u}_{p,i}(t)\breve{u}_{p,j}(t) | \mathbf{x}_p(t) = \mathbf{x}, \mathcal{H}_f \rangle$.

$$\frac{\partial}{\partial t}\breve{n}_p + \frac{\partial}{\partial x_j}\breve{n}_p\breve{u}_{p,j} = 0 \tag{2.75}$$

$$\frac{\partial}{\partial t}\rho_p\breve{\alpha}_p + \frac{\partial}{\partial x_j}\rho_p\breve{\alpha}_p\breve{u}_{p,j} = -\Gamma \tag{2.76}$$

$$\frac{\partial}{\partial t}\rho_p\breve{\alpha}_p\breve{u}_{p,i} + \frac{\partial}{\partial x_j}\rho_p\breve{\alpha}_p\breve{u}_{p,i}\breve{u}_{p,j} = -\frac{\partial}{\partial x_j}\rho_p\breve{\alpha}_p\,\delta\breve{R}_{p,ij} - \Gamma\,\breve{u}_{p,i} + F_{D,i} \tag{2.77}$$

$$\frac{\partial}{\partial t}\rho_p\breve{\alpha}_p\breve{h}_p + \frac{\partial}{\partial x_j}\rho_p\breve{\alpha}_p\breve{u}_{p,j}\breve{h}_p = -\Gamma\breve{h}_p + \Phi_p \tag{2.78}$$

$$\text{❶} + \text{❷} = \text{❸} + \text{❹} + \text{❺} + \text{❻}$$

where the terms noted ❶ correspond to the temporal variations, ❷ to the advection terms due to the mesoscopic motion, ❸ to the advection terms due to the uncorrelated motion, ❹ to the terms linked to the evaporation process, ❺ to the terms linked to drag force and ❻ to the terms linked to thermal conduction.

Closure models for the drag force in Eq. (2.77), have been proposed in Section 2.2.1. Closure for the terms linked to mass and heat transfer due to evaporation are worked on in Part III. In order to define closure models, some assumptions are needed:

H1 -The particles are considered as rigid spheres.

H2 -$\rho_p >> \rho_g$ so the only force exerted by the carrier phase on the dispersed phase is drag force.

H3 -Gravity is neglected.

H4 -Only diluted sprays are considered: $\breve{\alpha}_p < 0.0001$ and $1 - \breve{\alpha}_p \equiv 1$.

H5 -Considering H4, the effects of coalescence and collisions are neglected.

H6 -The spray is locally monodispersed.

Closure model for $\delta\breve{R}_{p,ij}$

Closure must be provided for $\delta\breve{R}_{p,ij}$. For the sake of simplicity, evaporation is not accounted for in the remaining of this section. Thus, the transport equation for the uncorrelated stress tensor is written as:

$$\begin{aligned}\frac{\partial}{\partial t}\rho_p\breve{\alpha}_p\delta\breve{R}_{p,ij}+\frac{\partial}{\partial x_j}\rho_p\breve{\alpha}_p\delta\breve{R}_{p,ij}\breve{u}_{p,j} = &- 2\frac{\rho_p\breve{\alpha}_p}{\breve{\tau}_p}\delta\breve{R}_{p,ij}-\rho_p\breve{\alpha}_p\delta\breve{R}_{p,im}\frac{\partial\breve{u}_{p,j}}{\partial x_m}\\ &- \rho_p\breve{\alpha}_p\delta\breve{R}_{p,mj}\frac{\partial\breve{u}_{p,i}}{\partial x_m}-\frac{\partial}{\partial x_m}\delta\breve{Q}_{p,ijm}.\end{aligned} \tag{2.79}$$

In Eq. (2.79), the term representing the 3^{rd} order particle uncorrelated velocity correlation tensor $\delta\breve{Q}_{p,ijm}=\langle\breve{u}_{p,i}\breve{u}_{p,j}\breve{u}_{p,m}\rangle$ needs closure as well.

Several approaches have been proposed for the closure of $\delta\breve{R}_{p,ij}$. Simonin *et al.* (2002) proposed a method consisting in directly solving Eq. (2.79) i.e. the six components of the tensor. However, this would be too expensive for the LES of complex configurations and does not overcome the difficulty of modeling $\delta\breve{Q}_{p,ijm}$. Based on the transport equation for this term:

$$\begin{aligned}\frac{\partial}{\partial t}\rho_p\breve{\alpha}_p\delta\breve{Q}_{p,ijm}+\frac{\partial}{\partial x_j}\rho_p\breve{\alpha}_p\delta\breve{Q}_{p,ijm} = &- 3\frac{\rho_p\breve{\alpha}_p}{\breve{\tau}_p}\delta\breve{Q}_{p,ijm}+\rho_p\breve{\alpha}_p\delta\breve{Q}_{p,njm}\frac{\partial}{\partial x_n}\breve{u}_{p,i}\\ &+ \rho_p\breve{\alpha}_p\delta\breve{Q}_{p,inm}\frac{\partial}{\partial x_n}\breve{u}_{p,j}-\rho_p\breve{\alpha}_p\delta\breve{Q}_{p,ijn}\frac{\partial}{\partial x_n}\breve{u}_{p,m}\\ &+ \delta\breve{R}_{p,ij}\frac{\partial}{\partial x_n}\rho_p\breve{\alpha}_p\delta\breve{R}_{p,mn}+\delta\breve{R}_{p,jm}\frac{\partial}{\partial x_n}\rho_p\breve{\alpha}_p\delta\breve{R}_{p,in}\\ &+ \delta\breve{R}_{p,im}\frac{\partial}{\partial x_n}\rho_p\breve{\alpha}_p\delta\breve{R}_{p,jn}-\frac{\partial}{\partial x_n}\rho_p\breve{\alpha}_p\delta\breve{M}_{p,ijmn},\end{aligned} \tag{2.80}$$

where $\delta\breve{M}_{p,ijmn}=\langle\breve{u}_{p,i}\breve{u}_{p,j}\breve{u}_{pm}\breve{u}_{p,n}\rangle$ is the 4^{rd}-order particle uncorrelated velocity correlation tensor. Assuming equilibrium of $\delta\breve{Q}_{p,ijm}$ and neglecting any deformation terms (2^{nd}, 3^{rd} and 4^{th} terms on the RHS of Eq. (2.80)), the transport equation reduces to (Moreau (2006)):

$$\begin{aligned}3\frac{\rho_p\breve{\alpha}_p}{\breve{\tau}_p}\delta\breve{Q}_{p,ijm} = &\ \delta\breve{R}_{p,jm}\frac{\partial}{\partial x_n}\rho_p\breve{\alpha}_p\delta\breve{R}_{p,in}+\delta\breve{R}_{p,im}\frac{\partial}{\partial x_n}\rho_p\breve{\alpha}_p\delta\breve{R}_{p,jn}\\ &+ \delta\breve{R}_{p,ij}\frac{\partial}{\partial x_n}\rho_p\breve{\alpha}_p\delta\breve{R}_{p,mn}-\frac{\partial}{\partial x_n}\rho_p\breve{\alpha}_p\delta\breve{M}_{p,ijmn}.\end{aligned} \tag{2.81}$$

It is now necessary to model the 4^{th} order term $\delta\breve{M}_{p,ijmn}$. Simonin (1996) proposed to consider the Gaussian value of $\delta\breve{M}_{p,ijmn}$ in order to obtain a closure model:

$$\delta\breve{M}_{p,ijmn}=\delta\breve{R}_{p,ij}\delta\breve{R}_{p,mn}+\delta\breve{R}_{p,im}\delta\breve{R}_{p,jn}+\delta\breve{R}_{p,in}\delta\breve{R}_{p,jm}. \tag{2.82}$$

Finally combining Eqs. (2.81) and (2.82) leads to (Kaufmann (2004)):

$$\delta\breve{Q}_{p,ijm}=\frac{\breve{\tau}_p}{3}\left(\delta\breve{R}_{p,ml}\frac{\partial}{\partial x_l}\delta\breve{R}_{p,ij}+\delta\breve{R}_{p,jl}\frac{\partial}{\partial x_l}\delta\breve{R}_{p,im}+\delta\breve{R}_{p,il}\frac{\partial}{\partial x_l}\delta\breve{R}_{p,jm}\right), \tag{2.83}$$

which can be directly introduced in Eq. (2.79). However, this method is computationally very expensive and modeling the $\delta\breve{R}_{p,ij}$ tensor can follow simpler paths:

Simonin *et al.* (2002) introduced the particle RUE as half the trace of $\delta\breve{R}_{p,ij}$:

$$\delta\breve{\theta}_p=\frac{1}{2}\delta\breve{R}_{p,ll}. \tag{2.84}$$

Then Eq. (2.77) can be rewritten as follows:

$$\frac{\partial}{\partial t}\rho_p\breve{\alpha}_p\breve{u}_{p,i} + \frac{\partial}{\partial x_j}\rho_p\breve{\alpha}_p\breve{u}_{p,i}\breve{u}_{p,j} = -\frac{\partial}{\partial x_j}\frac{2}{3}\rho_p\breve{\alpha}_p\delta\breve{\theta}_p - \frac{\partial}{\partial x_j}\rho_p\breve{\alpha}_p\,\delta\breve{R}^*_{p,ij} + F_{D,i}, \tag{2.85}$$

where $\delta\breve{R}^*_{p,ij}$ is the deviatoric part of $\delta\breve{R}_{p,ij}$, similar to the viscosity contribution in the theory of diluted gases. $\delta\breve{\theta}_p$ is the spherical part, similar to a pressure term:

$$\delta\breve{R}^*_{p,ij} = \delta\breve{R}_{p,ij} - \frac{2}{3}\delta\breve{\theta}_p\delta_{ij}\ . \tag{2.86}$$

A transport equation for the particle RUE is derived from and substitutes the set of 2^{nd} order particle correlations conservation equations for the dispersed phase (Eq. (2.79)):

$$\frac{\partial}{\partial t}\rho_p\breve{\alpha}_p\delta\breve{\theta}_p + \frac{\partial}{\partial x_j}\rho_p\breve{\alpha}_p\breve{u}_{p,j}\delta\breve{\theta}_p = -\frac{\partial}{\partial x_j}\rho_p\breve{\alpha}_p\delta\breve{Q}_{p,iij} - \rho_p\breve{\alpha}_p\left[\delta\breve{R}^*_{p,ij} + \frac{2}{3}\delta\breve{\theta}_p\delta_{ij}\right]\frac{\partial}{\partial x_j}\breve{u}_{p,i} + W_\theta, \tag{2.87}$$

where W_θ is a source term linked to drag force and its expression is deduced from Eq. (2.34):

$$W_\theta = \frac{2\rho_p\breve{\alpha}_p}{\breve{\tau}_p}\delta\breve{\theta}_p\ . \tag{2.88}$$

A closure model for $\delta\breve{Q}_{p,iim}$ is proposed hereinafter and there is only one more unclosed term left in Eq. (2.87), $\delta\breve{R}^*_{p,ij}$. Different closure models for this term are studied in Part II.

Closure model for $\delta\breve{Q}_{p,iim}$

Eq. (2.87) for particle RUE is very similar to the transport equation for fluid temperature (with the exception of the last two terms on the RHS, that are linked to evaporation and drag force source terms). Kaufmann *et al.* (2005) proposed a simpler model consisting in modeling $\delta\breve{Q}_{p,iim}$ in analogy with the Fick's law for the fluid temperature:

$$\frac{1}{2}\delta\breve{Q}_{p,iim} = -\kappa_{RUM}\frac{\partial\delta\breve{\theta}_p}{\partial x_m}, \tag{2.89}$$

where κ_{RUM} stands for the uncorrelated diffusion coefficient and is modeled in analogy with the RANS two-fluid approach (Simonin (1996)):

$$\kappa_{RUM} = \frac{10}{27}\breve{\tau}_p\delta\breve{\theta}_p. \tag{2.90}$$

2.3 Final set of conservation equations for the dispersed phase in the EE approach

In the remaining of the manuscript, the Mesoscopic Eulerian Approach is worked on (hereinafter it will be referred indistinctly as MEF or EE). Part II is dedicated to the *a posteriori* analysis of the closure models developped by Masi (2010) in the particle-laden slab HIT flow configuration. Part III presents a study on the evaporation of fuel droplets. Different evaporation models are compared and a new approach for the computation of the evaporation process of isolated droplets in AVBP is proposed. Finally, Part IV presents an example of joint application of the model for the closure of the RUM terms retained in Part II and the new approach for the evaporation presented in Part III. The configuration chosen is the MERCATO bench, whose experimental data were acquired at ONERA (Toulouse, France) (García-Rosa (2008)), and computed using EE (Sanjosé (2009)) and EL approaches (Senoner (2010)) in AVBP.

The final set of conservation equations for the dispersed phase that are transported in AVBP and considered in the rest of this work is:

$$\frac{\partial}{\partial t}\breve{n}_p + \frac{\partial}{\partial x_j}\breve{n}_p\breve{u}_{p,j} = 0 \tag{2.91}$$

$$\frac{\partial}{\partial t}\rho_p\breve{\alpha}_p + \frac{\partial}{\partial x_j}\rho_p\breve{\alpha}_p\breve{u}_{p,j} = -\Gamma \tag{2.92}$$

$$\begin{aligned}\frac{\partial}{\partial t}\rho_p\breve{\alpha}_p\breve{u}_{p,i} + \frac{\partial}{\partial x_j}\rho_p\breve{\alpha}_p\breve{u}_{p,i}\breve{u}_{p,j} = &- \Gamma\,\breve{u}_{p,i} + F_{D,i} \\ &- \frac{\partial}{\partial x_j}\rho_p\breve{\alpha}_p\left[\delta\breve{R}^*_{p,ij} + \frac{2}{3}\delta\breve{\theta}_p\delta_{ij}\right]\end{aligned} \tag{2.93}$$

$$\frac{\partial}{\partial t}\rho_p\breve{\alpha}_p\breve{h}_p + \frac{\partial}{\partial x_j}\rho_p\breve{\alpha}_p\breve{u}_{p,j}\breve{h}_p = -\Gamma\breve{h}_p + \Phi_p \tag{2.94}$$

$$\begin{aligned}\frac{\partial}{\partial t}\rho_p\breve{\alpha}_p\delta\breve{\theta}_p + \frac{\partial}{\partial x_j}\rho_p\breve{\alpha}_p\breve{u}_{p,j}\delta\breve{\theta}_p = &- \Gamma\delta\breve{\theta}_p + W_\theta - \frac{\partial}{\partial x_j}\rho_p\breve{\alpha}_p\delta\breve{Q}_{p,iij} \\ &- \rho_p\breve{\alpha}_p\left[\delta\breve{R}^*_{p,ij} + \frac{2}{3}\delta\breve{\theta}_p\delta_{ij}\right]\frac{\partial}{\partial x_j}\breve{u}_{p,i}.\end{aligned} \tag{2.95}$$

Note that in the set of equations (2.91)- (2.95), evaporation terms are present. Particularly, Eq. (2.93) includes a term linked to the evaporation process (the first term in the RHS) that did not appeared in Eq. (2.85), where evaporation was neglected. Similarly, Eq. (2.95) accounts for evaporation effects through the first term in the RHS that did not appear in Eq. (2.87).

2.3.1 Transport equations for the dipersed phase in compressed form

Similarly to Section 2.1, the conservation equations for the dispersed phase can be written in a compressed form. For the particle phase, one has:

$$\frac{\partial}{\partial t}\mathbf{w_p} + \nabla\cdot\mathcal{F}_p = \mathbf{s}_p, \tag{2.96}$$

where $\mathbf{w}_p = (\breve{n}_p, \rho_p\breve{\alpha}_p, \rho_p\breve{\alpha}_p u_{p,i}, \rho_p\breve{\alpha}_p\breve{h}_p, \rho_p\breve{\alpha}_p\delta\breve{\theta}_p)^T$ is the vector of conservative variables for the dispersed phase, $\mathcal{F}_p$ is the flux tensor composed by two parts, one due to convection by the mesoscopic motion ($\mathcal{F}_p^M$) and one due to the uncorrelated motion ($\mathcal{F}_p^U$). $\mathbf{s}_p$ is the vector of source terms.

Convective fluxes due to the mesoscopic motion, $\mathcal{F}_p^M$ and to the uncorrelated motion $\mathcal{F}_p^U$

The tensor of fluxes read:

$$\mathcal{F}_p^M = \begin{pmatrix} \breve{n}_p\breve{u}_{p,j} \\ \rho_p\breve{\alpha}_p\breve{u}_{p,j} \\ \rho_p\breve{\alpha}_p\breve{u}_{p,i}\breve{u}_{p,j} \\ \rho_p\breve{\alpha}_p\breve{u}_{p,j}\breve{h}_p \\ \rho_p\breve{\alpha}_p\breve{u}_{p,j}\delta\breve{\theta}_p \end{pmatrix}, \qquad \mathcal{F}_p^U = \begin{pmatrix} 0 \\ 0 \\ \rho_p\breve{\alpha}_p\left[\delta\breve{R}^*_{p,ij} + \frac{2}{3}\delta\breve{\theta}_p\delta_{ij}\right] \\ 0 \\ \rho_p\breve{\alpha}_p\delta\breve{Q}_{p,iij} \end{pmatrix}. \tag{2.97}$$

Vector of source terms, s_p

There are two contributions to the source terms: the first one is linked to the exchanges with the gas phase ($\mathbf{s}_{g-p}$) and the second one is linked to the uncorrelated motion ($\mathbf{s}_\theta$). $\mathbf{s}_{g-p}$ groups the source terms of mass, momentum

and energy with the gas phase whereas $\mathbf{s}_\theta$ contains only one term due to the exchanges between the uncorrelated and the correlated motions. This term applies to the particle RUE transport equation. The vectors of source terms read:

$$\mathbf{s}_p = \mathbf{s}_{g-p} + \mathbf{s}_\theta \tag{2.98}$$

$$\mathbf{s}_{g-p} = \begin{pmatrix} 0 \\ -\Gamma \\ -\Gamma \breve{u}_{p,i} + F_{D,i} \\ -\Gamma \breve{h}_p + \Phi_p \\ -\Gamma \delta\breve{\theta}_p + W_\theta \end{pmatrix}, \qquad \mathbf{s}_\theta = \begin{pmatrix} 0 \\ 0 \\ 0 \\ 0 \\ -\rho_p \breve{\alpha}_p \left[\delta \breve{R}^*_{p,ij} + \frac{2}{3} \delta\breve{\theta}_p \delta_{ij} \right] \frac{\partial}{\partial x_j} \breve{u}_{p,i} \end{pmatrix}. \tag{2.99}$$

Inverse coupling between the dispersed and the gaseous phases

The source terms vector in Eq. (2.4) $\mathbf{s}_{p-g}$ has not been defined yet. It represents the coupling terms that include the influence of the particle phase on the gaseous phase. It reads:

$$\mathbf{s}_{p-g} = \begin{pmatrix} \Gamma \delta_{k,F} \\ -\Gamma \breve{u}_{p,i} - F_{D,i} \\ \Pi_g + \Gamma \frac{1}{2} \breve{u}^2_{p,i} - \breve{u}_{p,i} F_{D,i} \end{pmatrix} \tag{2.100}$$

where $\Gamma \frac{1}{2} \breve{u}^2_{p,i}$ and $\breve{u}_{p,i} F_{D,i}$ represent the gaseous kinetic energy transfer due to evaporation and drag force respectively. Π_g is the sensible energy transfer rate due to evaporation and thermal conduction. Γ and Π_g will be defined in Part III.

Chapter 3

Transport equations for LES of dispersed two-phase flows

Nowadays, the available computational power limits the use of DNS to academic configurations. When a second phase is taken into account, the complexity of the problem increases. The use of DNS becomes then prohibitive, especially in complex comfigurations. In LES, the equations are filtered, the large scales of the motion are resolved and only the high frequency scales, smaller than the filter width, are modeled.

In turbulent flows the largest scales strongly depend on the geometry of the system while the smallest ones present an universal behavior which is determined almost entirely by the rate at which they receive energy from the large scales (flow Reynolds number Re (Eq. (3.1))), and by the fluid viscosity. In such flows, LES has therefore a clear advantage compared to RANS since it is easier to develop models for the smallest structures than models for the whole range of scales.

The application of LES to two-phase flows is more recent than for purely gaseous flows. Fox (2012) provides a review of the different approaches for Large Eddy simulation of two-phase flows, pointing out the main fields of application of each approach, as well as their advantages, drawbacks and a summary of the closures and models for the sub-grid scale terms.

3.1 LES equations for the gaseous phase

The transition from laminar to turbulent flow is characterized by the Reynolds number Re, a dimensionless number representing the ratio of inertial to viscous forces:

$$Re = \frac{\mathcal{L}\mathcal{U}}{\nu}, \tag{3.1}$$

where $\mathcal{L}$ the characteristic size of the flow, $\mathcal{U}$ the characteristic velocity and ν the fluid kinematic viscosity. The higher the Reynolds number, the more turbulent the flow.

The velocity in a turbulent flow suffers significant variations in time and space. It is characterized by the pressence of vortices or eddies of different sizes. These eddies are in fact vortical structures that interact. The energy cascade (Richardson (1922)) suggests that the kinetic energy is essentially fed by the turbulence at the largest scales and is then transferred to smaller and smaller scales until its dissipation by the viscous forces at the smallest scales (Pope (2000)).

When the Reynolds number large enough, the smallest eddies of the flow can be characterized (Kolmogorov (1941)) being ϵ the dissipation rate of the flow, Kolmogorov (1941) stated that a unique set of length, velocity and time scales can be expressed for the smallest scales:

$$\eta \equiv (\nu^3/\epsilon)^{1/4}, \tag{3.2}$$
$$u_\eta \equiv (\epsilon\nu)^{1/4}, \tag{3.3}$$
$$\tau_\eta \equiv (\nu/\epsilon)^{1/2}. \tag{3.4}$$

where η refers to the smallest scales of the flow.

It is then possible to link the length, velocity and time scales of the smallest eddies to those of the largest eddies depending only on the Reynolds number:

$$\eta/l_0 \sim Re^{-3/4}, \tag{3.5}$$
$$u_\eta/u_0 \sim Re^{-1/4}, \tag{3.6}$$
$$\tau_\eta/\tau_0 \sim Re^{-1/2}, \tag{3.7}$$

where the subscript 0 refers to the largest scales of turbulence.

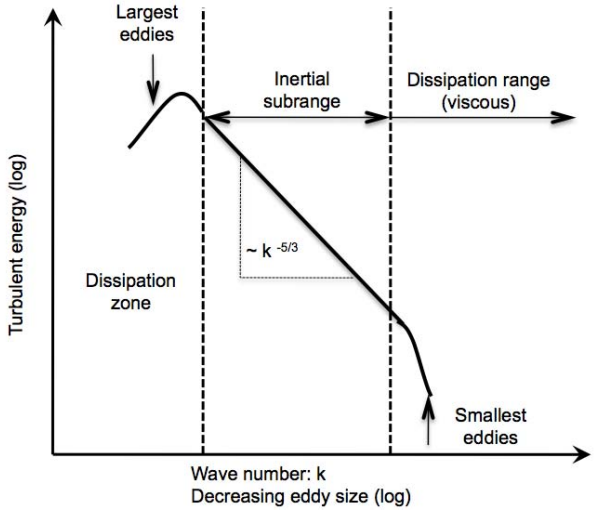

Figure 3.1: *Example of energy spectrum showing the distinction between integral, inertial and dissipation zones. Source Pope (2000).*

The energy spectrum $E(\kappa)$ represents the turbulent contribution os all scales to the turbulent kinetic energy. Figure 3.1 shows an example of energy spectrum. Three main zones can be distinguished (Pope (2000)):

- The integral or energy containing zone: the largest eddies belong to this part. They are characterized by the lowest frequencies and their size is comparable to the largest scales of the flow.
- The inertial zone represents the large eddies breaking into smaller ones and transferring their energy to smallest eddies.
- The dissipation range contains the high frequency structures, i.e. the smallest eddies. The viscous forces act in this zone converting the turbulent energy of the eddies into heat.

3.1.1 Filtering procedure

The separation of the small and large scales is achieved through the application of a low-pass filter G_Δ to the exact equations (Leonard (1974)). The filtered quantity $\overline{\Phi}$ is defined as the convolution of the non-filtered quantity Φ

with the spatial filter G_Δ, whose characteristic lenght is Δ:

$$\overline{\Phi}(x) = \int \Phi(x) G_\Delta(x' - x)\, dx'. \tag{3.8}$$

The filtered quantity or resolved large scale field, $\bar{\Phi}$, is calculated solving its transport equation. The unsolved residual field Φ' contains all the flow scales smaller than the filter size 2Δ:

$$\Phi' = \Phi - \overline{\Phi}. \tag{3.9}$$

For variable density flows, it is useful to use a mass weighted filtering or Favre averaging (Favre (1969)) in order to avoid unclosed terms due to density fluctuations:

$$\hat{\phi} = \frac{1}{\bar{\rho}} \overline{\rho\phi}. \tag{3.10}$$

In the context of this work, both phases are compressible, so Favre averaging is applied to both the gaseous and the dispersed phases.

3.1.2 Filtered Navier-Stokes equations

The final set of filtered Navier-Stokes equations for the gas phase are directly obtained by filtering Eqs. (2.1)-(2.3):

$$\frac{\partial}{\partial t}\overline{\rho_g} + \frac{\partial}{\partial x_j}\overline{\rho_g}\hat{u}_{g,j} = 0 \tag{3.11}$$

$$\frac{\partial}{\partial t}\overline{\rho_g}\hat{u}_{g,i} + \frac{\partial}{\partial x_j}\overline{\rho_g}\hat{u}_{g,i}\hat{u}_{g,j} = -\frac{\partial}{\partial x_j}\left[\overline{P_g}\delta_{ij} - \overline{\tau_{g,ij}} + \overline{\rho_g} T_{g,ij}\right] \tag{3.12}$$

$$\frac{\partial}{\partial t}\overline{\rho_g}\hat{E}_g + \frac{\partial}{\partial x_j}\overline{\rho_g}\hat{E}_g\hat{u}_{g,j} = -\frac{\partial}{\partial x_j}\left[\hat{u}_{g,i}(\overline{P_g}\delta_{ij} - \overline{\tau_{g,ij}}) + \overline{q_{g,j}} + \overline{\rho_g} Q_{g,j})\right]. \tag{3.13}$$

where the subgrid terms read:

$$T_{g,ij} = \widehat{u_{g,i}u_{g,j}} - \hat{u}_{g,i}\hat{u}_{g,j} \tag{3.14}$$

$$Q_{g,j} = \widehat{u_{g,j}E_g} - \hat{u}_{g,j}\hat{E}_g. \tag{3.15}$$

The subgrid-scale terms are modeled by their dissipative effects on the computed scales following the idea of energy transfer from the largest to the smallest scales (Kolmogorov (1941)). The Boussinesq hypothesis (Boussinesq (1877)) assumes that the energy transfer mechanism from the resolved to the subgrid scales is analogous to the molecular diffusion mechanism. Replacing the molecular viscosity by a turbulent kinematic viscosity ν_t, the fluid subgrid model is written:

$$T_{g,ij} - \frac{1}{3}T_{g,ll} \approx 2\nu_t \left(\hat{S}_{g,ij} - \frac{1}{3}\delta_{ij}\hat{S}_{g,ll}\right), \tag{3.16}$$

where

$$\hat{S}_{g,ij} = \frac{1}{2}\left(\frac{\partial \hat{u}_{g,i}}{\partial x_j} + \frac{\partial \hat{u}_{g,j}}{\partial x_i}\right). \tag{3.17}$$

In Eq. (3.16) only the turbulent viscosity ν_t needs to be modeled. Various models for the turbulent viscosity are available in AVBP (Smagorinsky (Smagorinsky (1963)), WALE (Ducros *et al.* (1998)), Filtered Smagorinsky (Ducros *et al.* (1996)), Dynamic Smagorisnsky model (Germano *et al.* (1991), Lilly (1992)) and the k-equation model). As it is not the scope of this work, the model used here is briefly presented in Section 3.1.3.

The subgrid-scale heat flux $Q_{g,j}$ model needs the determination of the turbulent thermal conductivity λ_t, that is, the thermal conductivity due to the residual turbulent motion. $Q_{g,j}$ is written as:

$$Q_{g,j} = -\frac{\lambda_t}{\overline{\rho_g}}\frac{\partial \hat{T}_g}{\partial x_j}, \tag{3.18}$$

with

$$\lambda_t = \frac{\overline{\rho_g}\nu_t\overline{Cp_g}}{Pr_t}. \tag{3.19}$$

In the LES presented in this work, the turbulent Prandtl number Pr_t has been set to 0.6.

Finally, the remaining filtered terms are approximated as follows:

$$\overline{\tau_{g,ij}} = 2\mu_g\left(\hat{S}_{g,ij} - \frac{1}{3}\delta_{ij}\hat{S}_{g,ll}\right), \tag{3.20}$$

$$\overline{q_{g,j}} = \lambda_g\frac{\partial\hat{T}_g}{\partial x_j}, \tag{3.21}$$

$$\overline{P} = \overline{\rho_g r}\hat{T}_g. \tag{3.22}$$

3.1.3 WALE model for the gaseous turbulent viscosity

Multiple models for the evaluation of the dissipative effects of the subgrid-scales (Lesieur (1997), Pope (2000)) exist. There are also several options to model the turbulent viscosity in AVBP. However, all the LES presented in this work have been performed with the WALE (Wall-Adapting Local Eddy-viscosity) model (Ducros *et al.* (1998)). This model automatically adapts the subgrid viscosity on boundary layer flows while preserving the dissipative effects of turbulence in HIT flows.

The WALE turbulent viscosity reads:

$$\nu_t = (C_w\Delta)^2\frac{(s^d_{ij}s^d_{ij})^{3/2}}{(\hat{S}_{g,ij}\hat{S}_{g,ij})^{5/2} + (s^d_{ij}s^d_{ij})^{5/4}}. \tag{3.23}$$

where C_w is the same constant as in the Smagorinsky model, fixed to $C_w = 0.4929$. s^d_{ij} is the residual part in the resolved rate-of-deformation tensor:

$$s^d_{ij} = \hat{S}_{g,im}\hat{S}_{g,mj} + \hat{\Omega}_{g,im}\hat{\Omega}_{g,mj} - \frac{1}{3}\delta_{ij}\left[\hat{S}_{g,nl}\hat{S}_{g,nl} + \hat{\Omega}_{g,nl}\hat{\Omega}_{g,nl}\right], \tag{3.24}$$

where $\hat{\mathbf{\Omega}}_g$ is the filtered rotation rate tensor:

$$\hat{\mathbf{\Omega}}_{g,ij} = \frac{1}{2}\left(\frac{\partial\hat{u}_{g,i}}{\partial x_j} - \frac{\partial\hat{u}_{g,j}}{\partial x_i}\right). \tag{3.25}$$

3.2 LES equations for the dispersed phase

Filtering the mesoscopic Eulerian equations is done in analogy with the filtering of the gaseous phase equations presented in Section 3.1.1. Favre averaging is performed replacing the gaseous density ρ_g in Eq. (3.26) by the mesoscopic particle volume fraction $\breve{\alpha}_p$:

$$\overline{\alpha_p}\hat{\phi} = \overline{\breve{\alpha}_p\breve{\phi}}\,. \tag{3.26}$$

An equivalence between the Favre average based on $\breve{\alpha}_p$ and the particle number density $\breve{n}_p$ can be obtained assuming that the dispersed phase is locally monodisperse, i.e. within the filter size. Thus, the Favre average also reads:

$$\overline{\breve{n}_p\breve{\phi}} = \overline{\frac{6\breve{\alpha}_p}{\pi d^3}\breve{\phi}} = \overline{n_p}\hat{\phi}. \tag{3.27}$$

In the remaining of this chapter, the notation $\breve{.}$ will be abandoned for the sake of simplicity.

3.2.1 Filtered Mesoscopic Eulerian equations

The final set of LES equations for the dispersed phase reads:

$$\frac{\partial}{\partial t}\overline{n_p} + \frac{\partial}{\partial x_j}\overline{n_p}\hat{u}_{p,j} = 0 \tag{3.28}$$

$$\frac{\partial}{\partial t}\rho_p\overline{\alpha_p} + \frac{\partial}{\partial x_j}\rho_p\overline{\alpha_p}\hat{u}_{p,j} = -\overline{\Gamma} \tag{3.29}$$

$$\begin{aligned}\frac{\partial}{\partial t}\rho_p\overline{\alpha_p}\hat{u}_{p,i} + \frac{\partial}{\partial x_j}\rho_p\overline{\alpha_p}\hat{u}_{p,i}\hat{u}_{p,j} = &- \overline{\Gamma}\,\hat{u}_{p,i} + \overline{F_{D,i}} \\ &- \frac{\partial}{\partial x_j}\rho_p\overline{\alpha_p}\left[\widehat{\delta R^*_{p,ij}} + \frac{2}{3}\widehat{\delta\theta_p}\delta_{ij} + T_{p,ij}\right]\end{aligned} \tag{3.30}$$

$$\frac{\partial}{\partial t}\rho_p\overline{\alpha_p}\widehat{h_p} + \frac{\partial}{\partial x_j}\rho_p\overline{\alpha_p}\hat{u}_{p,j}\widehat{h_p} = -\overline{\Gamma}\widehat{h_p} + \overline{\Phi_p} \tag{3.31}$$

$$\begin{aligned}\frac{\partial}{\partial t}\rho_p\overline{\alpha_p}\widehat{\delta\theta_p} + \frac{\partial}{\partial x_j}\rho_p\overline{\alpha_p}\hat{u}_{p,j}\widehat{\delta\theta_p} = &- \overline{\Gamma}\widehat{\delta\theta_p} + \overline{W_\theta} - \frac{\partial}{\partial x_j}\rho_p\overline{\alpha_p}\widehat{\delta Q_{p,iij}} \\ &- \overline{\rho_p\breve{\alpha}_p\left[\delta\breve{R}^*_{p,ij} + \frac{2}{3}\delta\breve{\theta}_p\delta_{ij}\right]\frac{\partial}{\partial x_j}\breve{u}_{p,i}}.\end{aligned} \tag{3.32}$$

In the set of equations Eq. (3.28) - (3.32) several terms need closure. In this section, the closure approximations for the source terms due to drag force and evaporation are recalled. The filtered evaporation source terms here presented correspond to the classical model implemented in AVBP. The filtered terms corresponding to the models presented in Part III are computed similarly.

- Filtered source terms linked to evaporation:
  - Mass evaporation rate:

$$\overline{\Gamma} \approx \pi\overline{n}_p d\overline{Sh}\frac{\overline{\mu}}{Sc_F}ln(1+\overline{B}_M), \tag{3.33}$$

$$\overline{Sh} \approx 2 + 0.55\overline{Re}_p^{1/2}Sc_F^{1/3}, \tag{3.34}$$

$$\overline{B}_M \approx \frac{Y_{F,\zeta}(\hat{T}_p) - \hat{Y}_F}{1 - Y_{F,\zeta}(\hat{T}_p)}. \tag{3.35}$$

  - Sensible energy variation rate du to thermal conduction:

$$\overline{\Phi}_p \approx \overline{\Gamma}(\hat{h}_p - h_{s,F}(\hat{T}_p)) - \pi\overline{n}_p d\overline{Nu}(\hat{T}_p - \hat{T}), \tag{3.36}$$

$$\overline{Nu} \approx 2 + 0.55\overline{Re}_p^{1/2}Pr^{1/3}. \tag{3.37}$$

- Filtered source terms linked to drag force:
  - Momentum variation rate due to drag:

$$\overline{F}_{D,i} \approx \frac{\rho_p\overline{\alpha}_p}{\overline{\tau}_p}(\hat{u}_i - \hat{u}_{l,i}). \tag{3.38}$$

- Filtered source term linked to the RUM:
  - Rate of RUE variation due to drag force:

$$\overline{W_\theta} \approx -\frac{2\rho_p\overline{\alpha}_p}{\overline{\tau}_p}\hat{\delta\theta}_p, \tag{3.39}$$

where the filtered particle relaxation time is approximated as follows:

$$\overline{\tau}_p \approx (1 + 0.15\overline{Re}_p^{0.687})\frac{\rho_p d^2}{18\overline{\mu}}, \tag{3.40}$$

and the filtered particle Reynolds number:

$$\overline{Re}_p \approx \frac{|\hat{u} - \hat{u}_p|d}{\overline{\nu}}. \tag{3.41}$$

Special attention is needed for the terms related to the Random Uncorrelated Motion:

- $T_{p,ij}$ is due to the subgrid correlated motion and is analogous to the fluid Reynolds tensor (Eq. (3.16)):

$$T_{p,ij} = \widehat{u_{p,i}u_{p,j}} - \hat{u}_{p,i}\hat{u}_{p,j}. \tag{3.42}$$

  Analogous to the subgrid scale models used for the LES of the gaseous equations, Moreau *et al.* (2009) propose to close the sub-grid correlated motion tensor $T_{p,ij}$ with a voscosity-type Smagorinsky model. However, due to the compressible nature of the mesoscopic dispersed phase, the compression part of the mesoscopic velocities is not negligible. In order to model the subgrid scale compression effects, Moreau *et al.* (2009) use the Yoshizawa model. Thus, the subgrid scale stress tensor is model as:

$$T_{p,ij} = \frac{2}{3}C_{p,Y}\Delta^2||\widehat{S}_p||^2\delta_{ij} - 2(C_{p,S}\Delta)^2||\widehat{S}_p^*||\widehat{S}_p^*. \tag{3.43}$$

  where $||\widehat{S}_p|| = \sqrt{2\widehat{S}_{p,ij}\widehat{S}_{p,ij}}$.
  The dispersed phase rate-of-strein tensors are given by:

$$\widehat{S}_{p,ij} = \frac{1}{2}\left(\frac{\partial\hat{u}_{p,i}}{\partial x_j} + \frac{\partial\hat{u}_{p,j}}{\partial x_i}\right), \tag{3.44}$$

$$\widehat{S}^*_{p,ij} = \widehat{S}_{p,ij} - \frac{1}{3}\frac{\partial\hat{u}_{p,k}}{\partial x_k}\delta_{ij}. \tag{3.45}$$

$$\tag{3.46}$$

- $\widehat{\delta Q_{p,iij}}$ is modeled similarly to $\delta\breve{Q}_{p,iij}$ in Eq. (2.89):

$$\widehat{\delta Q_{p,iij}} = -\hat{\kappa}_{RUM}\frac{\partial\widehat{\delta\theta_p}}{\partial x_j}, \tag{3.47}$$

  where $\hat{\kappa}_{RUM} = \frac{10}{27}\overline{\tau}_p\delta\hat{\theta}_p$.

- The filtered RUE production term is written as:

$$\overline{\rho_p\breve{\alpha}_p\underbrace{\left[\delta\breve{R}^*_{p,ij} + \frac{2}{3}\delta\breve{\theta}_p\delta_{ij}\right]}_{\delta\breve{R}_{p,ij}}\frac{\partial}{\partial x_j}\breve{u}_{p,i}} = \rho_p\overline{\alpha_p}\widehat{\delta R_{p,ij}}\frac{\partial\hat{u}_{p,i}}{\partial x_j} - \underbrace{\left[\overline{\rho_p\breve{\alpha}_p\delta\breve{R}_{p,ij}\frac{\partial\breve{u}_{p,i}}{\partial x_j}} - \rho_p\overline{\alpha_p}\widehat{\delta R_{p,ij}}\frac{\partial\hat{u}_{p,i}}{\partial x_j}\right]}_{\overline{U}^t_\theta}, \tag{3.48}$$

where $\widehat{\delta R_{p,ij}} = \widehat{\delta R^*_{p,ij}} + \frac{2}{3}\widehat{\delta\theta_p}\delta_{ij}$. $\delta\hat{\theta}_p$ is captured through its transport equation (Eq. 3.32). $\delta\hat{R}^*_{p,ij}$ is evaluated through the models described in Part II using filtered quantities.

$\overline{U}^t_\theta$ is a RUE production term due to the subgrid scale motion and is assumed to have a dissipative effect on the subgrid correalted energy. Assuming equilibrium in the subgrid correlated energy, Moreau (2006) modeled $\overline{U}^t_\theta$ as:

$$\overline{U}^t_\theta = T_{p,ij}\frac{\partial\hat{u}_{p,i}}{\partial x_j}. \tag{3.49}$$

For more details the reader is encouraged to see Moreau (2006) and Riber (2007).

Part II

Modeling the Random Uncorrelated Stress Tensor

Chapter 4

Modeling the RUM stress tensor

This Chapter, inspired in the work of Masi (2010), is dedicated to the closure models for the deviatoric part of the Random Uncorrelated Motion (RUM) stress tensor ($\delta\breve{R}^{*}_{p,ij}$) appearing for the MEF approach in the momentum (Eq. (2.93)) and Random Uncorrelated Energy equations (Eq. (2.95)). Such tensor may be compared to the fluid stress tensor due to thermal agitation in the Navier-Stokes equations for the gaseous phase. As stated in Chapter 2, the second order uncorrelated velocity correlation tensor, or RUM tensor $\delta\breve{R}_{p,ij}$, is splitted into an spherical part, the so-called RUE ($\delta\breve{\theta}_p$) and a deviatoric part $\delta\breve{R}^{*}_{p,ij}$. Section 2.2.4 presented the development of a transport equation for the RUE, while the deviatoric part remained unclosed. In this Chapter, several closure models for the deviatoric RUM stress tensor are proposed. In this part of the manuscrit evaporation effects are neglected.

Simonin *et al.* (2002) proposed to close the deviatoric RUM stress tensor using a viscosity assumption, the so-called VISCO model (Section 4.2). This model has proven to give satisfactory results in *a posteriori* inertial particle-laden HIT flows simulations (Kaufmann (2004), Riber (2007), Kaufmann *et al.* (2008), Vié (2010)). However, Riber (2007) showed that it failed when performing *a posteriori* tests in mean-sheared flows (Hishida *et al.* (1987)). Recently, Masi (2010) proposed new models for the closure of $\delta\breve{R}^{*}_{p,ij}$, that are briefly recalled in this Chapter. These new models are specially developped for the deviatoric RUM stress tensor and make use of solution procedures originally developped in the context of gaseous turbulent flows. She performed an *a priori* analysis of a particle-laden turbulent planar jet (Fig. 4.1) proposed and validated models on this configuration with mean shear. The corresponding *a posteriori* study of the same configuration is presented in Chapter 5.

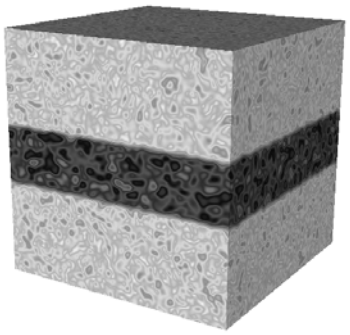

Figure 4.1: *Particle-laden turbulent planar jet configuration (Particle-laden HIT slab). Initial carrier phase velocity magnitude field.*

4.1 Preliminary considerations

In this Part of the manuscript, and in order to respect the notation used by Masi (2010), the equations are written using $\breve{n}_p$ instead of $\rho_p\breve{\alpha}_p$. In a monodisperse context, both quantities are proportional:

$$\breve{\alpha}_p = \frac{d_p^3 \cdot \pi \cdot \breve{n}_p}{6}. \tag{4.1}$$

Several quantites that are used throughout this Chapter are here defined. The RUM anisotropy stress tensor reads:

$$b^*_{p,ij} = \frac{\delta\breve{R}_{p,ij}}{2\delta\breve{\theta}_p} - \frac{1}{3}\delta_{ij} = \frac{\delta\breve{R}^*_{p,ij}}{2\delta\breve{\theta}_p}. \tag{4.2}$$

The particle rate-of-strain is the symmetric part of the mesoscopic particle velocity gradient:

$$S_{p,ij} = \frac{1}{2}\left(\frac{\partial\breve{u}_{p,i}}{\partial x_j} + \frac{\partial\breve{u}_{p,j}}{\partial x_i}\right). \tag{4.3}$$

The mesoscopic vorticity or rotation tensor $\mathbf{\Omega}$ reads:

$$\Omega_{p,ij} = \frac{1}{2}\left(\frac{\partial\breve{u}_{p,i}}{\partial x_j} - \frac{\partial\breve{u}_{p,j}}{\partial x_i}\right). \tag{4.4}$$

The mesoscopic velocity-gradient tensor is thus defined as:

$$\frac{\partial\breve{u}_{p,i}}{\partial x_j} = \mathbf{S}^* + \frac{1}{3}\{\mathbf{S}\}\mathbf{I} + \mathbf{\Omega}, \tag{4.5}$$

where $\mathbf{I}$ is the identity matrix, bold notation denotes three-dimensional (3D) second order tensors and $\{.\}$ represents the tensor trace. Asterisk is used to denote traceless tensors when associated with bold notation, otherwise means "deviatoric". The deviatoric particle rate-of-strain accounts for shearing and the spherical part for contraction or expansion.

The alignment between the particle rate-of-strain tensor and the rotation tensor provides information about the configuration of the flow. For information on the local behavior of the tensors the reader is referred to the works of Lund & Rogers (1994), Simonin (1991), George & Hussein (1991) and Masi (2010)).

4.2 A local equilibrium assumption

In order to be coherent with the notation used by Masi (2010), the equations for the RUM model proposed by Simonin *et al.* (2001) are here rewritten.

The transport equation for the 2^{nd} order particle velocity stress tensor $\delta\breve{R}_{p,ij}$ reads:

$$\frac{\partial}{\partial t}\breve{n}_p\delta\breve{R}_{p,ij} + \frac{\partial}{\partial x_j}\breve{n}_p\delta\breve{R}_{p,ij}\breve{u}_{p,j} = -2\frac{\breve{n}_p}{\breve{\tau}_p}\delta\breve{R}_{p,ij} - \breve{n}_p\delta\breve{R}_{p,ik}\frac{\partial\breve{u}_{p,j}}{\partial x_k} - \breve{n}_p\delta\breve{R}_{p,kj}\frac{\partial\breve{u}_{p,i}}{\partial x_k} - \frac{\partial}{\partial x_k}\delta\breve{Q}_{p,ijk}. \tag{4.6}$$

Neglecting all transport terms, Eq. (4.6) reduces to:

$$\delta\breve{R}_{p,ij} = -\frac{\breve{\tau}_p}{2}\left[\delta\breve{R}_{p,ik}\frac{\partial\breve{u}_{p,j}}{\partial x_k} + \delta\breve{R}_{p,kj}\frac{\partial\breve{u}_{p,i}}{\partial x_k}\right]. \tag{4.7}$$

The RUM stress tensor is then splitted into an spherical and a deviatoric part (Eq. (2.86)). Substracting the trace leads:

$$\begin{aligned}\delta\breve{R}^*_{p,ij} = \; & - \frac{\breve{\tau}_p}{2}\left[\frac{2}{3}\delta\breve{\theta}_p\left(\frac{\partial\breve{u}_{p,i}}{\partial x_j} + \frac{\partial\breve{u}_{p,j}}{\partial x_i} - \frac{2}{3}\frac{\partial\breve{u}_{p,m}}{\partial x_m}\delta_{ij}\right)\right] \\ & - \frac{\breve{\tau}_p}{2}\left[\delta\breve{R}^*_{p,kj}\frac{\partial\breve{u}_{p,i}}{\partial x_k} + \delta\breve{R}^*_{p,ik}\frac{\partial\breve{u}_{p,j}}{\partial x_k} - \frac{2}{3}\delta\breve{R}^*_{p,mn}\frac{\partial\breve{u}_{p,m}}{\partial x_n}\delta_{ij}\right].\end{aligned} \tag{4.8}$$

In order to close the deviatoric RUM stress tensor $\delta\breve{R}^*_{p,ij}$, a condition of equilibrium may be assumed. Assuming light anisotropy leads to neglect the 2^{nd} term in the RHS of Eq. (4.8) giving the known viscosity-like model (Simonin *et al.* (2001)):

$$\delta\breve{R}^*_{p,ij} = -\frac{\breve{\tau}_p}{2}\left[\frac{2}{3}\delta\breve{\theta}_p\left(\frac{\partial\breve{u}_{p,i}}{\partial x_j}+\frac{\partial\breve{u}_{p,j}}{\partial x_i}-\frac{2}{3}\frac{\partial\breve{u}_{p,m}}{\partial x_m}\delta_{ij}\right)\right] = -2\nu_{RUM}S^*_{p,ij}, \tag{4.9}$$

where $\nu_{RUM} = \breve{\tau}_p\delta\breve{\theta}_p/3$ is the so-called RUM viscosity.

This model has been extensively used to perform Eulerian-Eulerian simulations (Kaufmann *et al.* (2008), Riber (2007), Riber *et al.* (2009), Sanjosé (2009), Vié *et al.* (2009), Dombard (2011)). Riber (2007) showed that this model conducts to a re-laminarization of the dispersed phase flow when in the presence of mean shear (configuration of Hishida *et al.* (1987)). Hereinafter, Eq. (4.9) will be referred to as “VISCO" model.

Note that the viscosity model assumes that the deviatoric RUM and the particle rate-of-strain are related by a linear equation through an eddy-viscosity which uses the particle relaxation time as timescale. This assumption may be related to the kinetic theory of diluted gases. It implies that molecular motion adjust rapidly to the changes imposed by the local strain. This basic assumption at the basis of the VISCO model is violated when the Knudsen number (Kn, a dimensionless number relating the particle relaxation time and the mesoscopic shear timescale) is large.

4.3 A viscosity-type model for axisymmetric tensors

Masi (2010) adapted an idea of Jovanović & Otić (2000) suggested for turbulent flows to the dispersed phase behaving in one-component limit state. According to numerical onservations of turbulent flows, the tensors are assumed axisymmetric with respect to a preferential direction. That is, fluctuations are developed in a privileged direction of the flow. They can be written in bilinear form using eigenvalues (Batchelor (1946), Chandrasekhar (1950)). By using the second invariants of the rate-of-strain ($\mathbf{S}$, Eq. (4.3)), the anisotropy ($\mathbf{b}$) tensors, and the signs of their third invariants, one may write the following equation for $\delta\breve{R}^*_{p,ij}$:

$$\delta\breve{R}^*_{p,ij} = sign(III_S)sign(III_b)II_b^{1/2}2\delta\breve{\theta}_p\frac{S^*_{p,ij}}{S}. \tag{4.10}$$

The magnitude of the rate-of-strain tensor reads:

$$S = II_S^{1/2} = \{\mathbf{S}^{*2}\}^{1/2}, \tag{4.11}$$

S is the second invariant of the rate-of-strain tensor. The third dimensional invariant reads:

$$III_S = \{\mathbf{S}^{*3}\}, \tag{4.12}$$

The same invariants can be defined for the anisotropy tensor $\mathbf{b}$ respectively noted: II_b and III_b.

In Eq. (4.10), the product of the invariants' signs accounts for the possibility of both tensors being in the same configuration of contraction or expansion if positive, or in the opposite configuration if negative. Numerical simulations (Masi (2010)) showed that III_b is locally positive and only the sign of III_S changes, and that $\mathbf{b}$ behaves in one-component limit state, which gives $II_b = \frac{2}{3}$. Taking into account these considerations, the Eq. (4.10) leads to:

$$\delta\breve{R}^*_{p,ij} = sign(III_S)\left(\frac{2}{3}\right)^{1/2}2\delta\breve{\theta}_p\frac{S^*_{p,ij}}{S}. \tag{4.13}$$

Equation (4.13) still accounts for the possibility of reverse exchanges of energy through $sign(III_S)$. Under these assumptions, the sign of III_S reproduces both positive and negative viscosities, and thus energy exchanges from the RUM to the mesoscopic motion are accounted for. Equation (4.13) may be rewritten without including the sign of the third invariant of $\mathbf{S}$:

$$\delta\breve{R}^*_{p,ij} = -\left(\frac{2}{3}\right)^{1/2}2\delta\breve{\theta}_p\frac{S^*_{p,ij}}{S}. \tag{4.14}$$

Hereinafter, Eq. (4.14) will be referred as “AXISY" model and Eq. (4.13) as “AXISY-C", “-C" standing for *corrected*, since the model includes a correction in the form of $sign(III_S)$.

4.3.1 Two different timescales

Section 4.2 presented a model for the deviatoric RUM stress tensor using the particle relaxation time $\breve{\tau}_p$ as timescale for the relationship between $\delta\breve{R}^*_{p,ij}$ and $S^*_{p,ij}$ (Eq. (4.9)). The so called AXISY model presented in Section 4.3 uses instead the mesoscopic-shear timescale to relate both tensors (Eq. (4.14)):

$$\underbrace{\frac{\breve{\tau}_p}{3}}_{VISCO} \longrightarrow \underbrace{\frac{II_b^{1/2}}{S}}_{AXISY} . \tag{4.15}$$

Hence, VISCO and AXISY are both eddy-viscosity models differing in their timescale: $\mathcal{F}(\breve{\tau}_p)$ for VISCO and $\mathcal{F}(S^{-1})$ for AXISY.

4.4 Quadratic algebraic approximation

Assuming equilibrium of stress components (i.e. neglecting all transport terms) in Eq. (4.8) and applying an iterative procedure invoking the isotropic approximation ($\delta\breve{R}^*_{p,ij} = 0$) at the zeroth-order approximation, Zaichik developped a non-linear model that, at the first approximation, is equivalent to VISCO model. The second approximation gives:

$$\delta\breve{R}^*_{p,ij} = -\frac{2\breve{\tau}_p\delta\breve{\theta}_p}{3}S^*_{p,ij} + \frac{2\breve{\tau}_p^2\delta\breve{\theta}_p}{6}\left(S^*_{p,ik}\frac{\partial\breve{u}_{p,j}}{\partial x_k} + S^*_{p,jk}\frac{\partial\breve{u}_{p,i}}{\partial x_k} - \frac{2}{3}S^*_{p,mn}\frac{\partial\breve{u}_{p,m}}{\partial x_n}\delta_{ij}\right). \tag{4.16}$$

Equation (4.16) is referred as “QUAD" model in Masi (2010). It has not been implemented in AVBP and analysis nor results concerning this model are presented in this work. However, it is a necessary step for the understanding of the model presented in Section 4.4.1.

4.4.1 A “rescaled" quadratic algebraic approximation.

Masi (2010) used Eq. (4.15) to construct a new non-linear model from Eq. (4.16). Replacing $\breve{\tau}_p$ with the timescale S^{-1} (cf Section 4.3.1) and applying the same iterative procedure to Eq. (4.8) that has been applied to obtain Eq. (4.16) leads to:

$$\delta\breve{R}^*_{p,ij} = -2\left(\frac{2}{3}\right)^{1/2}\delta\breve{\theta}_p\frac{S^*_{p,ij}}{S} + \frac{2\delta\breve{\theta}_p}{S^2}\left(S^*_{p,ik}\frac{\partial\breve{u}_{p,j}}{\partial x_k} + S^*_{p,jk}\frac{\partial\breve{u}_{p,i}}{\partial x_k} - \frac{2}{3}S^*_{p,mn}\frac{\partial\breve{u}_{p,m}}{\partial x_n}\delta_{ij}\right). \tag{4.17}$$

Equation (4.17) at the first order leads to “AXISY" model (Eq. (4.14)), if one-component limit state is assumed and a positive viscosity is used. It can be rewritten for the anisotropy tensor $\mathbf{b}^*$:

$$\mathbf{b}^* = -\left[\left(\frac{2}{3}\right)^{1/2} - \frac{2}{3}\{\mathbf{S}^+\}\right]\mathbf{S}^{*+} - (\mathbf{S}^{*+}\mathbf{\Omega}^+ - \mathbf{\Omega}^+\mathbf{S}^{*+}) + 2\left(\mathbf{S}^{*+2} - \frac{1}{3}\{\mathbf{S}^{*+2}\}\mathbf{I}\right), \tag{4.18}$$

where the superscript $^+$ stands for dimensionless tensors (normalization by $II_S^{1/2}$). The assessment of the model on the mean components of the stress tensor showed that including a coefficient of 0.5 in Eq. (4.18) produces better agreement in the particle-laden turbulent planar jet configuration (Fig. 4.1) of (Masi (2010)). Hereinafter, Eq. (4.18) will be referred as “QUAD-MOD" model. It has been implemented in AVBP with a coefficient of 0.5 for the study of Chapter 5 for the configuration shown in Fig. 4.1.

4.5 A local weak-equilibrium assumption

In the context of gaseous turbulence, Rodi (1972) introduced a “weak-equilibrium" assumption which does not need to neglect the transport terms in the stress equations. Instead, it supposes that the spatial and temporal variations of the stresses are related to the variations of the kinetic energy. The equilibrium hypothesis is thus transposed onto the anisotropy tensor. From this idea, Pope (1975) suggested an effective-viscosity approach. Several authors (Gatski & Speziale (1993), Girimaji (1996), Wallin & Johansson (2000)) contributed to the development of the so-called Algebraic Stress Models (ASM) where an “E", for explicit, is often added (EASM).

From this idea, Masi (2010) proposed an implicit equation for the modelisation of the RUM (Eq. (4.22)) and used the methods of Gatski & Speziale (1993), Girimaji (1996) and Wallin & Johansson (2000) to develop explicit solutions for it. Here, the main steps leading to Eq. (4.22) are recalled and the explicit solutions obtained presented.

Introducing the same “weak-equilibrium" assumption to the RUM anisotropy stress tensor leads:

$$\frac{D}{Dt} b^*_{p,ij} = 0, \tag{4.19}$$

or using Eq. (4.2) gives:

$$\frac{D}{Dt} \delta\breve{R}_{p,ij} = \frac{\delta\breve{R}_{p,ij}}{\delta\breve{\theta}_p} \frac{D}{Dt} \delta\breve{\theta}_p. \tag{4.20}$$

Injecting Eq. (2.79) and (2.95) into Eq. (4.20) and assuming equality between third-order correlations yields:

$$\delta\breve{R}_{p,ij} \left(-\frac{\delta\breve{R}_{p,nm}}{2\delta\breve{\theta}_p} \frac{\partial\breve{u}_{p,n}}{\partial x_m} \right) = -\frac{1}{2} \delta\breve{R}_{p,kj} \frac{\partial\breve{u}_{p,i}}{\partial x_k} - \frac{1}{2} \delta\breve{R}_{p,ik} \frac{\partial\breve{u}_{p,j}}{\partial x_k}. \tag{4.21}$$

The term inside the parenthesis represents the production of the local RUM kinetic energy by shear and compression (normalized by $2\delta\breve{\theta}_p$). Equation (4.21) may be written for the anisotropy tensor:

$$\mathbf{b}^* \left(-2\{\mathbf{b}^*\mathbf{S}^*\} \right) = -\frac{2}{3}\mathbf{S}^* - \left(\mathbf{b}^*\mathbf{S}^* + \mathbf{S}^*\mathbf{b}^* - \frac{2}{3}\{\mathbf{b}^*\mathbf{S}^*\}\mathbf{I} \right) + \left(\mathbf{b}^*\mathbf{\Omega} - \mathbf{\Omega}\mathbf{b}^* \right), \tag{4.22}$$

which is a non-linear implicit system. Masi (2010), developped explicit solutions for Eq. (4.22) following the ideas of Gatski & Speziale (1993), Girimaji (1996) and Wallin & Johansson (2000). They are briefly recalled in Sections 4.5.1 - 4.5.3. The family of models arising from the explicit solutions of Eq. (4.22) will be referred as “$2\Phi EASM$" models.

Equation (4.22) is a more generalized form of equilibrium “production-dissipation" that contains the models presented in previous sections.

In order to provide an explicit solution, Eq. (4.22) is rearranged as follows:

$$\mathbf{b}^+ = -\mathbf{S}^+ - \left(\mathbf{b}^+\mathbf{S}^+ + \mathbf{S}^+\mathbf{b}^+ - \frac{2}{3}\{\mathbf{b}^+\mathbf{S}^+\}\mathbf{I} \right) + \left(\mathbf{b}^+\mathbf{\Omega}^+ - \mathbf{\Omega}^+\mathbf{b}^+ \right), \tag{4.23}$$

where $\mathbf{b}^+ = \frac{3}{2}\mathbf{b}^*$, $\mathbf{S}^+ = \mathbf{S}^*/(-2\{\mathbf{b}^*\mathbf{S}^*\})$ and $\mathbf{\Omega}^+ = \mathbf{\Omega}/(-2\{\mathbf{b}^*\mathbf{S}^*\})$. According to Pope (1975), the anisotropy can be expressed in a general form:

$$\mathbf{b}^+ = \sum_{\varsigma} G^{(\varsigma)} T^{(\varsigma)}, \tag{4.24}$$

where a set of ten tensors $T^{(\varsigma)}$ and coefficients $G^{(\varsigma)}$ is needed to form the integrity basis shown in Table 4.1. The coefficients are presented in Table 4.2. They are functions of the five dimensionless invariants:

$$\eta_1 = \{\mathbf{S}^{+2}\},\ \eta_2 = \{\mathbf{\Omega}^{+2}\},\ \eta_3 = \{\mathbf{S}^{+3}\},\ \eta_4 = \{\mathbf{S}^{+}\mathbf{\Omega}^{+2}\},\ \eta_5 = \{\mathbf{S}^{+2}\mathbf{\Omega}^{+2}\}, \tag{4.25}$$

the denominator D reading:

$$D = 3 - \frac{7}{2}\eta_1 + \eta_1^2 - \frac{15}{2}\eta_2 - 8\eta_1\eta_2 + 3\eta_2^2 - \eta_3 + \frac{2}{3}\eta_1\eta_3 - 2\eta_2\eta_3 + 21\eta_4 + 24\eta_5 + 2\eta_1\eta_4 - 6\eta_2\eta_4. \tag{4.26}$$

$T^{(1)} = \mathbf{S}^{+}$	$T^{(6)} = \mathbf{\Omega}^{+2}\mathbf{S}^{+} + \mathbf{S}^{+}\mathbf{\Omega}^{+2} - \frac{2}{3}\{\mathbf{S}^{+}\mathbf{\Omega}^{+2}\}\mathbf{I}$
$T^{(2)} = \mathbf{S}^{+}\mathbf{\Omega}^{+} - \mathbf{\Omega}^{+}\mathbf{S}^{+}$	$T^{(7)} = \mathbf{\Omega}^{+}\mathbf{S}^{+}\mathbf{\Omega}^{+2} - \mathbf{\Omega}^{+2}\mathbf{S}^{+}\mathbf{\Omega}^{+}$
$T^{(3)} = \mathbf{S}^{+2} - \frac{1}{3}\{\mathbf{S}^{+2}\}\mathbf{I}$	$T^{(8)} = \mathbf{S}^{+}\mathbf{\Omega}^{+}\mathbf{S}^{+2} - \mathbf{S}^{+2}\mathbf{\Omega}^{+}\mathbf{S}^{+}$
$T^{(4)} = \mathbf{\Omega}^{+2} - \frac{1}{3}\{\mathbf{\Omega}^{+2}\}\mathbf{I}$	$T^{(9)} = \mathbf{\Omega}^{+2}\mathbf{S}^{+2} + \mathbf{S}^{+2}\mathbf{\Omega}^{+2} - \frac{2}{3}\{\mathbf{S}^{+2}\mathbf{\Omega}^{+2}\}\mathbf{I}$
$T^{(5)} = \mathbf{\Omega}^{+}\mathbf{S}^{+2} - \mathbf{S}^{+2}\mathbf{\Omega}^{+}$	$T^{(10)} = \mathbf{\Omega}^{+}\mathbf{S}^{+2}\mathbf{\Omega}^{+2} - \mathbf{\Omega}^{+2}\mathbf{S}^{+2}\mathbf{\Omega}^{+}$

Table 4.1: *The integrity basis for fully three-dimensional flows. Reproduced from Masi (2010).*

$G^{(1)} = -\frac{1}{2}(6 - 3\eta_1 - 21\eta_2 - 2\eta_3 + 30\eta_4)/D$	$G^{(6)} = -9/D$
$G^{(2)} = -(3 + 3\eta_1 - 6\eta_2 + 2\eta_3 + 6\eta_4)/D$	$G^{(7)} = 9/D$
$G^{(3)} = (6 - 3\eta_1 - 12\eta_2 - 2\eta_3 - 6\eta_4)/D$	$G^{(8)} = 9/D$
$G^{(4)} = -3(3\eta_1 + 2\eta_3 + 6\eta_4)/D$	$G^{(9)} = 18/D$
$G^{(5)} = -9/D$	$G^{(10)} = 0$

Table 4.2: *Coefficients associated to the integrity basis. Reproduced from Masi (2010).*

Singularities may appear when the denominator D vanishes. For this reason Gatski & Speziale (1993) proposed a regularization procedure applied to the two-dimensional formulation to ensure stability. In practice the 2D formulation is also used for three-dimensional flows. Two-dimensional flows are mean-free in one of the three directions. According to Gatski & Speziale (1993) in that case only three tensors from the integrity basis (Table 4.1) are needed: $T^{(1)}$, $T^{(2)}$ and $T^{(3)}$. Moreover, in 2D: $\eta_3 = \eta_4 = 0$ and $\eta_5 = \frac{1}{2}\eta_1\eta_2$. The expression for 2D flows reads:

$$\mathbf{b}^{+} = -\frac{3}{3 - 2\eta_1 - 6\eta_2}\left[\mathbf{S}^{+} + \left(\mathbf{S}^{+}\mathbf{\Omega}^{+} - \mathbf{\Omega}^{+}\mathbf{S}^{+}\right) - 2\left(\mathbf{S}^{+2} - \frac{1}{3}\{\mathbf{S}^{+2}\}\mathbf{I}\right)\right]. \tag{4.27}$$

4.5.1 Modeling the non-linearity

Equation (4.27) is implicit. In order to provide an explicit expression, an equation for $-2\{\mathbf{b}^{*}\mathbf{S}^{*}\}$ has to be provided. $\mathbf{b}^{*}$ and $\mathbf{S}^{*}$ are both axisymmetric tensors, $\mathbf{b}^{*}$ behaving in one-component limit state and $\mathbf{S}^{*}$ in axisymmetric expansion (Masi (2010)). Assuming alignment between the tensors and axisymmetric directions leads to:

$$-2\{\mathbf{b}^{*}\mathbf{S}^{*}\} = 2\left(\frac{2}{3}\right)^{1/2} II_s^{1/2}. \tag{4.28}$$

Equation (4.28) is invariant by definition. Using Eq. (4.28) to normalize the tensors in Eq. (4.27) guarantees that the 2D form is always non-singular. Re-writting the denominator for two-dimensional flows using the variable change $\eta^2 = \eta_1$, $\zeta^2 = -\eta_2$ leads to:

$$D = 3 - 2\eta^2 + 6\zeta^2, \tag{4.29}$$

which in the limit case where $\zeta^2 = 0$, η^2 must be greater than $\frac{3}{2}$ in order to avoid D becoming zero. This condition is always fulfilled. Combination of Eq. (4.27) and Eq. (4.28) will be referred to as “2ΦEASM1" model.

4.5.2 An explicit solution accounting for non-linearity I

Girimaji (1996) suggested a fully-explicit and consistent solution for 2D flows in the context of gaseous turbulence. Masi (2010) adapted the same approach to provide an explicit solution to Eq. (4.22). Equation (4.22) is rewritten

in Girimaji's notation as follows:

$$\mathbf{b}^* \left(L_1^0 - L_1^1\{\mathbf{b}^*\mathbf{S}^+\}\right) = L_2\mathbf{S}^+ + L_3\left(\mathbf{b}^*\mathbf{S}^+ + \mathbf{S}^+\mathbf{b}^* - \frac{2}{3}\{\mathbf{b}^*\mathbf{S}^+\}\mathbf{I}\right) - L_4\left(\mathbf{b}^*\mathbf{\Omega}^+ - \mathbf{\Omega}^+\mathbf{b}^*\right) \tag{4.30}$$

where $L_1^0 = 0$, $L_1^1 = 2$, $L_2 = -\frac{2}{3}$, $L_3 = -1$ and $L_4 = -1$ and where the normalization is done dividing by $II_S^{1/2}$. The general representation of the anisotropy tensor in 2D reads:

$$\mathbf{b}^* = G_1\mathbf{S}^+ + G_2\left(\mathbf{S}^+\mathbf{\Omega}^+ - \mathbf{\Omega}^+\mathbf{S}^+\right) + G_3\left(\mathbf{S}^{+2} - \frac{1}{3}\{\mathbf{S}^{+2}\}\mathbf{I}\right) \tag{4.31}$$

where the coefficients G are:

$$G_2 = \frac{L_4}{\eta_1 L_1^1},\ G_3 = -\frac{2L_3}{\eta_1 L_1^1}, \tag{4.32}$$

and

$$G_1^2 = -\frac{1}{\eta_1 L_1^1}\left[L_2 + \frac{1}{3}\eta_1 L_3 G_3 - 2\eta_2 L_4 G_2\right]. \tag{4.33}$$

Here $\eta_1 = \{\mathbf{S}^{+2}\}$ and $\eta_2 = \{\mathbf{\Omega}^{+2}\}$. Unfortunately, as η_2 is always negative, Eq. (4.33) admits real solutions only for $\eta_1 \geq -\eta_2$. In the implementation of this model, local negative values will be set to zero. Concerning the sign of G_1, in the simplest case it is taken as negative. Combination of Eq. (4.31) and the coefficients in Eq. (4.32) and (4.33) (with negative sign) will be referred to as "2ΦEASM2" model.

4.5.3 An explicit solution accounting for non-linearity II

Another technique to provide explicit solutions was suggested by Wallin & Johansson (2000) in the context of turbulent gaseous flows and used in the context of the RUM by Masi (2010) to provide new explicit solution to Eq. (4.22). Using the integrity basis of Table 4.1, Eq. (4.23) is written for the dispersed phase, using the notation of Wallin & Johansson (2000), as follows:

$$N\mathbf{b}^* = -A_1\mathbf{S}^+ - A_2\left(\mathbf{b}^*\mathbf{S}^+ + \mathbf{S}^+\mathbf{b}^* - \frac{2}{3}\{\mathbf{b}^*\mathbf{S}^+\}\mathbf{I}\right) + \left(\mathbf{b}^*\mathbf{\Omega}^* - \mathbf{\Omega}^*\mathbf{b}^*\right), \tag{4.34}$$

where

$$N = A_3 + A_4(-2\{\mathbf{b}^*\mathbf{S}^+\}), \tag{4.35}$$

$A_1 = \frac{2}{3}$, $A_2 = 1$, $A_3 = 0$, $A_4 = 2$ and the normalization is done as in Section 4.5.2. In very diluted flows, as $A_3 = 0$, the polynomial of N is depressed to the second order and reads:

$$N = 2\eta_1 + 2\eta_2. \tag{4.36}$$

N admits real solutions only for $\eta_1 \geq -\eta_2$. As it has been done for 2ΦEASM2 model, local negative values are set to zero. Concerning the sign of N it must lead to a positive sign of the production and hence it will be chosen as positive in the simplest case. Masi (2010) developped the limit solutions for three and two-dimensional flows. Here, only the 2D form is presented. The final equation for the anisotropy tensor reads:

$$\mathbf{b}^* = G_1 T^{(1)} + G_2 T^{(2)} + G_3 T^{(3)}, \tag{4.37}$$

where the coefficients of the model depend on N as follows:

$$G_1 = -\frac{A_1 N}{Q},\ G_2 = -\frac{A_1}{Q},\ G_3 = 2\frac{A_1 A_2}{Q}, \tag{4.38}$$

with

$$Q = N^2 - 2\eta_2 - \frac{2}{3}AA_2^2\eta_1. \tag{4.39}$$

Hereinafter this model will be referred to as "2ΦEASM3". 2ΦEASM2 and 2ΦEASM3 models lead to the same solution under the two-dimensional flows assumption. Since only the 2D form has been implemented in AVBP, only results using the 2D formulation will be shown in this work. The reader is encouraged to see Masi (2010) for more details about the development of the models briefly presented in this section.

4.5.4 Model correction

Section 4.3 showed that it is possible to acoount for a reverse exchange in the energy by introducing a correction by means of $sign(III_S)$. In the so-called "2ΦEASM" models, the reverse sign in the energy exchange is related to the sign of the coefficient G_1, which is the same than that of the scalar quantity $\{\mathbf{b}^*\mathbf{S}^*\}$. This coefficient is negative in single-phase turbulent flows ("weak-equilibrium", Girimaji (1996)). However, in dispersed phase interacting with turbulent flows, it is usual to have a reverse exchange of energy from the RUM to the mesoscopic motion, which would correspond to a reverse sign of G_1. Masi (2010) proposed to model this reverse exchange of energy in the 2ΦEASM models in the same way than in AXISY-C, giving the so-called "2ΦEASM-C" models.

2ΦEASM1-C model is constructed by including in Eq. (4.28) the sign of the third invariant of $\mathbf{S}$, $sign(III_S)$, as follows:

$$-2\{\mathbf{b}^*\mathbf{S}^*\} = -2sign(III_S)\left(\frac{2}{3}\right)^{1/2} II_S^{1/2}\,. \tag{4.40}$$

The coefficient G_1 of the model 2ΦEASM2 obtained by Eq. (4.33) is rewritten as

$$G_1 = sign(III_S)\frac{\sqrt{2\eta_1 + 2\eta_2}}{2\eta_1} \tag{4.41}$$

giving the so-called 2ΦEASM2-C model.

Finally, 2ΦEASM3-C model is obtained through a modification of the quantity N (Eq. (4.36)) as follows:

$$N = -sign(III_S)\sqrt{2\eta_1 + 2\eta_2}\,. \tag{4.42}$$

4.6 A hierarchy of models: Classification

Figure 4.2 shows a classification of the models presented in this Chapter taking into account wether they are linear or not and depending on the timescale they use (cf Section 4.3.1). There are two linear models: VISCO and AXISY that differ on their timescale ($\mathcal{F}(\check{\tau}_p)$ for VISCO and $\mathcal{F}(S^{-1})$ for AXISY). QUAD is a non-linear model using the timescale of VISCO. However, since QUAD-MOD (a non-linear model using $\mathcal{F}(S^{-1})$ as timescale) showed better *a priori* results in the particle-laden turbulent planar jet configuration (Masi (2010)) than QUAD only QUAD-MOD has been implemented in AVBP and no results using QUAD model will be shown here. Finally, all 2ΦEASM models are non-linear models using $\mathcal{F}(S^{-1})$ as characteristic timescale.

4.7 Verification of the realizability conditions of the model

It is well known in gaseous turbulence, that certain models for the Reynolds stress tensor, containing closure assumptions relating algebraically unknown correlations to the known quantities, may not have a solution for a given set of initial and boundary conditions in the sense that the realizability conditions (Vachat (1977), Schumann (1977)) may be violated. The problem of non-realizable solutions has already been found in complicated analytical models for the turbulence. In particular, negative energies may develop (André *et al.* (1976)) and some properties of the turbulence can be violated (Orszag (1970)). Such realizability conditions for single-flow are written (Schumann (1977), Ortega (1987)):

$$R_{\alpha\beta} \geq 0 \qquad \text{for} \qquad \alpha = \beta, \tag{4.43}$$

$$R_{\alpha\beta}^2 \leq R_{\alpha\alpha}R_{\beta\beta} \qquad \text{for} \qquad \alpha \neq \beta. \tag{4.44}$$

Here, $R_{\alpha\beta}$ is any velocity based stress tensor. Summation is adopted for latin indices but not for greek indices. These conditions are the consequence of real velocities and Schwarz's inequality. Equation (4.43) implies non-negative energies and Eq. (4.44) states that the cross-correlations between different components of the fluctuating

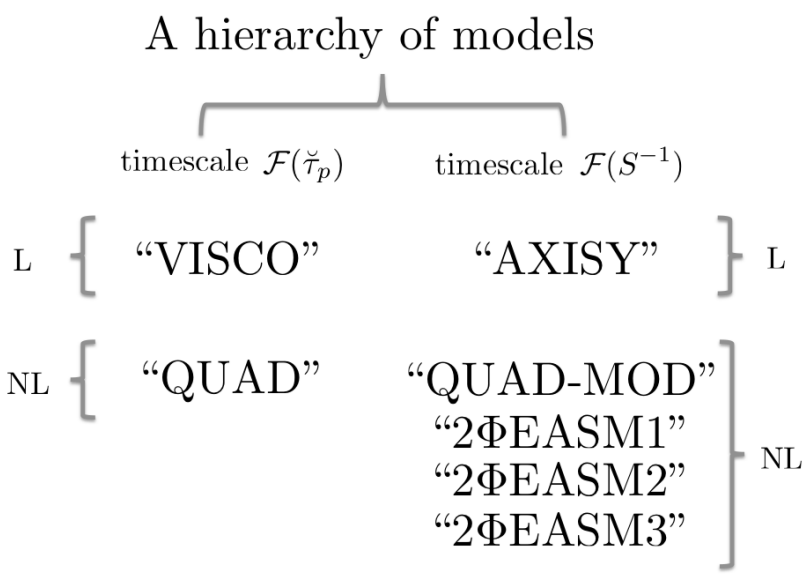

Figure 4.2: *Schematic representation of models. L=Linear, NL=Non-Linear constitutive relations. Modified from Masi (2010).*

velocity are bounded by the magitude of the autocorrelations. Another condition must be added to the set of Eqs. (4.43)-(4.44):

$$det(R_{\alpha\beta}) \geq 0. \tag{4.45}$$

Equation (4.45) can be rearranged as follows:

$$\frac{R_{12}R_{23}R_{31}}{R_{11}R_{22}R_{33}} \geq \frac{1}{2}\left[\frac{R_{12}^2}{R_{11}R_{22}} + \frac{R_{23}^2}{R_{22}R_{33}} + \frac{R_{31}^2}{R_{11}R_{33}} - 1\right]. \tag{4.46}$$

Equation (4.46) implies that the cross-correlations can not take arbitrary values (i.e. if two are well correlated with the same signs, the third one must be positive). Equation (4.43) to (4.46) produce five independent inequalities. However, Schumann (1977) showed that only three are independent.

Regarding the applicability of these conditions to numerical simulations, Deardorff (1973) and André *et al.* (1976) proposed to clip the non-realizable solutions at each time step and at every node of the grid. That is, for all points where the inequalities (4.43) - (4.46) do not hold, the stress tensor components take a new value corresponding to the equal sign of the condition. However, as Schumann (1977) showed, these changes may depend upon the orientation of the system and lead to nonsteady and noninvariant models. However, situations where the stress tensor is close to the extreme state of equality in the realizability conditions are rare and models which do not guarantee the realizability conditions at every location and instant might still be valid in most applications.

The models presented in this Chapter for the RUM stress tensor may lead to non-physical solutions in centain conditions. Since the realizability of the models is not always verified and in order to avoid imaginary solutions, the approach of Deardorff (1973) and André *et al.* (1976) has been retained to guarantee that the solutions produced by the models verify the realizability conditions. Since only three inequalities are independent, only Eqs. (4.43) and (4.44) have been implemented in AVBP. However, a number of tests including Eq. (4.45), and checking that the order on which the conditions are verified has no impact on the instantaneous fields, have been performed. The final set of equations retained for the conditioning of the models is:

$$\delta\breve{R}_{p,\alpha\beta} \geq 0 \quad \text{for} \quad \alpha = \beta, \tag{4.47}$$

$$\delta\breve{R}^2_{p,\alpha\beta} \leq \delta\breve{R}_{p,\alpha\alpha}\delta\breve{R}_{p,\beta\beta} \quad \text{for} \quad \alpha \neq \beta. \tag{4.48}$$

In the cases where conditioning is required, a third equation is to guarantee that $\delta\breve{R}^*_{p,ij}$ remains a traceless tensor so:

$$\delta\breve{R}^*_{p,ij} = 0 \quad \text{for} \quad i = j\ . \tag{4.49}$$

This conditioning has been applied to all the simulations presented in this work.

Chapter 5

Modeling the RUM: an a posteriori analysis.

In this Chapter, the different models for the deviatoric part of the RUM stress tensor presented in Chapter 4 are validated *a posteriori* against projected fields (cf Appendix A) issued from Euler-Lagrange calculations performed with the code NTMIX-2Φ (cf Appendix A). The test case chosen is presented in Section 5.1. It consists in a Direct Numerical Simulation (DNS) of a temporal particle-laden turbulent planar jet subject to a homogeneous isotropic decaying turbulence (Fig. 4.1). This test case aims at being representative of a control volume in the periphery of a hollow-cone spray (Fig. 5.1), where the flow is subjected to a strong mean shear. It is indeed a model of the local behavior of the dispersed phase in mean-sheared unsteady, inhomogeneous turbulent flows.

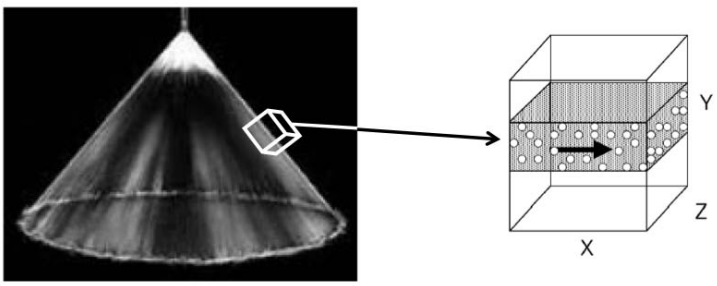

Figure 5.1: *Generic representation of the flow in a hollow-cone spray. Modified from Vermorel (2003).*

Masi (2010) performed an *a priori* analysis of the performances of the RUM models in this configuration (a simplified sketch is shown in Fig. 5.3). She performed Euler-Lagrange simulations for different particle inertia (i.e. Stokes numbers) and different levels of initial gaseous turbulence in the HIT field (i.e. acoustic Reynolds numbers, Re^{ac}) with the code NTMIX-2Φ. The *a priori* analysis uses particle Eulerian fields extracted from Euler-Lagrange DNS by means of a projection algorithm (Kaufmann *et al.* (2008)). Then, the models are tested against “exact" Eulerian fields. Statistics are computed over all the planes (XZ) of the slab. Since these planes may be considered as planes of homogeneity, the average gives an estimation of the theoretical ensemble average computed over a large number of particle and fluid realizations. Instantaneous fields are shown in the (XY) plane at the coordinate $Z = 0$ (Fig. 5.2).

The results obtained from the *a priori* analysis of the RUM models using the Eulerian projection of the Lagrangian fields computed with NTMIX-2Φ (Masi (2010)) are compared with *a posteriori* Euler-Euler simulations of the same configuration performed with the code AVBP. The *a priori* study of the exact Lagrangian computations of this configuration was used for the validation of the models presented in Chapter 4. The results of Masi (2010)

are not influenced by the choice of the RUM model. Indeed, the *a priori* analysis consists in the calculation of the RUM quantities ($\delta\breve{\theta}_p$, the RUM production terms and the components of the deviatoric RUM stress tensor) from the fields issued from an exact Lagrangian simulation. That is, from the fields of particle number density and velocity, the values of RUE and the other RUM quantities are calculated for every physical time at which the analysis is performed. Indeed, in the Lagrangian equations, there are no unclosed terms related to RUM, so no RUM modeling is needed. On the other hand, in the *a posteriori* simulations performed with AVBP, the choice of the model has an influence since the discrete phase flow field is affected by the field at the previous timestep, while the *a priori* results are obtained postprocessing exact Lagrangian simulations. There is then an effet of history in the *a posteriori* simulation. The magnitude of this effect is very difficult to quantify and this task is out of the scope of this work.

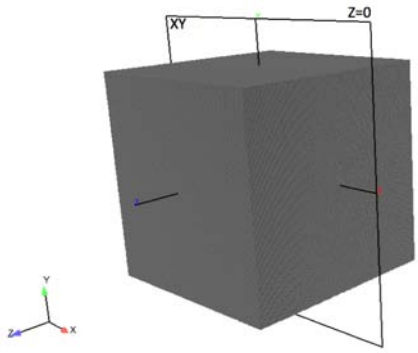

Figure 5.2: *Sketch of the (XY) cutting plane located at* $Z = 0$ *used to show instantaneous fields.*

This Chapter is organized as follows. In Section 5.1 the configuration, along with the initial and boundary conditions, and the numerical setup used for the simulations with AVBP, are presented. Section 5.2 presents a validation of the carrier phase flow. In Sections 5.3, a first validation for a low turbulent case ($Re^{ac} = 5500$) with a mean inertia ($St \sim 1$) is presented: statistics of low and high order moments along with instantaneous fields of the main moments are shown. Section 5.4 shows the results obtained for both a higher and a lower inertia ($St \sim 3$ and $St \sim 0.33$) flow. Section 5.5 shows the application to a higher turbulent case ($Re^{ac} = 20000$, $St \sim 1$). For all test cases, comparisons with the "exact" Eulerian fields obtained by Masi (2010) are provided. For the sake of simplicity, the term "Lagrangian" is used here to denote the *a priori* Eulerian fields coming from the projection of the Euler-Lagrange computations with NTMIX-2Φ (with the sense "from-Lagrangian") in order to distinguish them from the *a posteriori* Euler-Euler results obtained with AVBP, which will be referred to as "Eulerian".

5.1 Description of the test case

Figure 5.3 shows a simplified sketch of the configuration chosen to assess the *a posteriori* performances of the RUM models presented in Chapter 4. It consists in a temporal particle-laden turbulent planar jet embedded in a homogeneous decaying isotropic turbulence first studied by Vermorel (2003). The simulation domain is a cubic box with periodic boundary conditions in all directions. A slab with a mean gaseous velocity whose shape is a double hyperbolic tangent is added in the centrer of the box. Solid particles are added to the slab. Diluted conditions are assumed, and one-way coupling between the gas and the dispersed phase is taken into account. In fact, since the configuration is in diluted regime, it can be assumed that the dispersed phase has no impact on the carrier phase. A definition of the quantities used for the normalization and the equivalent in NTMIX-2Φ is briefly presented in Section 5.1.3, more details can be found in Dombard (2011).

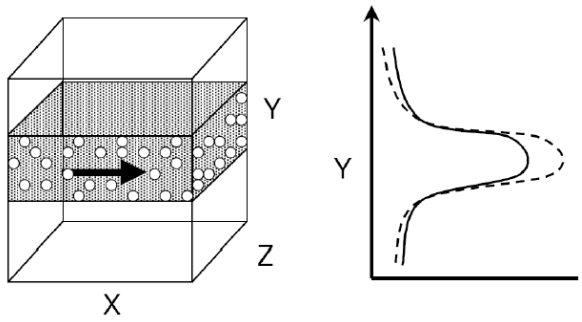

Figure 5.3: *Simplified sketch of the particle-laden turbulent planar jet configuration. (Extracted from Vermorel (2003)).*

5.1.1 Initial and boundary conditions

The initial condition for the carrier phase is the same for NTMIX-2Φ and AVBP in all cases. A slab with a gaseous mean velocity (U) is added to a homogeneous decaying isotropic turbulence. In this way, the jet is already turbulent at the initial time. The slab width L_{slab} is $0.25L_{box}$, where L_{box} is the length of the cube. The HIT is initialized with a Passot-Pouquet spectrum (Passot & Pouquet (1987)), setting the most energetic lengthscale to $L_e = 0.4L_{ref}$, where L_{ref} is a reference length. The choice of L_e yields initial turbulent eddies with a size approximately equal to one quarter of the slab width. This allows the jet to develop additional velocity fluctuations from the mean velocity gradient (Masi (2010)). The initial velocity profile in the slab is imposed as a hyperbolic-tangent profile:

$$\phi(y) = \phi^o + f(y)\left(\phi^i - \phi^o\right), \tag{5.1}$$

$$f(y) = \frac{1}{2}\left(1 + tanh\frac{\frac{1}{2}L_{slab} - |y|}{2\delta_\theta}\right), \tag{5.2}$$

where ϕ^i and ϕ^o denote the velocity in and outside the jet, y is the vertical coordinate and δ_θ refers to the initial momentum thickness of the slab.

For the low turbulence case, the initial turbulent Reynolds number based on Le is $Re \approx 73$. For the high turbulence case, it is approximately $Re \approx 264$.

In NTMIX-2Φ, particles are randomly embedded at the initial time at the same velocity than the gas phase. For the low turbulence cases, 80 millions particles are introduced in the domain, 210 millions for the high turbulence case. The corresponding particle velocities compared to the initial fluid velocities for both cases are listed in Table 5.1. Note that the initial particle volume fraction profile from NTMIX-2Φ has a very steep gradient at the periphery of the slab. The 3^{rd} order schemes implemented in AVBP are however not capable of handling such a steep gradient. For this reason, the initial particle volume fraction in AVBP has been initialized with a hyperbolic-tangent profile (Eq. (5.1)). A very low particle volume fraction field (six orders of magnitude lower than the value in the slab) is added to the whole domain to simulate the zones where no particles are present. Regarding the initial RUE profile, in NTMIX-2Φ it is initially equal to zero. However, due to the transport equation for RUE solved in AVBP, the RUM would never develop. A RUE profile is thus imposed at the initial time for the simulations with AVBP since all the terms on the RHS of the RUE transport equation directly depend on RUE. This initial RUE profile has been initialised in AVBP with two narrow hyperbolic-tangent profiles on each side of the slab, in order to mimic two “relaxed" Dirac’s delta functions. This profile is assumed equivalent to the RUE profile of the NTMIX-2Φ calculation close to the initial time.

Boundary conditions are periodic in all directions for both codes.

The mesh used for the simulations is a 128^3 grid for NTMIX-2Φ and the low turbulence case. It is a 256^3 grid for the high turbulence simulations. Dombard (2011) analyzed the impact of the mesh resolution on the dispersed phase in this configuration using AVBP. He deduced that although the carrier phase is converged for a given mesh,

it might not be the case for the dispersed phase. Increasing the mesh resolution in the Euler-Euler simulations leads to better agreement for the dispersed phase RMS quantities statistics. For this reason in AVBP, a 256^3 grid is used for both the low and the high turbulence cases. Some cases have also been performed on a 512^3 grid to assess the mesh resolution and for result comparison purposes. All meshes are composed by hexahedric cells.

Velocity	**Low turbulence**	**High turbulence**
MEAN-X	$U_p^0 = U_f^0$	$U_p^0 = U_f^0$
MEAN-Y	$V_p^0 = V_f^0 = 0$	$V_p^0 = V_f^0 = 0$
MEAN-Z	$W_p^0 = W_f^0 = 0$	$W_p^0 = W_f^0 = 0$
FLUCTUATION-X	$u_p^{0'} = 0$	$u_p^{0'} = 0$
FLUCTUATION-Y	$v_p^{0'} = v_f^{0'}$	$v_p^{0'} = 0$
FLUCTUATION-Z	$w_p^{0'} = w_f^{0'}$	$w_p^{0'} = 0$

Table 5.1: *Initial particle velocity conditions.*

5.1.2 Summary of test cases

The configuration is unsteady and depends only on initial conditions and parameters of the carrier and the dispersed phases. These parameters and initial conditions differ depending on the inertia and turbulence level simulated. Different levels of turbulence have been simulated. For the low Reynolds case (LR), three different values of particle inertia have been simulated. For the higher Reynolds (HR) case, one Stokes number has been simulated. Table 5.2 summarizes the test cases presented in this work. The symbol # represents the different RUM models tested for each case. Not all the RUM models have been evaluated for each case. Indeed, the results obtained in cases LR_St1_# and LR_St3_# allowed to distinguish the models that produced the best results. Those models were afterwards tested on both a lower inertia (LR_St033_#) and a higher turbulence cofigurations (HR_St1_#) along with the classical model VISCO and noRUM when possible. Table 5.3 shows the different models tested and in which configuration.

keyword	$\mathbf{Re^{ac}}$	**St**
LR_St_#	5500	1
LR_St3_#	5500	3
LR_St033_#	5500	0.333
HR_St1_#	20000	1

Table 5.2: *Matrix of the tests presented in this chapter.*

	Case			
RUM model	**LR_St1_#**	**LR_St3_#**	**LR_St033_#**	**HR_St1_#**
noRUM	X	X(unstable)	X(unstable)	X(unstable)
VISCO	X(unstable)	X(unstable)	X	X(unstable)
AXISY	X	X	-	-
AXISY-C	X	X	-	-
QUAD-MOD	X	X	X	X
2ΦEASM1	X	X	-	-
2ΦEASM1-C	X	X	-	-
2ΦEASM3	X	X	X	X
2ΦEASM3-C	X	X	-	-

Table 5.3: *Matrix of the RUM models tested on each case.*

Note that some simulations performed with the VISCO model or without taking into account the contribution

of the RUM in the dispersed phase equations (noRUM model) were not numerically stable with the numerical setup chosen (cf Section 5.1.4). In all cases, the VISCO and noRUM models were tested as they may be taken as a reference for the comparison, since they were the only two models for the Random Uncorrelated Motion available until now in AVBP.

5.1.3 Normalization

This Section provides a summary of the quantities used for normalization that are needed to compare the results issued from AVBP and NTMIX-2Φ. Indeed, NTMIX-2Φ uses non-dimensional variables, while AVBP does not. In this Section, asterisk will denote non-dimensional quantities to make the difference with dimensional ones. This notation will be abandoned afterwards.

The reference length is chosen as $L_{ref} = 10^{-3}m$, it is an arbitrary value. The simulation domain is a cubic box of size $L^*_{box} = 2\pi$. The carrier phase is composed of pure air (density $\rho_f = 1.138\ kg/m^3$, dynamic viscosity μ_f) at constant pressure $P_{ref} = 101325\ Pa$ and temperature $T_{ref} = 300\ K$ ($\gamma = 1.4$). Particles have the same temperature as the carrier fluid. Under these conditions, the speed of sound in the flow is:

$$c = \sqrt{\gamma \frac{P_{ref}}{\rho_{ref}}}\ , \tag{5.3}$$

the reference time reads:

$$t_{ref} = \frac{L_{ref}}{c}\ . \tag{5.4}$$

The non-dimensional numbers characterizing the carrier phase are:

- The acoustic Reynolds number, Re^{ac}:
$$Re^{ac} = \frac{cL_{ref}}{\nu_f}\ , \tag{5.5}$$
where $\nu_f = \mu_f/\rho_f$ is the kinematic viscosity of the carrier fluid.
- The Mach number, M:
$$M = \frac{U}{c}\ , \tag{5.6}$$
where U is the mean velocity of the carrier phase.
- The turbulence intensity:
$$I = \frac{u'}{U}\ , \tag{5.7}$$
where u' is the fluctuating velocity of the carrier phase

For the characterization of the dispersed phase the Stokes number is used:

- Dynamic Stokes number, St:
$$St = \frac{\tau^F_{fp}}{\tau_f}\ , \tag{5.8}$$
where $\tau^F_{fp} = \langle 1/\tau_p \rangle^{-1}_p$ is the characteristic particle relaxation time and τ_f is a characteristic timescale of the carrier flow.

In fact, in the *a posteriori* simulations the Stokes number used corresponds to the one of the *a priori* analysis. The Stokes number in the *a priori* analysis is computed over a characteristic timescale of the turbulence seen by the particles (Deutsch & Simonin (1991)). Such a timescale is estimated using the Tchen equilibrium in the z-direction (which is mean-flow free) (Simonin (1991)). The Stokes number is defined as done in Masi (2010). She estimates

the Stokes number and τ_{fp}^{F} at the end of a simulation of reference, referred as "$St = 1$". The Stokes number of all other simulations is evaluated comparing the particle density (ρ_p), which is the only parameter modified. For example, the simulation called "$St = 3$" is initialized with a particle density which is three times larger than the particle density in the simulation $St = 1$, all other parameters remaining unchanged.

In order to calculate the dimensional values of the parameters for the calculation with AVBP, the following procedure is used (Dombard (2011)):

From the chosen values for the reference lenght $L_{ref} = 10^{-3}\ m$, mean pressure $P_f = 101325\ Pa$ and temperature $T_f = 300\ K$, the speed of sound is calculated ($c = 352.9\ m/s$, Eq. (5.3)). The acoustic Reynolds number Re^{ac} and the Mach number M are conserved since they are, by definition, dimensionless quantities. They allow to evaluate the convective Reynolds number, Re^{c}:

$$Re^{c} = \frac{UL_{box}}{\nu_f} = \frac{U}{c}\frac{L_{box}}{L_{ref}}\frac{c \cdot L_{ref}}{\nu_f} = M \cdot L_{box} \cdot Re^{ac}\ . \tag{5.9}$$

The mean velocity of the jet, is calculated from the Mach number and the sound speed:

$$U = M \cdot c\ . \tag{5.10}$$

The kinematic viscosity is:

$$\nu_f = \frac{cL_{ref}}{Re^{ac}}\ , \tag{5.11}$$

which allows to evaluate the dynamic viscosity needed for AVBP:

$$\mu_f = \nu_f \cdot \rho_f . \tag{5.12}$$

Specifying the convective Reynolds number, the initial mean velocity of the jet along with the charateristics of the carrier fluid (pressure, temperature, density and viscosity), the gaseous fluid is defined. The characteristics of the initial carrier flow field are described in Section 5.1.1.

Regarding the dispersed phase, the characteristics of the solid particles need to be defined:

The Stokes number must be the same in the Lagrangian and the Eulerian calculations:

$$St^{NTMIX-2\Phi} = St^{AVBP}\ . \tag{5.13}$$

The characteristic fluid timescales between NTMIX-2Φ and AVBP are linked:

$$\tau_f = \tau_f^{*} \cdot t_{ref} = \tau_f^{*}\frac{L_{ref}}{c}\ , \tag{5.14}$$

where the superscript $*$ denotes a non-dimensional time. Throughout this Chapter, the reference time t_{ref} will be used to characterize the physical time of the Eulerian simulation for which results are compared. In the Lagrangian simulation, since NTMIX-2Φ uses non-dimensional quantities, $t_{ref}^{*} = 1$. The particle relaxation time is calculated assuming a Stokes regime, so no Schiller-Naumann correction (Schiller & Nauman (1935), Eq. (2.39)) is taken into account. Note that, the Schiller-Naumann correction is accounted for in the Euler-Euler simulations. However, since the relative velocity between particles and fluid is small, the Schiller-Naumann correction has a very limited influence on the results in this configuration. Simulations performed on all the cases studied in this Chapter with 2ΦEASM3 model (not presented here for the sake of conciseness) and without taking into account the Schiller-Naumann correction did not show any noteworthy difference.

$$\tau_p = \frac{4}{3}\frac{\rho_p d_p}{\rho_f \frac{24}{Re_p}||u_{rel}||} = \frac{1}{18}\frac{\rho_p d_p^2}{\rho_f \nu_f}\ , \tag{5.15}$$

where $||u_{ref}||$ is the relative velocity between the particles and the carrier fluid.

Equation (5.15) the allows to calculate the particle density ρ_p:

$$\rho_p = \frac{18\rho_f\nu_f}{d_p^2}\tau_p = \frac{18\rho_f\nu_f}{d_p^2}\tau_{fp}^{F*} \cdot t_{ref}\ . \tag{5.16}$$

The particle diameter can be chosen arbitrarly, however, the Stokes regime must be conserved, and the particle's relaxation times must be as similar as possible between the Lagrangian and the Eulerian simulations. In this case, the particle diameter used for the Lagrangian calculations with NTMIX-2Φ is too small, leading to dimensional values of the diameter for AVBP lower than $1\mu m$. This may lead to numerical stability problems when performing calculations with AVBP: in AVBP, variables $\breve{\alpha}_p$ and $\breve{n}_p$ are transported whereas the particle diameter is reconstructed. Small values of d_p may lead to very small values of $\breve{\alpha}_p$, close to the zero machine, which may produce numerical errors affecting the results or the stability of the code when reconstructing the diameter. A higher value of the particle diameter is therefore chosen for the Euler-Euler computations: $d_p = 2\mu m$ for all cases.

Table 5.4 shows the values of the parameters used for the different simulations performed at low turbulence ($Re^{ac} = 5500$, $St \sim 1$). For case LR_St3_# only the particle density is modified :$\rho_p = 3.633 \cdot 10^4 kg/m^3$. For case LR_St033_#, $\rho_p = 0.4037 \cdot 10^4 kg/m^3$. Table 5.5 shows the parameters of the high turbulence simulation (case HR_St1_#).

Parameter	**AVBP**
L_{box}	$2\pi \cdot 10^{-3}$ $[m]$
Re^{ac}	5500 $[-]$
M	0.15 $[-]$
I	0.1 $[-]$
Re^{c}	5183.63 $[-]$
P_f	101325 $[Pa]$
T_f	300 $[K]$
ρ_f	1.138 $[kg/m^3]$
ν_f	$6.42 \cdot 10^{-5}$ $[m^2/s]$
μ_f	$7.31 \cdot 10^{-5}$ $[kg/m \cdot s]$
c	352.9 $[m/s]$
U	52.935 $[m/s]$
u'	5.2935 $[m/s]$
t_{ref}	$2.834 \cdot 10^{-6}$ $[s]$
St	1
d_p	$2 \cdot 10^{-6}$ $[m]$
$\frac{\mathcal{W}_p}{\mathcal{W}_f}$	3.69 $[-]$
ρ_p	$1.2111 \cdot 10^4$ $[kg/m^3]$

Table 5.4: *Summary of AVBP initial parameters for the low turbulence mean inertia case (LR_St1_#).*

Parameter	**AVBP**
Re^{ac}	20000 $[-]$
Re^{c}	18850 $[-]$
ν_f	$1.7645 \cdot 10^{-5}$ $[m^2/s]$
μ_f	$2.008001 \cdot 10^{-5}$ $[kg/m \cdot s]$
St	1
d_p	$2 \cdot 10^{-6}$ $[m]$
ρ_p	$2.417 \cdot 10^3$ $[kg/m^3]$

Table 5.5: *Summary of AVBP initial parameters for the high turbulence case (HR_St1_#). Only the parameters which differ from those of the LR_St1_# case are shown.*

5.1.4 Numerical setup

Details about NTMIX-2Φ and the numerical setup used for the Euler-Lagrange reference simulations can be found in Appendix A. AVBP simulations have been performed using 3^{rd} order numerical scheme TTGC (Colin *et al.* (2000)) coupled with artificial dissipation (AD) for the dispersed phase. No ADis applied on the gaseous phase. The particle AV sensor used is CMS-Lite (Sanjosé (2009)). The values for the 2^{nd}-order (ϵ^2) and 4^{th}-order (ϵ^4) parameters are shown in Table 5.6. These values have been optimized for the LR_St1_2ΦEASM1 test case. All other simulations have been performed with exactly the same numerical setup. Thus, the only difference between simulations is the RUM model (besides the carrier phase turbulence level and the particle inertia when Re^{ac} and St change). In order to avoid numerical problems in the regions of void numerical dissipation is applied for particle number densities lower than $2 \cdot 10^7 m^{-3}$, which corresponds to a minimal particle volume fraction of $8.37 \cdot 10^{-11}$. Moreover, only positive values of RUE are kept to avoid unphysical phenomena.

Note that in the Euler-Euler approach, there is no lower limit in terms of numerical resolution. Compared with the gaseous flow, where the Kolmogorov length scale represents the lower limit for the energy transfer, there is no length scale at which it may be considered that the energy is completely dissipated. For solid, non-deformable particles, the particle diameter may be considered as the smallest length scale. On the contrary, for deformable particles or liquid droplets, compressibility and deformation effects make this assumption not valid. This characteristic of the dispersed flow treated with an Euler-Euler approach derives from the equations of conservation themselves. For this reason, the numerical scheme and the resolution of the mesh grid may have an enlarged importance compared to single-phase flows.

– Gaseous phase –

AV sensor	ϵ^2	ϵ^4
no AV	0.00	0.00

– Dispersed phase –

AV sensor	ϵ^2	ϵ^4
CMS-Lite	0.55	0.00

Table 5.6: *Artificial Dissipation parameters for all the simulation performed with AVBP.*

5.2 Gas phase validation

This Section presents a validation of the carrier phase flow. Comparisons between the Euler-Euler (AVBP) and Euler-Lagrange (NTMIX-2Φ) simulations at low and high Reynolds numbers are proposed in terms of mean and root mean squared fluctuations (RMS) fluid velocities as well as turbulent kinetic energy (q_f^2).

Since the simulations are performed taking into account the effect of the carrier flow on the dispersed phase, but not the effect of the particles on the carrier fluid (i.e. one-way coupling) it is not needed to verify the carrier phase flow for every simulation. Moreover, the carrier fluid flow is the same for all inertia (i.e. same Stokes number) if the level of turbulence (i.e. the Reynolds number) is the same. This means that all the simulations of a given case have the same carrier fluid flow whatever the RUM model used. Also, all simulations at low turbulence (LR_St1_#, LR_St3_# and LR_St033_#) share the same carrier fluid flow at the same instant.

Section 5.2.1 presents a validation of the carrier phase flow for the low turbulence cases (LR_St1_#, LR_St3_#, LR_St033_#). Section 5.2.2 presents the results for the high turbulence case (HR_St1_#).

5.2.1 Low turbulence case

This section presents the validation of the carrier fluid flow for cases LR_St1_#, LR_St3_# and LR_St033_#. Mean and RMS velocities in the three directions, along with the turbulent kinetic energy profiles at times corresponding to 5, 40 and $80t_{ref}$ are shown. Instantaneous fields of fluid velocity magnitude are also shown.

Figures 5.4, 5.5 and 5.6 show the profiles of the mean velocity and the product of the fluid density ρ_f and the RMS fluid velocity in the X-, Y- and Z-directions respectively. Note that X-direction is the main direction of the flow. The agreement between AVBP and NTMIX-2Φ is very good for both the mean and the RMS values in all directions. Some discrepancies appear in the profiles of V_g which are due to small differences in the fluid density between AVBP and NTMIX-2Φ. Both codes solve the compressible NS equations, however, they differ in the numerical schemes they use, which may lead to small discrepancies. Nevertheless, the differences remain small and appear only in the Y- and Z- directions, where the order of magnitude of the velocity is much smaller than in the X-direction. This is also the reason why the RMS profiles are shown multiplied by the fluid density. Since the quantity transported in AVBP is the product of the density and the velocity, it has been chosen as the quantity to be shown. However, the mean velocities are shown without taking into account the density in order to show the order of magnitude of this difference. Finally in order to assess the quality of the carrier phase flow, Fig. 5.7 shows the profiles of turbulent kinetic energy at the three times chosen for the analysis. Since the profiles are very similar, it is guaranteed that the fluid flow is almost the same in the simulations performed with AVBP and with NTMIX-2Φ. Thus, the discrepancies that may appear between the simulations performed with the different RUM models are due to the models themselves and not to potential differences in the fluid phase flow.

In order to provide a qualitative comparison, the instantaneous fields of the fluid velocity magnitude are shown in Fig. 5.8 at 5, 40 and $80t_{ref}$. The results of both approaches are very close for the three times.

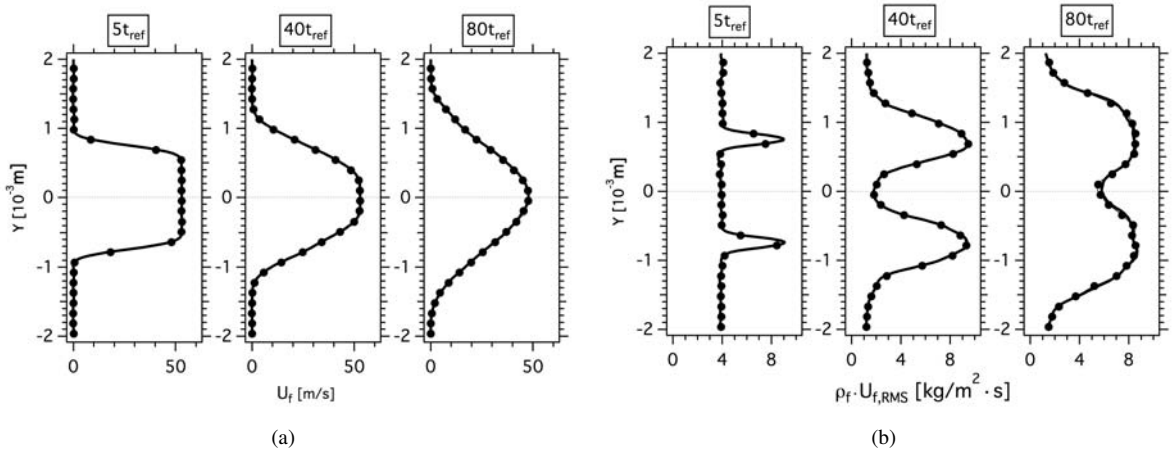

(a) (b)

Figure 5.4: *Comparison of AVBP (—) and NTMIX-2Φ (–•–) carrier phase velocities in X-direction. LR_St1_# case. (a) Mean velocity (U_f) and (b) RMS velocity times the fluid density ($\rho_f U_{f,RMS}$).*

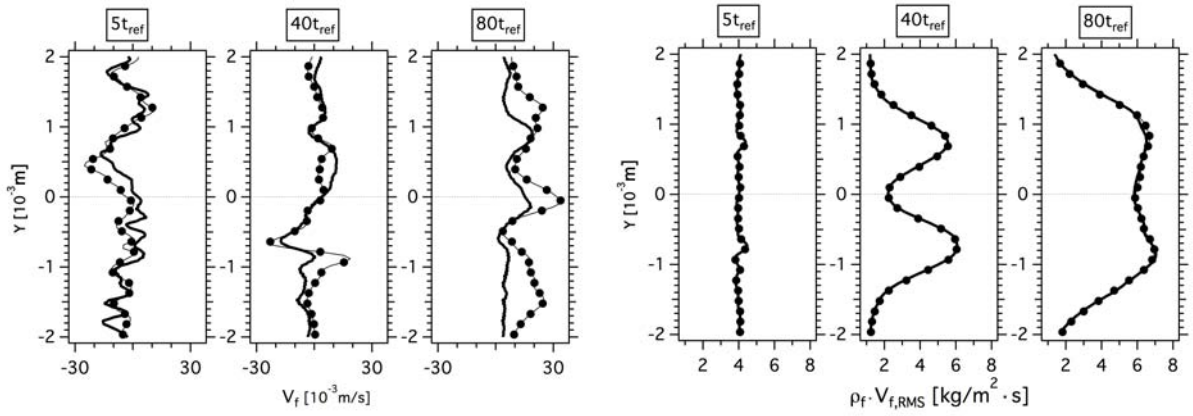

(a) (b)

Figure 5.5: *Comparison of AVBP (—) and NTMIX-2Φ (–•–) carrier phase velocities in Y-direction. LR_St1_# case. (a) Mean velocity (V_f) and (b) RMS velocity times the fluid density ($\rho_f V_{f,RMS}$).*

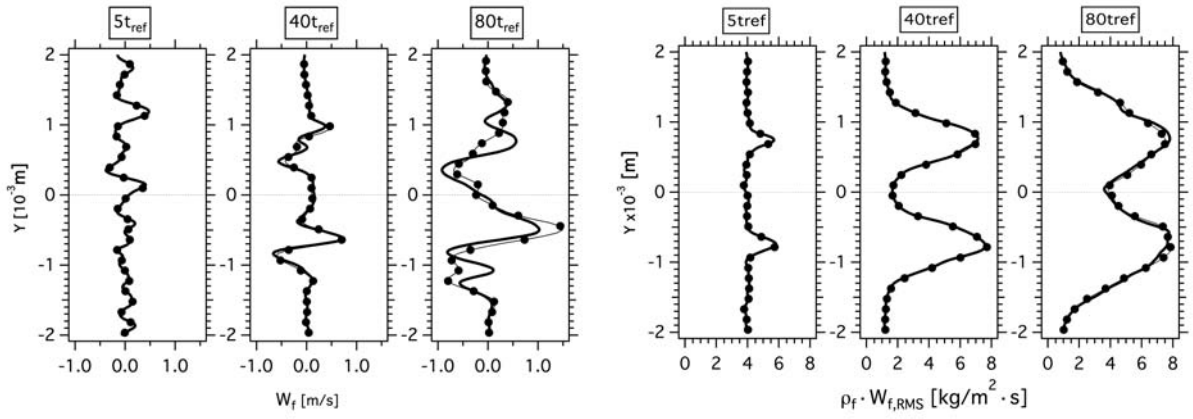

(a) (b)

Figure 5.6: *Comparison of AVBP (—) and NTMIX-2Φ (–•–) carrier phase velocities in Z-direction. LR_St1_# case. (a) Mean velocity (W_f) and (b) RMS velocity times the fluid density ($\rho_f W_{f,RMS}$).*

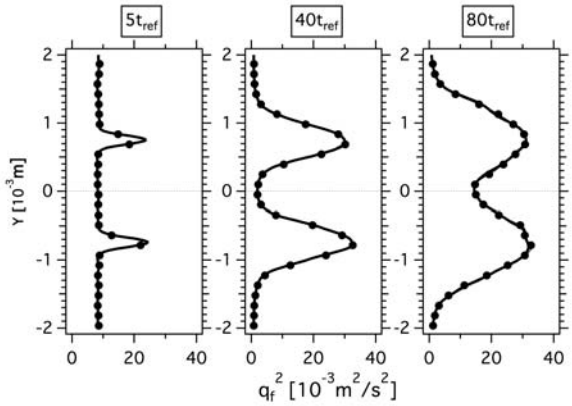

Figure 5.7: *Comparison of AVBP (—) and NTMIX-2Φ (–●–) carrier phase turbulent kinetic energies (q_f^2). LR_St1_# case.*

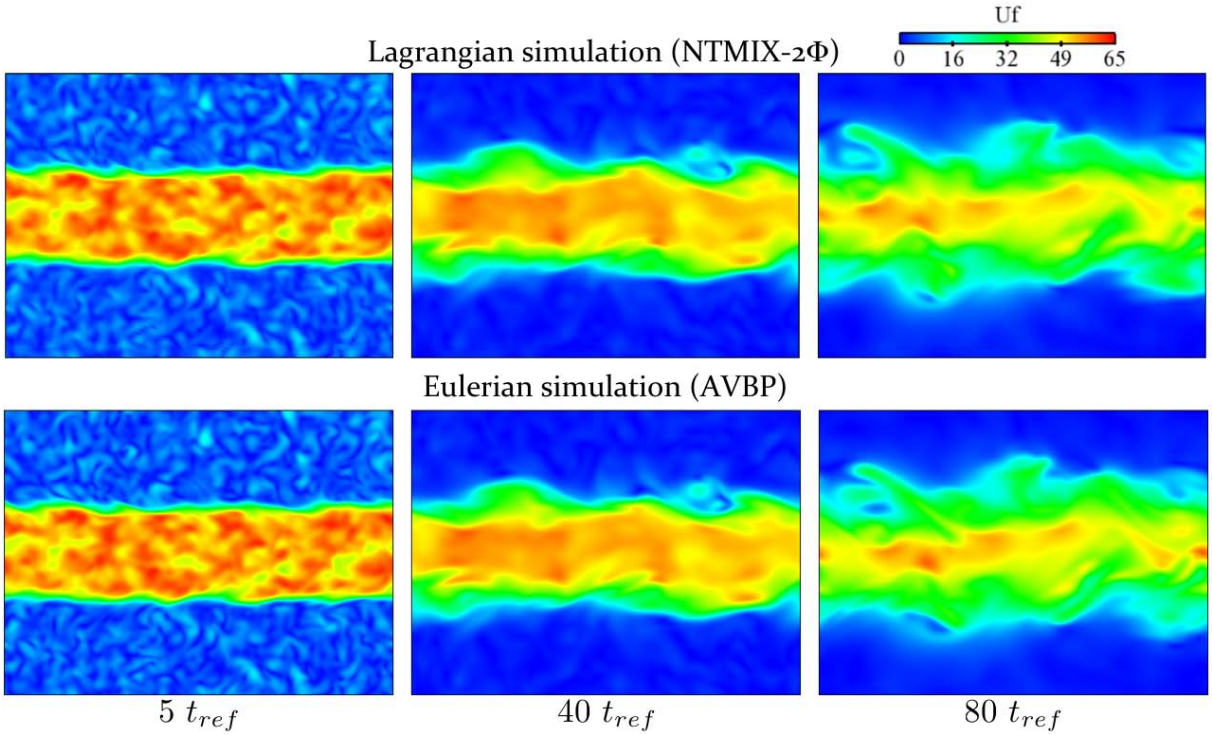

Figure 5.8: *Comparison of instantaneous NTMIX-2Φ and AVBP carrier phase fields ($[m/s]$) at* 5, 40 *and* $80t_{ref}$*. LR_St1_# case.*

5.2.2 High turbulence case

The carrier phase flow is modified with the Reynolds number changes. For this reason, it is necessary to verify that the carrier fluid flow keeps the same for the Lagrangian and the Eulerian simulations also for the HR_St1_# case. Since for the low turbulence cases, the agreement for the carrier phase profiles was very good, a good agreement is also expected in this case. The high turbulence Euler-Lagrnage simulations have been carried out only up to $70t_{ref}$ due to limited computational resources. Comparisons between Euler-Euler and Euler-Lagrange results are therefore shown at that time. Figure 5.9 shows the instantaneous carrier phase velocity magnitude fields for the Euler-Lagrange and the Euler-Euler simulations at $70t_{ref}$. It provides a qualitative assessment of the gaseous phase simulations of both codes. The results are very similar although the differences between the two simulations are more visible than in the low turbulence case (Fig. 5.8). In order to provide quantitative results, the profiles of mean and RMS velocities in the three spatial directions are compared at $70t_{ref}$. The profile of turbulent kinetic energy is also displayed on Fig. B.4. The same profiles corresponding to 5 and $40t_{ref}$ can be found in Appendix B. The agreement, as expected, is very good. The same discrepancies in the mean Y- and Z-velocity are present in this case due to differences in the fluid density profiles. The agreement for the RMS velocity and the turbulent kinetic energy profiles is again very good.

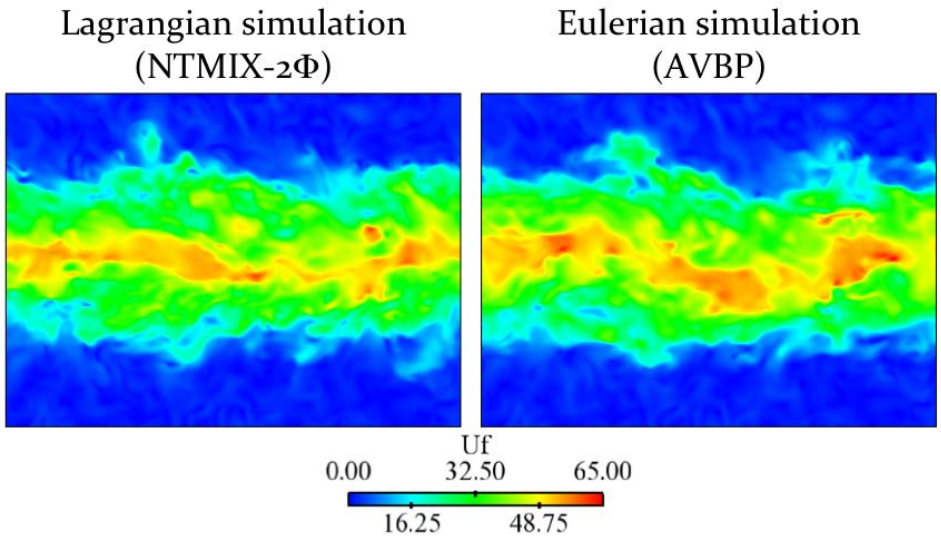

Figure 5.9: *Comparison of instantaneous NTMIX-2Φ and AVBP carrier phase fields* ($[m/s]$) *at* $70t_{ref}$. *HR_St1_# case.*

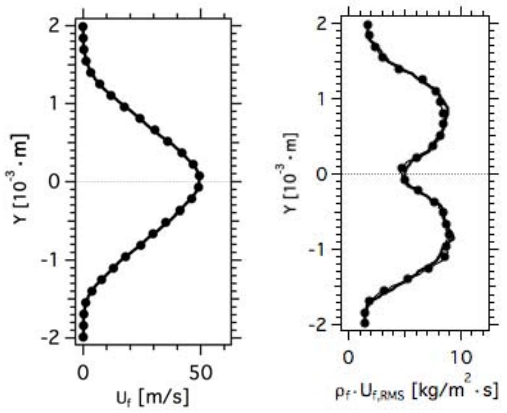

(a) (b)

Figure 5.10: *Comparison of AVBP (—) and NTMIX-2Φ (–•–) carrier phase velocities in X-direction. HR_St1_# case. (a) Mean velocity (U_f) and (b) RMS velocity times the fluid density ($\rho_f U_{f,RMS}$) at* $70t_{ref}$.

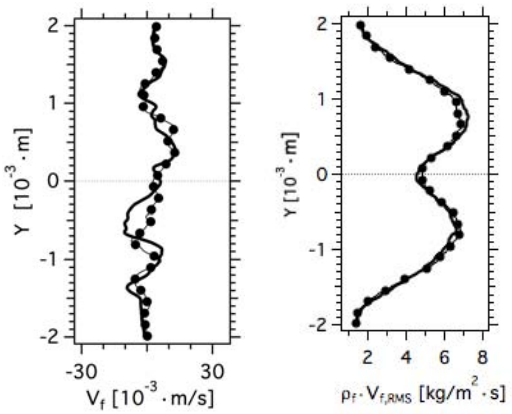

(a) (b)

Figure 5.11: *Comparison of AVBP (—) and NTMIX-2Φ (–•–) carrier phase velocities in Y-direction. HR_St1_# case. (a) Mean velocity (U_f) and (b) RMS velocity times the fluid density ($\rho_f U_{f,RMS}$) at* $70t_{ref}$.

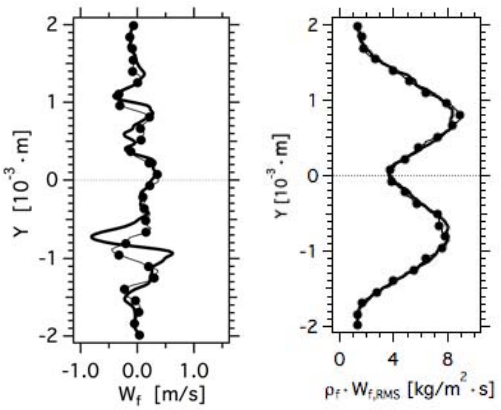

(a) (b)

Figure 5.12: *Comparison of AVBP (—) and NTMIX-2Φ (–●–) carrier phase velocities in Z-direction. HR_St1_# case. (a) Mean velocity (U_f) and (b) RMS velocity times the fluid density ($\rho_f U_{f,RMS}$) at* $70t_{ref}$.

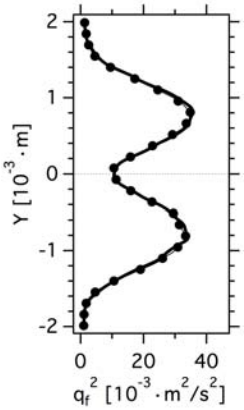

Figure 5.13: *Comparison of AVBP (—) and NTMIX-2Φ (–●–) carrier phase turbulent kinetic energy (q_f^2) at* $70t_{ref}$. *HR_St1_# case.*

5.3 Dispersed phase validation. Case LR_St1_#

The simulations of case LR_St1_# with the six models proposed in Chapter 4 and their corrected versions have been performed with AVBP. This case corresponds to a low turbulence, mean inertia simulation. The characteristic particle relaxation time is $\tau_{fp}^F \sim 13 t_{ref}$.

The VISCO model crashed after few iterations. Indeed, the particle RUE is considerably overestimated using VISCO for this range of particle inertia. Particle RUE has a diffusion effect in the fields of mesoscopic particle number density and particle volume fraction, as well as in the particle velocity fields. VISCO producing too much RUE from the beginning of the calculation, it leads to an excessive diffusion of the particles towards the periphery of the jet, creating empty zones which can not be handled numerically by the code. This behavior was somehow already pointed out by the *a priori* analysis of Masi (2010): VISCO overpredicted the shear-component of the deviatoric RUM stress tensor ($\delta\breve{R}^*_{p,12}$) and underpredicted the diagonal components ($\delta\breve{R}^*_{p,11}$, $\delta\breve{R}^*_{p,22}$ and $\delta\breve{R}^*_{p,33}$). In fact, the two models using $\breve{\tau}_p$, the characteristic particle relaxation time, as timescale (VISCO and QUAD) showed the same behavior, QUAD even overpredicting all the components of the tensor. Confirming the *a priori* analysis, the simulations with AVBP and QUAD model have not been possible either, since this model crashed even before VISCO does. In both cases a huge overproduction of particle RUE, makes the simulation unstable. For this reason, no results are displayed concerning these two models for LR_St1_# case.

Section 5.3.1 presents the statistics of the main low-order moments and RMS mean particle number density and particle velocity for three times: at the beginning of the simulation ($5t_{ref}$, after approx. $0.38\tau_{fp}^F$), at the middle ($40t_{ref}$, after $3.07\tau_{fp}^F$) and at the end of the simulation ($80t_{ref}$, after $6.15\tau_{fp}^F$). Results obtained in a particle-laden stationary HIT configuration (Février *et al.* (2005)) showed that at least three particle relaxation times are required to obtain statistics not influenced by the initial condition. This means that results at $5t_{ref}$ are not discriminatory to evaluate the performance of the models, and that results after $40t_{ref}$ must be taken into account to assess the validity of the models in this case. The results at $80t_{ref}$ allow to confirm the conclusions drawn at $40t_{ref}$. Instantaneous fields of particle number density and particle velocity at the end of the simulation are also displayed. Section 5.3.2 presents the statistics of the main high-order moments, including the particle RUE and the total particle agitation as well as the mean profiles of the tensor components and RUM production rates. Instantaneous fields of RUE at the end of the simulation are also shown. Complementary data can be found in Appendix C.

5.3.1 Low order moments

Low order moments such as the particle number density or the particle velocity are important since they define the main characteristics of a given dispersed phase flow field. In the presence of turbulence, the root-mean-square (RMS) values are of importance too, since they measure the fluctuations in the flow. These are in fact the variables of interest in most industrial applications. However, in this configuration, the particle preferential concentration (Squires & Eaton (1991*a*)) is an important parameter too. Indeed, in turbulent flows, the particles tend to accumulate in low-vorticity and high-shear regions, creating both high concentration and empty zones close to each other. This produces very steep particle number density gradients in the flow field similarly to a highly compressible gaseous flow. This behavior is strongly related to the particle number density and the particle velocity divergency fields. The preferential concentration is measured by the so-called “segregation" parameter, noted seg:

$$\text{seg} = \frac{\langle \breve{n}_p^2 \rangle}{\langle \breve{n}_p \rangle^2} \, . \tag{5.17}$$

Figure 5.14 shows the statistics of the particle number density for three different times along the simulation. The values are normalized by the initial particle number density at the center of the slab. The results at $5t_{ref}$ are presented to show that when the simulation is close to the begining, the results are very influenced by the initial condition. Indeed, Figs. 5.14(a), 5.15(a), 5.16(a), 5.17(a) and 5.18(a) show that all models give the same results. All models perform equally in the prediction of the particle number density and the particle velocity at 5, 40 and $80t_{ref}$, except AXISY and its corrected version AXISY-C. Figure 5.14(b) shows that both models predict peaks at the borders of the plateau located at the center of the slab. Note that the peaks are stronger for AXISY than for AXISY-C. At $80t_{ref}$ (Fig. 5.14(c)), the two peaks have disappeared, but both models overestimate the maximum of $\langle \breve{n}_p \rangle$ at the center of the slab. Regarding the mean particle velocity (Fig. 5.15), all models give very close results. Figure 5.15(a) underlines a slight inaccuracy of the projection algorithm. Indeed, the profiles obtained by projection from NTMIX-2Φ deviate from the hyperbolic tangent profile at the borders of the jet. This is due to the steepness of the velocity gradient or to a lack of particles in this region in the Lagrangian sumulations, which introduces errors when projected onto the Eulerian grid.

The profiles of particle RMS number density (Fig. 5.16) and particle RMS velocity (Fig. 5.17) produced by the models are also very similar. However, AXISY predicts a steeper gradient at the periphery of the slab. AXISY-C and QUAD-MOD give the same maximum level of RMS number density but both models predict lower levels towards the periphery producing a thinner slab. QUAD-MOD underestimates the maximum RMS particle velocity and AXISY behaves even worse. This behavior is already visible at $40t_{ref}$ and remains at $80t_{ref}$.

Figure 5.18 shows the profiles of particle segregation at 5, 40 and $80t_{ref}$. AVBP is not able to capture the initial shock. This is due to the influence of numerics which are not capable of handling such highly compressible dispersed phase flows.

A qualitative analysis of the instantaneous fields of the particle number density and particle velocity (Figs. 5.19 and 5.20) is not sufficiently discriminatory. Indeed, from the instantaneous fields of these variables, the noRUM model arises as the model who performs the best, but Section 5.3.2 will explain the reasons for this behavior. Indeed, the noRUM model does not take into account the Random Unocrrelated Motion and thus, the balance between the mesoscopic energy, the RUE and the total particle energie is not correct. Taking this into account, only AXISY shows a clear weakness if compared to the rest of the models.

In conclusion, the results concerning the low order moments do not allow to differenciate between the models, and are definitely not sufficient to discard a model in front of the others. Analysing the statistics of the higher order moments is therefore necessary.

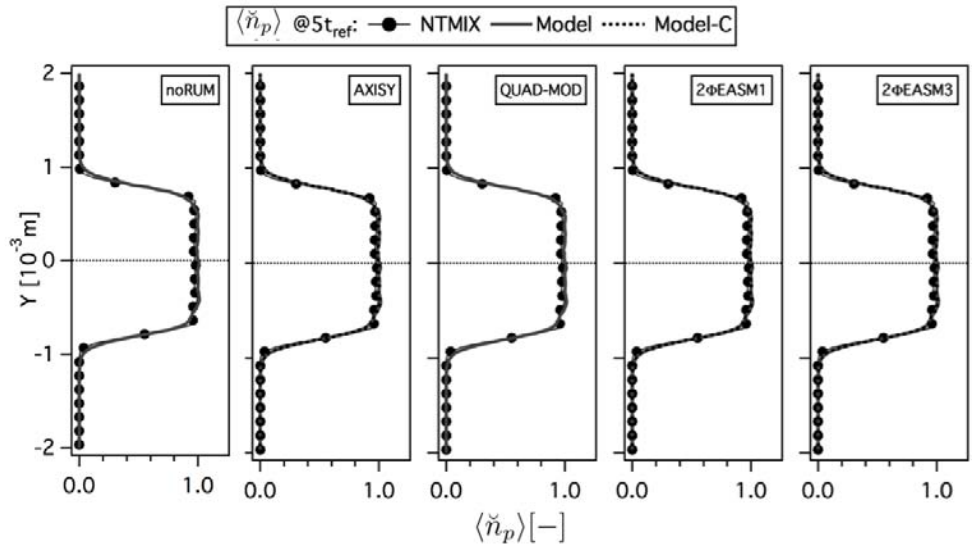

(a)

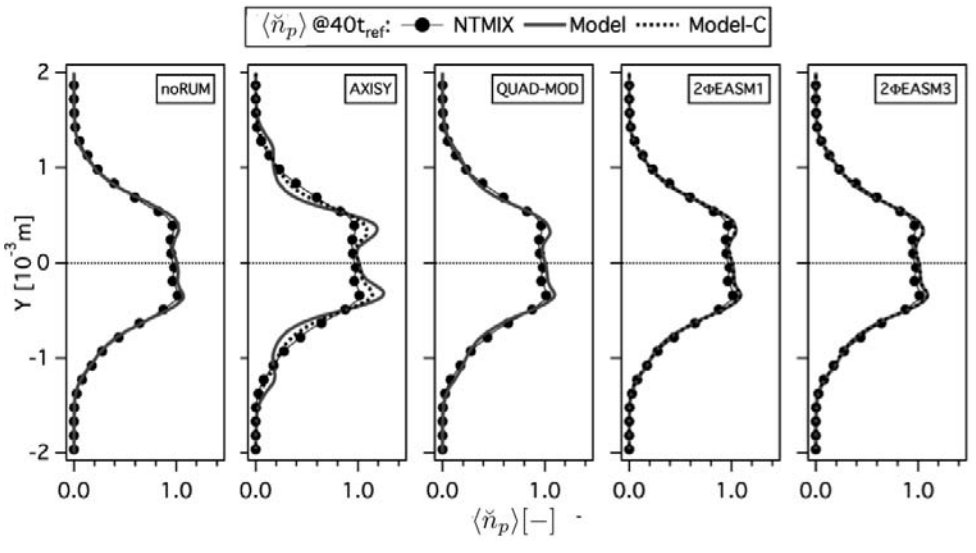

(b)

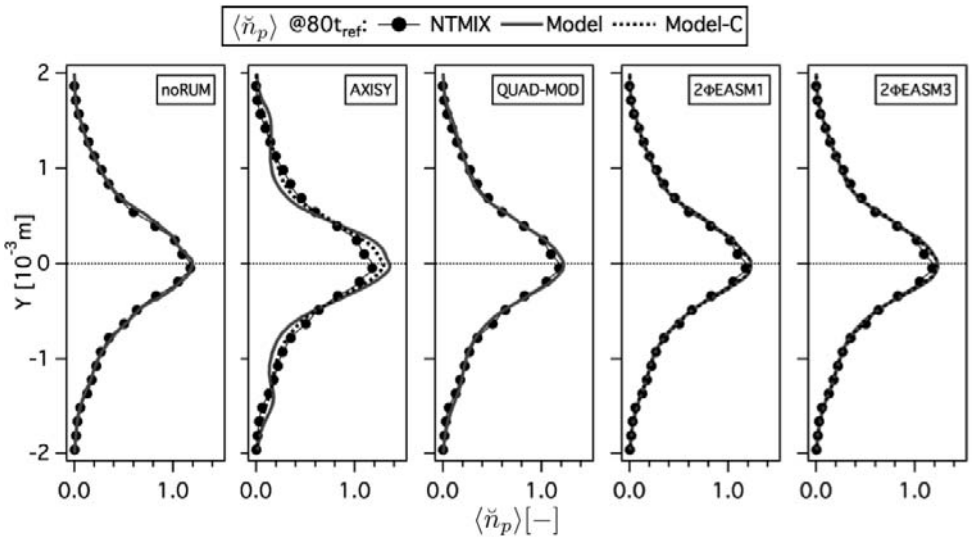

(c)

Figure 5.14: *Comparison of Eulerian and Lagrangian mean particle number density ($< \check{n}_p >$) at 5, 40 and 80t_{ref}. Normalized by the initial particle number density at the center of the slab. LR_St1_# case.*

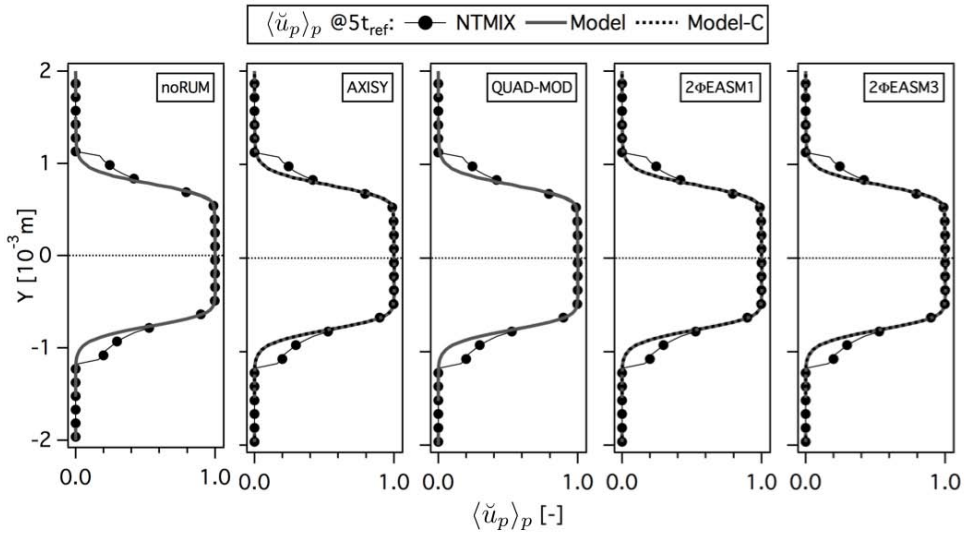

(a)

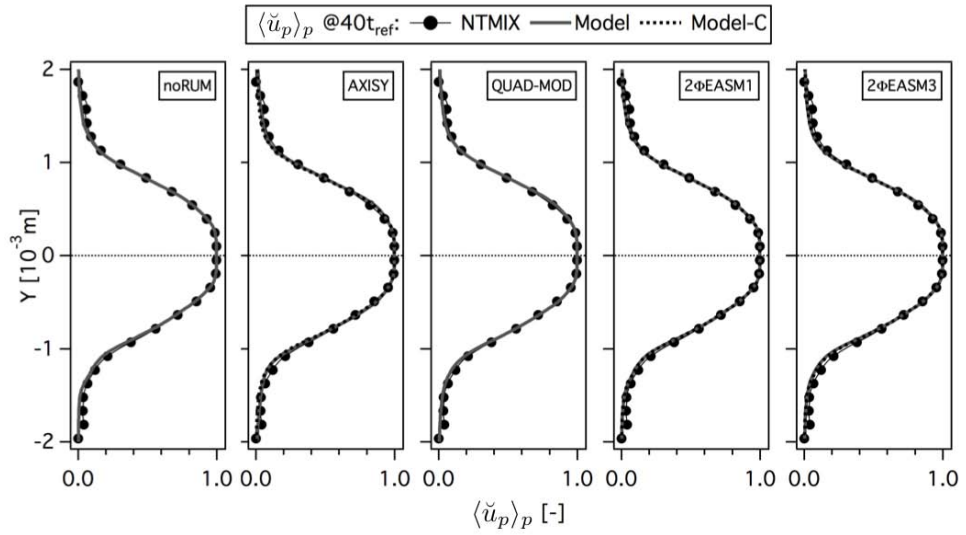

(b)

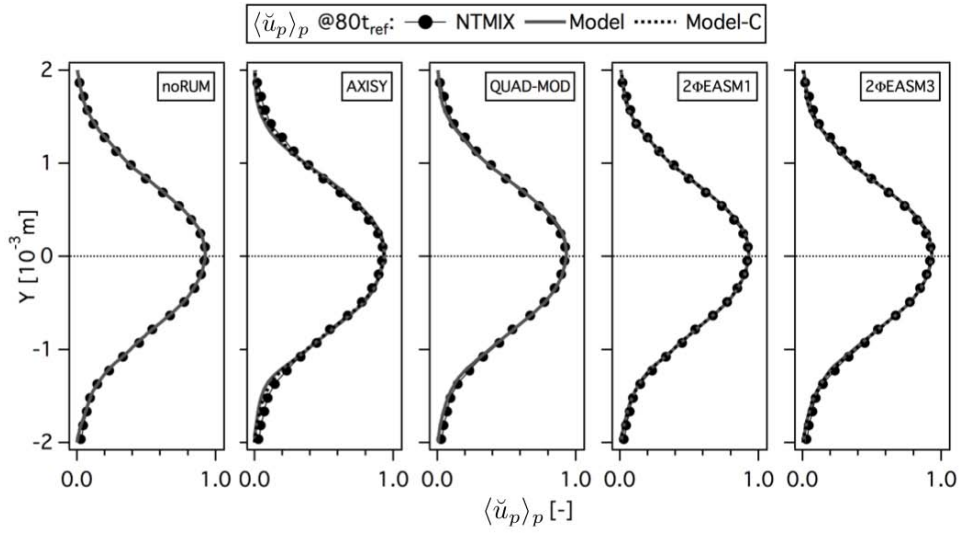

(c)

Figure 5.15: *Comparison of Eulerian and Lagrangian mean particle velocity in X-direction ($< \breve{u}_p >_p$) at 5, 40 and 80t_{ref}. Normalized by the initial particle velocity in X-direction at the center of the slab. LR_St1_# case.*

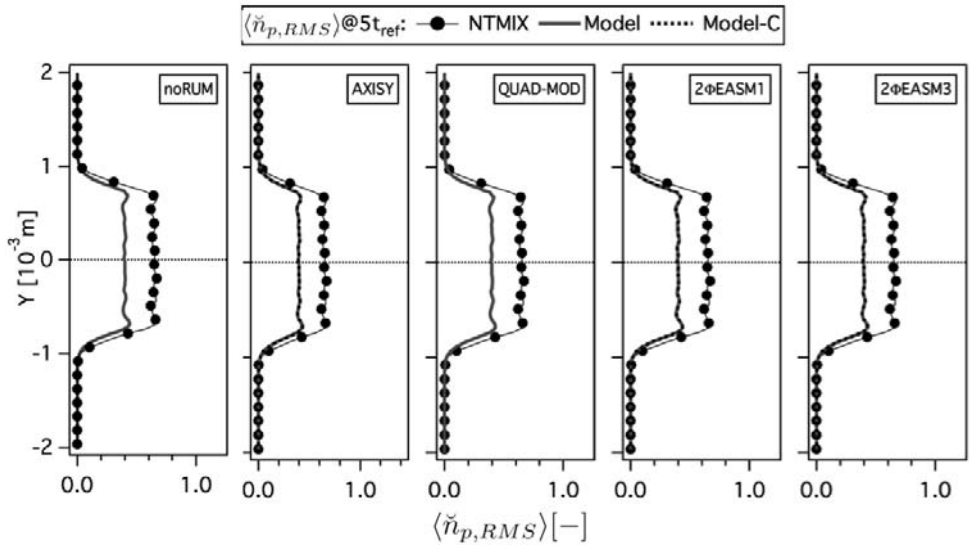

(a)

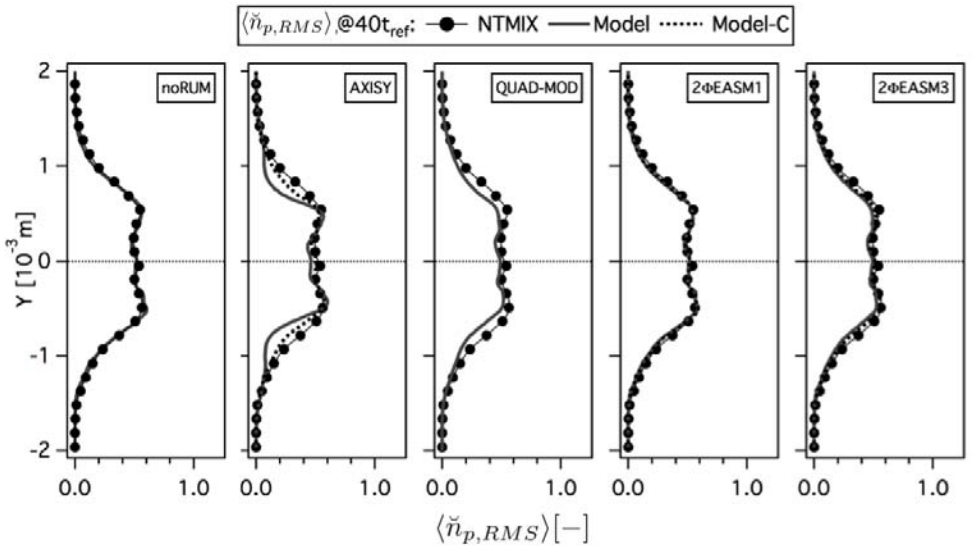

(b)

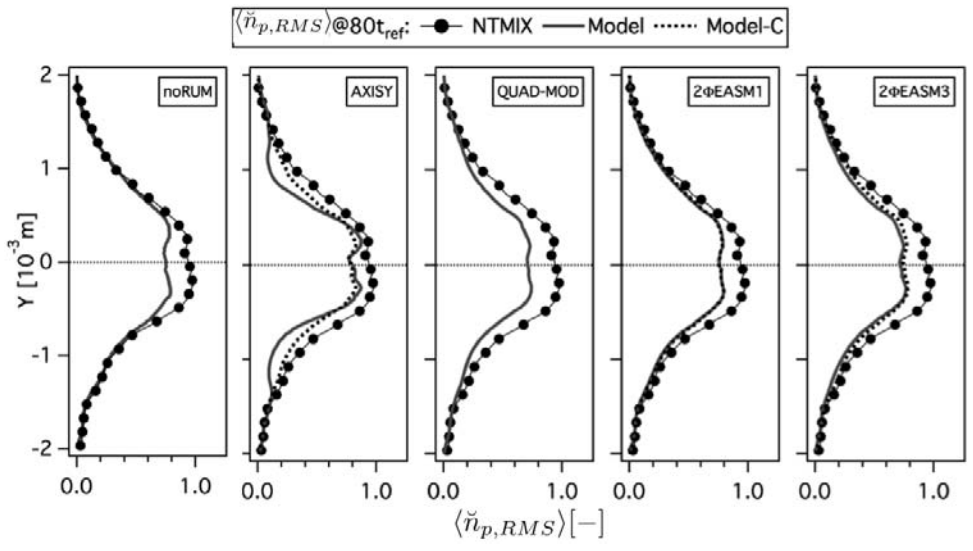

(c)

Figure 5.16: *Comparison of Eulerian and Lagrangian RMS particle number density ($< \breve{n}_{p,RMS} >$) at 5, 40 and 80t_{ref}. Normalized by the initial particle number density at the center of the slab. LR_St1_# case.*

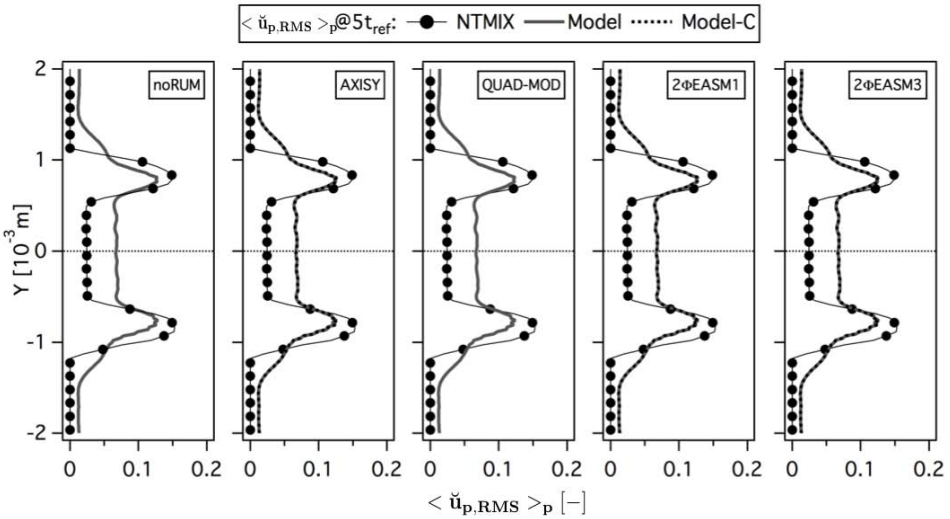

(a)

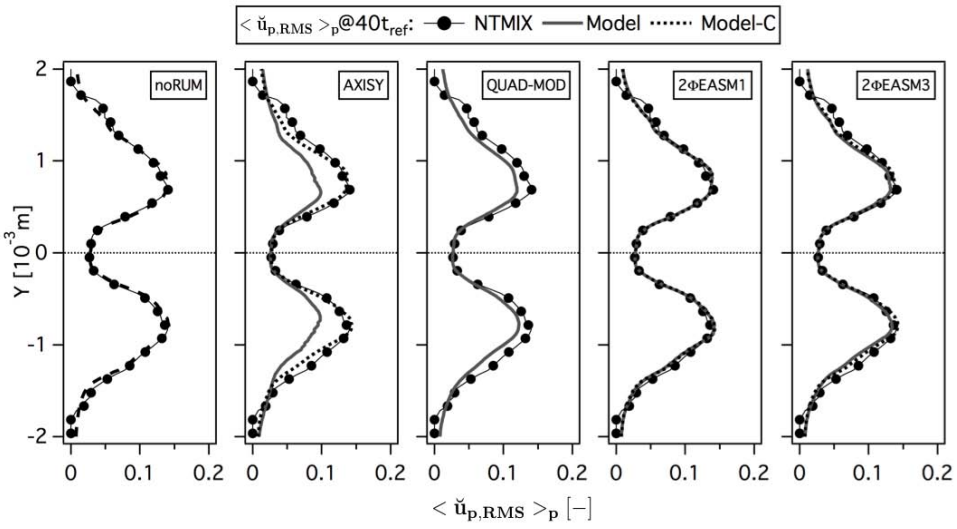

(b)

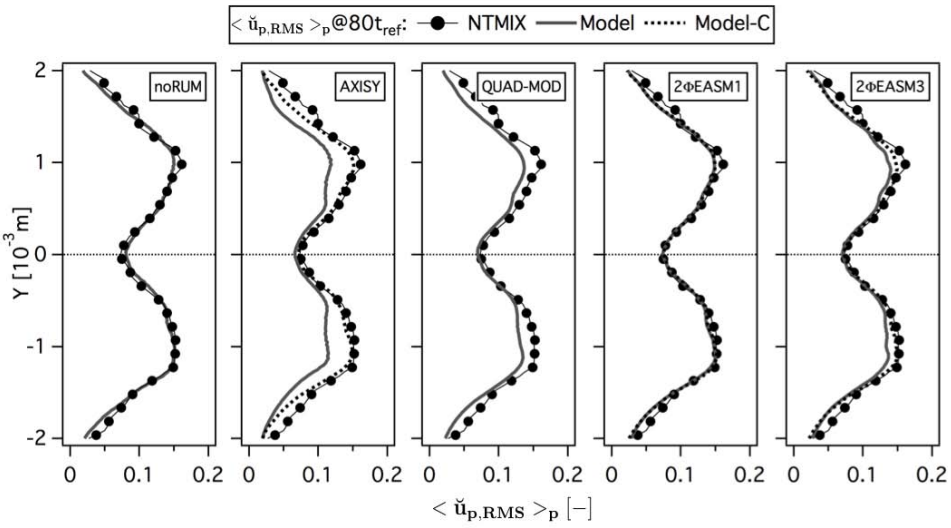

(c)

Figure 5.17: *Comparison of Eulerian and Lagrangian RMS particle velocity in X-direction ($< \breve{u}_{p,RMS} >_p$) at 5, 40 and 80t_{ref}. Normalized by the initial particle velocity in X-direction at the center of the slab. LR_St1_# case.*

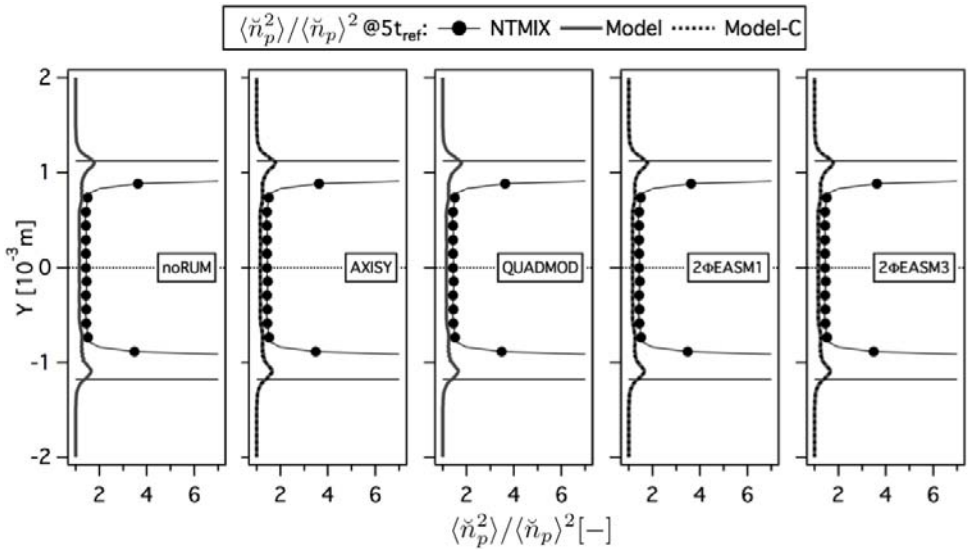

(a)

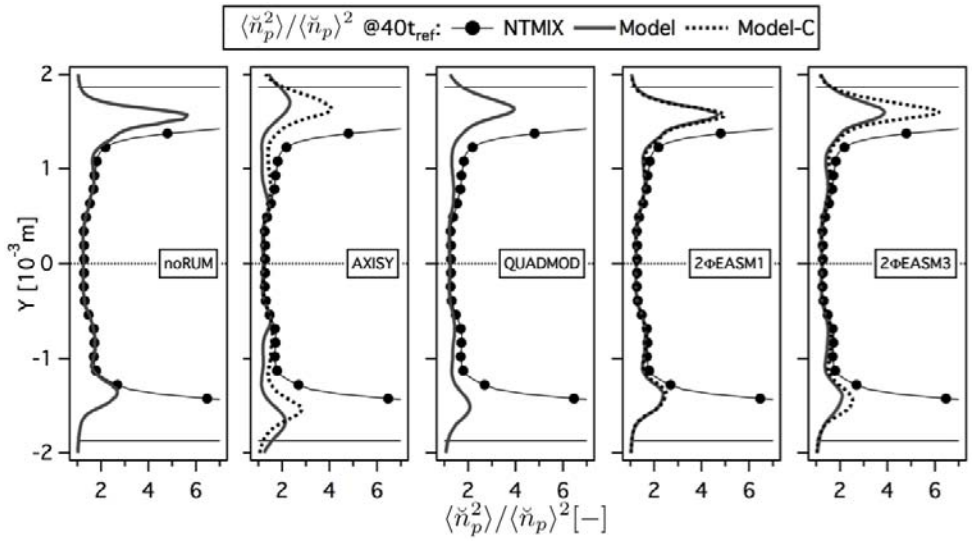

(b)

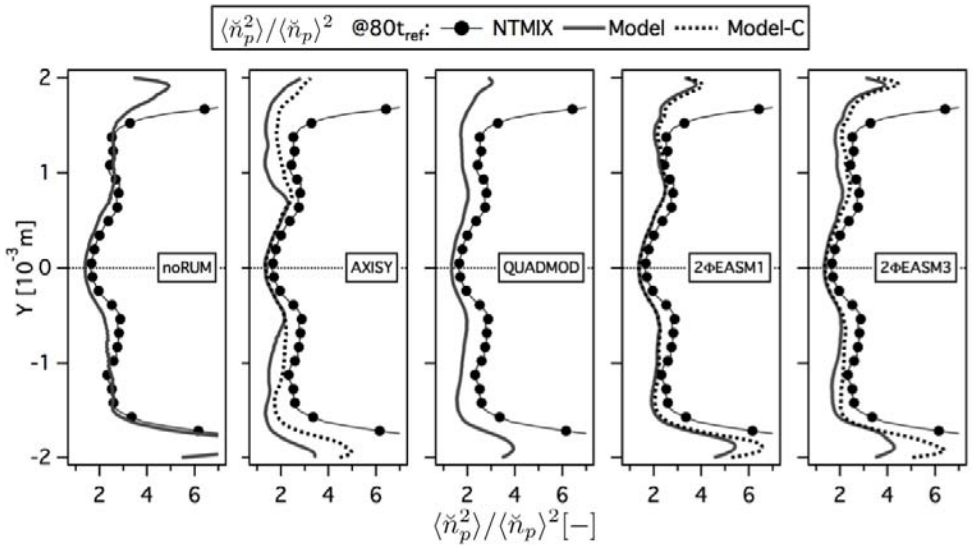

(c)

Figure 5.18: *Comparison of Eulerian and Lagrangian RMS particle segregation ($< \breve{n}_p^2 > / < \breve{n}_p >^2$) at 5, 40 and 80$t_{ref}$. LR_St1_# case.*

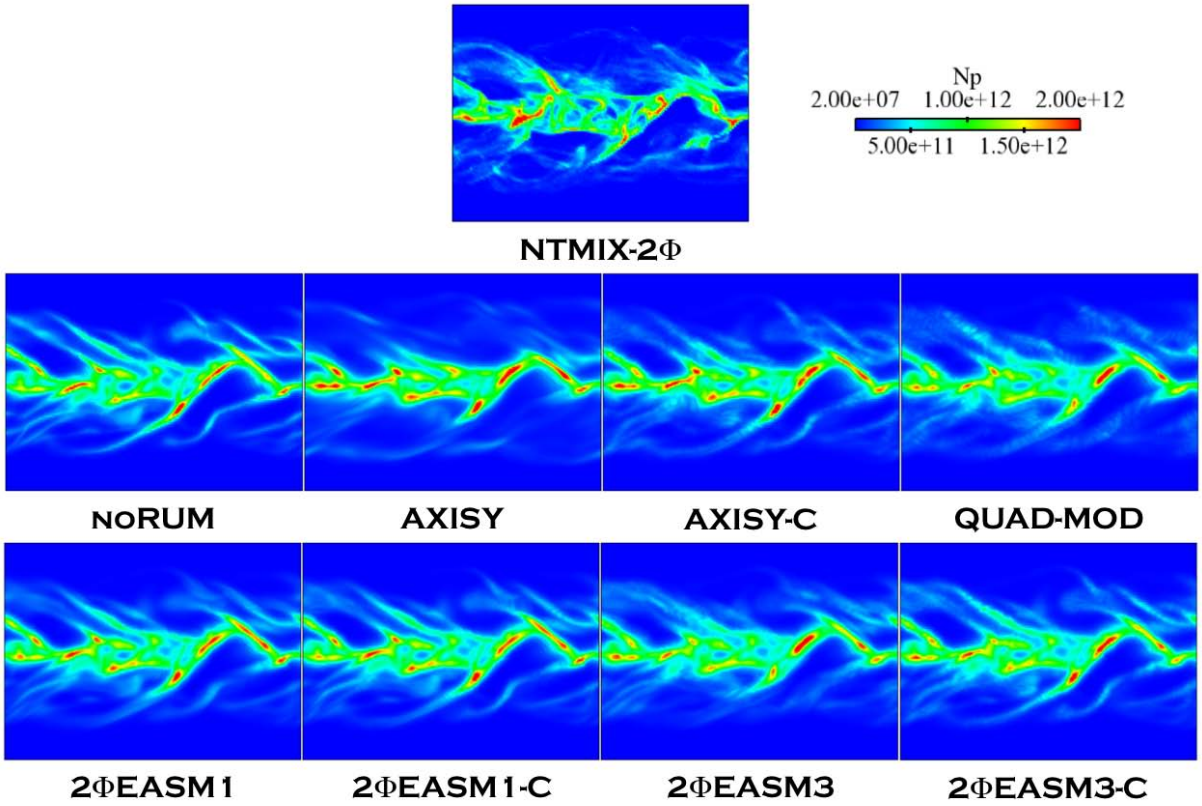

Figure 5.19: *Comparison of Lagrangian (NTMIX-2Φ) and Eulerian particle number density (N_p) at 80t_{ref}. LR_St1_# case.*

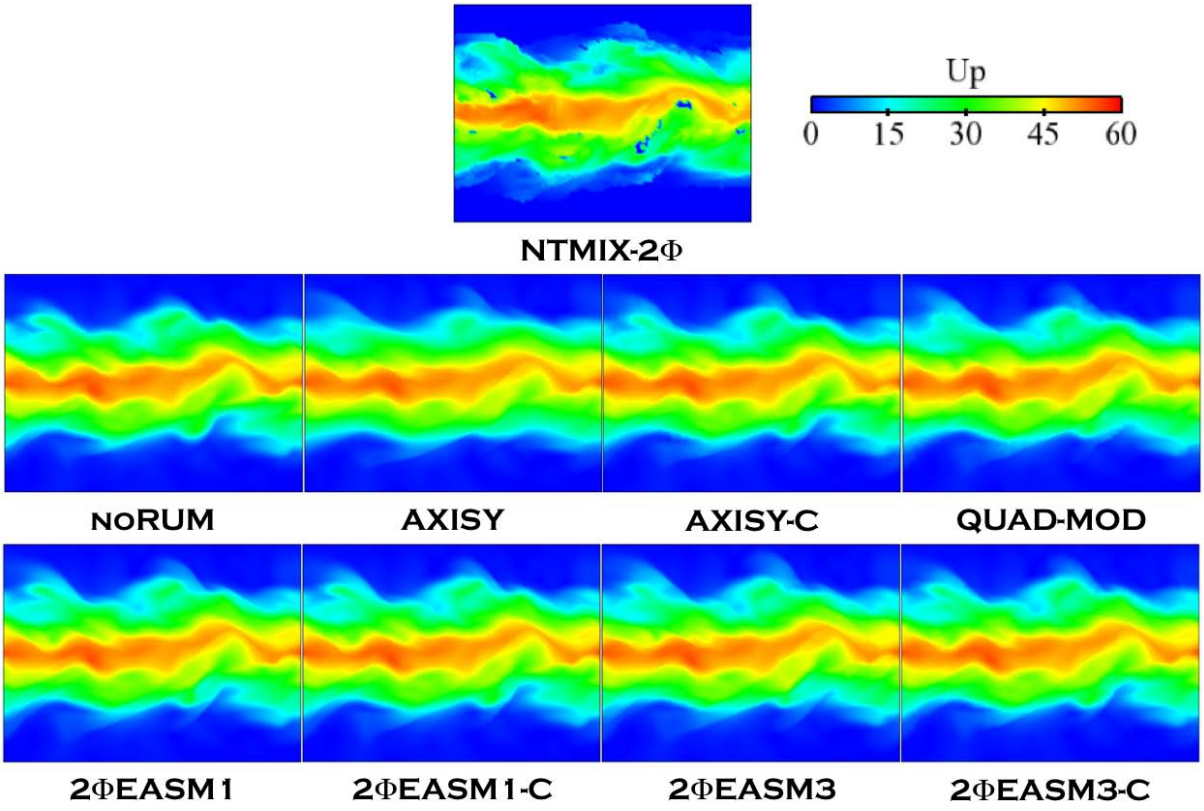

Figure 5.20: *Comparison of Lagrangian (NTMIX-2Φ) and Eulerian particle velocity magnitude (U_p) at 80t_{ref}. LR_St1_# case.*

5.3.2 High order moments

The analysis of the higher order moments such as the RUE ($\delta\breve{\theta}_p$) and mesoscopic energy ($\breve{q}_p^2$) energies, is expected to enable to discriminate which models produce better *a posteriori* results in mean-sheared configuration. In industrial applications, the only high-order moment really taken into account is the total energy or total particle agitation ($q_p^2 = \breve{q}_p^2 + \delta q_p^2$). The importance of the Random Uncorrelated Motion is due to the particle trajectory crossing (PTC, Falkovich *et al.* (2002)). Indeed, the prediction of the RUE is crucial in applications (industrial or not) where particle collision and/or coalescence are taken into account (such as fluidized beds or non-diluted regimes, i.e. injector-close zones in sprays). If the RUE is not well predicted, the dispersed phase will not have enough energy for collisions or coalescence. For example, if $\delta\breve{\theta}_p$ is overestimated, it may lead to a relaminarization of the dispersed phase flow (Riber (2007)). Masi (2010) performed an *a priori* analysis of the particle-laden temporal turbulent planar-jet studied here taking into account the particle collisions. Masi rewrote the models presented in Chapter 4 to the case of a colliding dispersed phase in diluted regime (one-way coupling with the gas phase). However, as in AVBP the possibility of taking into account collisions or coalescence is not available yet, these phenomena have not been studied here. Nevertheless, collisions may be taken into account in AVBP with minor modifications along with the implementation of the corresponding RUM models.

Figure 5.21 shows the predicted mean RUE profiles at 5, 40 and $80t_{ref}$. While AXISY overestimates the particle RUE, 2ΦEASM1 underestimates it. QUAD-MOD, 2ΦEASM3 and AXISY-C provide correct levels of RUE. However, QUAD-MOD and 2ΦEASM3 are able to recover the good profile at $40t_{ref}$ while AXISY-C underestimates the RUE level at $40t_{ref}$ and predicts a correct value at $80t_{ref}$. Figure 5.22 shows the mesoscopic energy $\breve{q}_p^2$ and the total energy $q_p^2 = \breve{q}_p^2 + \delta q_p^2$ for the three simulation times. The main conclusions obtained comparing the statistics of δq_p^2, $\breve{q}_p^2$ and q_p^2 are:

1. The main contribution to the total agitation q_p^2 comes from the mesoscopic motion (i.e. from $\breve{q}_p^2$), while the RUM has a limited impact for such particle inertia.

2. The models that overestimate the particle RUE (e.g. AXISY), predict a lower value of the mesoscopic energy. In the same way, the models that underestimate the RUM energy (e.g. 2ΦEASM1) produce higher values of $\breve{q}_p^2$ than the Lagrangian reference. In all cases, the final energy budget gives the correct amount of total agitation (q_p^2).

The analysis of the high-order models is completed with the statistics of the productions of RUE by shear and by compression. The production (Fig. 5.23) is defined as:

$$P_{RUM}^{Shear} = -\delta\breve{R}_{p,ij}^{*}\frac{\partial u_i}{\partial x_j}. \tag{5.18}$$

The production by compression (Fig. 5.24) depends on the divergence of the particle velocity and reads:

$$P_{RUM}^{Compression} = -\frac{2}{3}\delta\breve{\theta}_p\left[\frac{\partial u_i}{\partial x_i}\right] . \tag{5.19}$$

QUAD-MOD and 2ΦEASM3 give the best predictions of P_{RUM}^{Shear}. However, the profile of $P_{RUM}^{Compression}$ produced by 2ΦEASM3 is closer to the reference than that of QUAD-MOD. AXISY greatly overestimates the production by shear. As well, the production by compression is no longer a production term but a dissipation term when using this model. A test performed without taking into account the production by compression term (Eq. (5.19)) in the RUE transport equation using the AXISY model has shown that the overestimation of RUE was much larger neglecting this term, confirming the dissipative nature of $P_{RUM}^{Compression}$ in AXISY model. Finally for all models, the shear term is one order of magnitude larger than the compression term.

The main components of the deviatoric RUM stress tensor are also shown (Figs. 5.25 - 5.28). The diagonal components ($\delta\breve{R}^*_{p,11}$, $\delta\breve{R}^*_{p,22}$ and $\delta\breve{R}^*_{p,33}$) are well predicted by QUAD-MOD and 2ΦEASM3 models, greatly underpredicted by AXISY-C, 2ΦEASM1 and 2ΦEASM1-C models and slightly underpredicted by AXISY and 2ΦEASM3-C models. In fact, the *a priori* analysis showed that the diagonal components have a limited impact in the prediction of the mean RUE compared to the components out of the diagonal. $\delta\breve{R}^*_{p,12}$ is shown in Fig. 5.28 for all the models. QUAD-MOD and 2ΦEASM3 profiles agree well with the Lagrangian reference, AXISY-C produces as well good results, which is coherent with the RUE predictions of this three models. The good agreement in the shear component for AXISY-C helps to overcome the small underestimation of the diagonal components. On the contrary, AXISY greatly overestimates this component, which has a direct impact on P^{Shear}_{RUM} terms and creates large amounts of RUE (Fig. 5.21). Regarding 2ΦEASM1 models (with and without correction), both models underestimate all components of the deviatoric RUM stress tensor, and thus underestimate the RUE as well. In fact, the correction seems to have a more limited impact on this model than predicted by *a priori* analysis. In the case of the 2ΦEASM3-C model, the *a priori* analysis showed that the correction improved the predictions of the deviatoric tensor components (and thus the productions and the RUE). In the *a posteriori* simulations, the correction has the opposite effect: it gives worse agreement.

A qualitative comparison of the model predictions for RUE is shown in Fig. 5.29. It shows the instantaneous fields of RUE at $80t_{ref}$ (5 and $40t_{ref}$ fields can be found in Appendix C). All models capture the zones where the RUE must be located referencing to the Lagrangian simulations. However, AXISY gives too high levels and the structures overlap giving two continuous bands located at the limits of the slab. The rest of the models are able to correctly reproduce the structures. 2ΦEASM1 and 2ΦEASM1-C show again very similar results but the predicted level of RUE is smaller than the Lagrangian reference, as for 2ΦEASM3-C and AXISY models. QUAD-MOD and 2ΦEASM3 give the best predictions for both the location of the structures and the level of RUE.

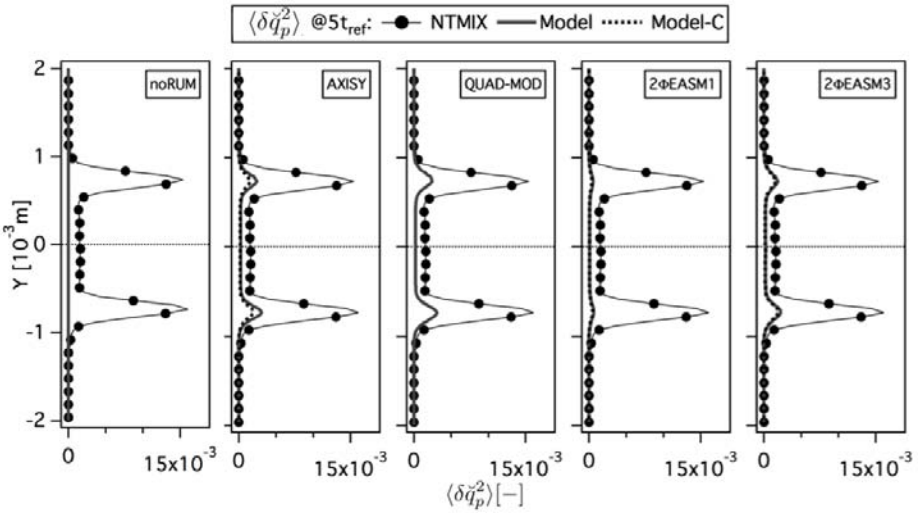

(a)

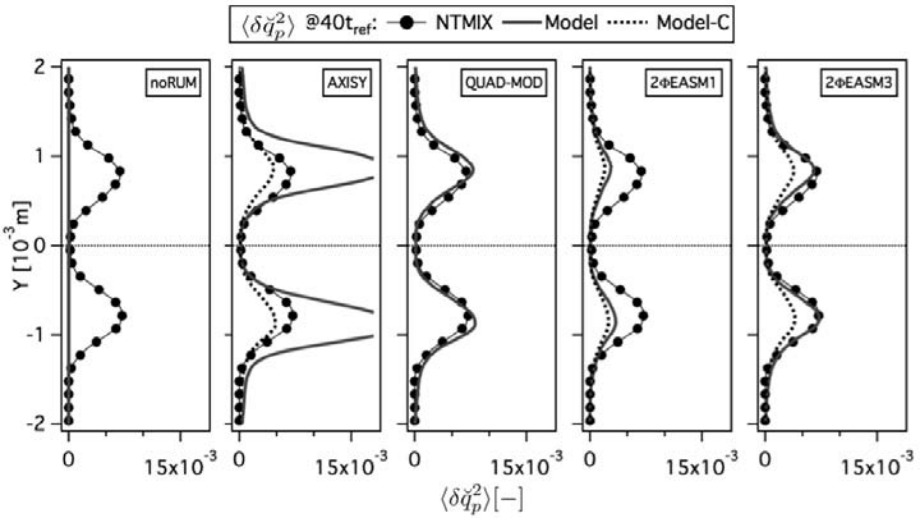

(b)

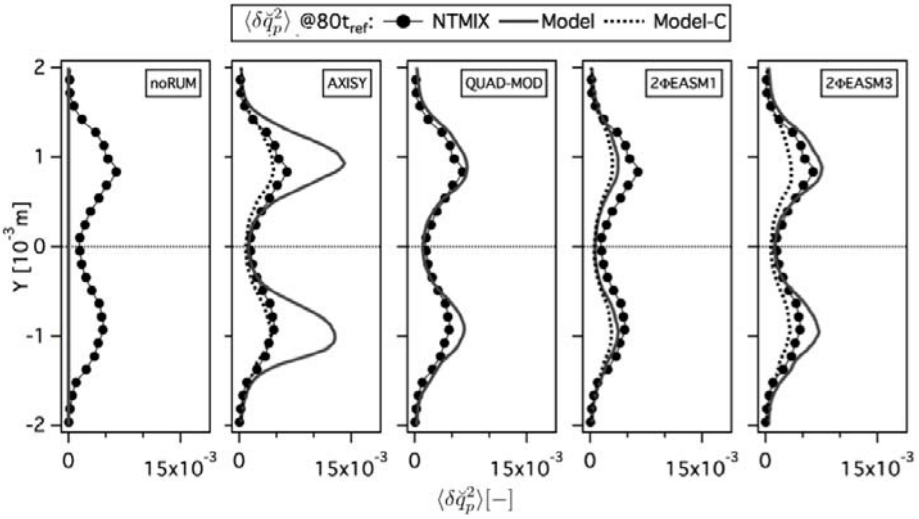

(c)

Figure 5.21: *Comparison of Eulerian and Lagrangian mean Random Uncorrelated Energy ($< \delta\breve{\theta}_p >_p$) at 5, 40 and 80$t_{ref}$. Normalized by the square of the initial particle velocity in X-direction at the center of the slab. LR_St1_# case.*

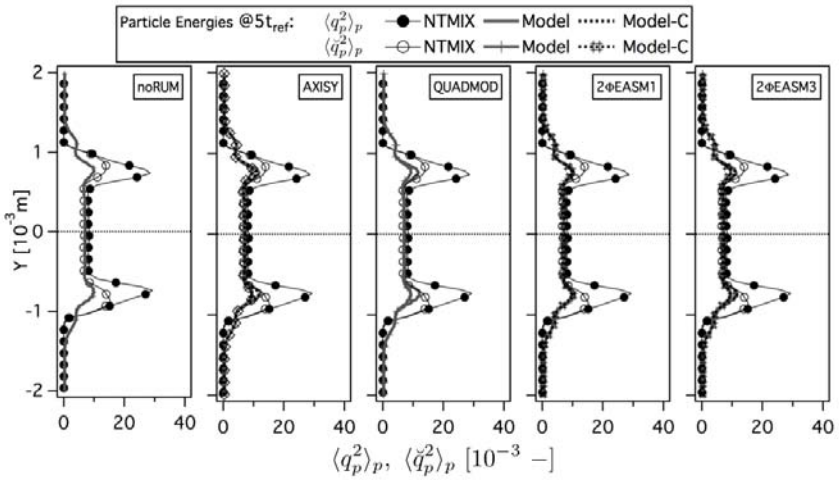

(a)

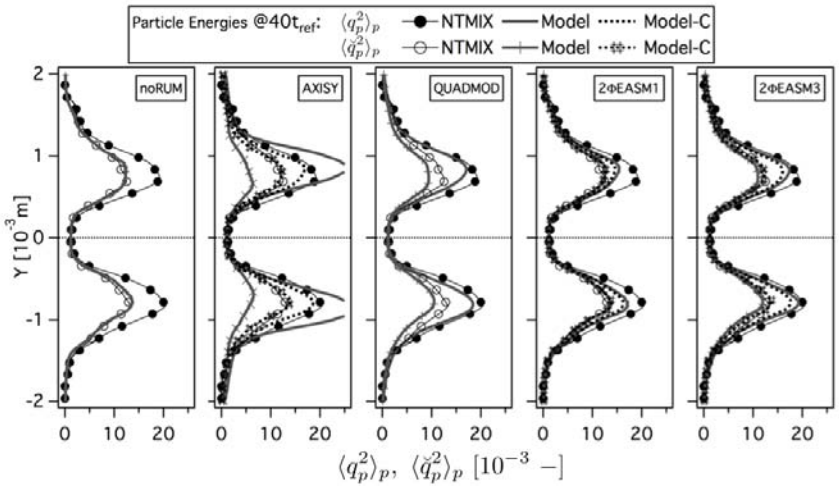

(b)

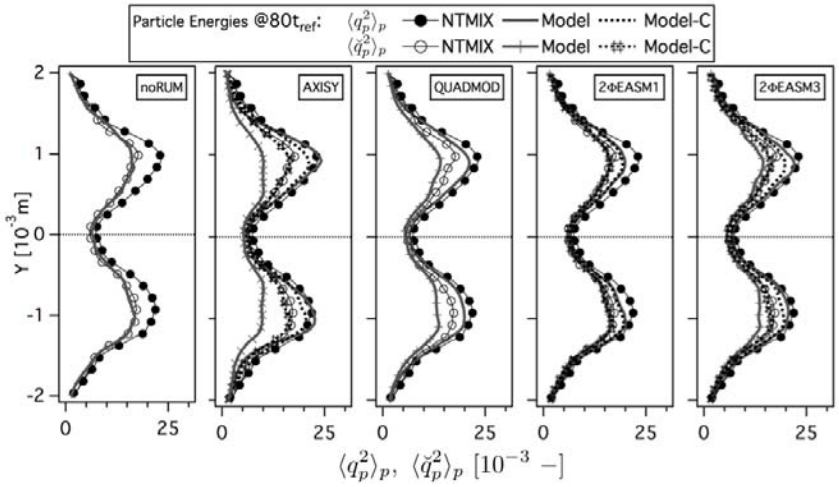

(c)

Figure 5.22: *Comparison of Eulerian and Lagrangian mean total energy ($< q_p^2 >_p$) and mean mesoscopic energy ($\langle \breve{q}_p^2 \rangle_p$) at 5, 40 and 80$t_{ref}$. Normalized by the square of the initial particle velocity in X-direction at the center of the slab. LR_St1_# case.*

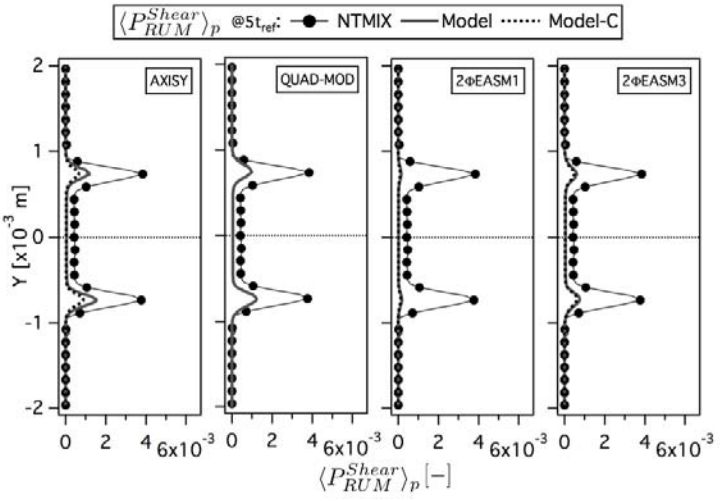

(a)

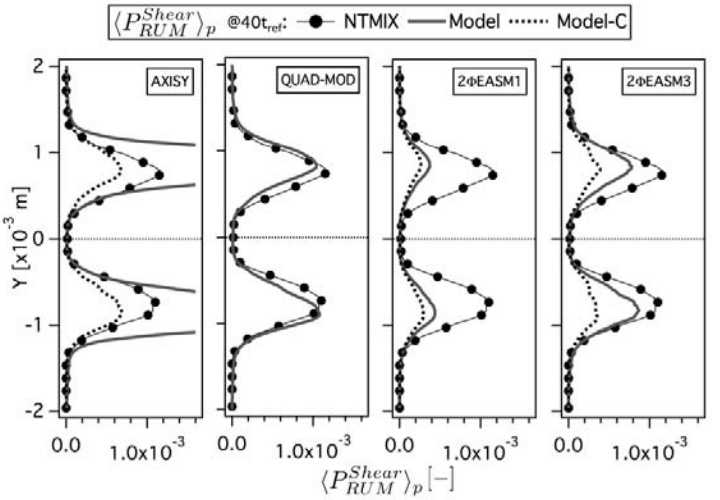

(b)

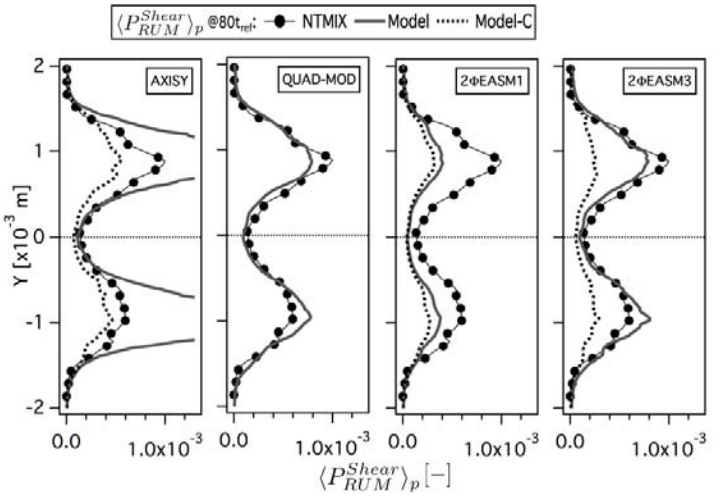

(c)

Figure 5.23: *Comparison of Eulerian and Lagrangian mean productions of RUM energy by shear ($< P_{RUM}^{Shear} >_p$) at 5, 40 and 80t_{ref}. Normalized by the square of the initial particle velocity in X-direction at the center of the slab and the reference time (t_{ref}). LR_St1_# case.*

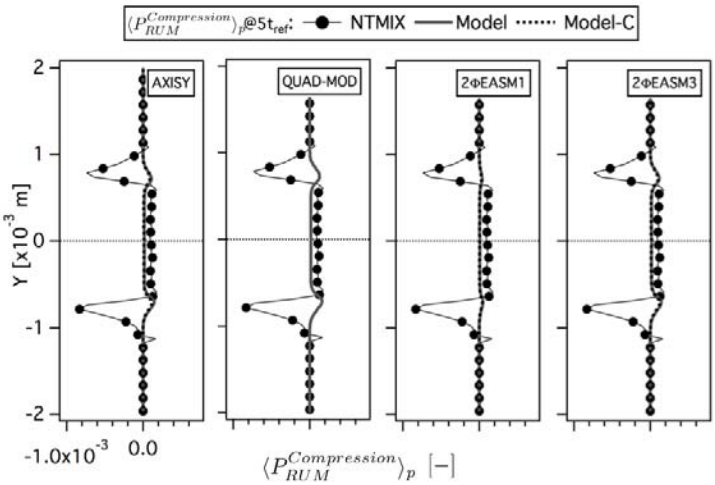

(a)

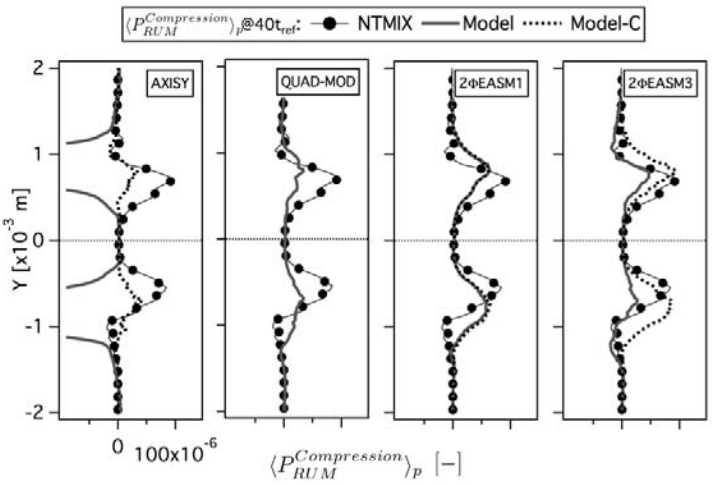

(b)

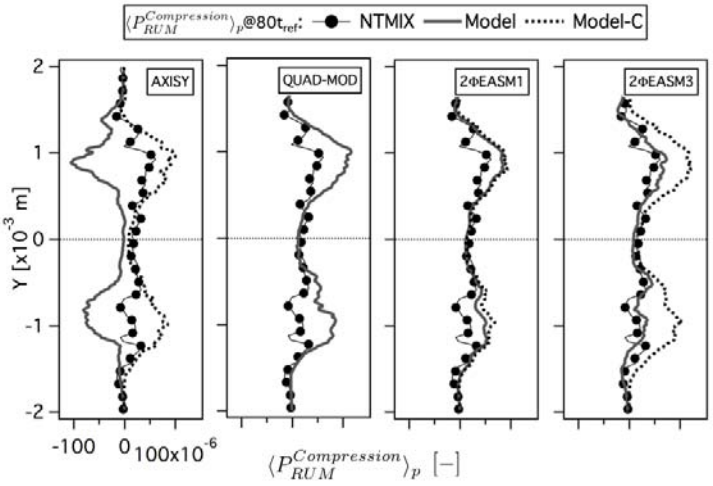

(c)

Figure 5.24: *Comparison of Eulerian and Lagrangian mean productions of RUM energy by compression ($< P_{RUM}^{Compression} >_p$) at 5, 40 and 80$t_{ref}$. Normalized by the square of the initial particle velocity in X-direction at the center of the slab and the reference time (t_{ref}). LR_St1_# case.*

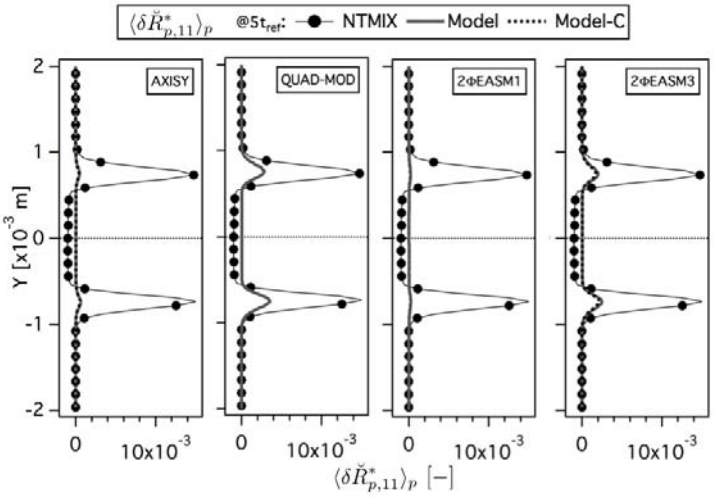

(a)

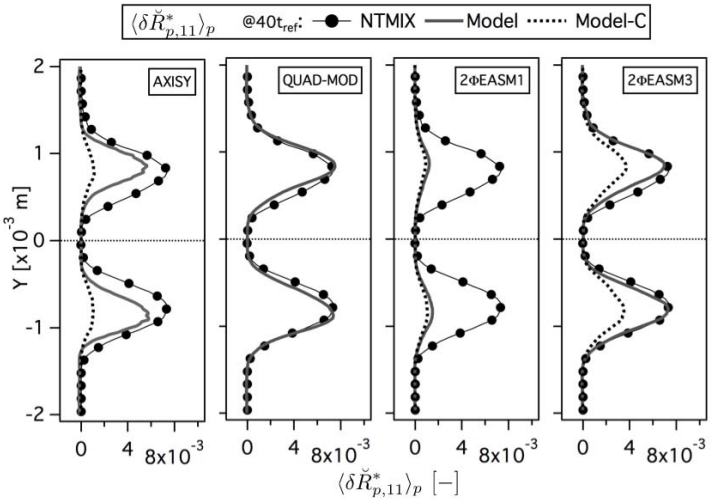

(b)

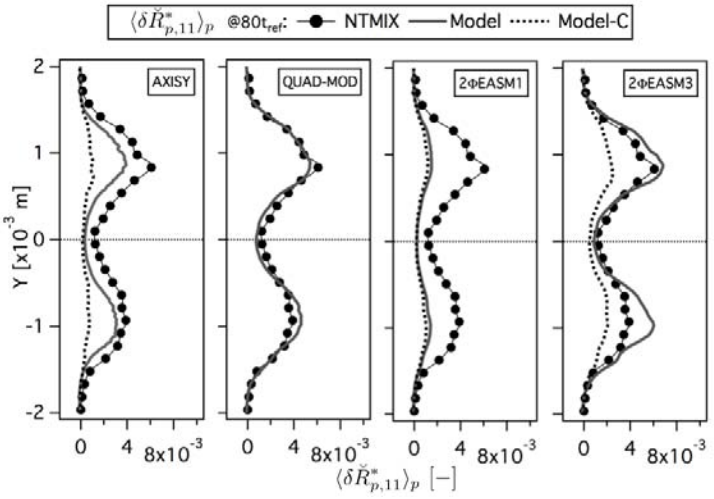

(c)

Figure 5.25: *Comparison of Eulerian and Lagrangian mean deviatoric RUM stress tensor XX component ($< \delta \breve{R}^*_{p,11} >_p$) at 5, 40 and 80$t_{ref}$. Normalized by the square of the initial particle velocity in X-direction at the center of the slab. LR_St1_# case.*

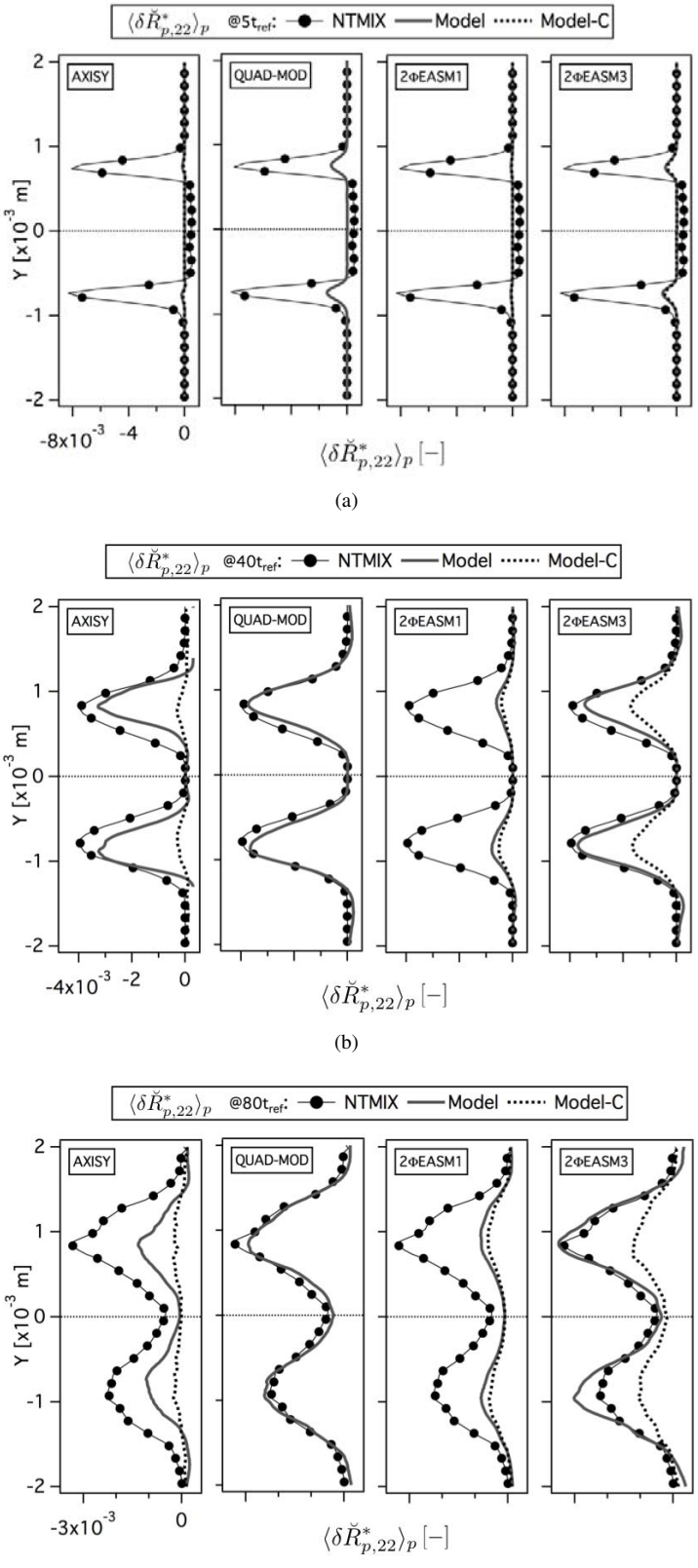

Figure 5.26: *Comparison of Eulerian and Lagrangian mean deviatoric RUM stress tensor YY component ($< \delta \breve{R}^*_{p,22} >_p$) at 5, 40 and 80$t_{ref}$. Normalized by the square of the initial particle velocity in X-direction at the center of the slab. LR_St1_# case.*

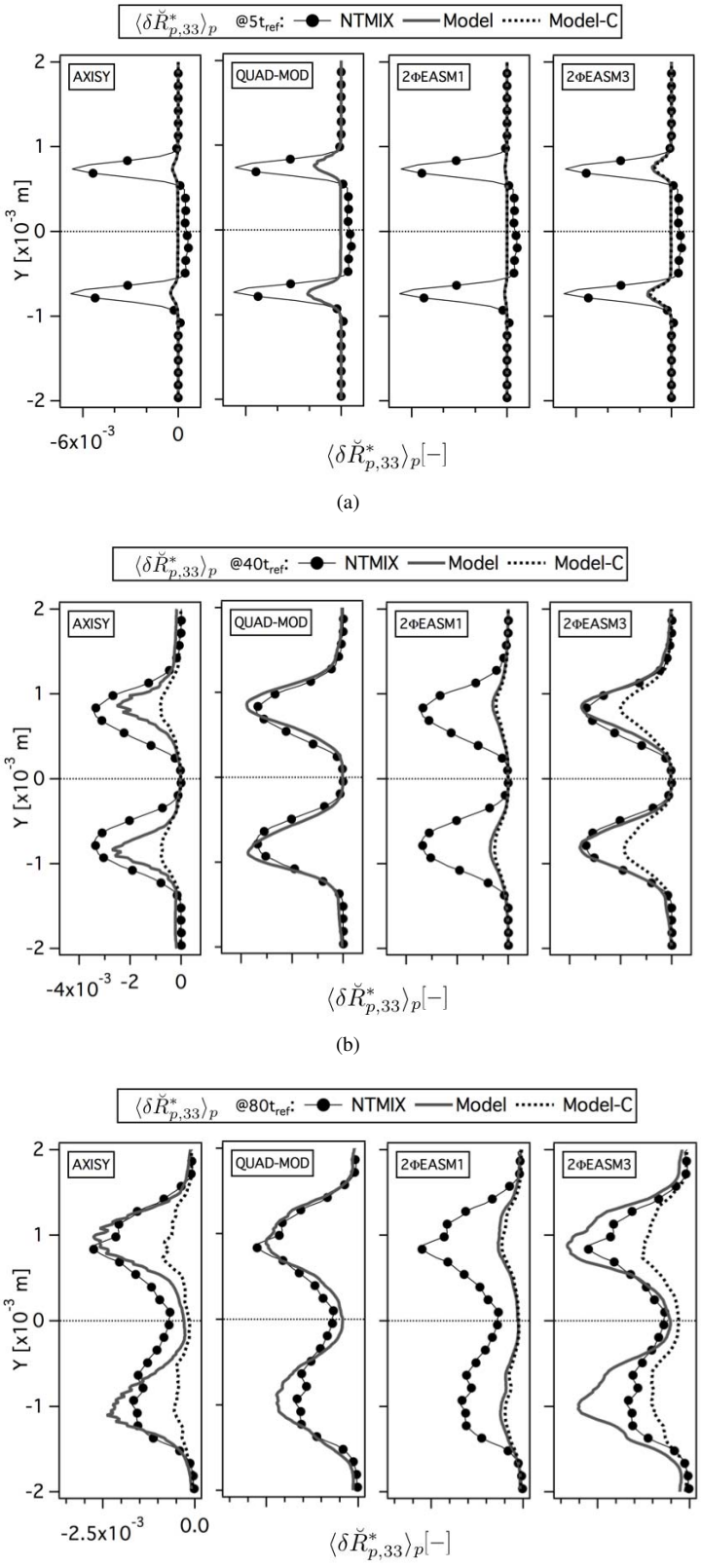

Figure 5.27: *Comparison of Eulerian and Lagrangian mean deviatoric RUM stress tensor ZZ component ($< \delta \breve{R}^*_{p,33} >_p$) at 5, 40 and 80$t_{ref}$. Normalized by the square of the initial particle velocity in X-direction at the center of the slab. LR_St1_# case.*

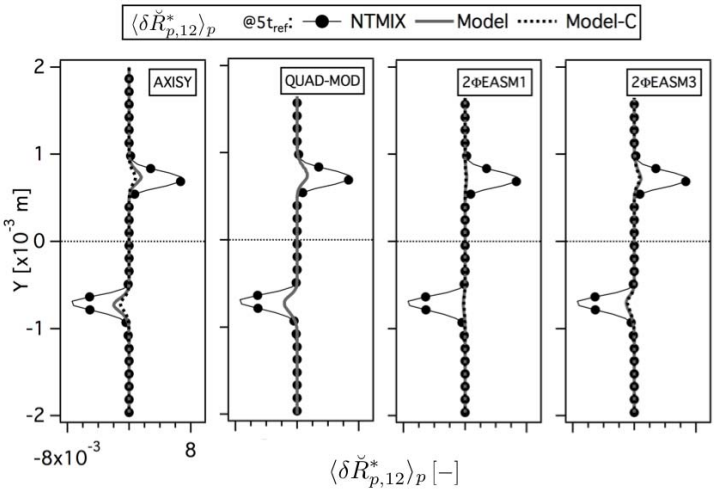

(a)

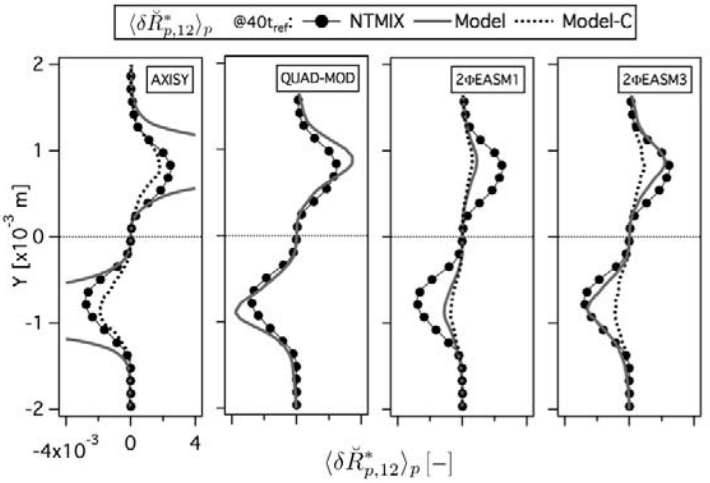

(b)

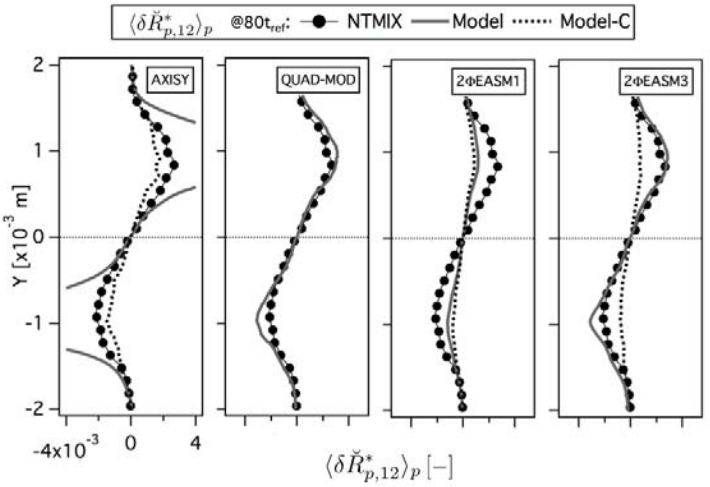

(c)

Figure 5.28: *Comparison of Eulerian and Lagrangian mean deviatoric RUM stress tensor XY component ($< \delta \breve{R}^*_{p,12} >_p$) at 5, 40 and 80$t_{ref}$. Normalized by the square of the initial particle velocity in X-direction at the center of the slab. LR_St1_# case.*

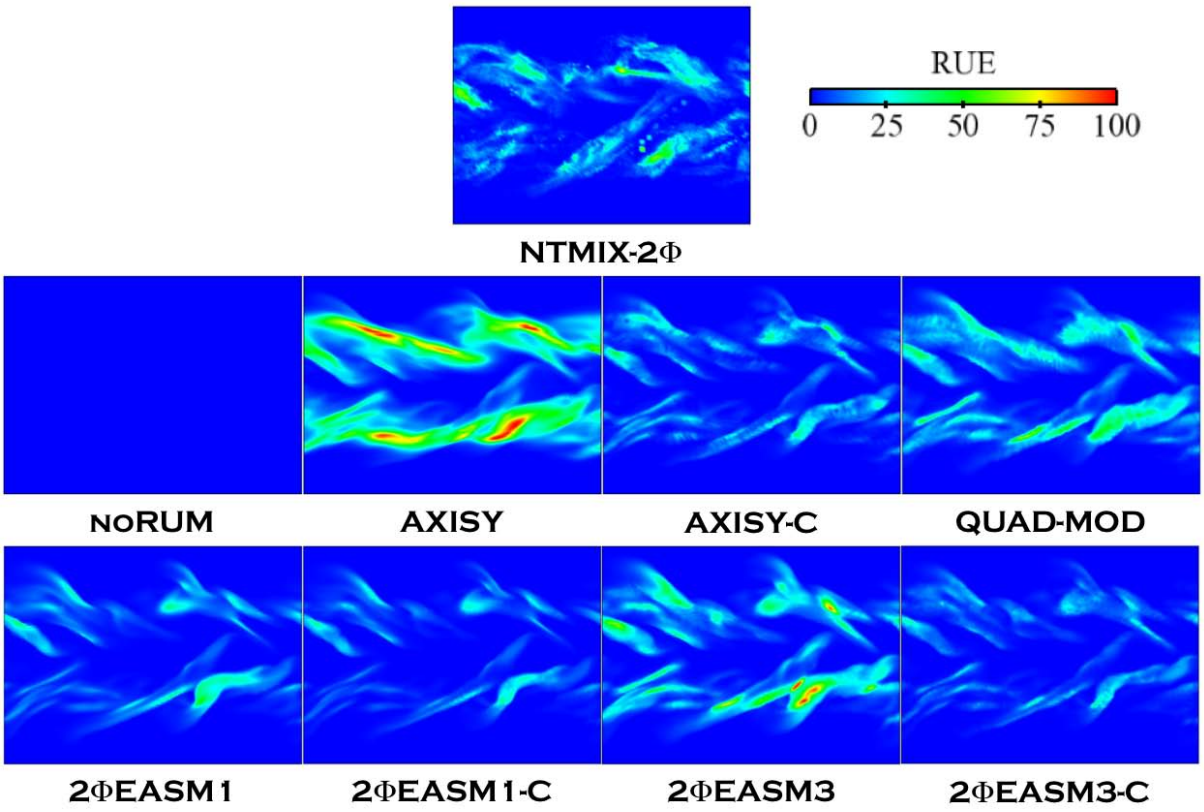

Figure 5.29: *Comparison of Lagrangian (NTMIX-2Φ) and Eulerian Random Uncorrelated Energy at* $80t_{ref}$*. LR_St1_# case.*

5.3.3 Effect of the user-defined artificial dissipation

Artificial dissipation (AD) is required in AVBP to guarantee the stability of the simulation using a centered numerical scheme (TTGC). It plays an important role in the development of the two-phase flow simulation itself. Artificial dissipation is applied in two steps. First, a sensor detecting too steep gradients to be resolved on the current grid is computed. There are several expressions for this sensor in AVBP which can take values from 0 to 1, 0 being no AD applied and 1 denotes where the maximum value of AD is applied in the domain. Second, a certain amount of 2^{nd} (shock capturing) and 4^{th} (background dissipation) AD is applied depending on the sensor value and user-defined coefficients. As a matter of fact, the AV sensor (CMS-Lite) used during this work seems to act similarly to the RUM, i.e. it has an effect of diffusion in the fields of the particle number density and velocity. Actually, there seems to exist an inverse correlation between the activation of the AV sensor and the RUE.

The models which are not able to predict the correct amount of RUE (e.g. noRUM) compensate the lack of diffusion naturally produced by the model by a higher amount of AD, which artificially smoothes the gradients and allows the code to complete the simulation. On the contrary, the AV sensor activates much less when models which overestimate the RUE are used (e.g. AXISY). The noRUM model for example, is able to correctly predict the low order moments such as the particle number density, the particle velocity and their RMS values. AD helps to stabilize the code producing an effect that mimics the one of the RUM. However, it is not able to produce RUE and thus it predicts a wrong repartition between the energies (the only contribution to the total energy is the mesoscopic energy, which leads to an underestimation of q_p^2). On the one hand, a correct balance between the RUM and the mesoscopic energy is a key point to reproduce complex effects such as PTC or collisions/coalescence. On the other hand, the effect of RUM becomes more important as the particle inertia increases. This means that while at $St = 1$ the simulations with models which underpredict the RUE are stable enough (due to the AD) to complete the calculation, it is not guaranteed that these models will keep valid at larger Stokes (Section 5.4.1).

Recently, another numerical scheme called PSI (Lamarque (2007), Roux *et al.* (2010)) has been implemented in AVBP. This residual distribution scheme is lower order than TTGC, but positive and linear preserving, which are interesting properties to capture shocks or very steep gradients. No AD is required when using PSI. Some tests performed during this work have shown that this scheme diffused too much at the limits of the slab due to the initial condition gradients. Thus, the slab spreads in the Y-direction, giving worse predictions of the low order and high order moments than the combination of TTGC scheme with a higher amount of AD. This effect was already visible after $5t_{ref}$ only. For this reason, the use of PSI scheme was quickly discarded in this configuration.

Figure 5.30 shows profiles of AV sensor for all models (included the calculation without RUM (noRUM)) at 5, 40 and $80t_{ref}$. It should be pointed out that due to the steep gradients at the limits of the slab in the initial solution, the AV sensor initially activates whatever the RUM model, and always at the same locations and with the same strength. This helps the code to overcome that extreme initial condition. Afterwards, the differences between the models are clear: AXISY, which greatly overestimates the RUE, needs less AD than 2ΦEASM1, which underestimates the RUE. Since Euler-Euler simulations need the application of a certain amount of AD in order to numerically stabilize the computations, the goal is then to find a model which presents good compromise between RUM and AD. That is, a model able to capture the physical phenomena related to RUM and that limits the action of AD to the dissipation of numerical instabilities. QUAD-MOD and 2ΦEASM3 seem good candidates.

Figure 5.31 shows an instantaneous field AV sensor at $80t_{ref}$. When neglecting the RUM contribution (noRUM model), the AV sensor is activated in a wider way and with a higher level than when using a RUM model. The sensor is very little activated with AXISY model. 2ΦEASM3 model seems again to be the best compromise.

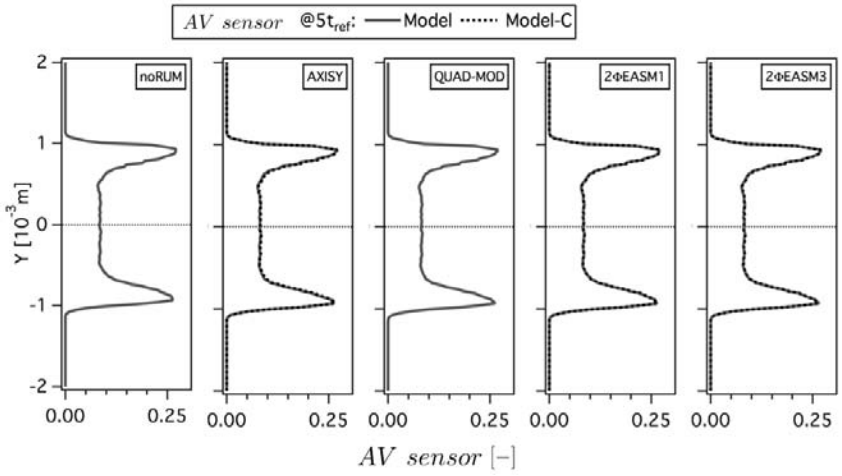

(a)

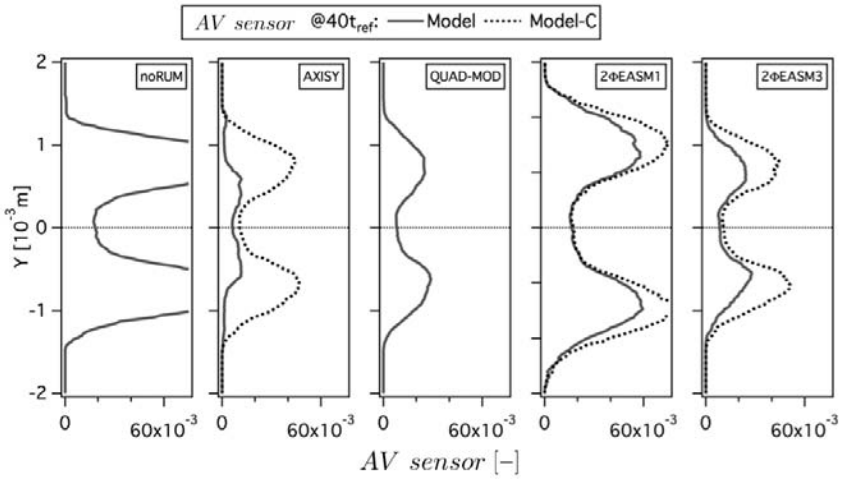

(b)

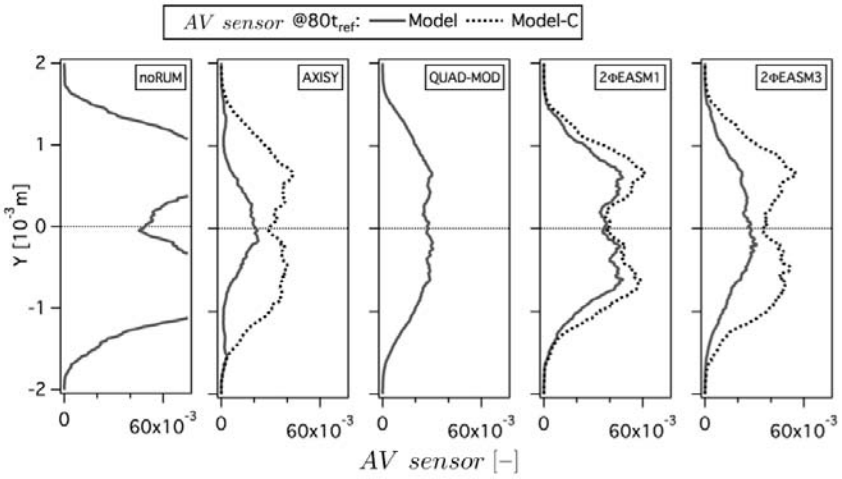

(c)

Figure 5.30: *Mean Artificial Viscosity sensor activation at 5, 40 and 80t_{ref}. LR_St1_# case.*

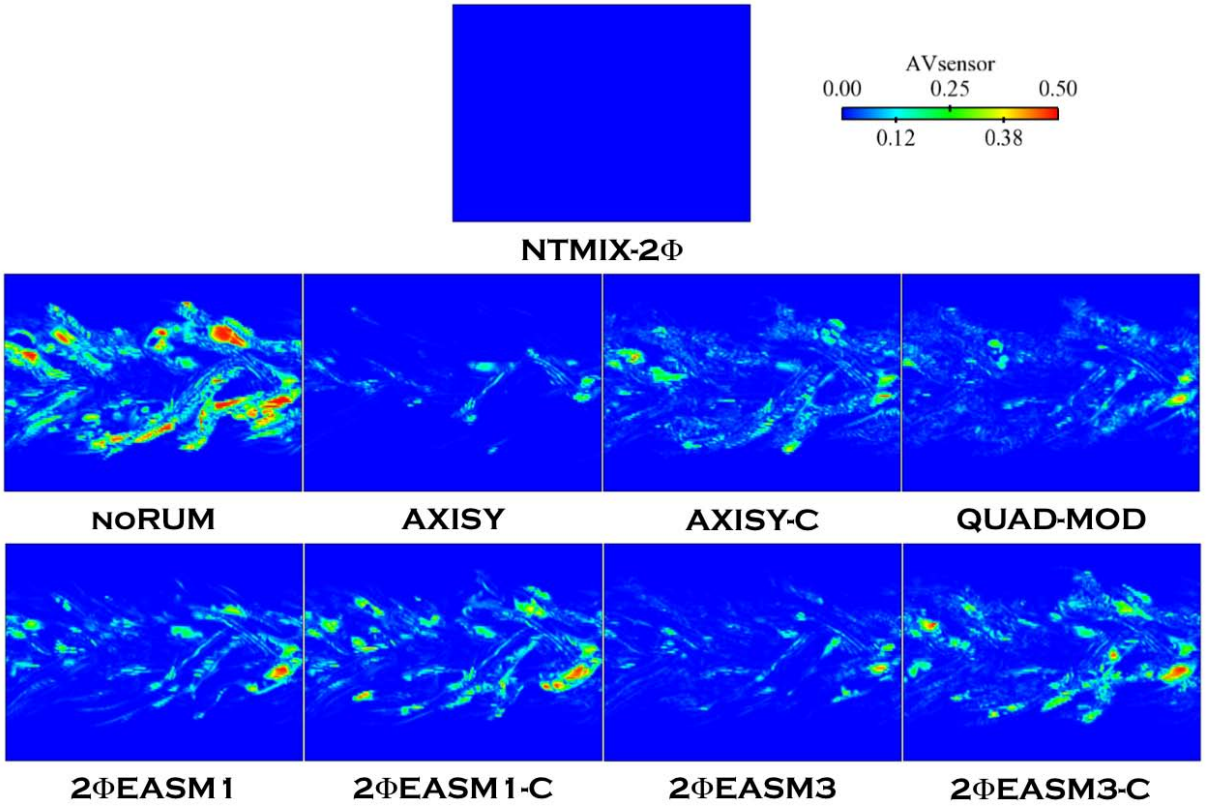

Figure 5.31: *Comparison of AV sensor levels at* $80t_{ref}$*. LR_St1_# case.*

5.3.4 Effect of mesh resolution

The effect of mesh resolution is studied in this Section. Case LR_St1_# has been computed on a 512^3 hexahedrical grid with the 2ΦEASM3 model. That is, the resolution has been doubled compared to the 256^3 mesh used in the computations presented in the previous sections. It is conjectured that the mesh resolution has an important impact on high order moments statistics of the dispersed phase. This effect has already been studied by Dombard (2011) on the Euler-Euler simulations. However, the mesh resolution may impact the Euler-Lagrange simulations too. Due to limited computational resources, the simulation has been carried out until $40t_{ref}$ and with one model only. 2ΦEASM3 has been chosen to perform the high resolution simulation following the results obtained in Sections 5.3.1-5.3.3. Furthermore, only the low order moments and the RUE have been computed.

Figure 5.32(a) shows the statistics of the non-dimensional particle number density obtained from the Euler-Lagrange computation performed with NTMIX-2Φ and the Euler-Euler computations performed with AVBP using 2ΦEASM3 model and two different grids. Mesh_256 corresponds to the simulation on a 256^3 grid and Mesh_512 to the 512^3 grid simulation. The numerical setups are the same for the two Euler-Euler calculations, including the Artificial Dissipation parameters. The scales of the graphs have been stretched to highlight the differences between the two meshes, otherwise they are not visible and the profiles given by the two meshes superpose and there is no noticeable difference. Figure 5.32(b) shows the profiles of the non-dimensional particle velocity. At the center of the slab, Mesh_256 matches the reference NTMIX-2Φ, the same happens with Mesh_512. However, at the periphery of the jet, only the simulation performed with the high resolution mesh (Mesh_512) reproduces the opening of the jet. Indeed, Mesh_512 sticks to the profile of NTMIX-2Φ except at some points where the differences are attributed to the projection algorithm used to recontruct the Eulerian fields from the Euler-Lagrange computation with NTMIX-2Φ.

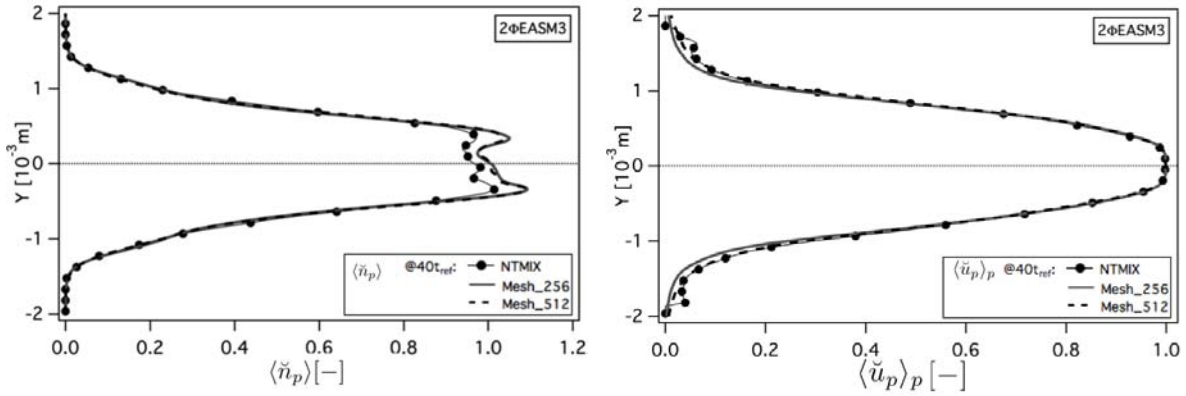

(a) Non-dimensional mean particle number density.

(b) Non-dimensional mean particle velocity.

Figure 5.32: *Comparison between Lagrangian and Eulerian results. The Lagrangian computation has been performed on a* 128^3 *mesh grid. Mesh_256 corresponds to the Eulerian simulation on a* 256^3 *mesh and Mesh_512 to the Eulerian simulation on a* 512^3 *mesh.*

The increase in mesh resolution improves the predictions of RMS particle number density profiles (Fig. 5.33(a)) as well. The profile corresponding to Mesh_512 captures the maximum level predicted by NTMIX-2Φ at the peaks located at the periphery. However, the opening of the jet is the same as for Mesh_256, narrower than the corresponding to NTMIX-2Φ. On the contrary, Fig. 5.33(b) shows the RMS particle velocity statistics. The increase in mesh resolution leads to a decrease in the maximum value of the profile. Otherwise, the opening of the jet is wider in Mesh_512 case. Note that the projection algorithm produces inaccurate results at the periphery of the slab for NTMIX-2Φ computations. The accuracy of the reference values at the periphery and thus the jet opening can not be assessed in this case.

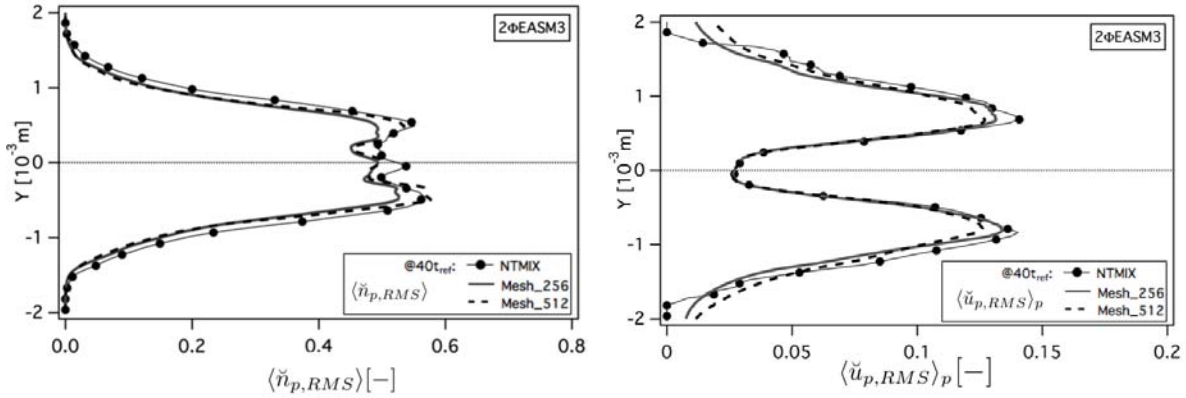

(a) Non-dimensional RMS particle number density.

(b) Non-dimensional RMS particle velocity.

Figure 5.33: *Comparison between Lagrangian and Eulerian results. The Lagrangian computation has been performed on a* 128^3 *mesh grid. Mesh_256 corresponds to the Eulerian simulation on a* 256^3 *mesh and Mesh_512 to the Eulerian simulation on a* 512^3 *mesh.*

Figure 5.34 shows the segregation profiles for both mesh resolutions. Mesh_512 simulation predicts a higher segregation peak than Mesh_256 at one of the borders of the slab. However, the position of the second peak has moved outwards the slab and its level has decreased. On both meshes, the level is too low compared to NTMIX-2Φ, except at the center of the slab, where both simulations give a good approximation of preferential concentration. Note that, the projection errors due to the presence of too few particles in the computational cells at the periphery of the slab on the Lagrangian simulation, provide very high segregation levels in that zone. However, the stretching on the graphs scale allows a better comparison between the simulations. Indeed, the accuracy with NTMIX-2Φ decreases when reaching the periphery.

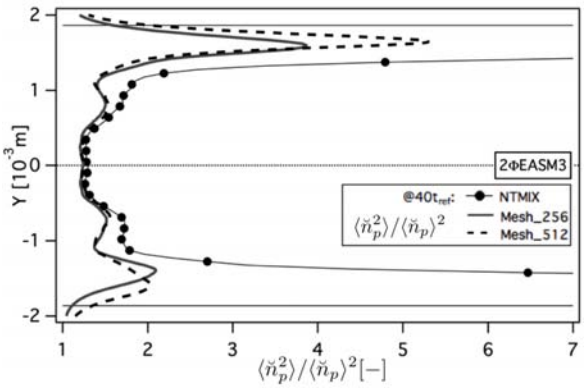

Figure 5.34: *Comparison between Lagrangian and Eulerian results. The Lagrangian computation has been performed on a* 128^3 *mesh grid. Mesh_256 corresponds to the Eulerian simulation on a* 256^3 *mesh and Mesh_512 to the Eulerian simulation on a* 512^3 *mesh.*

The high order moments statistics analyzed for Mesh_512 simulation reduce to the energy profiles. The finer the mesh resolution the higher the RUE level, which leads to a slight overprediction of RUE (Fig. 5.35(a)). The total agitation profiles are very similar, excepted at the slab borders where the total particle agitation predicted by Mesh_512 case is higher (Fig. 5.35(c)). The overprediction of RUE leads to a slight underprediction of the mesoscopic energy compared to Mesh_256 case (Fig. 5.35(b)). In general, increasing the mesh resolution has only a limited impact on the statistics of the dispersed phase.

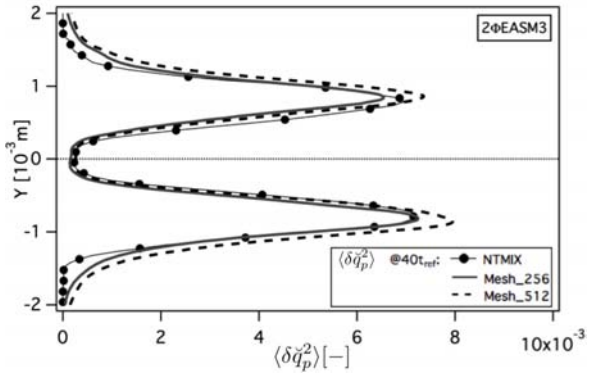

(a) Non-dimensional RUE.

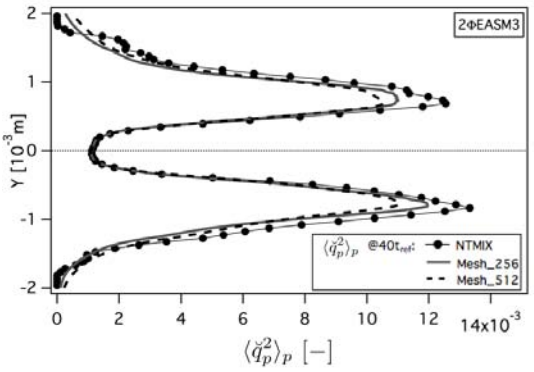

(b) Non-dimensional particle mesoscopic energy.

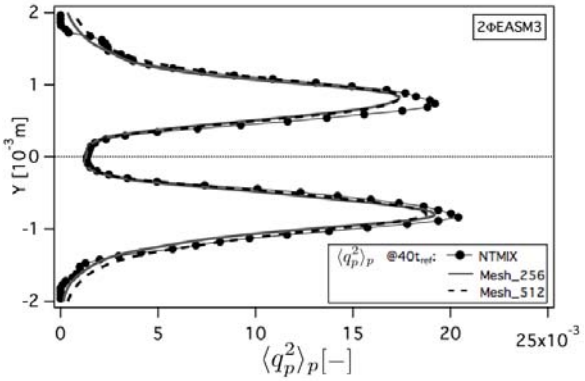

(c) Non-dimensional total particle energy.

Figure 5.35: *Comparison between Lagrangian and Eulerian results. The Lagrangian computation has been performed on a* 128^3 *mesh grid. Mesh_256 corresponds to the Eulerian simulation on a* 256^3 *mesh and Mesh_512 to the Eulerian simulation on a* 512^3 *mesh.*

That is not the case for the instantaneous fields. Fig. 5.36 shows the instantaneous fields of particle number density at $40t_{ref}$. The regions where the differences between 2ΦEASM3_256 and 2ΦEASM3_512 cases are the most visible have been highlighted using circles and arrows. Increasing the mesh resolution has an important impact on the particle number density fields. Indeed, the small structures are better captured as well as the diffusion at the periphery of the jet. The empty zones, as well as the zones of high concentration are also more precisely reproduced when the mesh resolution is increased. In Fig. 5.37 the only visible effect on the particle velocity fields is an increased diffusion at the borders (Fig. 5.37). Compared to NTMIX-2Φ, Mesh_256 gives the best qualitative results. Nevertheless, the statistics of Mesh_512 case are in better agreement with the Lagrangian reference at the periphery. The inaccuracy of the projection algorithm hinders any conclusion at this respect. Regarding the RUE fields (Fig. 5.38), 2ΦEASM3_512 predicts, in general, higher RUE levels (Fig. 5.38). Confirming the statistics (Fig. 5.35(a)), the RUE is slightly overpredicted when the mesh resolution is increased. Euler-Lagrange results on a higher resolution grid are nevertheless needed in order to compare Eulerian and Lagrangian results on the same conditions.

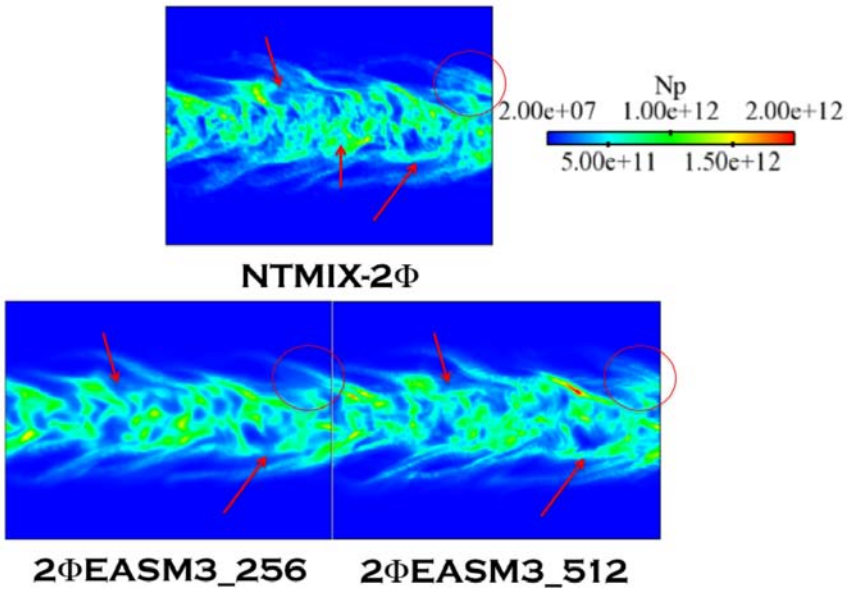

Figure 5.36: *Comparison betwenn Lagrangian and Eulerian particle number density instantaneous fields at* $40t_{ref}$*. The Lagrangian computation has been performed in a* 128^3 *grid. 2ΦEASM3_256 corresponds to the Eulerian simulation on a* 256^3 *mesh and 2ΦEASM3_512 to an Eulerian simulation on a* 512^3 *mesh.*

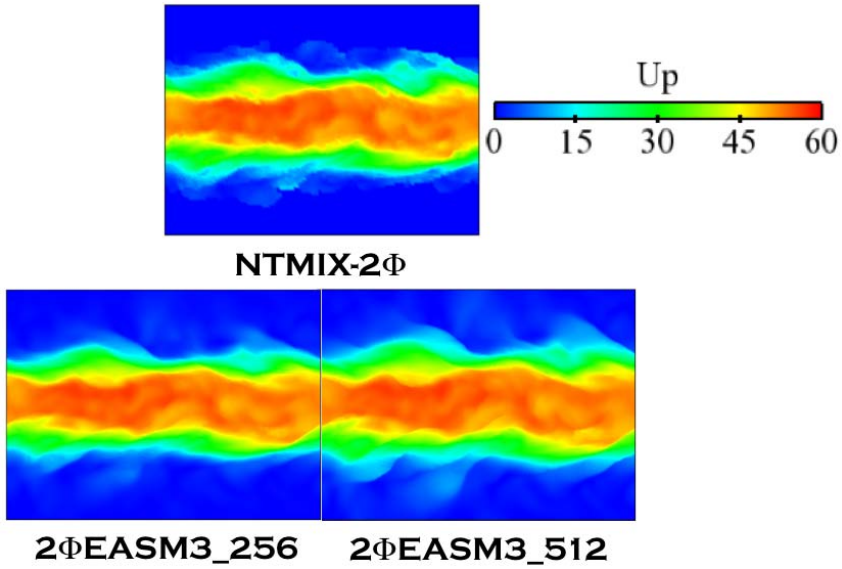

Figure 5.37: *Comparison between Lagrangian and Eulerian particle velocity instantaneous fields at* $40t_{ref}$*. The Lagrangian computation has been performed in a* 128^3 *grid. 2ΦEASM3_256 corresponds to the Eulerian simulation on a* 256^3 *mesh and 2ΦEASM3_512 to an Eulerian simulation on a* 512^3 *mesh.*

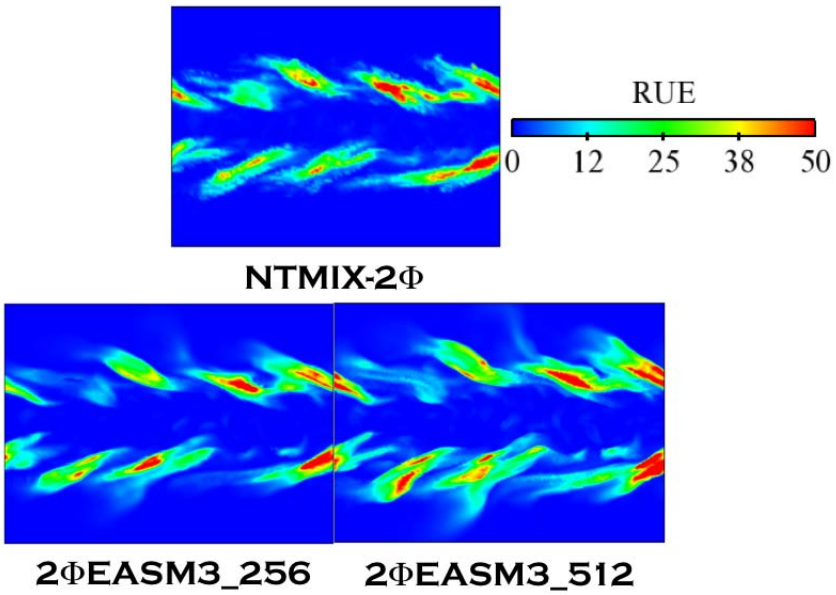

Figure 5.38: *Comparison between Lagrangian and Eulerian RUE instantaneous fields at* $40t_{ref}$*. The Lagrangian computation has been performed in a* 128^3 *grid. 2ΦEASM3_256 corresponds to the Eulerian simulation on a* 256^3 *mesh and 2ΦEASM3_512 to an Eulerian simulation on a* 512^3 *mesh.*

5.4 Performances of the RUM models at different inertia

In real applications the particle or droplet size can range from less than $1\mu m$ (once they have evaporated) up to millimeters (at injection). The range of particle Stokes numbers encountered is thus very large. This implies that the performances of the different models presented in Chapter 4 must be analyzed on a wide range of Stokes numbers too. Masi (2010) performed an *a priori* analysis for many Stokes numbers. This work only presents three, the most significative ones.

The results presented in Section 5.3 distinguished 2ΦEASM3 and QUAD-MOD as the models giving the best predictions for the low and the high-order moments for a $Re^{ac} = 5500$ and $St \sim 1$ particle-laden turbulent sheared flow. The particles in case LR_St3_# are very inertial. Février *et al.* (2005) performed simulations on particle-laden decaying HIT, the results showed that as the particle inertia increases, the contribution of the RUM component to the particle velocity increases too. The phenomena of particles being pushed towards the upper and lower outer regions observed on LR_St1_# case is expected to increase. This Section aims at analyzing if the two models still behave correctly at $St \sim 3$ (Section 5.4.1) confirming the potential of the 2ΦEASM3 and QUAD-MOD models.

Then in Section 5.4.2, the ability of the two models to correctly predict the dispersed phase in a low inertia case is tested. Indeed, the Stokes number in LR_St033_# case ($St \sim 0.33$) is very close to the value of the Stokes number for which the preferential concentration phenomenon is maximal in this configuration, creating empty spaces close to regions of very high particle concentration. The particle density gradients are thus very steep and difficult to handle numerically potentially leading to simulation crashes.

5.4.1 High inertia case: Stokes=3

All RUM models are tested here in a low turbulence high inertia case. The Stokes number is $St \sim 3$. The particle relaxation time is $\tau_{fp}^F \sim 39$. The simulation has been performed up to $120t_{ref}$ ($3.07\tau_{fp}^F$). Note that results at $120t_{ref}$ will not be equivalent to those of LR_St1_# case at $40t_{ref}$ (equally $3.07\tau_{fp}^F$) since the corresponding physical time is not the same from the fluid flow point of view. All results are then shown at $120t_{ref}$. Additional results at 40 and $80t_{ref}$ can be found in Appendix D.

In this case, the AD model is not sufficient to allow the simulation without any RUM (noRUM model) to finish since numerical instabilities appear. This fact clearly reveals the importance of the RUM in this type of two-phase flow configurations.

Low order moments

At high inertia, the particle laden slab, subjected to strong flow shear at its limits, diffuses towards the periphery of the box as a result of the entrainment of particles by the fluid turbulence eddies. For this reason, the particle number density profiles (Fig. 5.39(a)) are much flatter than in the LR_St1_# case. As already pointed out, the AD is not able to sufficiently diffuse the profile for those models that underpredict the RUE (2ΦEASM1 and 2ΦEASM1-C) showing a higher level of $\breve{n}_p$ at the center of the jet. AXISY and its corrected version AXISY-C present the same behavior as for the mean inertia case. The maximum of $\breve{n}_p$ is highly overpredicted and consequently, the global shape of the profile is not well captured: the slope of the predicted profile is too high in the center and too low in the periphery. This effect is more visible for AXISY. On the contrary, QUAD-MOD and both 2ΦEASM3 or 2ΦEASM3-C models give very accurate results at the periphery and slightly overestimate the maximum level at the center line.

The initial guess of QUAD-MOD and 2ΦEASM3 as the best models seems to be confirmed by the predictions of the RMS values of $\breve{n}_p$ and $\breve{u}_p$. Indeed, the agreement with the Lagrangian results is very good for these two models (Fig. 5.40(a)). 2ΦEASM3 captures not only the good trend but also the correct level of $\breve{n}_{p,RMS}$. The agreement is slightly worse with QUAD-MOD. The effect of the correction is more pronounced at high inertia when compared to LR_St1_# case. The results obtained when using the correction in 2ΦEASM3 are worse than

when not using it. The same happens with 2ΦEASM1. However, it seems that when applied to the linear model (AXISY) the correction greatly improves the predictions. Figure 5.40(a) shows that AXISY-C and 2ΦEASM1-C reproduce the shape of the $\breve{n}_{p,RMS}$ profile although they overestimate the level of the peak at the center of the jet. On the contrary, AXISY and 2ΦEASM1 show a flatter profile at the periphery of the slab followed by a steeper slope near the center of the slab.

Regarding the particle velocity statistics, all models perfectly reproduce the mean particle velocity (Fig. 5.39(b)) and all models except AXISY produce acceptable RMS velocity profiles (Fig. 5.40(b)). Again, QUAD-MOD and 2ΦEASM3 give the best results together with 2ΦEASM1 (but 2ΦEASM1 fails to reproduce mean and RMS particle number density).

The instantaneous fields of particle number density (Fig. 5.42) and particle velocity (Fig. 5.43) produce a qualitative comparison of the performances of the models . The particle velocity is well predicted by all models (except AXISY that diffuses too much at the border of the jet) but there are important differences in the particle number density fields. AXISY produces a very concentrated jet at the center of the box and all the corrected models (AXISY-C, 2ΦEASM1-C and 2ΦEASM3-C) predict well defined filaments towards the periphery of the jet, which are not predicted by the Lagrangian reference simulations. 2ΦEASM is unable to recover the separated spots of high particle concentration at the center of the slab. QUAD-MOD shows a lot of wiggles (node-to-node or high-frequency oscillations). This can be avoided by adding some 4th-order artificial dissipation to the simulation. However, as the idea is to keep the same numerical setup for all the simulations performed, it has been decided to keep the results as they are shown. Indeed, the results for RUE could be biased by this additional dissipation term.

Figure 5.41 displays the segregation profiles. QUAD-MOD and 2ΦEASM3 agree very well with the Lagrangian results. As a matter of fact, the agreement is better in this case than in LR_St1_# case. There is less preferential concentration effect at this inertia, the slab being flattened, the segregation peaks at the limits of the jet present in LR_St1_# case (cf Fig 5.18(c)) have disappeared. The segregation then shows a more uniform profile. The model correction increases the segregation for all models, that is largely overestimated. All the corrected profiles are very similar. Similarly, AXISY, which produces a very flat profile at the periphery, produces very small values of segregation in this region.

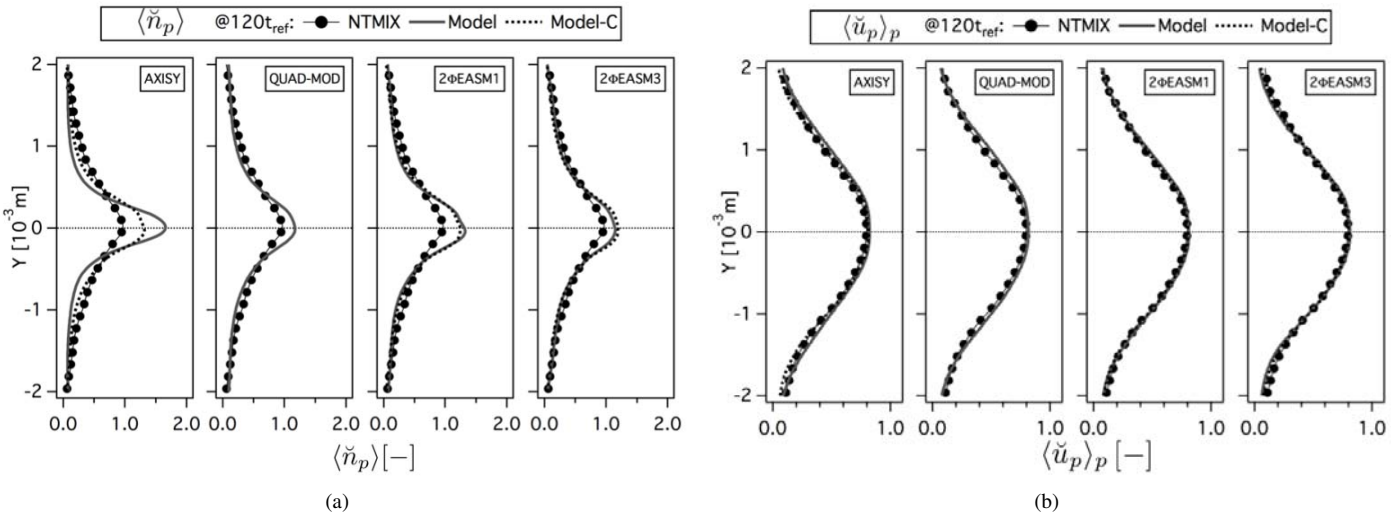

Figure 5.39: *Comparison of Eulerian and Lagrangian (a) mean particle number density (*$< \breve{n}_p >$*, normalized by the initial particle number density at the center of the slab) and (b) mean particle velocity in X-direction (*$< \breve{u}_p >_p$*, normalized by the initial particle velocity in X-direction at the center of the slab) at* $120t_{ref}$*. LR_St3_# case.*

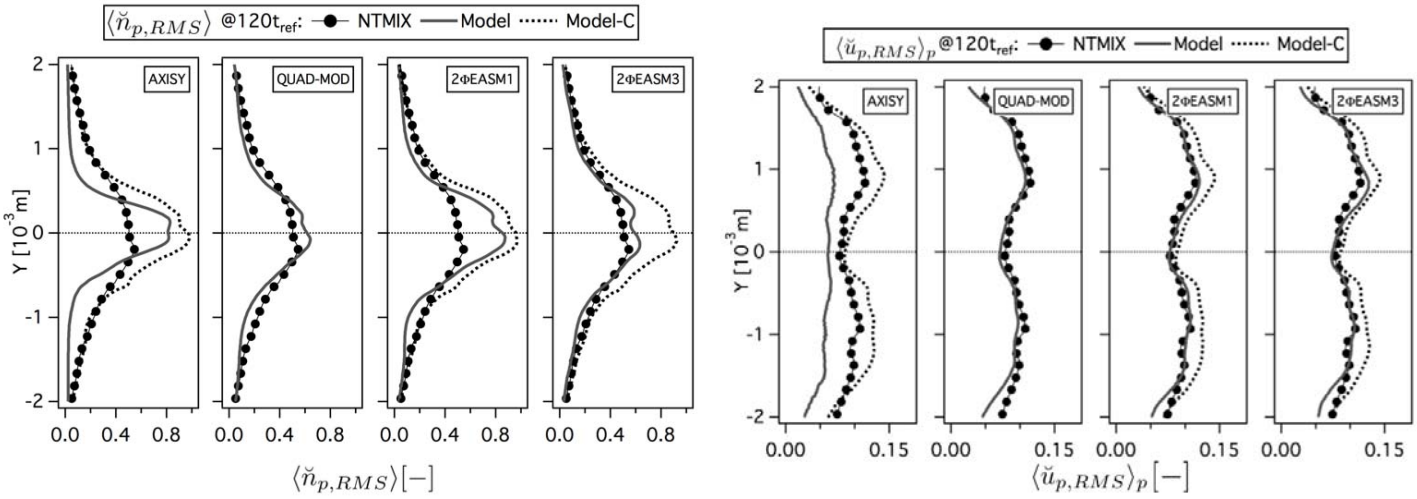

(a) (b)

Figure 5.40: *Comparison of Eulerian and Lagrangian (a) RMS particle number density ($< \breve{n}_{p,RMS} >$, normalized by the initial particle number density at the center of the slab) and (b) RMS particle velocity in X-direction ($< \breve{u}_{p,RMS} >_p$, normalized by the initial particle number density at the center of the slab)at 120t_{ref}. LR_St3_# case.*

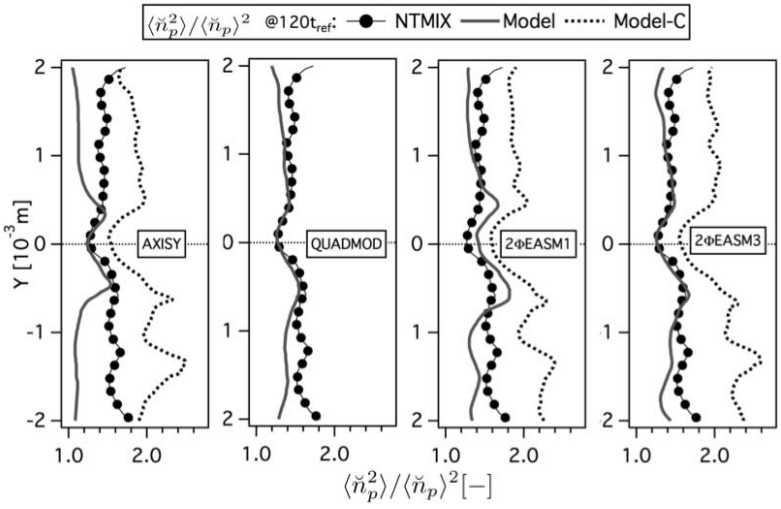

Figure 5.41: *Comparison of Eulerian and Lagrangian RMS particle segregation ($< \breve{n}_p^2 > / < \breve{n}_p >^2$) at 120$t_{ref}$. LR_St3_# case.*

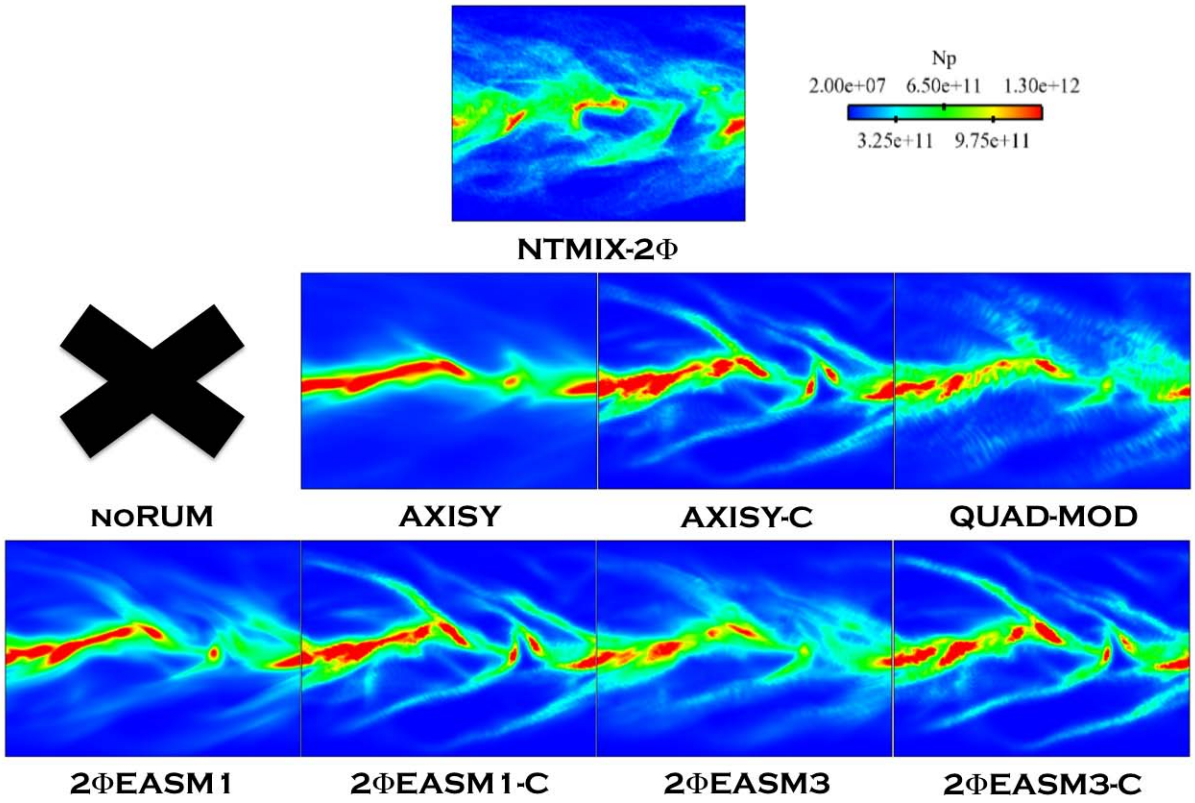

Figure 5.42: *Comparison of Lagrangian (NTMIX-2Φ) and Eulerian particle number density fields (N_p) at 120t_{ref}. LR_St3_# case.*

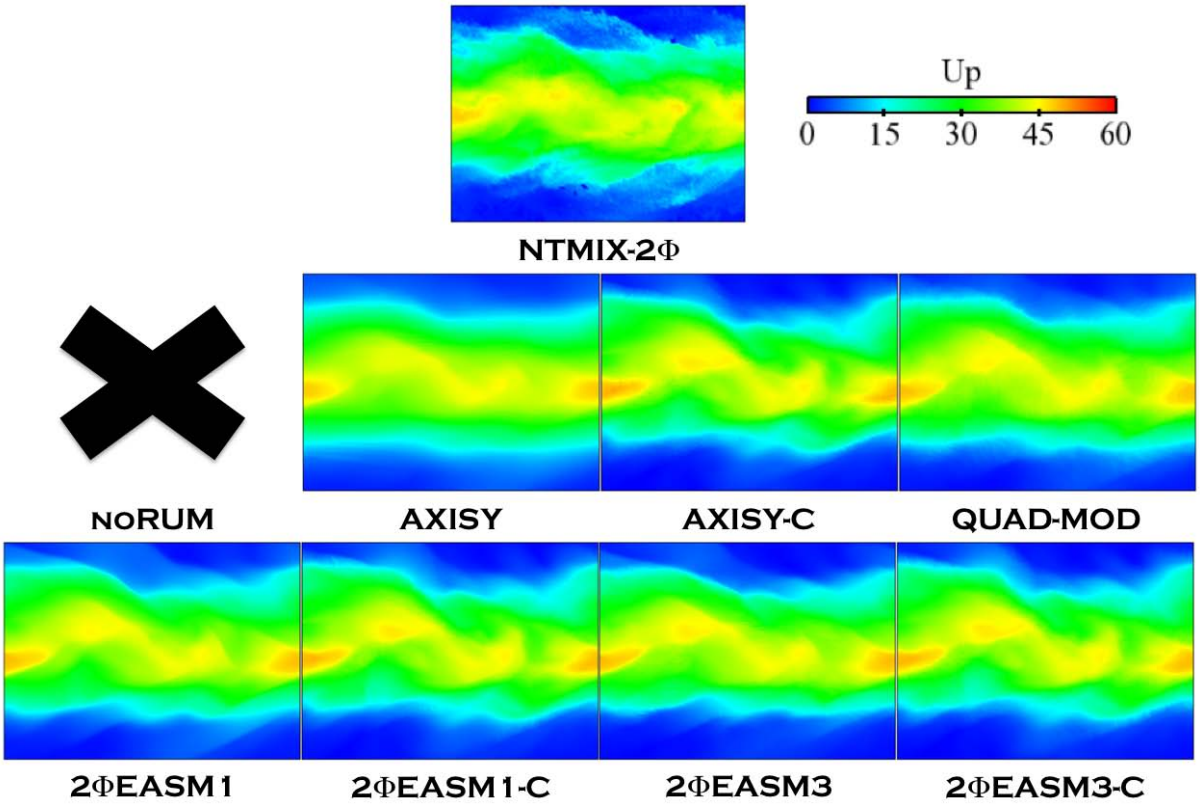

Figure 5.43: *Comparison of Lagrangian (NTMIX-2Φ) and Eulerian particle velocity magnitude fields (U_p) at 120t_{ref}. LR_St3_# case.*

High order moments

The analysis of the high-order moments reveals that, globally, the models have the same behavior for the high inertia case ($St = 3$) as observed in the mean inertia case ($St = 1$, cf Section 5.3). Indeed, 2ΦEASM3 and QUAD-MOD give the best agreement with the Lagrangian results. Figure 5.44(a) shows the mean RUE profiles. QUAD-MOD performs very well at the periphery of the slab but it is not able to recover the good level of the peaks and at the center of the jet. 2ΦEASM1 gives very similar predictions. The correction degrades the performances of the model, giving highly underestimated RUE levels. The same happens with 2ΦEASM3-C, while 2ΦEASM3 predicts the good shape and level of the profile, 2ΦEASM3-C underestimates the level over the whole width of the slab. The correction has the same impact on AXISY, AXISY-C underestimating the results. At the same time, AXISY predicts (as it did for LR_St1_# case) too high RUE values, especially for the peaks location. Figure 5.44(b) shows the mesoscopic energy ($\breve{q}_p^2$) profile and the total energy. The agreement of the non-linear models is very good when the correction is not taken into account. Indeed, the corrected models give good predictions of total agitation but overestimate the mesoscopic energy compensating the underestimation of the RUM energy. The linear model AXISY does not capture well the levels with or without correction. The performances on the RUE can be linked to the predictions of the RUM productions. As stated in Section 5.3.2, RUM production by shear is more important than RUM production by compression. For this reason, models that underestimate P_{RUM}^{Shear} (all the corrected models) underestimate as well the RUE. AXISY shows at high inertia the same behavior as observed in Fig. 5.23(c) for a mean inertial case. Even when the production by compression, $P_{RUM}^{Compression}$, Fig. 5.45(b), acts as a dissipation, P_{RUM}^{Shear} is so overestimated that it cannot be overcome by the dissipative effects and thus, the RUE level is too high. In this case, it is 2ΦEASM3 which gives the best predictions both for the shear and the compression productions. For comparisons, QUAD-MOD produces a level of P_{RUM}^{Shear} too low and overestimates $P_{RUM}^{Compression}$.

The results for the components of the deviatoric RUM stress tensor are in agreement with those of LR_St1_# case. Indeed, AXISY slightly underestimates the diagonal components, but due to the huge overestimation of the shear component, it shows too high values of P_{RUM}^{Shear} and thus of δq_p^2. When applying the correction to this model, the levels of all components are damped resulting in productions and RUE levels that are too low (Figs. 5.46 and 5.47). QUAD-MOD slightly underestimates the diagonal components but gives very good agreement for the shear component (the most important) and thus predicts acceptable values of RUE. 2ΦEASM1 model has an intermediate behavior between AXISY and AXISY-C. In any case, it is 2ΦEASM3 that gives the best predictions for the components of the tensor, the productions as well as for the energies. The instantaneous RUE fields shown in Fig. 5.48 confirm this statement. 2ΦEASM1 and 2ΦEASM3 produce fields in very good agreement with NTMIX-2Φ. 2ΦEASM3, however, reproduces better local RUE values. QUAD-MOD is also able to reproduce the shape of the RUE field, however, wiggles are clearly present.

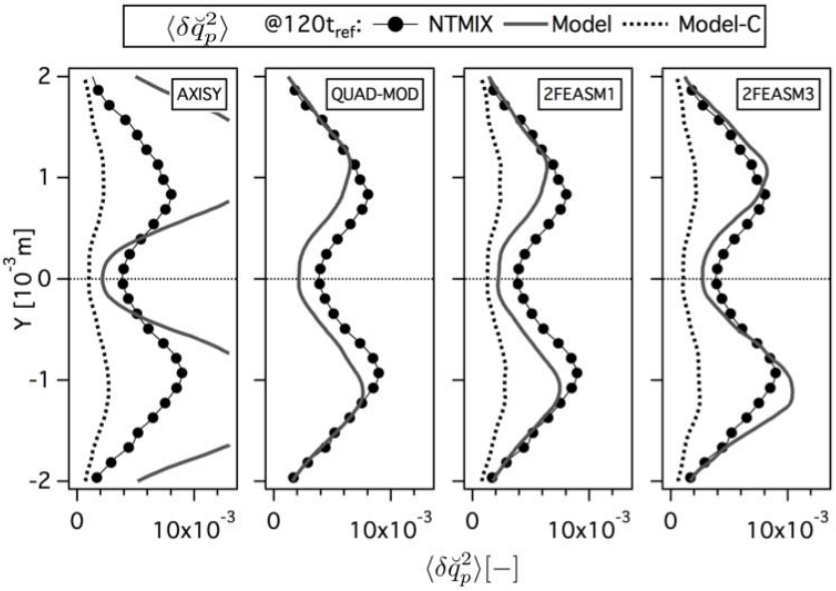

(a)

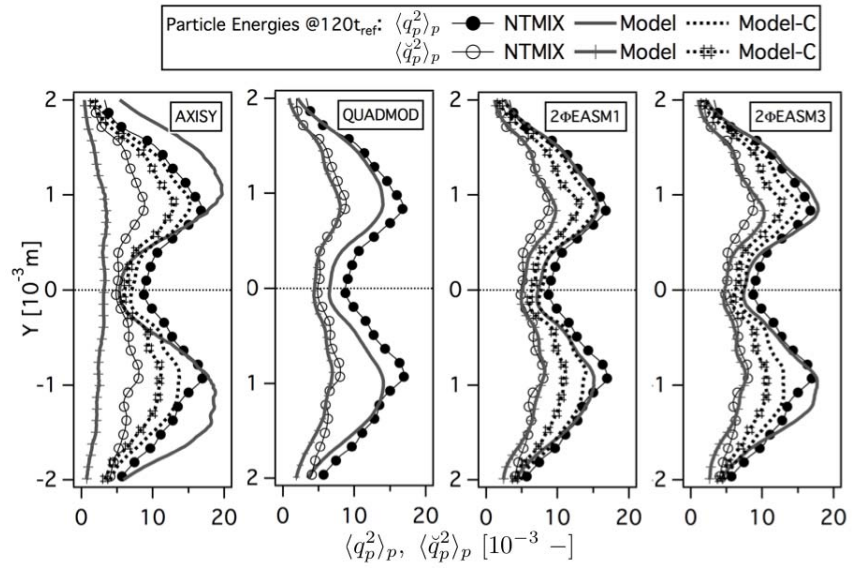

(b)

Figure 5.44: *Comparison of Eulerian and Lagrangian (a) mean Random Uncorrelated Energy (δq_p^2) and (b) mean total (q_p^2) and mesoscopic ($\breve{q}_p^2$) particle energies at 120t_{ref}. Normalized by the square of the initial particle velocity in X-direction at the center of the slab. LR_St3_# case.*

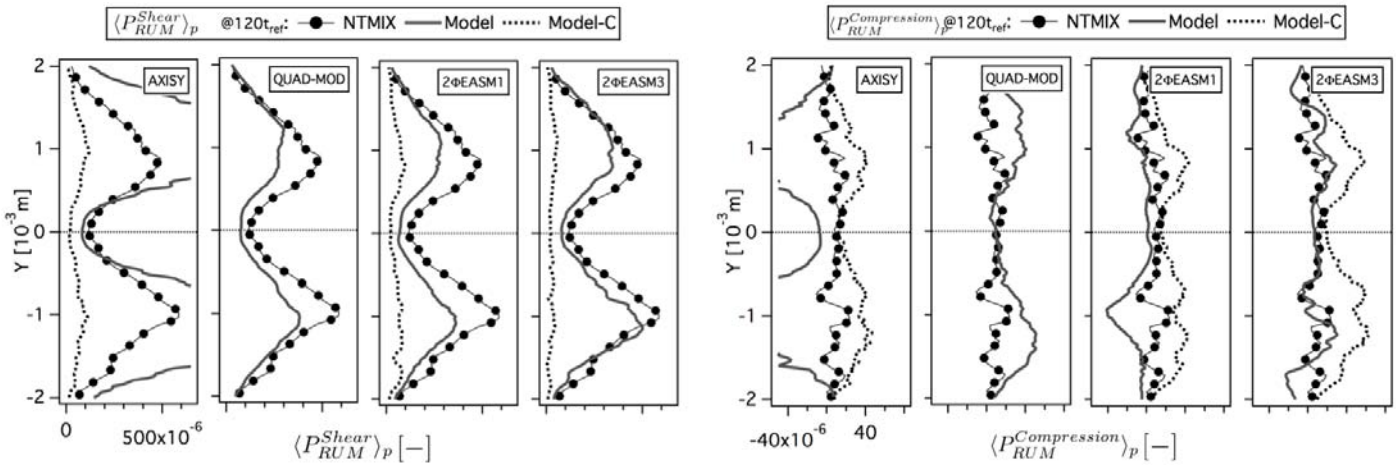

(a) (b)

Figure 5.45: *Comparison of Eulerian and Lagrangian (a) mean production of RUM energy by shear ($< P_{RUM}^{Shear} >_p$) and (b) mean productions of RUM energy by compression ($< P_{RUM}^{Compression} >_p$) at 120$t_{ref}$. Normalized by the square of the initial particle velocity in X-direction at the center of the slab and the reference time (t_{ref}). LR_St3_# case.*

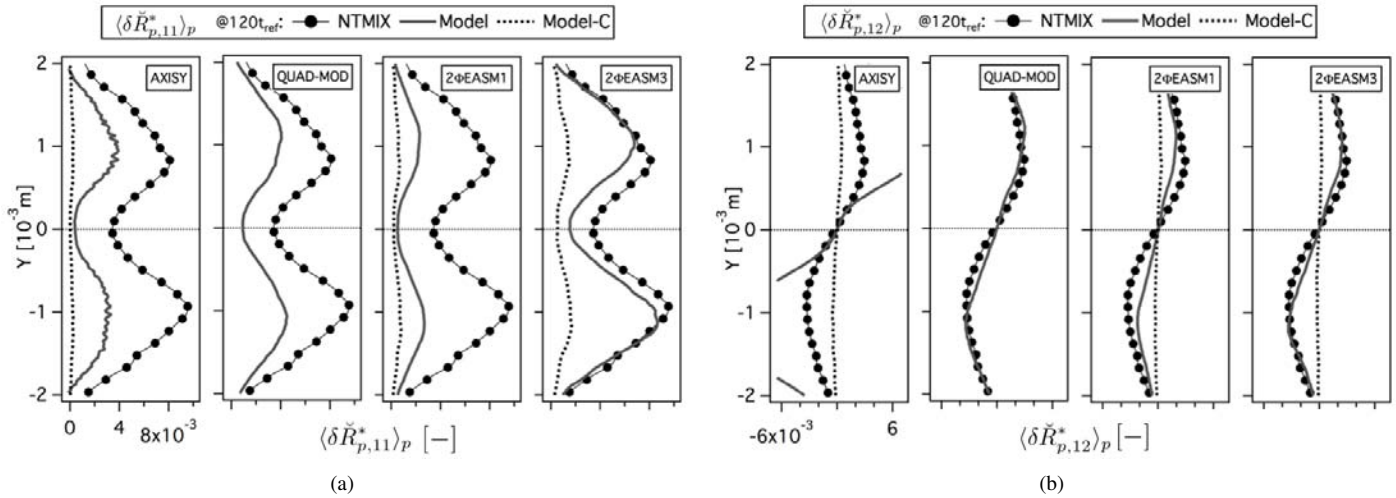

(a) (b)

Figure 5.46: *Comparison of Eulerian and Lagrangian (a) mean deviatoric RUM stress tensor XX component ($< \delta \breve{R}_{p,11}^{*} >_p$) and (b) mean deviatoric RUM stress tensor XY component ($< \delta \breve{R}_{p,12}^{*} >_p$) at 120$t_{ref}$. Normalized by the square of the initial particle velocity in X-direction at the center of the slab. LR_St3_# case.*

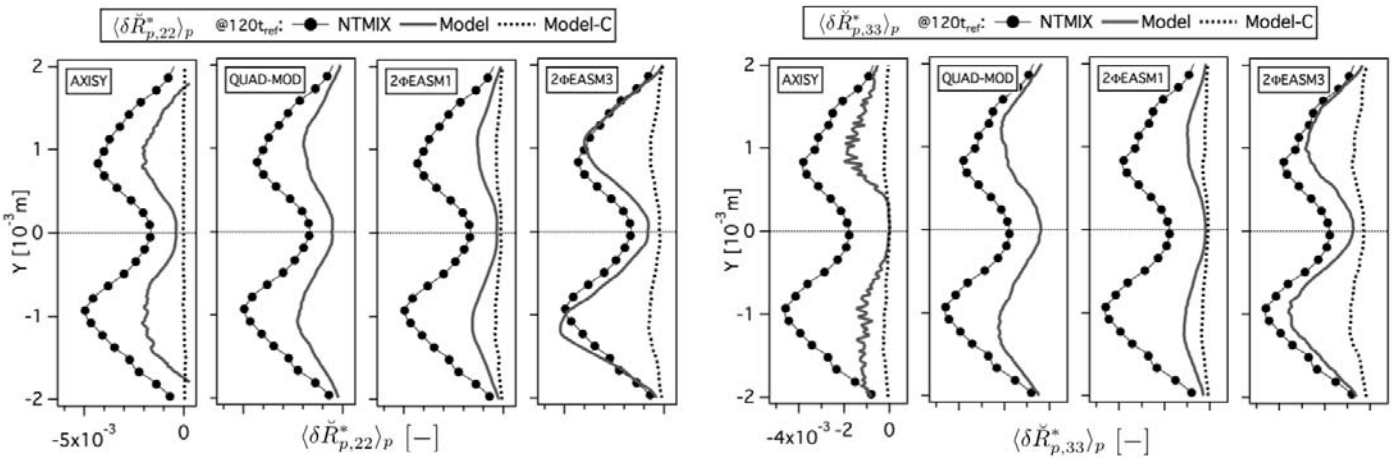

(a) (b)

Figure 5.47: *Comparison of Eulerian and Lagrangian (a) mean deviatoric RUM stress tensor YY component ($< \delta \breve{R}^*_{p,22} >_p$) and (b) mean deviatoric RUM stress tensor ZZ component ($< \delta \breve{R}^*_{p,33} >_p$) at 120$t_{ref}$. Normalized by the square of the initial particle velocity in X-direction at the center of the slab. LR_St3_# case.*

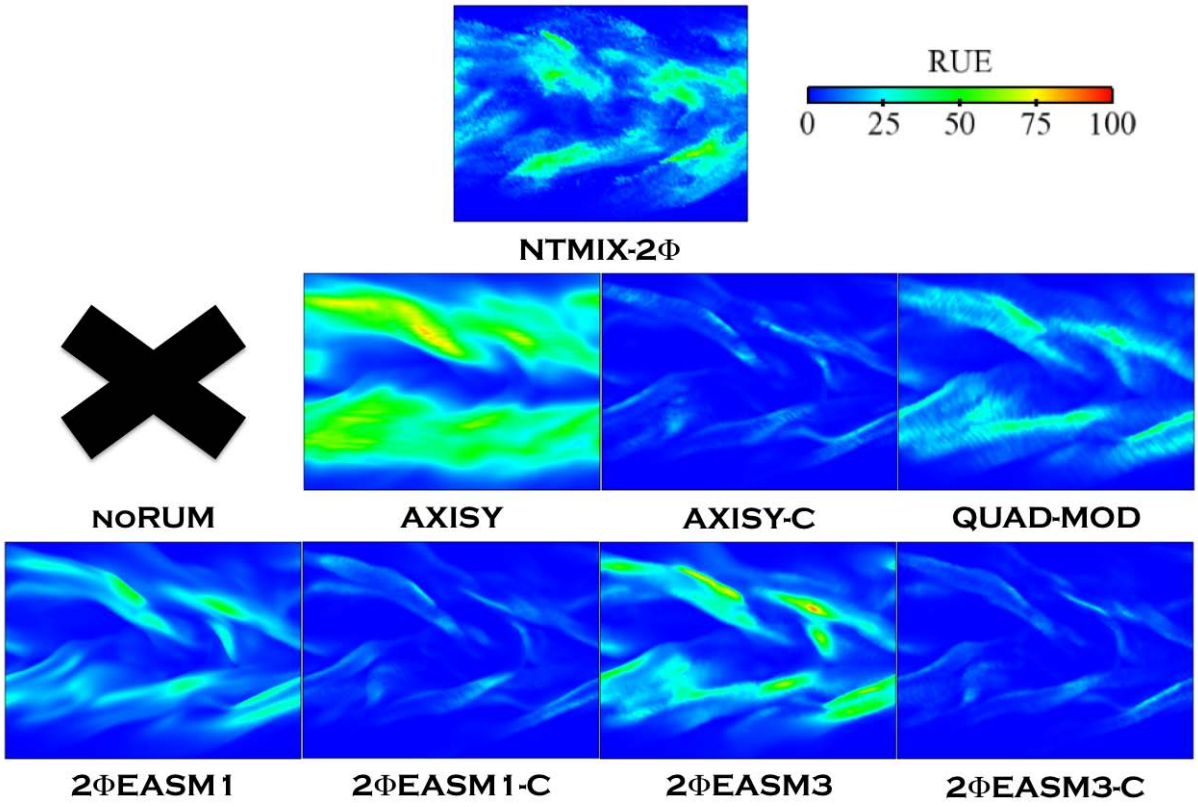

Figure 5.48: *Comparison of Lagrangian (NTMIX-2Φ) and Eulerian Random Uncorrelated Energy (δq_p^2) at 120t_{ref}. LR_St3_# case.*

Effect of Artificial Dissipation

For this case (LR_St3_#), where AD is not powerful enough to allow the whole calculation without RUM (noRUM) to finish, the activation of the AV sensor is very reduced when the models giving the best predictions (2ΦEASM3 and QUAD-MOD) are used. This effect can be observed in Fig. 5.49 where the profiles of the AV sensor are shown. Again, as it happened with LR_St1_# case, the AD activates when the RUM models do not predict the correct level of RUE. This fact is confirmed by Fig 5.50 where the instantaneous fields of AV sensor at $120t_{ref}$ are shown. Indeed, non-corrected 2ΦEASM# models do not need much artificial viscosity. QUAD-MOD however, needs much more artificial viscosity to overcome the problems due to the high-frequency oscillations.

In fact, it seems that, unexpectedly, the AV sensor CMS-Lite activates at the same locations where the RUE is maximal. This may be due to a need to diffuse the steep concentration and velocity gradients. When the RUM model correctly predicts the RUE field, the RUE diffuses those gradients, but in those cases where the RUE is not active or its value is too low to diffuse the gradients, the sensor activates to stabilize the simulation. The AV sensor has not been developped to this purpose and the effects observed are more a matter of coincidence.

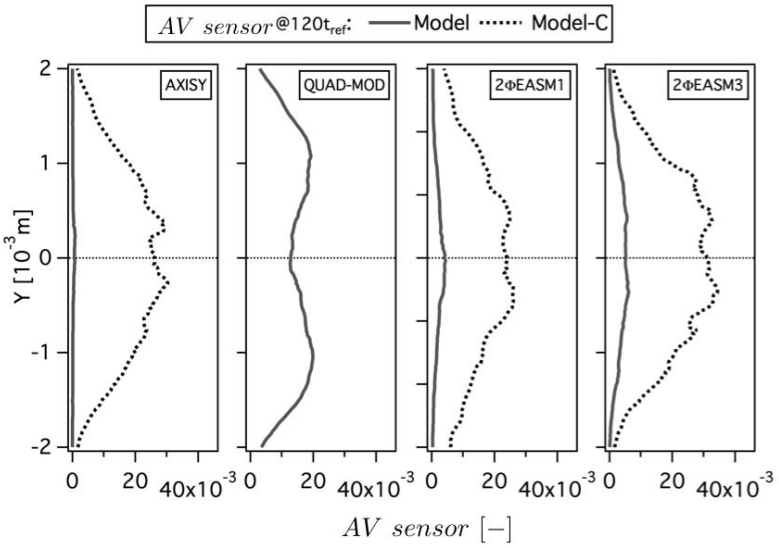

Figure 5.49: *Mean Artificial Viscosity sensor activation at $120t_{ref}$. LR_St3_# case.*

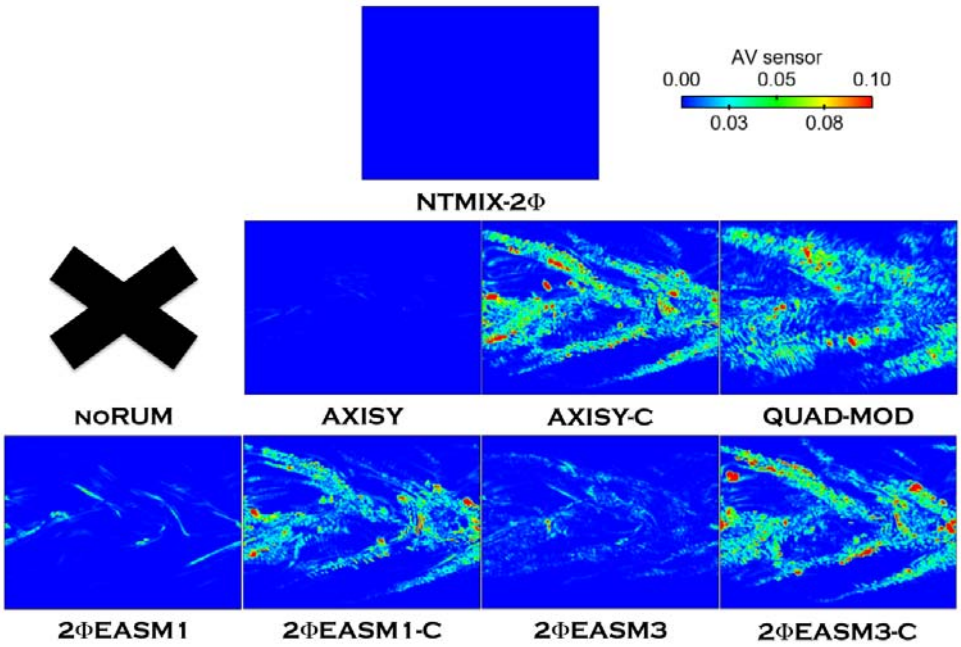

Figure 5.50: *Fields of Artificial Viscosity sensor activation at* $120t_{ref}$*. LR_St3_# case.*

5.4.2 Low inertia case: Stokes=0.33

Sections 5.3 and 5.4.1 have shown the results of the RUM models proposed in Chapter 4 in a low turbulence case for mean ($St \sim 1$) and high ($St \sim 3$) inertia respectively. From the assessment of the models, both qualitatively and quantitatively, two models (QUAD-MOD and 2ΦEASM3) have been identified as the ones giving the best performances when compared with the Lagrangian reference.

In this Section, the capability of QUAD-MOD and 2ΦEASM3 to correctly predict the low and high order moments in a case of low turbulence and low inertia is analyzed. The Reynolds number keeps the same ($Re^{ac} = 5500$) but the Stokes number is now $St \sim 0.33$. The particle relaxation time is $\tau_{fp}^F \sim 4.33$. This case is in fact an extreme case. Indeed, as already pointed out, the preferential concentration effect is maximal at $St = 0.3$, which creates empty spaces close to very high concentration spots. The steep concentration gradients between both zones are very difficult to handle numerically and the Artificial Diffusion is expected not to be powerful enough to diffuse them.

Only noRUM, VISCO, QUAD-MOD and 2ΦEASM3 models have been tested in this case. noRUM crashed shortly after $5t_{ref}$. In contrast to LR_St1_# and LR_St3_# cases, VISCO model was able to complete the whole simulation. This is due to the dependency of the model to $\breve{\tau}_p$ (Eq. 4.9). Since $\delta\breve{R}^*_{p,ij}$ is directly proportional to $\breve{\tau}_p$ in the VISCO model, the RUE production at small inertia (small particle response time) is reduced when decreasing the Stokes number. In this case, the overestimation of RUE observed in cases St=1 and St=3 is no longer present.

Results are shown at $80t_{ref}$. Complementary data at 5, 20 and $40t_{ref}$ can be found in Appendix E.

Figures 5.51(a) and 5.51(b) show the mean particle number density and the mean particle velocity profiles. Figure 5.52 shows the RMS particle number density and particle velocity profiles, included here for the sake of simplicity. Figure 5.53 shows the mean segregation profiles. The three models (VISCO, QUAD-MOD and 2ΦEASM3) give the same results for the low order moments, the mean and the RMS quantities and the segregation. The RMS particle number density and segregation profiles are underestimated by all models. There are no differences on the instantaneous fields either (Figs. 5.54 and 5.55). None of the models captures the empty spaces inside the slab as predicted by the Lagrangian reference. This is due to the reduced contribution of RUE in this configuration (as conjectured).

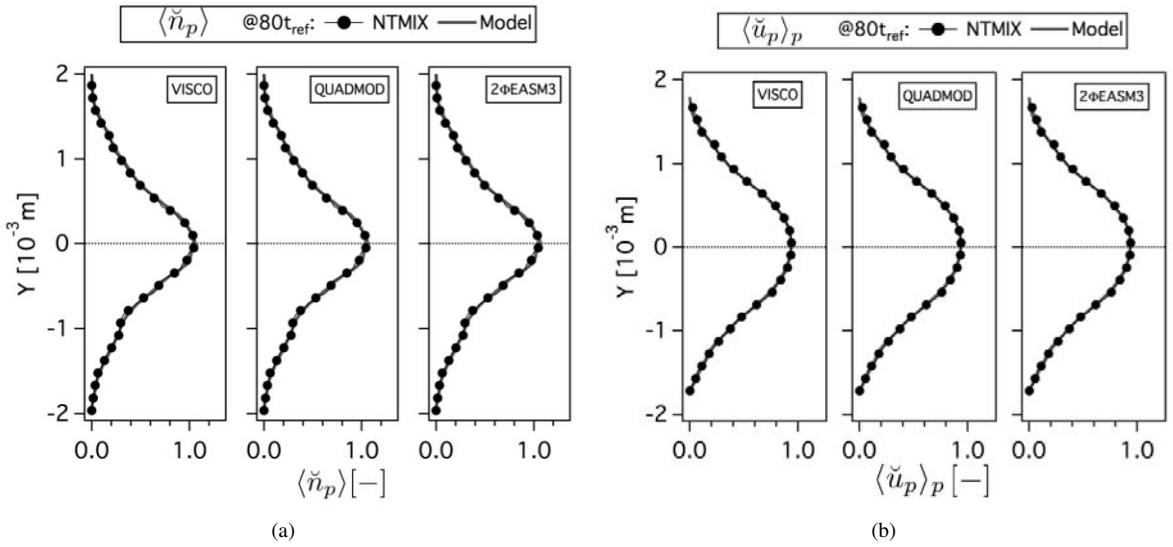

(a) (b)

Figure 5.51: *Comparison of Eulerian and Lagrangian (a) mean particle number density ($< \breve{n}_p >$, normalized by the initial particle number density at the center of the slab) and (b) mean particle velocity in X-direction ($< \breve{u}_p >_p$, normalized by the initial particle velocity in X-direction at the center of the slab) at $80t_{ref}$. LR_St033_# case.*

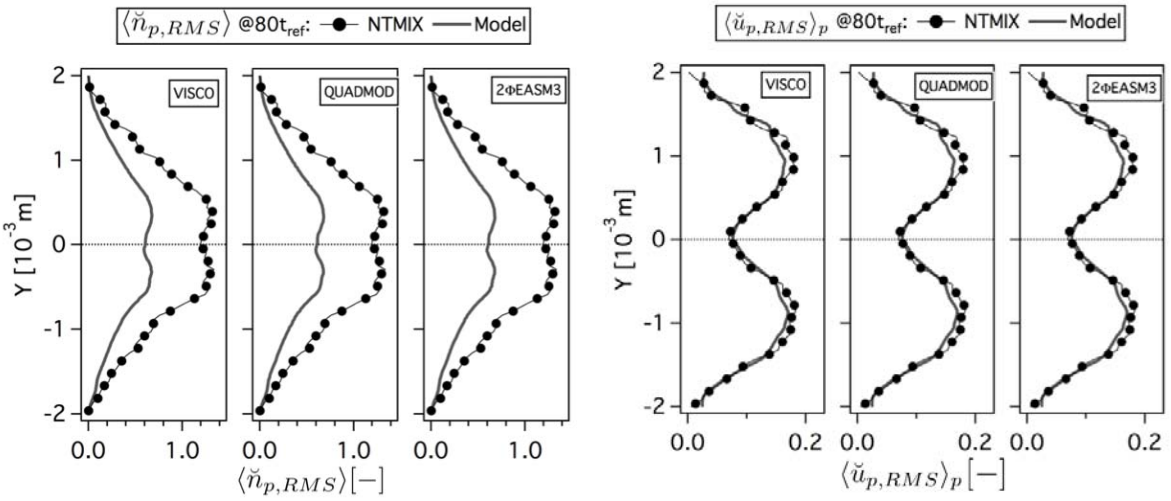

(a) (b)

Figure 5.52: *Comparison of Eulerian and Lagrangian (a) RMS particle number density ($< \breve{n}_{p,RMS} >$, normalized by the initial particle number density at the center of the slab) and (b) RMS particle velocity in X-direction ($< \breve{u}_{p,RMS} >_p$, normalized by the initial particle number density at the center of the slab) at 80t_{ref}. LR_St033_# case.*

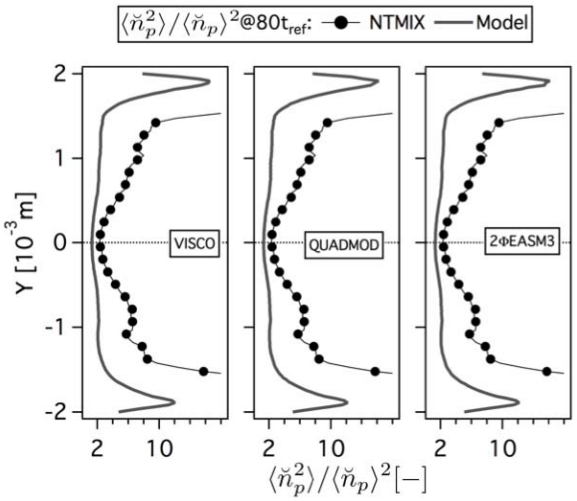

Figure 5.53: *Comparison of Eulerian and Lagrangian RMS particle segregation ($< \breve{n}_p^2 > / < \breve{n}_p >^2$) at 80$t_{ref}$. LR_St033_# case.*

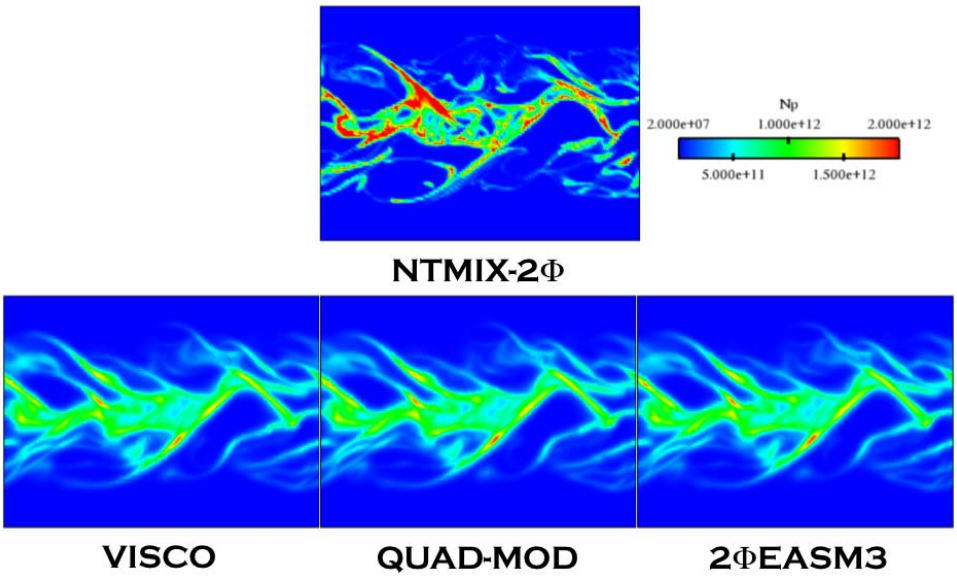

Figure 5.54: *Comparison of Lagrangian (NTMIX-2Φ) and Eulerian particle number density (N_p) at 80t_{ref}. LR_St033_# case.*

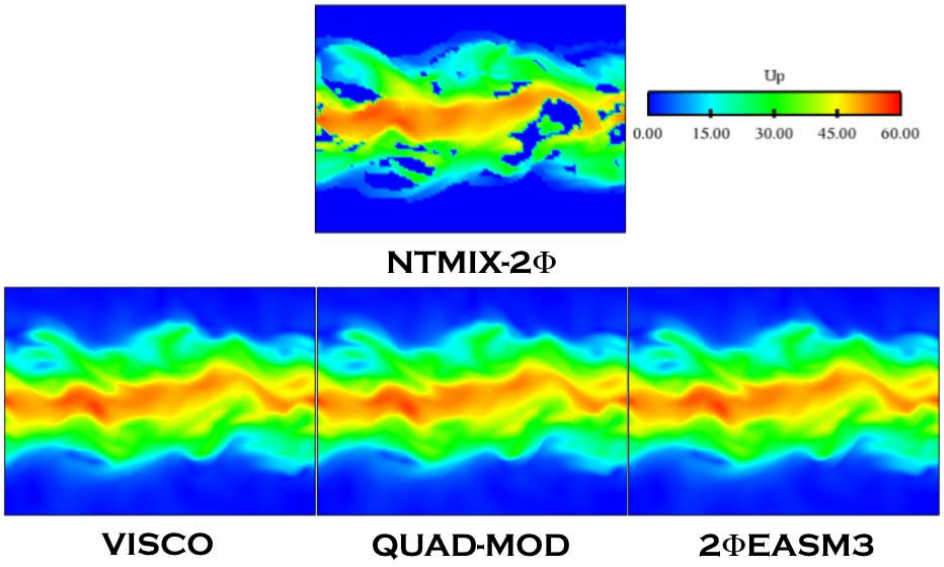

Figure 5.55: *Comparison of Lagrangian (NTMIX-2Φ) and Eulerian particle velocity magnitude (U_p) at 80t_{ref}. LR_St033_# case.*

Indeed, compared to $\breve{q}_p^2$, δq_p^2 is much smaller (Figs. 5.56(a) and 5.56(b)). The main contribution to the total particle agitation comes from the mesoscopic energy ($\breve{q}_p^2$) and thus the RUM has a very limited effect. However, Fig. 5.56(a) shows that VISCO is not able to produce the correct level of RUE. Even when the low order moments are well predicted, this model will not work in configurations with collisions or coalescence without being modified (besides the fact that it crashes for mean and high inertia). On the other hand, QUAD-MOD and 2ΦEASM3 provide very good agreement with the Lagrangian reference. They give very good results for the low order moments providing the correct repartition between the mesoscopic and the RUE at the same time. Indeed, the RUM productions (Fig. 5.57) as well as the deviatoric RUM tensor components (Figs. 5.58 and 5.59) are very accurately predicted by both models, whose results are in fact very similar.

The qualitative analysis of the instantaneous fields of RUE shows that, while VISCO underestimates the RUE, QUAD-MOD and 2ΦEASM3 correctly predict the locations where the RUE is predicted by NTMIX-2Φ. However, only the largest structures are reproduced. This is probably due to a lack of resolution of the Eulerian calculation (Dombard (2011)) which prevents from capturing the small structures caused by the high segregation.

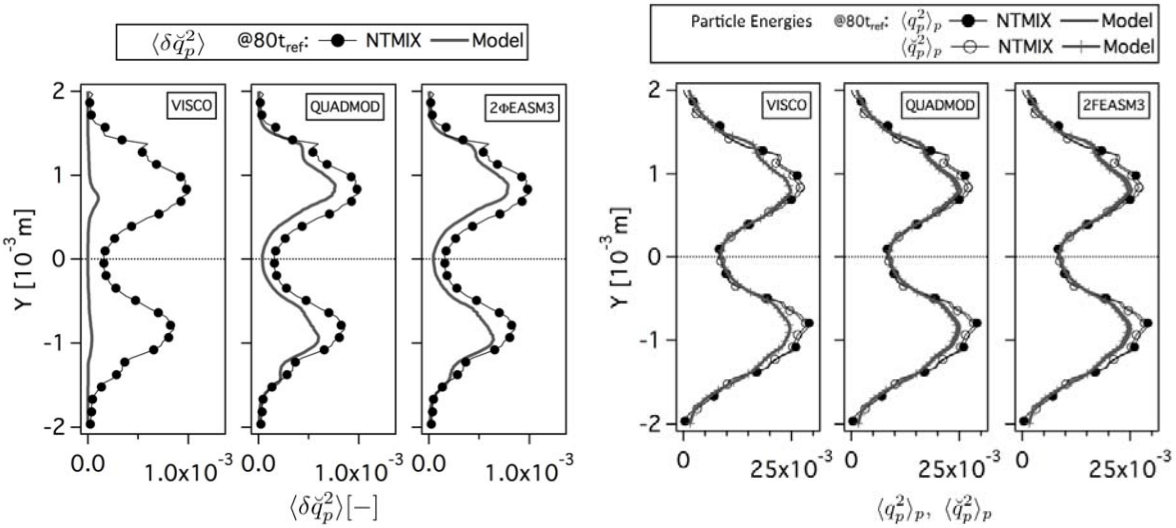

(a) (b)

Figure 5.56: *Comparison of Eulerian and Lagrangian (a) mean Random Uncorrelated Energy (δq_p^2) and (b) mean total (q_p^2) and mesoscopic ($\breve{q}_p^2$) particle energies at $80t_{ref}$. Normalized by the square of the initial particle velocity in X-direction at the center of the slab. LR_St033_# case.*

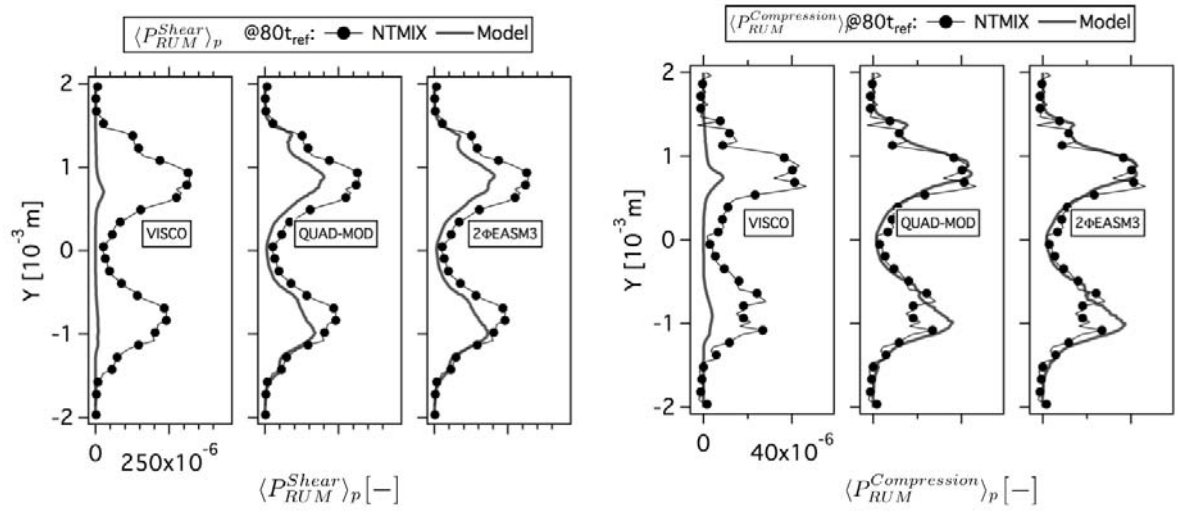

(a) (b)

Figure 5.57: *Comparison of Eulerian and Lagrangian (a) mean production of RUM energy by shear ($< P_{RUM}^{Shear} >_p$) and (b) mean productions of RUM energy by compression ($< P_{RUM}^{Compression} >_p$) at 80$t_{ref}$. Normalized by the square of the initial particle velocity in X-direction at the center of the slab and the reference time (t_{ref}). LR_St033_# case.*

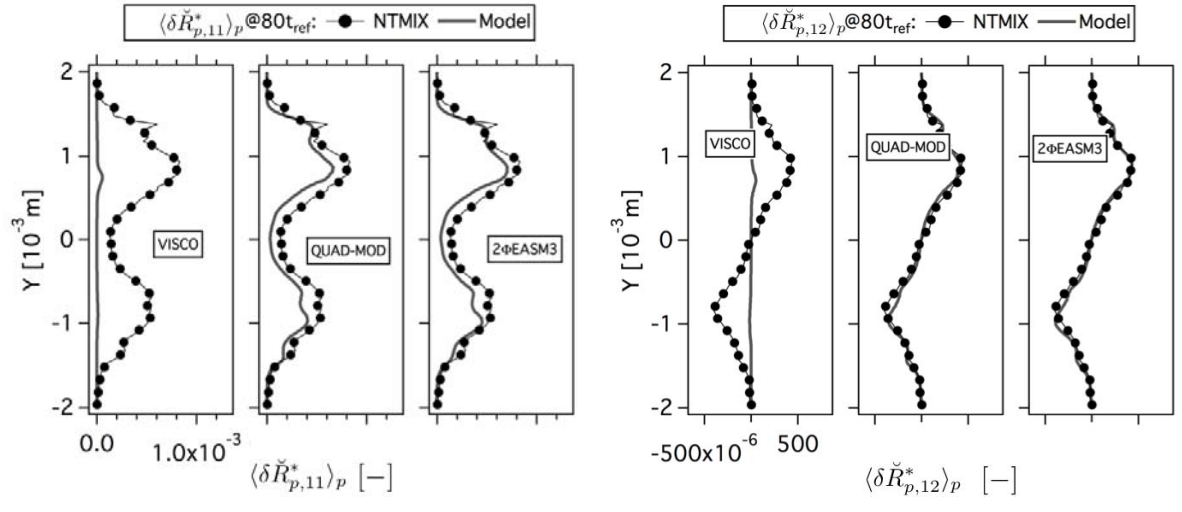

(a) (b)

Figure 5.58: *Comparison of Eulerian and Lagrangian (a) mean deviatoric RUM stress tensor XX component ($< \delta \breve{R}_{p,11}^* >_p$) and (b) mean deviatoric RUM stress tensor XY component ($< \delta \breve{R}_{p,12}^* >_p$) at 80$t_{ref}$. Normalized by the square of the initial particle velocity in X-direction at the center of the slab. LR_St033_# case.*

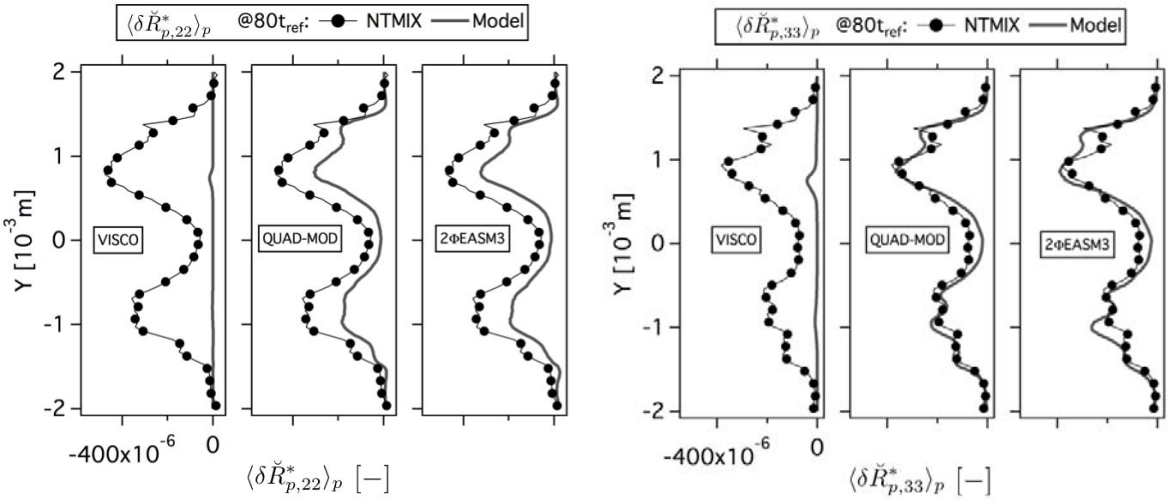

(a) (b)

Figure 5.59: *Comparison of Eulerian and Lagrangian (a) mean deviatoric RUM stress tensor YY component ($< \delta \breve{R}^*_{p,22} >_p$) and (b) mean deviatoric RUM stress tensor ZZ component ($< \delta \breve{R}^*_{p,33} >_p$) at 80$t_{ref}$. Normalized by the square of the initial particle velocity in X-direction at the center of the slab. LR_St033_# case.*

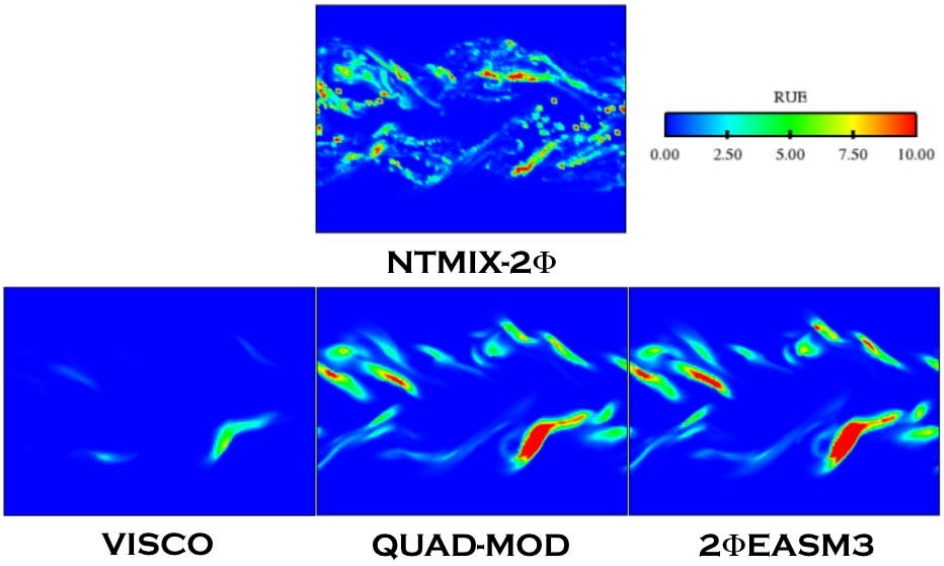

Figure 5.60: *Comparison of Lagrangian (NTMIX-2Φ) and Eulerian Random Uncorrelated Energy (δq_p^2) at 80t_{ref}. LR_St033_# case.*

5.5 High turbulent conditions

The performances of QUAD-MOD and 2ΦEASM3 models have been until now validated in a low turbulence case for three different inertia. However, the Reynolds numbers encountered in industrial configurations are very high and flows are, in general, much more turbulent. In this Section, both models are evaluated in a higher turbulence case ($Re^{ac} = 20000$, $St \sim 1$, $\tau_{fp}^F \sim 9.44$). This study aims at assessing the validity of these models and their application in more complex cases such as the MERCATO test rig presented in Part IV.

From the *a priori* results, it is expected that the interaction of the particle phase with the vortical structures of the carrier phase (stronger that in case LR_St1_#) will create much more smaller structures in the dispersed phase fields that in the low turbulence case. The entrainment of the particles by the eddies will create very thin filaments that will afterwards detach from the jet. The capability of QUAD-MOD and 2ΦEASM3 to capture this kind of small structures is analyzed in this Section.

The Euler-Lagrange simulation of this case has been performed in a 256^3 mesh (i.e. the resolution has been doubled compared to the low turbulence computations). This means that in order to achieve the same level of comparison as for the previous sections, it may be necessary to double the resolution of the grid used in the Eulerian simulations of this case.

Figure 5.61 shows the statistics for the particle number density and particle velocity at $70t_{ref}$ ($7.41\tau_{fp}^F$). The agreement with the Lagrangian reference is again very good for both models. They also give very good results in the RMS particle velocity (Fig. 5.62(b)). However, the levels obtained for the RMS particle number density (Fig. 5.62(a)) are too low. Figure 5.63 shows the segregation profiles. Both models give the same results. The segregation levels are too low compared to the reference. This behavior has already been observed in the low turbulence cases. It is again probably due to a lack of resolution.

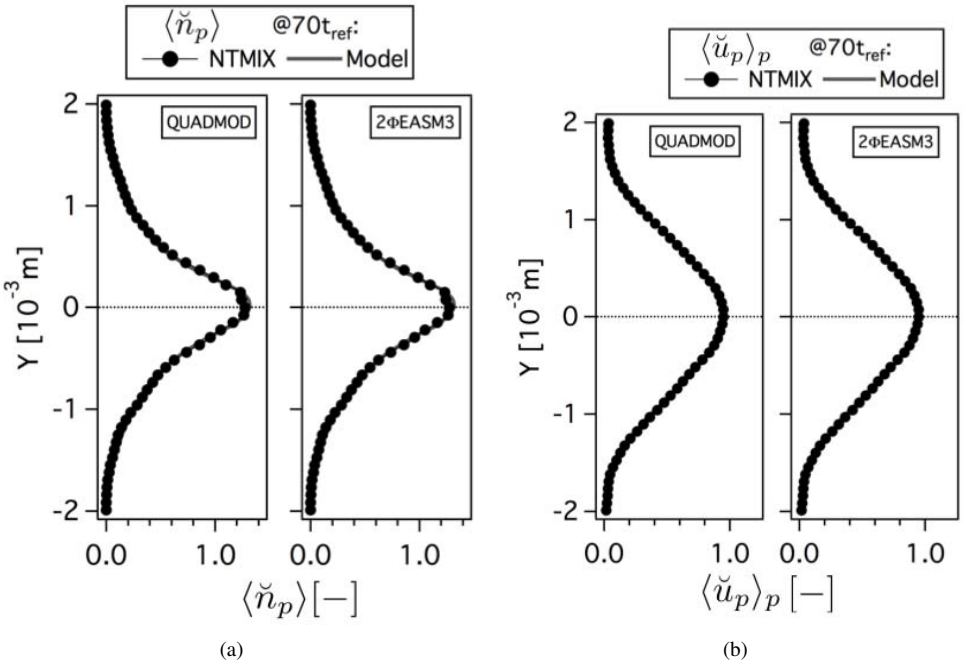

(a) (b)

Figure 5.61: *Comparison of Eulerian and Lagrangian (a) mean particle number density ($< \breve{n}_p >$, normalized by the initial particle number density at the center of the slab) and (b) mean particle velocity in X-direction ($< \breve{u}_p >_p$, normalized by the initial particle velocity in X-direction at the center of the slab) at $70t_{ref}$. HR_St1_# case.*

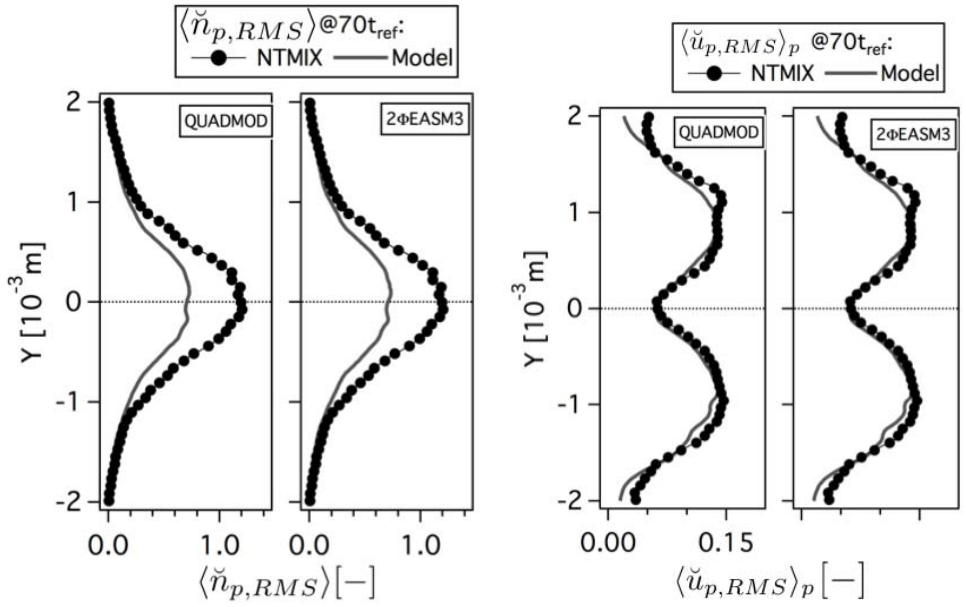

(a) (b)

Figure 5.62: *Comparison of Eulerian and Lagrangian (a) RMS particle number density (*$< \breve{n}_{p,RMS} >$*, normalized by the initial particle number density at the center of the slab) and (b) RMS particle velocity in X-direction (*$< \breve{u}_{p,RMS} >_p$*, normalized by the initial particle number density at the center of the slab)at 70*t_{ref}*. HR_St1_# case.*

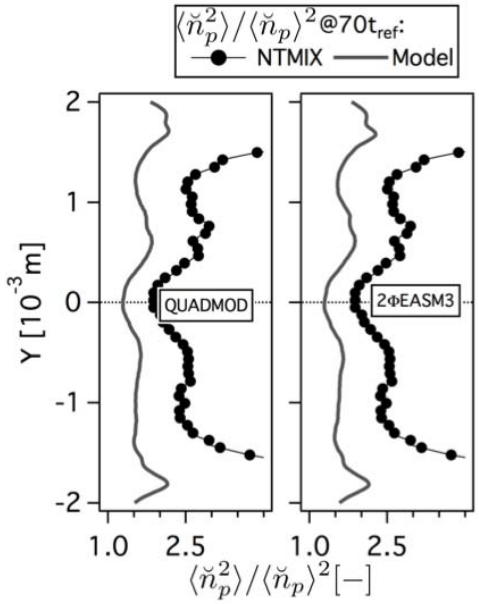

Figure 5.63: *Comparison of Eulerian and Lagrangian RMS particle segregation (*$< \breve{n}_p^2 > / < \breve{n}_p >^2$*) at 70*$t_{ref}$*. HR_St1_# case.*

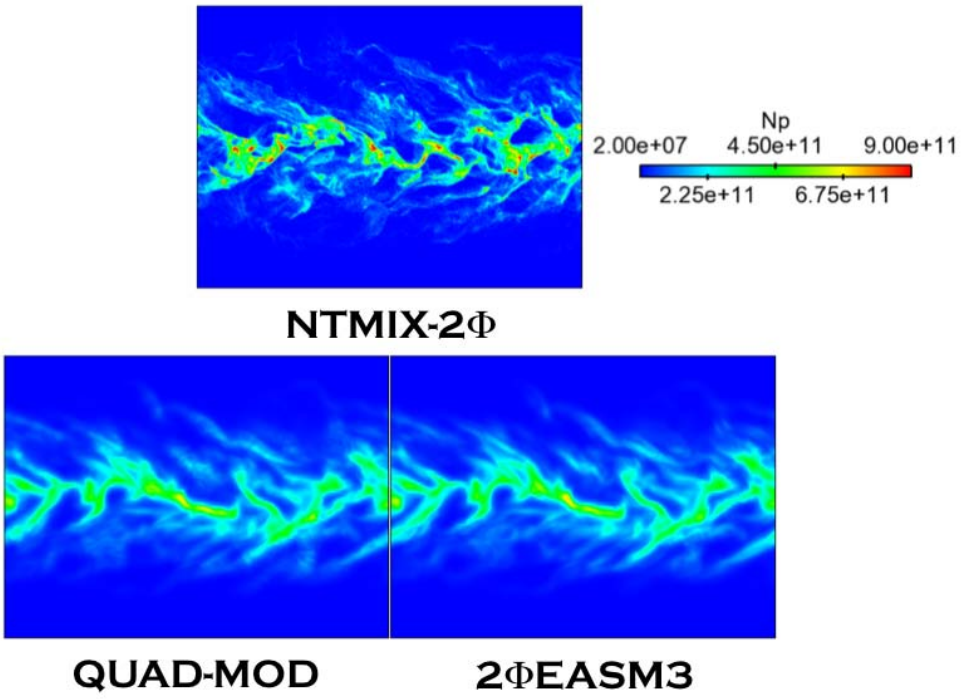

Figure 5.64: *Comparison of Lagrangian (NTMIX-2Φ) and Eulerian particle number density (N_p) at 70t_{ref}. HR_St1_# case.*

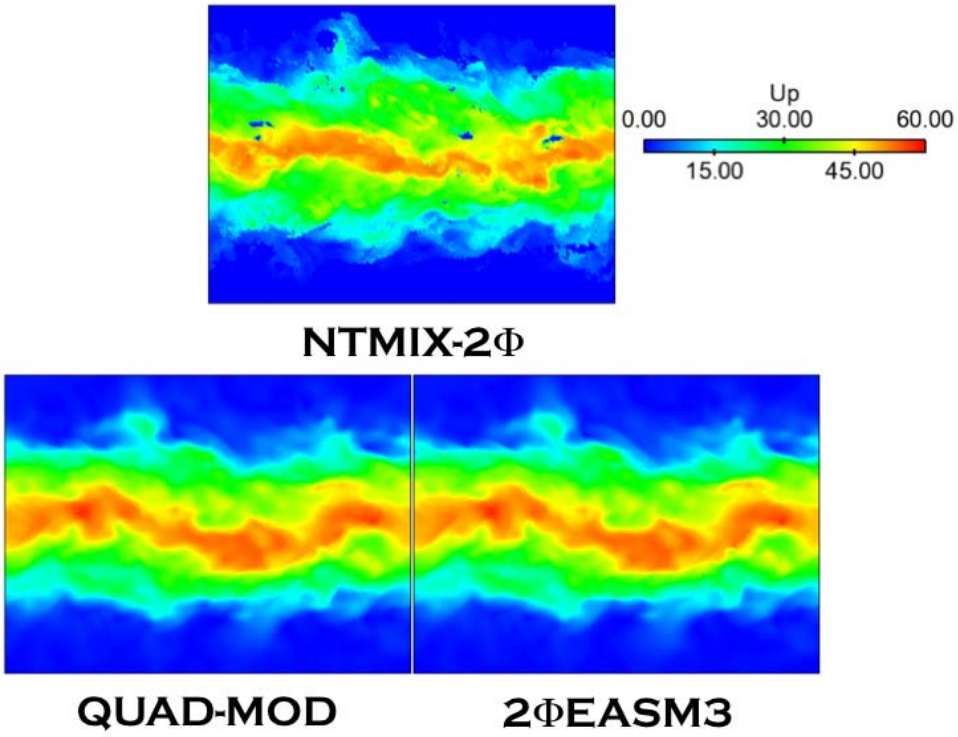

Figure 5.65: *Comparison of Lagrangian (NTMIX-2Φ) and Eulerian particle velocity magnitude (U_p) at 70t_{ref}. HR_St1_# case.*

Although the resolution of the Eulerian grid may not be enough, both models show good agreement for the profiles of RUE (Fig. 5.66(a)). However, none of them captures the level reached at the upper border of the jet. Nevertheless, both closures are able to reproduce the non-symmetric profile. The production by shear (Fig. 5.67(a)) is well predicted by both models. $\delta\breve{R}^*_{p,12}$ is equally well reproduced (Fig. 5.68(b)). 2ΦEASM3 provides better agreement for the production by compression (Fig. 5.67(b)), which may come from a better balance between the components belonging to the diagonal of the deviatoric RUM tensor. Even when at first sight QUAD-MOD seems to provide better agreement, its level is good for $\delta\breve{R}^*_{p,11}$ and $\delta\breve{R}^*_{p,22}$ components and too low for $\delta\breve{R}^*_{p,33}$. On the other hand, 2ΦEASM3 gives very good $\delta\breve{R}^*_{p,22}$ results and an overestimation of the $\delta\breve{R}^*_{p,11}$ and $\delta\breve{R}^*_{p,33}$ components. But the total balance between both terms is better than for QUAD-MOD.

Finally, the analysis of the instantaneous fields confirms that both models give very similar results.

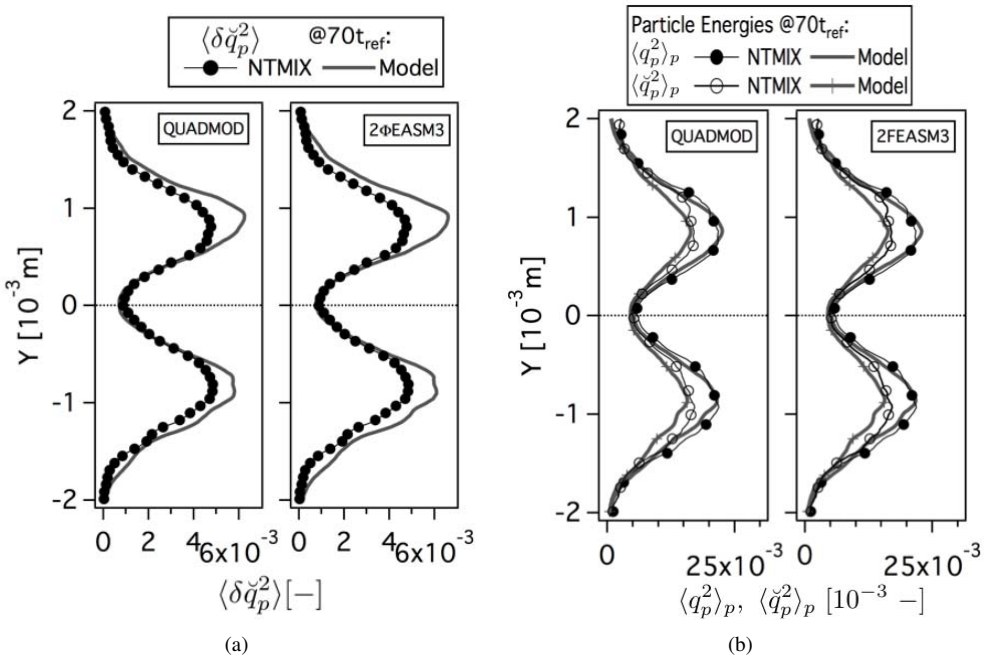

Figure 5.66: *Comparison of Eulerian and Lagrangian (a) mean Random Uncorrelated Energy (δq_p^2) and (b) mean total (q_p^2) and mesoscopic ($\langle\breve{q}_p^2\rangle_p$) particle energies at 70t_{ref}. Normalized by the square of the initial particle velocity in X-direction at the center of the slab. HR_St1_# case.*

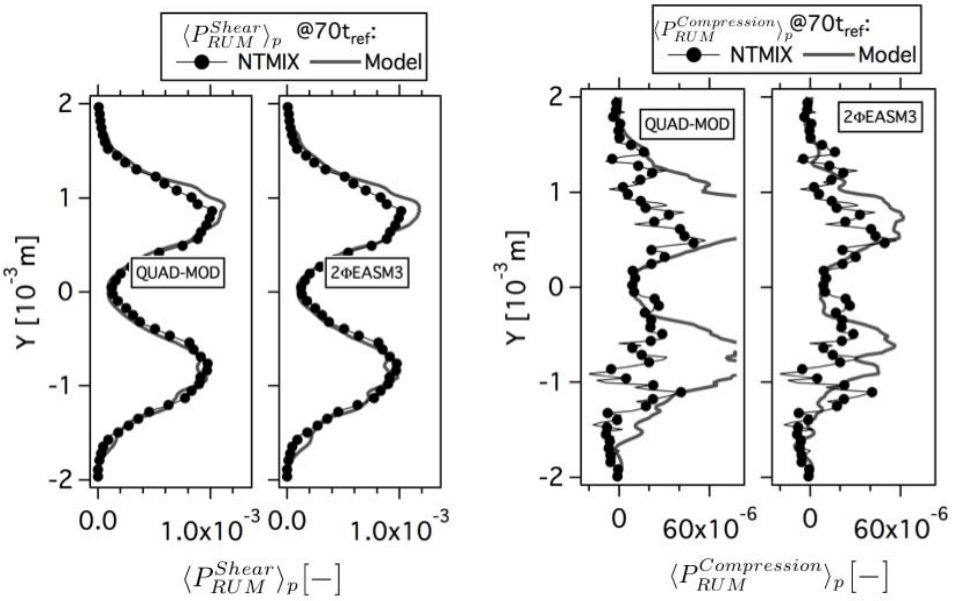

(a) (b)

Figure 5.67: *Comparison of Eulerian and Lagrangian (a) mean production of RUM energy by shear ($< P_{RUM}^{Shear} >_p$) and (b) mean productions of RUM energy by compression ($< P_{RUM}^{Compression} >_p$) at 70$t_{ref}$. Normalized by the square of the initial particle velocity in X-direction at the center of the slab and the reference time (t_{ref}). HR_St1_# case.*

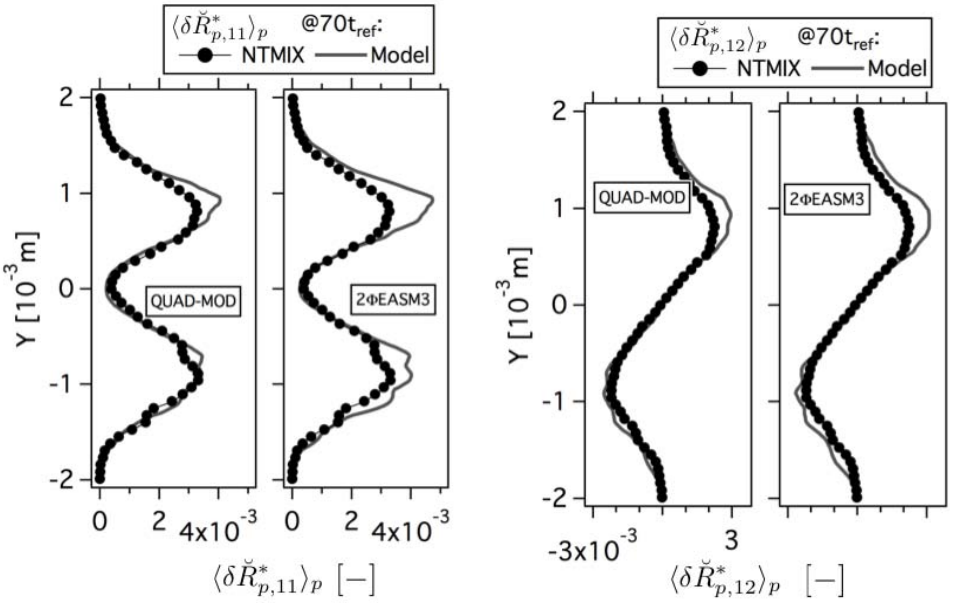

(a) (b)

Figure 5.68: *Comparison of Eulerian and Lagrangian (a) mean deviatoric RUM stress tensor XX component ($< \delta \breve{R}_{p,11}^{*} >_p$) and (b) mean deviatoric RUM stress tensor XY component ($< \delta \breve{R}_{p,12}^{*} >_p$) at 70$t_{ref}$. Normalized by the square of the initial particle velocity in X-direction at the center of the slab. HR_St1_# case.*

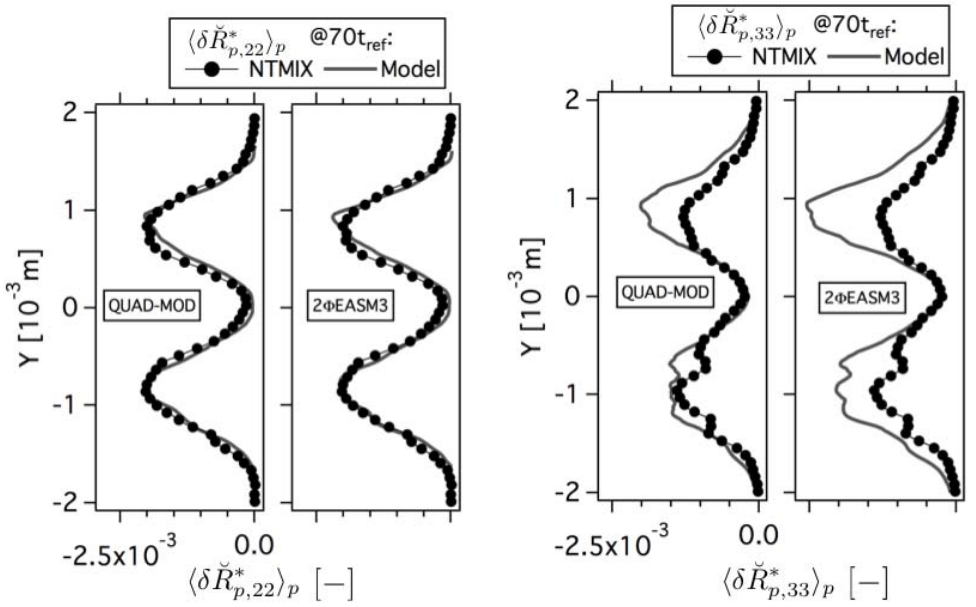

(a) (b)

Figure 5.69: *Comparison of Eulerian and Lagrangian (a) mean deviatoric RUM stress tensor YY component ($< \delta \breve{R}^*_{p,22} >_p$) and (b) mean deviatoric RUM stress tensor ZZ component ($< \delta \breve{R}^*_{p,33} >_p$) at 70$t_{ref}$. Normalized by the square of the initial particle velocity in X-direction at the center of the slab. HR_St1_# case.*

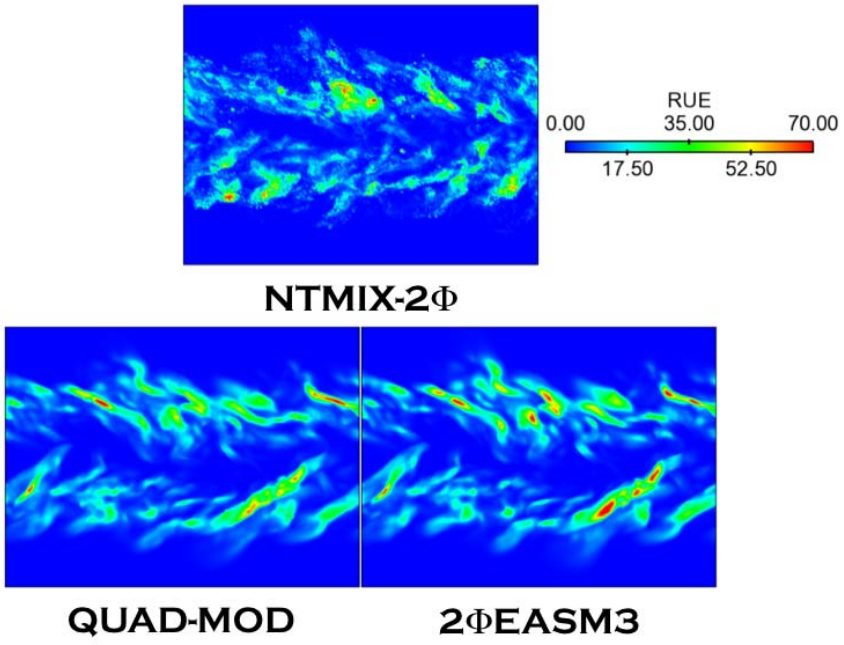

Figure 5.70: *Comparison of Lagrangian (NTMIX-2Φ) and Eulerian Random Uncorrelated Energy ($\delta \breve{q}_p$) at 70t_{ref}. HR_St1_# case.*

5.5.1 Effect of mesh resolution

Case HR_St1 has been computed on a higher resolution mesh grid (512^3 computational cells) with AVBP for 2ΦEASM3 model. Results are compared with the lower resolution mesh (256^3) and with the reference (Eulerian fields obtained by projection from Euler-Lagrange simulation performed on a 256^3 grid). Due to computational limitations in time and memory, the simulation has only been performed up to $40t_{ref}$ and only the fields of particle number density, particle velocity and RUE stored. The fields corresponding to the RUM stress tensor components and the productions are not accesible for this simulation.

Figures 5.71(a) and 5.71(b) shows the plane averages of the mesoscopic particle number density and particle velocity respectively. Increasing the mesh resolution does not have an impact on the statistics of these two quantities. Indeed, no noticeable difference exists on the profiles of the mean quantities. On the contrary, the profiles of the RMS quantities (Figs. 5.72(a) and 5.72(b)) are improved when using a higher resolution mesh for the computations. The RMS particle number density is improved of 25% approximately. The improvement on the RMS particle velocity is much more reduced. This improvement is transposed to the segregation profiles too (Fig. 5.73). The segregation level is highly increased at the center of the slab and the level of the maximal peaks at the periphery is greatly increased too. Thus, the agreement with the reference is improved.

Increasing the resolution of the mesh has a negative impact on the RUE profile (Fig. 5.74(a)). Indeed, the level of uncorrelated energy increases, which produces an overestimation of the RUE already overestimated with the lower resolution mesh. Nevertheless, the level increase is not very high and at the same time the mesoscopic energy statistics are improved (Fig. 5.74(b)). This leads to a slight overestimation of the total particle agitation, which is very accurately captured with the lower-resolution mesh (Fig. 5.74(c)).

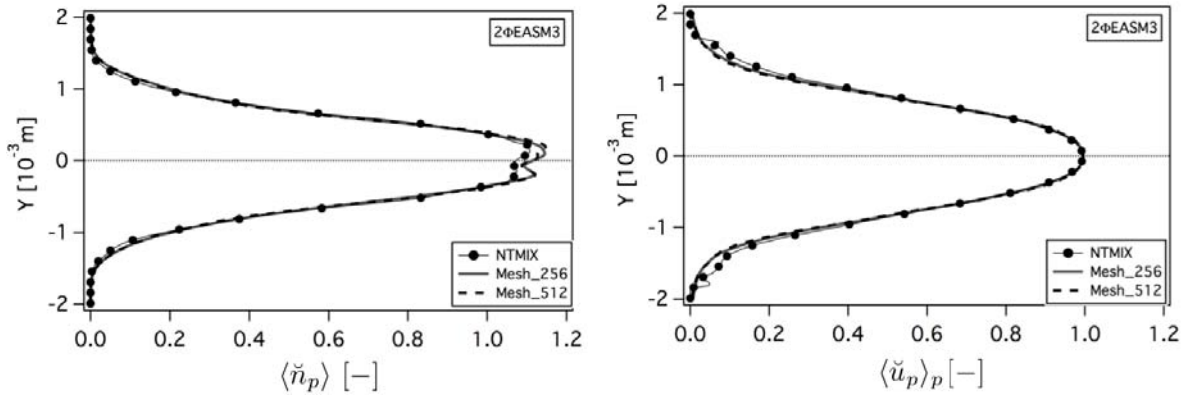

(a) Non-dimensional mean particle number density.

(b) Non-dimensional mean particle velocity.

Figure 5.71: *Comparison Lagrangian and Eulerian results. The Lagrangian computation has been performed in a* 128^3 *mesh grid. Mesh_256 corresponds to the Eulerian simulation on a* 256^3 *mesh and Mesh_512 to an Eulerian simulation on a* 512^3 *mesh.*

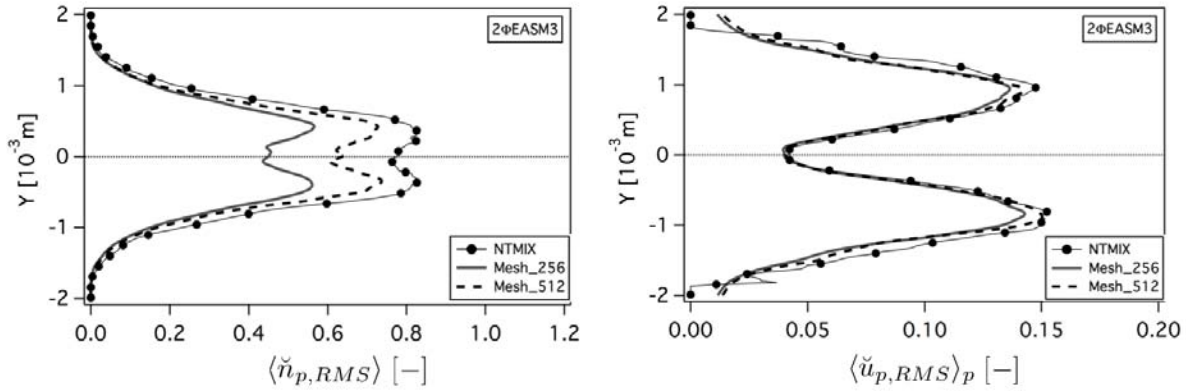

(a) Non-dimensional RMS particle number density.

(b) Non-dimensional RMS particle velocity.

Figure 5.72: *Comparison Lagrangian and Eulerian results. The Lagrangian computation has been performed in a* 128^3 *mesh grid. Mesh_256 corresponds to the Eulerian simulation on a* 256^3 *mesh and Mesh_512 to an Eulerian simulation on a* 512^3 *mesh.*

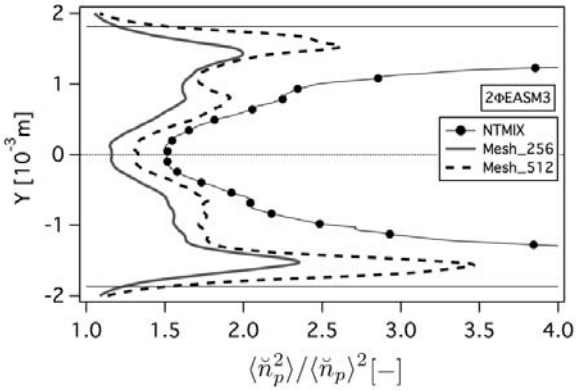

Figure 5.73: *Comparison Lagrangian and Eulerian particle segregation. The Lagrangian computation has been performed in a* 128^3 *mesh grid. Mesh_256 corresponds to the Eulerian simulation on a* 256^3 *mesh and Mesh_512 to an Eulerian simulation on a* 512^3 *mesh.*

Regarding the qualitative comparison of the instantaneous fields, the structures of particle number density (Fig. 5.75) are more defined when increasing the resolution, the diffusion seems to be reduced and thus the empty spaces and high concentration spots are better captured. However, the overall appearence of the fields has not changed much. Changes are even less obvious in the case of the particle velocity fields (Fig. 5.76), the fields corresponding to the Eulerian simulations with the two computational meshes are very similar and changes appear but may be due to small differences on the physical times of the simulations. The RUE field corresponding to the high resolution mesh (Fig. 5.77) is more defined than the one corresponding to the lower resolution grid. More small structures are present and the size of the spots of very high RUE has been reduced. This seems to be in disagreement with the increased level of the RUE average profiles (cf Fig. 5.74(a)), however, the number of small structures in the field has considerably increased which increases the global RUE level.

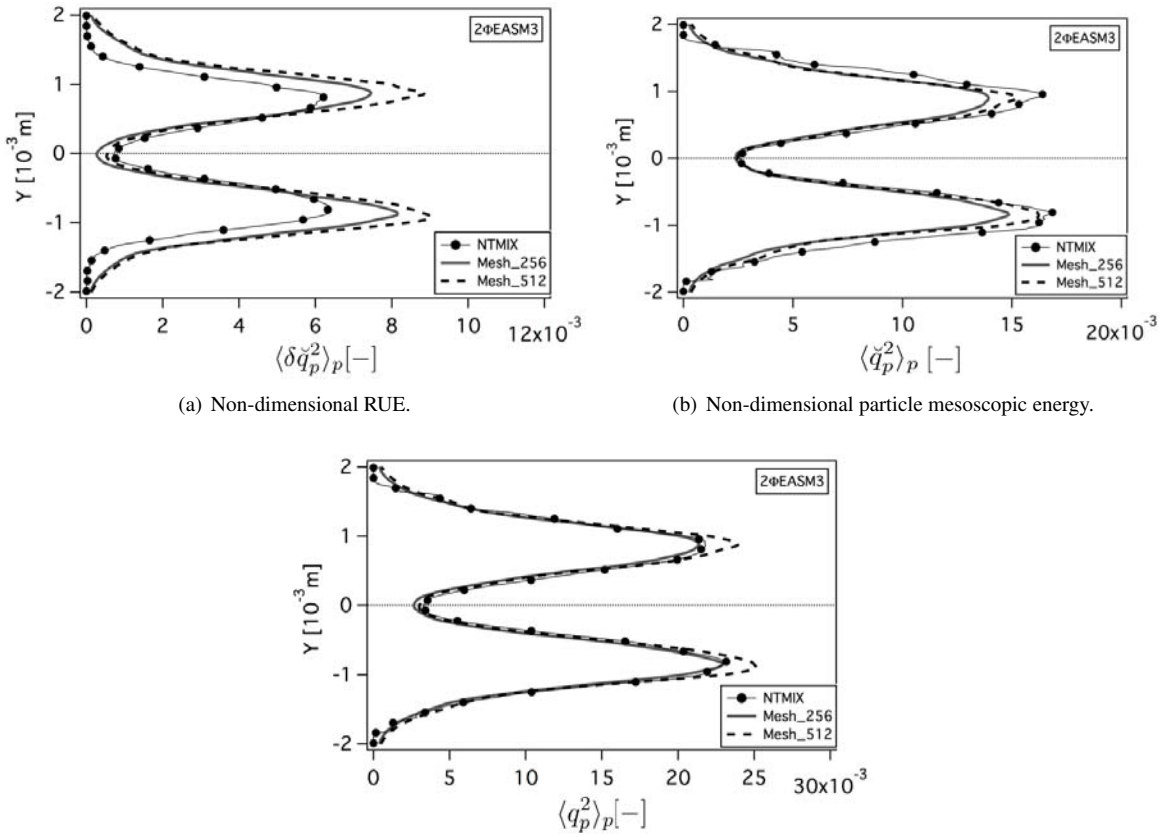

(a) Non-dimensional RUE.

(b) Non-dimensional particle mesoscopic energy.

(c) Non-dimensional total particle energy.

Figure 5.74: *Comparison Lagrangian and Eulerian results. The Lagrangian computation has been performed in a* 128^3 *mesh grid. Mesh_256 corresponds to the Eulerian simulation on a* 256^3 *mesh and Mesh_512 to an Eulerian simulation on a* 512^3 *mesh.*

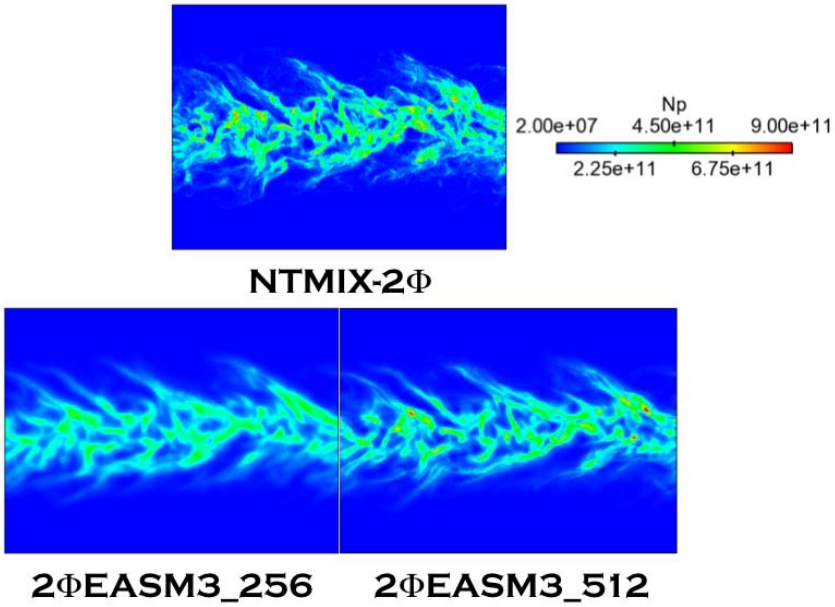

Figure 5.75: *Comparison Lagrangian and Eulerian particle number density instantaneous fields at* $40t_{ref}$*. The Lagrangian computation has been performed in a* 128^3 *mesh grid. 2ΦEASM3_256 corresponds to the Eulerian simulation on a* 256^3 *mesh and 2ΦEASM3_512 to an Eulerian simulation on a* 512^3 *mesh.*

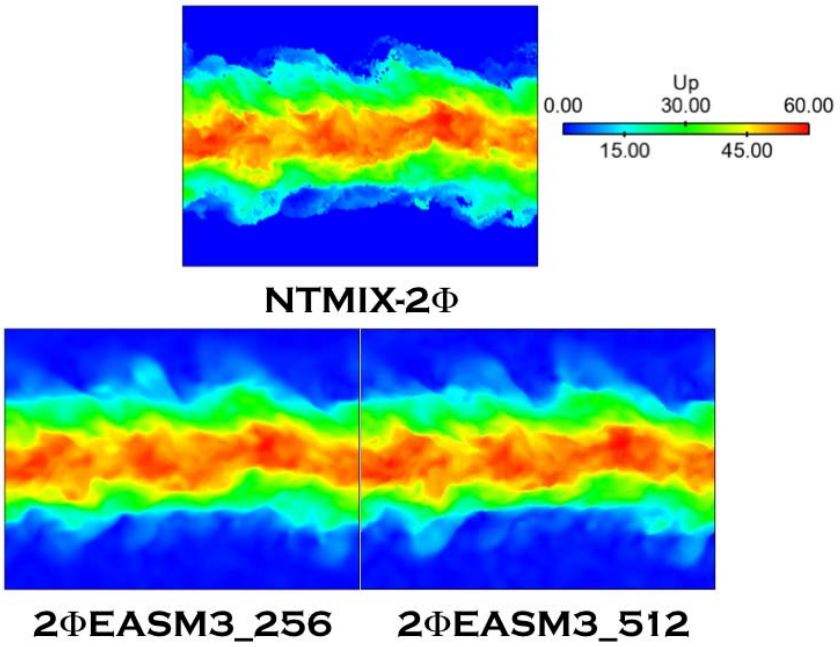

Figure 5.76: *Comparison Lagrangian and Eulerian particle velocity instantaneous fields at* $40t_{ref}$*. The Lagrangian computation has been performed in a* 128^3 *mesh grid. 2ΦEASM3_256 corresponds to the Eulerian simulation on a* 256^3 *mesh and 2ΦEASM3_512 to an Eulerian simulation on a* 512^3 *mesh.*

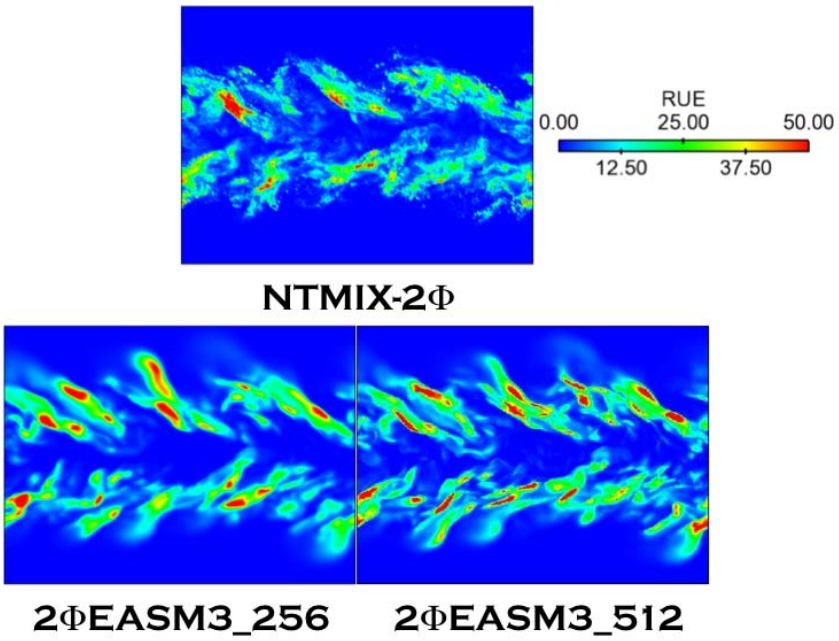

Figure 5.77: *Comparison Lagrangian and Eulerian RUE instantaneous fields at* $40t_{ref}$*. The Lagrangian computation has been performed in a* 128^3 *mesh grid. 2ΦEASM3_256 corresponds to the Eulerian simulation on a* 256^3 *mesh and 2ΦEASM3_512 to an Eulerian simulation on a* 512^3 *mesh.*

5.6 Conclusions

The different approaches for the modelisation of the deviatoric RUM tensor presented in Chapter 4 have been *a posteriori* validated in a configuration with mean shear. Comparisons with *a priori* results issued from exact Lagrangian calculations projected onto an Eulerian grid have been carried out for two levels of turbulence ($Re^{ac} = 5000,\ 20000$) and three levels of inertia ($St \sim 0.33,\ 1,\ 3$). The observations resulting from these tests are:

- The model based on a viscosity assumption and $\breve{\tau}_p$ as timescale, VISCO, crashes after a few iterations in all cases except for the low inertia case (LR_St0.33_#). When performing simulations without taking into account the contribution of the RUM (noRUM), only the low turbulence unity Stokes number case (LR_St1_#) is able to complete the simulation. If the turbulence is increased or the Stokes number changed, the simulation crashes before reaching the end. The rest of the models presented have been tested in low Reynolds, mean and high Stokes numbers with success (LR_St0.33_# and LR_St3_#).
- The results obtained in LR_St1_# and LR_St3_# cases show that AXISY model is too diffusive due to an overestimation of the RUE level. The correction (AXISY-C) improves the results by reducing the RUE levels and thus the diffusion of the particle number density and particle velocity fields. The overestimation of RUE seems to be characteristic of the linear models (VISCO and AXISY). Increasing the order of the model (QUAD-MOD) clearly improves the results. Indeed, from the comparisons performed in Sections 5.3 and 5.4.1, QUAD-MOD has been identified as one of the models to be retained.
- 2ΦEASM1 underestimates the RUE level at low turbulence and mean inertia. It gives better results when increasing the inertia. The correction (2ΦEASM1-C) has a very limited effect for this model. 2ΦEASM3 gives very good results at low turbulence for mean and high inertia and for higher turbulence and mean inertia. This model is to be retained for future simulations. In this case, the correction (2ΦEASM3-C) reduces the RUE level yielding a degradation of the results.
- For low turbulence and low inertia limit case (LR_St0.33_#) both QUAD-MOD and 2ΦEASM3 correctly downgrade: the RUM is reduced, giving accurate results. The two models have also been tested in a mean inertia and high turbulence case (HR_St1_#), also providing good agreement with the Lagrangian reference.

Special attention must be paid to artificial dissipation:

- AD is needed for all models at the beginning to numerically stabilize the simulation due to the presence of too steep gradients on the borders of the slab that the centered scheme TTGC is unable to handle.
- A link between the AD and the RUM has been observed: AD activates in the zones where RUE should be produced but is not because RUM has not been accounted for or because the RUM model behaves uncorrectly. The models that overestimate the RUE show very low levels of AD and *vice versa*.
- Although the models that underestimate RUE produce good results of the low order moments, AD is not able to substitute the RUM contribution in terms of high order moments and numerical stability.

The effect of the resolution needed to perform two-phase Eulerian calculations has also been adressed. Cases LR_St1_2ΦEASM3 and HR_St1_2ΦEASM3 have been simulated on a 512^3 grid. Due to limited computational resources, the simulations have been carried out until $40t_{ref}$ only. The profiles of mean and RMS particle number density and particle velocity, segregation and mean RUE have been compared with the simulations performed on the lower resolution (256^3) grid and the Lagrangian reference. Dombard (2011) studied the effect of the mesh resolution on this configuration showing that it has an important impact on the statistics of the high order moments. This statement has been confirmed by the results presented here. The mean particle number density and particle velocity statistics are not affected by the increase in mesh resolution. However, the instantaneous fields of particle number density are highly improved. The presence of small structures is better captured whit the 512^3 grid. The location of the spots of high and low particle concentration are better reproduced and the diffusion is reduced. The simulations in the higher resolution mesh provide a better prediction of the RMS particle number density

and particle velocity, especially on the higher turbulence simulation where the particle number density fluctuation level (very underestimated by the lower grid resolution simulation) is highly improved. The impact on the RMS particle velocity is much more limited. The RUE instantaneous fields are also improved when the grid resolution is increased. The shape of the Lagrangian field is better reproduce and the presence and location of the small structures are better captured. However, the mean RUE profiles are slightly overestimated by the higher resolution simulations, while the total particle agitation is less affected.

The presence of wiggles in the instantaneous fields for the QUAD-MOD model provided a reason to choose between 2ΦEASM3 and QUAD-MOD to perform the simulations of the configuration presented in Part IV. Those wiggles are due to high frequency oscillations coming from numerical errors and potential low grid resolution, which makes the simulation susceptible to numerical instabilities or to the need of additional AD. The reason why they only appear in QUAD-MOD has not been identified yet. It may mean that this particular model needs a higher resolution than the rest of the models. The simulations on a 512^3 mesh with QUAD-MOD have not been performed during this work due to a lack of time and computational resources.

Finally, the 2ΦEASM3 model provides very good agreement with the Lagrangian reference for all the cases tested. This model represents a good compromise in terms of reproduction of physical phenomena and AD. The model has been implemented in the code AVBP. On the short term, deeper analysis of the link between the RUM and the AD is however necessary for future studies. Recently, new AV sensors have been implemented in AVBP (Vié (2010)) which have proven to provide good results on particle-laden HIT and two-dimensional particle-laden spatial jet configurations (Dombard (2011)). On the mean and long term, the implementation of high-order upwind numerical schemes (de Chaisemartin (2009), Kah (2010)) in AVBP may solve the issues related to AD, providing simpler analysis of the performances of the RUM models.

Masi (2010) studied the impact of LES in the configuration studied here. The performances of the models were assessed and the coefficients of the dispersed phase turbulent viscosity model developed by Moreau (2006) adjusted. The model proposed by Moreau (2006) was implemented in AVBP by Riber (2007). The same study presented here in the case of a DNS approach needs to be conducted in the LES context in order to further validate the RUM models with the perspective of their application to LES simulations of industrial configurations.

2ΦEASM3 model correctly reproduces the level of RUE in this configuration, which allows the consideration of collisions in two-phase flows simulations, which was not the case of the model available until now (VISCO). The modification of the dispersed transport equations in not extremely difficult and Masi (2010) provided an extense Lagrangian data base on a colliding particle-laden turbulent planar jet which may be used for validation purposes as has been done here.

The effect of the grid resolution needs further analysis. First, it is desirable to perform simulations on the higher resolution mesh grid both with the Euler-Lagrange and the Euler-Euler approaches with the condition of being able to obtain detailed information on the deviatoric RUM stress tensor components and RUM production terms. Indeed, comparisons between Euler-Euler and Euler-Lagrange simulations performed with the same mesh resolution eliminates a possible source of differences between the simulations. Having access to the tensor components and production terms allows a deeper comparison.

Masi (2010) performed an analysis of the performances of the RUM models in the context of the LES of the particle-laden temporal planar jet configuration studied here. The results showed that 2ΦEASM3 behaves correctly when applied along with the model of Moreau (2006) for the dispersed phase turbulent viscosity (with minor modifications). This justifies the application of the 2ΦEASM3 model to the LES of the MERCATO configuration presented in Part IV. However, an *a posteriori* validation of the RUM models in the configuration presented her using LES is of great importance. Due to a lack of time, it has not been done during this work, but it is planned for the future.

Finally, the application of 2ΦEASM3 model to a complex semi-academic configuration is on sight. The configurations of Hishida *et al.* (1987) or Sommerfeld & Qiu (1993) are good candidates for this task. For both configurations, experimental data are available. For the configuration of Sommerfeld & Qiu (1993), numerical data obtained from Euler-Lagrange simulations (Apte *et al.* (2003*b*)) are available too. The Euler-Euler LES of both simulations with 2ΦEASM3 model is in prospect at CERFACS.

Lire la seconde partie de la thèse